# Ultra-Light Photovoltaic Composite Sandwich Structures

THÈSE N$^{O}$ 4138 (2008)

PRÉSENTÉE LE12 SEPTEMBRE 2008
À LA FACULTE SCIENCES ET TECHNIQUES DE L'INGÉNIEUR
LABORATOIRE DE TECHNOLOGIE DES COMPOSITES ET POLYMÈRES
PROGRAMME DOCTORAL EN SCIENCE ET GÉNIE DES MATÉRIAUX

ÉCOLE POLYTECHNIQUE FÉDÉRALE DE LAUSANNE

POUR L'OBTENTION DU GRADE DE DOCTEUR ÈS SCIENCES

PAR

Julien RION

ingénieur mécanicien diplômé EPF
de nationalité suisse et originaire de Vicques (JU)

acceptée sur proposition du jury:

Prof. P. Muralt, président du jury
Prof. J.-A. Månson, Dr Y. Leterrier, directeurs de thèse
Dr M. Borgeaud, rapporteur
Prof. W. Cantwell, rapporteur
Dr J. Moran, rapporteur

ÉCOLE POLYTECHNIQUE
FÉDÉRALE DE LAUSANNE

Suisse
2008

# ABSTRACT

The ultra-light photovoltaic sandwich structure is a new multifunctional structure concept enabling weight and thus energy to be saved in high-tech solutions such as solar cars, solar planes or satellites. The novelty of this approach is to use solar cells as a load carrying element in the structure. The aim of this work was to investigate the failure mechanisms of such ultra-light sandwich structure and their correlation with microstructure, processing pressure, and strength in order to obtain optimal design and processing. To this end, composite sandwich structures were extensively studied with weights in the range of 650 – 850 g/m$^2$, and comprising one 140 µm thick skin made of 0/90° carbon fiber-reinforced plastic (CFRP), one skin made of 130 µm thick mono-crystalline silicon solar cells, and a 29 kg/m$^3$ honeycomb core.

As a first step, core-to-skin bonding in a symmetric (CFRP / core / CFRP) sandwich, for which a design criterion was lacking, was especially studied. An adhesive deposition technique was developed enabling the adhesive weight used for core-to-skin bonding to be tailored. Based on adhesive contact angles, the formation of the adhesive fillets between honeycomb cell walls and skin was modeled. Core / skin debonding energy was measured and compared to core tearing energy measured with a new video-based method, and the failure mechanisms during skin peeling were investigated. It was thus ascertained that, to provide the highest debonding energy-to-weight ratio, the optimal adhesive weight was 35-40 g/m$^2$. Furthermore, in contrast with classic sandwich structures with thicker skins, it was observed that the bending strength of the ultra-light sandwich panels increased with adhesive weight. This was due to the formation of adhesive fillets, which significantly increased the bending stiffness of the thin CFRP skin, and thus increased the compressive load causing local instability of the skin. Models taking into account the increased skin stiffness showed that the best adhesive quantity required to increase the strength-to-weight ratio was ~40 g/m$^2$.

In a second step, the influence of processing pressure on the morphology and strength of symmetric (CFRP / core / CFRP) ultralight sandwich structures was investigated by using one-shot vacuum bag processing. This showed that higher processing pressures caused the formation of larger adhesive fillets and an increased waviness of the CFRP skin on vacuum bag side. These two effects had conflicting impacts on the strength of the structure. Waviness of the skin favored local instabilities, whereas adhesive menisci stabilized the skin. Modeling of the local instability of the skin by taking into account the waviness of the skin and the size of the menisci as a function of processing pressure enabled an optimal processing pressure of 0.7 bar to be identified, giving the highest strength-to-weight ratio.

The third step of the study was devoted to the mechanical analysis of the mono-crystalline silicon solar cells. The brittle behavior of the cells was confirmed, and the Weibull failure probability curve was established with the mean tensile strength at 221 MPa. It was demonstrated by experimental testing and finite element modeling (FEM) that the low strength of the cells compared to the intrinsic strength of silicon (~6.9 GPa) was not due to surface texturation of the cells used for increased efficiency, but to more severe surface or edge defects. FEM also showed that no significant reinforcing effect of the cells could be obtained with polymer encapsulation. In addition, thermo-mechanical stresses due to a mismatch of the coefficient of thermal expansion (CTE) between the Si cells and the polymer encapsulation were found to be negligible. In order to protect the cells against the environment, encapsulation of the cells was successfully carried out, using highly transparent fluoropolymer films treated with $SiO_2$ plasma sputtering for improved adhesion, together with silicone adhesive.

Finally, the integration of solar cells as a photovoltaic skin of an ultra-light sandwich structure was achieved using thin stress transfer ribbons to ensure load transfer between adjacent cells. It was observed that the cells were not damaged by sandwich panel processing, even in curved panels, thus showing that the processing windows of the different constituents were compatible. The asymmetric (Si / core / CFRP) photovoltaic sandwich structure with a weight equal to 800 g/m$^2$ and a specific power density equal to ~250 W/kg (i.e. 20 times more than standard commercial photovoltaic panels) demonstrated an equilibrated mechanical behavior, i.e. the CFRP skin, reinforcing ribbons, and solar cells had similar failure loads.

**Keywords:** ultra-light photovoltaic sandwich structure, failure micro-mechanisms, core-to-skin bonding, local skin instability, processing pressure, honeycomb core, mono-crystalline silicon.

# RESUME

Les structures sandwich photovoltaïques ultralégères représentent un nouveau concept de structure multifonctionnelle visant à économiser du poids, et par conséquent de l'énergie pour des applications telles que les voitures solaires de compétition, les planeurs solaires ou encore les satellites. La principale nouveauté de cette approche réside en l'utilisation des cellules solaires en silicium monocristallin en tant qu'élément structurel. Le but du projet était d'analyser les modes et mécanismes de rupture de ces structures sandwichs et de définir leur relation avec la microstructure et la pression de mise en œuvre afin d'identifier le dimensionnement et procédé de fabrication optimal. A cette fin, des structures sandwichs composites d'un poids de 650 à 850 g/m$^2$ ont été étudiées en détails. Ces structures étaient composées d'une peau en composite epoxy / fibres de carbone à 0 et 90° de 140 $\mu$m d'épaisseur, d'une peau faite de cellules solaires en silicium monocristallin et d'un cœur en nid d'abeille de 29 kg/m$^3$.

Dans un premier temps, le collage peau-cœur de structures sandwichs symétriques (carbone / cœur / carbone) a été spécialement étudié, étant donné qu'aucun critère de dimensionnement n'était disponible. Dans ce but, une méthode permettant un dosage précis de la quantité de colle a été développée. La formation des ménisques de colle entre les parois du nid d'abeille et les peaux a été modélisée sur la base des angles de contact de l'adhésif. L'énergie de décollement peau / cœur a été mesurée et comparée à l'énergie nécessaire pour déchirer le cœur en nid d'abeille, préalablement mesurée grâce à une nouvelle méthode fondée sur l'analyse d'images vidéo. Les mécanismes de rupture associés au pelage de la peau ont également été examinés. Ainsi, la quantité de colle conduisant au meilleur rapport énergie de décollement / poids a été déterminée à 35 – 40 g/m$^2$ pour la peau en fibres de carbone. Par ailleurs une augmentation de la résistance en flexion des panneaux sandwichs couplée à l'augmentation de la quantité d'adhésif a été mise en évidence. La formation des ménisques de colle augmentant de manière significative la rigidité en flexion des fines peaux en fibres de carbone explique l'amélioration de la résistance au flambage local des peaux. Un model analytique du flambage local des peaux prenant en compte leur augmentation de rigidité en flexion a permis de déterminer que la quantité d'adhésif conduisant au meilleur rapport solidité / poids était de ~40 g/m$^2$.

Dans un deuxième temps, l'influence de la pression de mise en œuvre sur la morphologie et la résistance de ces structures sandwichs ultralégères symétriques a été étudiée lors de cuissons de la structure sous sac à vide. Il a été observé que plus la pression de mise en œuvre était élevée, plus les ménisques de colle étaient grands et plus l'ondulation des peaux du côté du sac à vide était prononcée. Ces deux effets ont montré des influences antagonistes sur la résistance des structures sandwichs, l'ondulation des peaux favorisant le flambage local, tandis que les ménisques de colle stabilisaient les peaux. La modélisation du flambage local des peaux en prenant en compte ces deux effets a montré que la pression permettant d'atteindre le plus grand rapport solidité / poids était de 0.7 bar.

La troisième partie de l'étude a été consacrée à l'analyse mécanique de cellules solaires en silicium monocristallin. Leur comportement fragile s'est confirmé et la courbe de probabilité de rupture de Weibull correspondante a été déterminée, avec une contrainte moyenne à la rupture en traction de 221 MPa. Des tests mécaniques ainsi que des modélisations par éléments finis ont démontré que la faible résistance des cellules en comparaison de la résistance intrinsèque du silicium (~6.9 GPa) n'était pas due à la texturation de surface des cellules utilisée pour augmenter leur rendement photovoltaïque, mais plutôt à des défauts de surface ou de bords plus critiques. La modélisation a également montré que l'encapsulation des cellules avec des polymères ne pouvait pas renforcer significativement les cellules, et que les contraintes thermomécaniques dues aux différents coefficients d'expansion thermique du silicium et des polymères d'encapsulation étaient négligeables.

Aussi, de manière à protéger les cellules contre les effets de l'environnement, elles ont été encapsulées avec un film fluoropolymère sur lequel une couche de $SiO_2$ avait été préalablement déposée sous plasma afin d'améliorer l'adhésion avec l'adhésif silicone utilisé.

Finalement, l'intégration des cellules solaires comme peau photovoltaïque de structures sandwichs ultralégères a été réalisée en utilisant de fins rubans de renfort pour assurer le transfert de contraintes entre cellules adjacentes. Les cellules n'ont pas été endommagées lors de la fabrication des panneaux sandwichs, même lorsque ceux-ci étaient courbés, démontrant ainsi la compatibilité des fenêtres de mise en œuvre des diverses composants de la structure. La structure sandwich photovoltaïque asymétrique (Si /cœur / carbone) d'un poids de ~800 g/m$^2$ et d'une densité spécifique de puissance de ~250 W/kg (soit 20 fois plus élevée que les modules photovoltaïques commerciaux standards) a fait preuve d'un comportement mécanique équilibré, les forces à rupture des peaux en carbone, des rubans de renfort et des cellules solaires étant semblables.

**Mots-clés :** structure sandwich photovoltaïque ultralégère, micro-mécanismes de rupture, collage peau-cœur, flambage local des peaux, pression de mise en œuvre, cœur nid d'abeille, silicium monocristallin.

# REMERCIEMENTS

J’aimerais remercier ici toutes les personnes ayant contribué à l’aboutissement de ce projet, aussi bien scientifiquement, financièrement que humainement.

Tout d’abord, je remercie le Professeur Jan-Anders Månson de m’avoir permis de réaliser cette thèse dans son laboratoire. Je remercie également l’agence suisse pour la promotion de l’innovation (CTI, #8002.1, DCPP-NM) pour le soutien financier apporté à ce projet.

J’adresse bien sûr un merci tout particulier au Dr. Yves Leterrier qui a suivi ce travail, pour les conseils scientifiques et pour le temps passé à la correction des nombreux rapports et présentations. Un chaleureux merci également aux personnes ayant suivi ce projet et apporté des critiques constructives, soit Cristian Neagu, Pierre Dumont, Véronique Michaud et François Bonjour. Merci aussi à Sébastien Lavanchy pour ses conseils toujours très appréciés et à Fabio Demarco pour son aide technique.

D’autre part, ce travail de thèse est également le fruit de nombreuses collaborations. A ce titre, j’aimerais remercier la société Decision SA et en particulier Bertrand Cardis et Jean-Marie Fragnières pour les fructueuses et toujours très intéressantes discussions, et également de m’avoir permis de découvrir la réalité des composites « grandeur nature ». Merci également à la société Solvay, tout spécialement à Jean-Marie Blairon pour les nombreuses simulations par élément finis réalisées, et également à Padmanabhan Srinivasan et Paolo Toniolo de la division Solvay-Solexis pour le développement de films d’encapsulation fluoropolymères. Je remercie également les nombreuses personnes des différents laboratoires ayant apporté leur pierre à l’édifice, c’est-à-dire le professeur Christophe Ballif du PV-Lab de l’Institut de Microtechnique de Neuchâtel, Alain Nussbaumer du Laboratoire de la construction métallique (ICOM), Paul Liska du Laboratoire de photonique et interfaces (LPI) et Anastasios Vassilopoulos du Laboratoire de construction en composites (CCLab). J’aimerais par ailleurs remercier André Borschberg, Peter Frei, Dieter Siebenmann, Marcus Basien, Roger Ruppert et Philippe Lauper de Solar Impulse pour leur collaboration à ce projet. Mes remerciements vont aussi à Pascal Vuilliomenet qui n’a pas ménagé ces efforts pour coordonner les différents groupes liés à ce travail.

Les nombreux résultats expérimentaux de ce projet sont aussi dus à l’aide précieuse de tous les étudiants ayant effectué des projets de semestre ou de diplôme dans le cadre de cette thèse. Un grand merci donc à Catherine, Aurélie, Carl, Damien, Alain, Grégory,

Guillaume, Nina, Samuel, Hannes et Antoine. Le travail expérimental n’aurait également pas pu être réalisé sans les excellents montages réalisés par l’atelier de l’Institut des Matériaux et je tiens à remercier toute l’équipe.

Par ailleurs la réalisation de cette thèse a été grandement facilitée par la bonne ambiance que firent régner mes collègues de travail. Je tiens donc à les remercier à ce titre, et tout particulièrement Xavier, Christian, Manuel, Pierre, Laurence, Sébastien, Damien, Albert, Cristian et Rui pour les excellents moments partagés. J’ai également apprécié de partager mon bureau avec François durant ces 4 années. Je remercie également mes amis du STI Team pour les centaines de km parcourus dans la bonne humeur : toujours une grande source d’inspiration.

Finalement, je veux faire part de ma profonde gratitude à ma famille, mes parents en particulier, pour leur présence et leur soutient permanent durant cette thèse et les nombreuses années d’études précédentes. Bien sûr, la valeur de ce travail n’aurait à mes yeux qu’une valeur moindre sans la plus merveilleuse trouvaille que je fis dans ce laboratoire : Céline et son amour qui me comble chaque jour. Merci .

# LIST OF SYMBOLS AND ACRONYMS

| **Symbol** | **Description** | **Unit** |
|---|---|---|
| $a$ | Crack length | mm |
| $a_r$ | Real crack length in DCB test | mm |
| $A$ | Area of the meniscus on 2D cross-section | mm$^2$ |
| $A_{ABD}$ | Coefficient derived from the ABD matrix of the face | N/mm |
| $B$ | Width of sample | mm |
| $B_{ABD}$ | Coefficient derived from the ABD matrix of the face | N |
| $B_o$ | Bond number | |
| $c$ | Length of a side of a hexagonal cell | mm |
| $c_{3,4}$ | Integration constants | |
| $C$ | Compliance | mm/N |
| $d$ | Distance between the centroids of the sandwich faces $t_f + t_c$ | mm |
| $dP$ | Variation of potential energy | J |
| $dW$ | Variation of work of external forces | J |
| $D$ | Coefficient relating crack length and compliance | |
| $D_{ABD}$ | Coefficient derived from the ABD matrix of the face | Nmm |
| $D_B$ | Flexural stiffness of a sandwich beam | Nmm$^2$ |
| $D_f$ | Flexural stiffness of a sandwich face per unit width | Nmm |
| $D_P$ | Flexural stiffness of a peel arm in DCB | Nmm$^2$ |
| $e$ | Position of the neutral axis in flexion | mm |
| $E_f$ | Young’s modulus of sandwich face | N/mm$^2$ |
| $E_c$ | In-plane Young’s modulus of sandwich core | N/mm$^2$ |
| $E_{cz}$ | Out-of-plane compressive Young’s modulus of sandwich core | N/mm$^2$ |
| $E_{czt}$ | Out-of-plane tensile Young’s modulus of sandwich core | N/mm$^2$ |
| $E_{Si}$ | Young’s modulus of silicon | N/mm$^2$ |
| $F$ | Applied load | N |
| $g$ | Acceleration due to gravity: 9.81 | m/s$^2$ |
| $G$ | Strain energy release rate | J/m$^2$ |
| $G_{core}$ | Shear modulus of sandwich core | N/mm$^2$ |
| $G_c$ | Critical strain energy release rate or debonding energy | J/m$^2$ |
| $G_{Ic}$ | Critical strain energy release rate in mode I | J/m$^2$ |
| $h$ | Distance from neutral axis of the skin to surface of the skin | mm |

| | | |
|---|---|---|
| $h_D$ | Height of sessile drop | mm |
| $H$ | Depth of elastic foundation in sandwich for wrinkling | mm |
| $H_{def}$ | Depth of elastic foundation for skin buckling over defect | mm |
| $H_m$ | Height of adhesive meniscus on cross-section | mm |
| $I$ | Inertia moment | $mm^4$ |
| $k$ | Stiffness of elastic foundation | $N/mm^3$ |
| $k_1$ | Stress in the core at $z = 0$ in wrinkling | $N/mm^2$ |
| $K_1$ | Amplitude of sinusoidal stress in the core at $z = 0$ in wrinkling | $N/mm^2$ |
| $K_{IC}$ | Toughness of a material in mode I (crack opening) | $MPa\ m^{1/2}$ |
| $k_2$ | "Stiffness of elastic foundation / skin bending stiffness" in buckling model | $mm^{-4}$ |
| $k_3$ | "Compressive line load / skin bending stiffness" in buckling model | $mm^{-2}$ |
| $l$ | Half-wavelength of skin deformation in wrinkling | mm |
| $l_{cr}$ | Critical half-wavelength of skin deformation in wrinkling | mm |
| $l_0$ | Half-wavelength of preliminary imperfection of the skin | mm |
| $L$ | Length of sandwich beam | mm |
| $L_0$ | Overlap length of reinforcing ribbons | mm |
| $L_1$ | Span between inner loading points in 4-point bending | mm |
| $L_2$ | Span between outer supports in 4-point bending | mm |
| $L_3$ | Span between supports in 3-point bending | mm |
| $L_B$ | Length of sandwich considered for local buckling model | mm |
| $L_{cor}$ | Corrected span between supports in 3-point bending | mm |
| $L_D$ | Diameter of contact circle of sessile drop | mm |
| $L_G$ | Length of gap between solar cells | mm |
| $m$ | Weibull modulus | |
| $M$ | Bending moment | Nmm |
| $M_A$ | Adhesive areal weight | $g/m^2$ |
| $M_{A0}$ | Adhesive areal weight not forming menisci | $g/m^2$ |
| $n$ | Exponent relating crack length and compliance | |
| $N$ | Load per unit width (also called line load) | N/mm |
| $N_{Allen}$ | Wrinkling line load calculated with Allen's model | N/mm |
| $N_{Dimp}$ | Dimpling line load | N/mm |

| | | |
|---|---|---|
| $N_{Euler}$ | Wrinkling line load calculated with Euler’s model | N/mm |
| $N_{Hemp}$ | Wrinkling line load calculated with Hemp’s model | N/mm |
| $N_m$ | Wrinkling line load associated with half-wavelength $l_0$ | N/mm |
| $N_{Plantema}$ | Wrinkling line load calculated with Plantema’s model | N/mm |
| $N_{Yussuf}$ | Wrinkling line load calculated with Yusuff’s model | N/mm |
| $P$ | Load applied | N |
| $P_C$ | Critical load for crack propagation | N |
| $P_{cr}$ | Buckling load of a sandwich beam under compression | N |
| $P_b$ | Buckling load considering pure bending of beam | N |
| $P_f$ | Probability of failure | |
| $P_l$ | Liquid pressure: pressure in the adhesive meniscus | Pa |
| $P_s$ | Shear crimping load of sandwich | N |
| $P_v$ | Vapor pressure: air pressure outside the meniscus | Pa |
| $\Delta P$ | Pressure difference | Pa |
| $q$ | Load per unit length normal to the skin | N/mm |
| $q_{1,2,3,4,5}$ | Coefficients of wrinkling model | |
| $r$ | Radius | mm |
| $r_1$, $r_2$ | Radius of curvature | m |
| $r_i$ | Inner radius of climbing drum | mm |
| $r_o$ | Outer radius of climbing drum | mm |
| $R$ | Reaction force | N |
| $s$ | Size of honeycomb cells: diameter of inscribed circle | mm |
| $S_B$ | Shear stiffness of sandwich beam | N |
| $S_c$ | Shear strength of the core | N/mm$^2$ |
| $S_{broken}$ | Broken surface | mm$^2$ |
| $t$ | Thickness | mm |
| $t_c$ | Thickness of sandwich core | mm |
| $t_f$ | Thickness of sandwich face | mm |
| $t_p$ | Ply thickness in a laminate | mm |
| $t_R$ | Thickness of reinforcing ribbon | mm |
| $t_{tens}$ | Thickness of solar cell considered for tensile tests | mm |
| $t_{th}$ | Theoretical thickness of solar cell with homogenous rectangular section | mm |

| | | |
|---|---|---|
| $T$ | Shear force | N |
| $u$ | Displacement of core or skin in length direction in wrinkling | mm |
| $U$ | Elastic energy | J |
| $U_Q$ | Elastic energy stored in CT probe | J |
| $U_I$ | Elastic energy stored in unnotched CT probe | J |
| $V$ | Volume | $mm^3$ |
| $w$ | Out of plane displacement of skin or core in wrinkling | mm |
| $W$ | Amplitude of sinusoidal displacement w | mm |
| $w_o$ | Out-of-plane displacement of unloaded sandwich skin | mm |
| $W_o$ | Amplitude of sinusoidal displacement $w_o$ | mm |
| $w_1$ | Out-of-plane displacement of skin on elastic foundation | mm |
| $w_2$ | Out-of-plane displacement over the bonding defect | mm |
| $w_3$ | Beam center deflection in 3-point bending | mm |
| $w_4$ | Beam center deflection in 4-point bending | mm |
| $W_{CT}$ | Width of CT probe | mm |
| $W_m$ | Width of meniscus on cross-section | mm |
| $X_C$ | X coordinate of the center of meniscus surface circle | mm |
| $Y_C$ | Y coordinate of the center of meniscus surface circle | mm |
| $Z_c$ | Out-of-plane compressive strength of the core | $N/mm^2$ |
| $z_a$ | Length of elastic foundation | mm |

| | | |
|---|---|---|
| $\alpha$ | Ratio between real meniscus shape and triangular approximation | |
| $\beta$ | Slope of load/displacement curve during mechanical testing | N/mm |
| $\chi$ | “Measured waviness $W_{meas}$ / wave amplitude in model $W_0$” | |
| $\delta$ | Displacement of loading point | mm |
| $\delta_1$ | Distance between two rows of honeycomb cells | mm |
| $\delta_2$ | Crosshead displacement between two peak loads in CDP | mm |
| $\delta_{cor}$ | Corrected displacement of loading point | mm |
| $\Delta$ | Crack length correction with MBT method | mm |
| $\varepsilon_m$ | Local maximum strain in the skin | |
| $\phi$ | Angle | rad |

| | | |
|---|---|---|
| $\Phi$ | Broken area fraction of menisci | |
| $\gamma$ | Surface tension | N/m |
| $\gamma_{lv}$ | Surface tension of liquid / vapor interface | N/m |
| $\gamma_{sl}$ | Surface tension of liquid / solid interface | N/m |
| $\gamma_{sv}$ | Surface tension of solid / vapor interface | N/m |
| $\eta$ | Variation coefficient of core properties | |
| $\kappa$ | Ratio “foundation stiffness / peel arm bending stiffness” | $mm^{-1}$ |
| $\lambda$ | Ratio between max. stress and mean stress in solar cells | |
| $\nu$ | Poisson’s coefficient | |
| $\nu_c$ | Poisson’s coefficient of sandwich core | |
| $\theta$ | Contact angle | rad |
| $\theta_1$ | Contact angle of adhesive on Nomex surface | rad |
| $\theta_2$ | Contact angle of adhesive on prepreg surface | rad |
| $\rho$ | Specific mass | $kg/m^3$ |
| $\sigma_0$ | Stress parameter in Weibull distribution (63% failure) | $N/mm^2$ |
| $\sigma_f$ | Direct stress in the skin | $N/mm^2$ |
| $\sigma_{f,cr}$ | Dimpling stress in the skin | $N/mm^2$ |
| $\sigma_{Hoff}$ | Critical wrinkling stress in skin with Hoff and Mautner model | $N/mm^2$ |
| $\sigma_{mean}$ | Mean failure stress | $N/mm^2$ |
| $\sigma_{p0}$ | Stress in the ply at 0° in a 0/90° laminate | $N/mm^2$ |
| $\sigma_u$ | Stress parameter in Weibull distribution | $N/mm^2$ |
| $\sigma_z$ | Normal out-of-plane stress in the core | $N/mm^2$ |
| $\Sigma_z$ | Amplitude of sinusoidal normal out-of-plane stress in the core | $N/mm^2$ |
| $\sigma_{zm}$ | Maximum normal out of plane stress in the core | $N/mm^2$ |
| $\tau_c$ | Shear stress in the core | $N/mm^2$ |
| $\tau_{cr}$ | Lap shear strength | $N/mm^2$ |
| $\tau_{xz}$ | Shear stress in the core in xz plane | $N/mm^2$ |
| $\tau_{xzm}$ | Maximum shear stress in the core in xz plane | $N/mm^2$ |
| $T_{xz}$ | Amplitude of sinusoidal shear stress in the core in wrinkling | $N/mm^2$ |
| $\omega$ | Coefficient defined in buckling model | |
| $\xi$ | Adjusting coefficient between 0 and 1 | |

| | |
|---|---|
| $\psi$ | Coefficient defined in buckling model |
| $\zeta$ | Coefficient defined in buckling model |

| **Abbreviation** | **Definition** |
|---|---|
| CC | Compliance calibration |
| CDP | Climbing drum peel |
| CFRP | Carbon fibers reinforced plastic |
| CLT | Classic laminate theory |
| CSB | Cracked sandwich beam |
| CT | Compact Tension |
| Cz | Czochralski process for mono-crystalline silicon |
| DCB | Double cantilever beam |
| EVA | Ethylene Vinyl Acetate |
| FEM | Finite Element Modeling |
| FWT | Flatwise Tensile |
| FZ | Float-Zone technique for mono-crystalline silicon |
| GFRP | Glass fiber reinforced plastic |
| LVDT | Linear Variable Differential Transformer |
| MBT | Modified beam theory |
| NDT | Non-destructive testing |
| PEEK | PolyEthykEtherKetone |
| PET | Polyethylene terephthalate |
| PV | Photovoltaic |
| SCB | Single cantilever beam |
| SEM | Scanning electronic microscopy |

# TABLE OF CONTENTS

**CHAPTER 1. INTRODUCTION .......... 17**

**CHAPTER 2. STATE OF THE ART .......... 23**

2.1. SANDWICH STRUCTURES .......... 23
2.2. SOLAR CELLS MECHANICAL ANALYSIS AND ENCAPSULATION .......... 59

**CHAPTER 3. MATERIALS AND EXPERIMENTAL METHODS .......... 73**

3.1. MATERIALS .......... 74
3.2. EXPERIMENTAL METHODS .......... 77
3.3. NEW VIDEO-BASED CRACK LENGTH MEASUREMENT METHOD IN CANTILEVER BEAM TESTS .......... 83
3.4. TOUGHNESS MEASUREMENT OF EPOXY .......... 96

**CHAPTER 4. CORE TO SKIN BONDING OPTIMIZATION IN ULTRA-LIGHT SANDWICH STRUCTURES .......... 99**

4.1. PREDICTION OF THE ADHESIVE FILLET SIZE .......... 100
4.2. CORE-TO-SKIN DEBONDING ENERGY AND MECHANISMS .......... 114
4.3. CONCLUSIONS .......... 125

**CHAPTER 5. INFLUENCE OF ADHESIVE QUANTITY AND BONDING DEFECTS ON THE STRENGTH OF SANDWICH STRUCTURES .......... 127**

5.1. MATERIALS AND METHODS .......... 128
5.2. MODELING OF SKIN INSTABILITY PHENOMENA .......... 130
5.3. FAILURE ANALYSIS OF SANDWICHES WITH THIN PRE-CURED UD SKINS .......... 135
5.4. FAILURE ANALYSIS OF SANDWICHES WITH CROSS-PLY SKINS .......... 138
5.5. INFLUENCE OF BONDING DEFECTS ON SANDWICH FAILURE .......... 142
5.6. OPTIMIZATION OF THE STRENGTH TO WEIGHT RATIO IN SYMMETRIC SANDWICHES .......... 152
5.7. CONCLUSIONS .......... 157

**CHAPTER 6. PROCESS OPTIMIZATION OF ULTRALIGHT SANDWICH STRUCTURES .......... 159**

6.1. INFLUENCE OF THE CONSUMABLES ON SANDWICH FAILURE .......... 160
6.2. PERMEATION MEASUREMENT OF THE SKIN AND CONSUMABLES .......... 161
6.3. INFLUENCE OF PRESSURE ON SKIN WAVINESS AND FILLET SIZE .......... 165
6.4. INFLUENCE OF PROCESS PRESSURE ON STIFFNESS .......... 174
6.5. INFLUENCE OF PROCESS PRESSURE ON STRENGTH .......... 175
6.6. INFLUENCE OF CORE PROPERTIES ON STRENGTH .......... 180
6.7. CONCLUSIONS .......... 182

**CHAPTER 7. ASYMMETRIC SOLAR SANDWICH STRUCTURE .......... 185**

7.1. MECHANICAL ANALYSIS OF SOLAR CELLS .......... 186
7.2. NUMERICAL ANALYSIS OF STRESS CONCENTRATIONS IN TEXTURED SOLAR CELLS .......... 194
7.3. HONEYCOMB CORE-TO-SILVER BACK-CONTACT BONDING .......... 199
7.4. TENSILE STRENGTH OF SOLAR CELL SKIN .......... 203
7.5. DEVELOPMENT OF STRESS TRANSFER RIBBON .......... 207
7.6. ENCAPSULATION OF SOLAR CELLS .......... 209
7.7. PROTOTYPE 4 CELLS CURVED SANDWICH PANEL .......... 212
7.8. SUMMARY .......... 213

**CHAPTER 8. CONCLUSIONS AND PERSPECTIVES .......... 215**

8.1. GENERAL SUMMARY .......... 215
8.2. CONCLUDING DISCUSSION .......... 219
8.3. FUTURE DEVELOPMENTS .......... 223

**CHAPTER 9. APPENDIX .......... 225**

9.1. WOVEN CARBON FIBER SKINS .......... 226
9.2. EFFECT OF THE SILVER LAYER IN BENDING OF SOLAR CELLS .......... 227
9.3. THERMO-MECHANICAL PROPERTIES OF ENCAPSULATION POLYMERS .......... 229
9.4. POLYMER ENCAPSULATION MATERIALS .......... 231
9.5. TERRESTRIAL SOLAR SPECTRUM .......... 232
9.6. FEM SIMULATION OF STRESSES IN MULTILAYER SOLAR SKIN .......... 233
9.7. MECHANICAL STRENGTH OF AG ELECTRICAL CONNECTORS .......... 235

**CHAPTER 10. REFERENCES .......... 237**

# CHAPTER 1. INTRODUCTION

Saving natural resources and energy is one of the key challenges of the 21st century. In transportation, the most effective way to save energy is to diminish the moving mass, especially for aerial transportation. So, decreasing the weight of the structure of airplanes has become a main preoccupation for all aircraft constructors, from the biggest commercial airplanes [1, 2] (to reduce running costs) to small private airplanes [3, 4]. To this end, composite materials have already demonstrated their superiority and are now currently used in applications demanding high stiffness-to-weight ratios (as, for example, in aircraft building [5-7]). For more unusual applications, such as ultra-light solar aircraft, [8-10], competition solar cars, or satellite solar panels, the structures have to be pushed to their limits in order to save every gram. In these cases, sandwich construction provides one of the lightest and lowest-cost manufacturing concepts [11, 12].

Much literature is available on classic sandwich structures in the order of 10 kg/m$^2$, such as, for example, those used for boat construction or commercial airplanes. However, only a few studies are available on ultra-light sandwich structures in the order of 1 kg/m$^2$. Some of the results and design formulae used for the classic sandwich structures can be used for ultra-light sandwich structures, but as failure modes are often different with these structures, other models have to be developed. The manufacturing process for ultra-light sandwich structures is also quite different. For example, light cores are likely to crush if high autoclave pressure is used, so that the classic method using high pressure to diminish void content of the composite faces of the sandwich may not be applicable [13-15]. Therefore, a complete analysis of the design and fabrication of the structure is essential in order to achieve an optimal structure, i.e. with highest strength-to-weight ratio. The design of an optimized structure with the weight of each constituent of the structure minimized so that every part breaks at same load level was the first challenge of the present work.

In this work, sandwich structures with some of the lightest core and composite skins available were studied. As no design criterion was available for core-to-skin bonding, special attention was paid to optimizing the bonding joint so as to save as much weight as possible. This required a comprehensive study of the influence of processing and materials parameters on bonding joint formation. The characteristic length scales of the sandwich structures considered in this work were in the mm range (size of honeycomb cells and thickness of the structure), and also in the 10-100 µm range (skin thickness, size of the adhesive menisci). Microscopic failure mechanisms were therefore studied in order to understand the driving parameters and their relation to the intrinsic properties of the core and adhesive.

It was expected that the processing pressure would cause phenomena which have conflicting impacts on the strength of the sandwich structure. In fact, whereas sufficient pressure is necessary to ensure good skin compaction and reliable core-to-skin bonding, high pressure causes skin waviness which decreases the strength of the structure [16, 17]. The relation between processing pressure in the vacuum bag process, microstructure, and compressive strength of the skin was therefore studied. Identification of the optimal processing parameters enabling maximization of the quality and strength of the structure was thus the second challenge of this work.

Further minimization of the global weight using the best known materials can be achieved through material and process integration. This means that the materials and components have to participate in another function in addition to their primary one, without reducing the performance of either. Following this logic, the main idea of the present work was to use silicon photovoltaic cells as structural elements. In usual applications, the weight of the solar cells is simply added on to that of the structures, without having any structural utility. In fact, the stiffness and thickness of silicon cells are compatible with conventional carbon fiber-reinforced skins, so that they may be used for building stiff structural elements. However, silicon is very brittle and breaks at low deformations and therefore has to be used in a part having small deformations. Figure 1-1 illustrates this concept, with one composite skin of a sandwich structure being replaced by solar cells. These sandwich structures can be used to build stiff but ultra-light solar panels, flat or with a simple curvature, in zones with limited deformations.

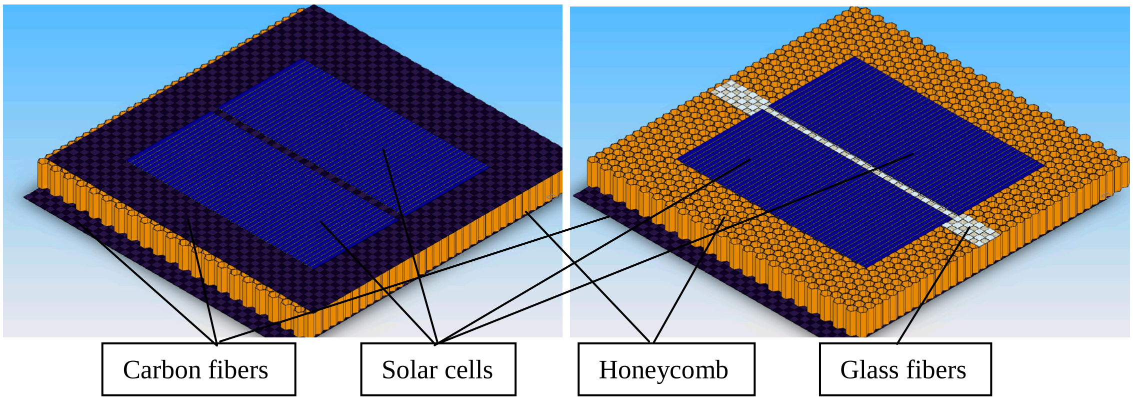

**Figure 1-1: Ultra-light solar panels. The left-hand figure represents the classic sandwich structure with honeycomb core, carbon fiber faces, and the solar cells glued onto the sandwich structure, often with polymer film in-between to avoid electrical short circuits. The right-hand figure represents the new sandwich structure with honeycomb core, one carbon face, and one face made of solar cells with local glass-fiber reinforcements. In both cases, an encapsulation film or glass has to be put on top to protect against environmental attacks.**

In the case of an asymmetric (Si / core / carbon) sandwich structure, the optimal process pressure previously mentioned could differ due to the very fragile nature of the thin monocrystalline silicon solar cells. The strength of the silicon solar cells must thus be determined in order to know precisely the acceptable load level during processing and application. In addition, the finite size of the cells and associated discontinuity requires special investigation of potential solutions so as to ensure stress transfer between cells. Finally, as the cells have to be protected against environmental attack, and as glass is too heavy for this application, the use of a protective polymer film was investigated.

Of course, all the different investigations and optimizations have to be applicable to the complete global structure. Figure 1-2 shows the multiple materials used in the structure.

All these materials have to be assembled in one or multiple steps, and so the processing parameters (for example, temperature, pressure) have to be compatible for all materials. The integration of the very brittle solar cells as load carrying elements in the sandwich structure by ensuring optimal processing compatibility with other constituents was thus the third and main challenge of this work.

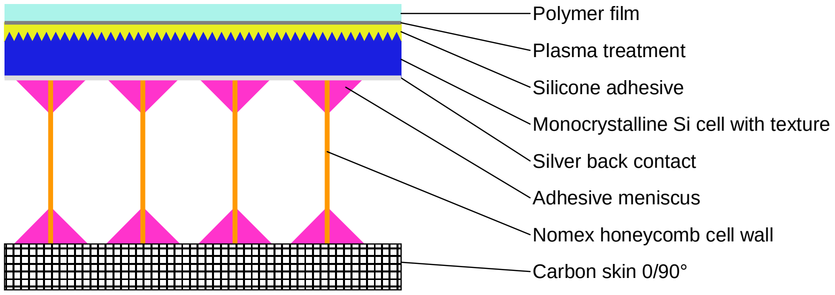
Polymer film
Plasma treatment
Silicone adhesive
Monocrystalline Si cell with texture
Silver back contact
Adhesive meniscus
Nomex honeycomb cell wall
Carbon skin 0/90°

**Figure 1-2: cross-section of an asymmetric sandwich structure with a solar cell as an upper skin**

The different steps and challenges of the study covering ultra-light sandwich structure optimization, solar cell analysis, and, finally, an investigation of asymmetric sandwich structures with a skin made of solar cells can be summarized in the flowchart represented in Figure 1-3.

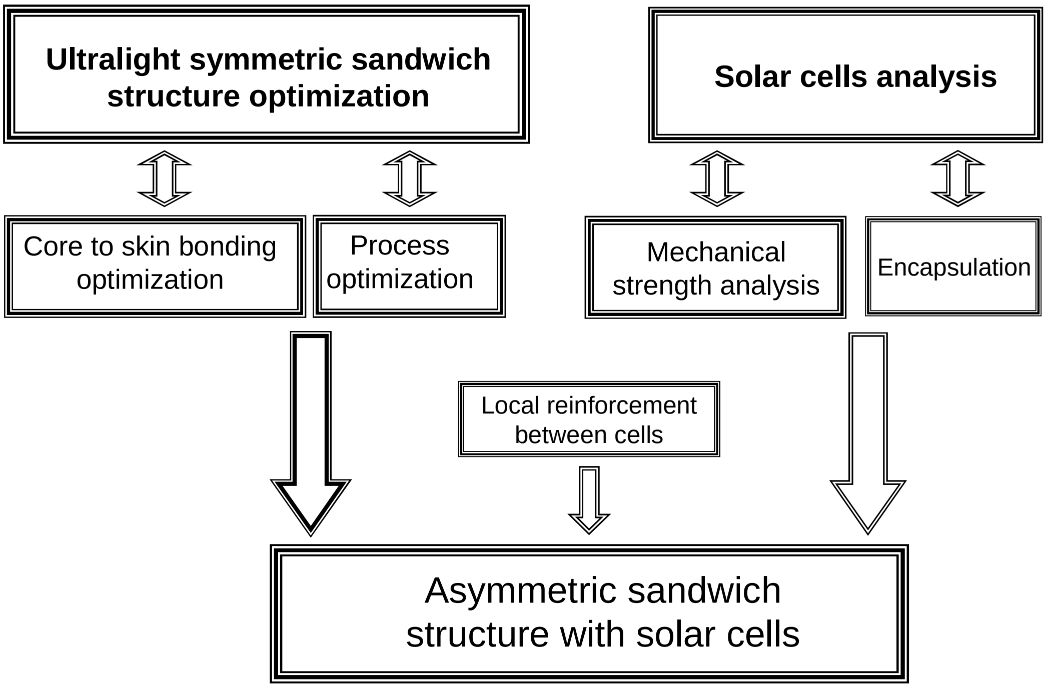
Ultralight symmetric sandwich structure optimization
Solar cells analysis
Core to skin bonding optimization
Process optimization
Mechanical strength analysis
Encapsulation
Local reinforcement between cells
Asymmetric sandwich structure with solar cells

**Figure 1-3: Project organization, with the two main research axes and the final goal.**

The present report is organized as following. Chapter 2 presents the state of the art in sandwich mechanics and processing, and also looks at the mechanical analysis of solar cells, and light encapsulation. Chapter 3 describes the materials and experimental methods used and developed in this work. The core-to-skin bonding and associated failure mechanisms are studied in chapter 4, and the influence of the bonding joint on bending strength is investigated in chapter 5. Chapter 6 then concentrates on the optimization of the processing pressure. The mechanical analysis and encapsulation of solar cells, and the integration of solar cells into sandwich structures is presented in chapter 7. Finally, chapter 8 summarizes the conclusions of this work.

# CHAPTER 2. STATE OF THE ART

## 2.1. Sandwich structures

### 2.1.1. Introduction

Since the first flight of an airplane, incessant research has aimed to reduce the weight of the structure, while keeping the strength and stiffness as high as possible. The use of sandwich structures appeared to be a very good solution to the problem and was first extensively used during the Second World War on the British Mosquito aircraft using balsa core and plywood faces. Since this date, continuous development of the structures has been achieved, improving and optimizing the different constituents, so that the sandwich structure can now be found in innumerable applications, from high-tech satellites to low-cost wooden furniture.

The basic idea of the sandwich concept is easily understood by observing the strain and stress state of a beam in pure bending: the maximum strains are on the upper and lower face of the beam, while the stresses near the neutral axis are low. To improve the strength and stiffness of the beam but with lower weight, it is judicious to place materials with high strength and stiffness where high strains occur, and to place soft, light material in the center where the strains are low. The application of these principles results in a structure with thin faces of high strength and stiffness bonded onto a very light core. The core has nevertheless several vital functions. Stiffness in the direction normal to the faces has to be sufficient to maintain a distance between the skins, and to sufficiently stabilize the skins in order to avoid local buckling when compressive stresses occur. Also the shear stiffness of the core must be sufficient to avoid sliding of the faces over each other, otherwise the sandwich will behave as two independent beams.

The application of these principles leads to a high increase of stiffness and strength with constant weight. Figure 2-1 illustrates the tremendous gain in strength and stiffness-to-weight ratio obtained by inserting a light core between two strong faces. Similarly, Figure 2-2 shows the benefits that can be obtained in term of stiffness-to-weight ratio by combining the core and skin material in comparison with the raw materials. The correct choice of the constituents, an understanding of the mechanical behavior of the structure, as well as the identification of the failure modes enable optimized structures to be designed with the highest strength- and stiffness-to-weight ratios.

Many books have focused on sandwich structures [18-24], so only the essential basics of sandwich theory and processing will be treated in the following sections, with emphasis on the more specific topics of this study.

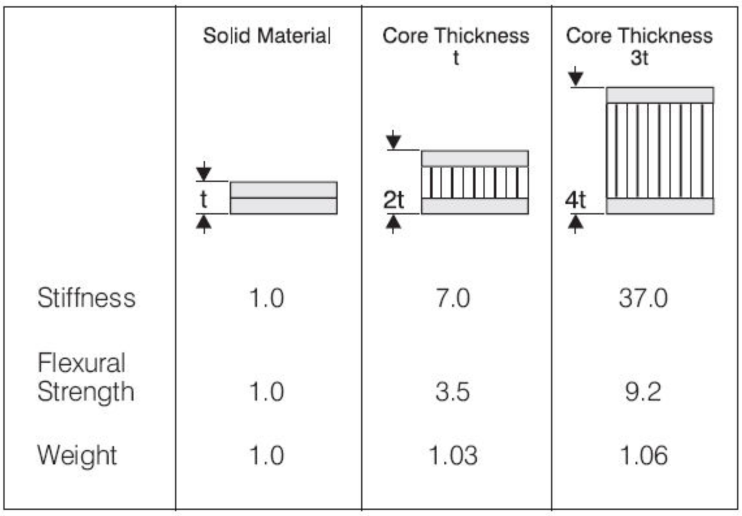

| | Solid Material | Core Thickness t | Core Thickness 3t |
|---|---|---|---|
| Stiffness | 1.0 | 7.0 | 37.0 |
| Flexural Strength | 1.0 | 3.5 | 9.2 |
| Weight | 1.0 | 1.03 | 1.06 |

**Figure 2-1: Relative weight and flexural properties of sandwich panels compared to those of solid panels (figure from [25])**

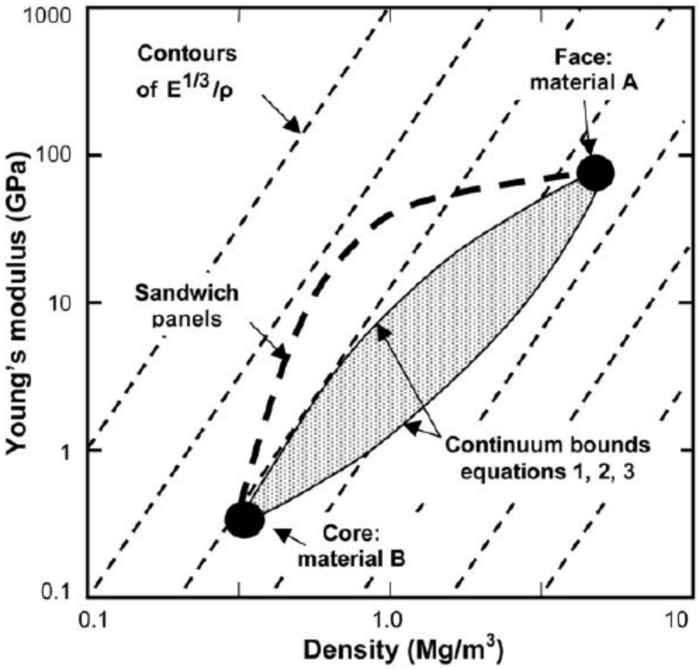

**Figure 2-2: Optimal stiffness-to-weight ratio. The oblique lines represent constant stiffness-to-weight ratio. By choosing a material with properties in-between core and skin material, only the grey zone can be covered. By combining the materials in sandwich panels, a zone with higher stiffness-to-weight ratio is obtainable (figure from[26])**

### 2.1.2. Constituent materials

The first step in designing a sandwich structure is the choice of the different constituents, depending on the application: the face, the core and the adhesive joint to bond the faces to the core. The different choice criteria are of course the mechanical properties of the constituents, but also the processing and the price which can vary over several orders of magnitude.

#### Face materials

The faces of sandwich structures (also commonly called skins or facesheets) can be made of any material available in thin sheet and having sufficient mechanical properties. The main criteria for the selection are the Young's modulus, the strength under tension and compression, the ability to be bonded adhesively, and sometimes also impact and environmental resistance. Metallic faces such as steel, aluminum or titanium sheets ensure high strength, stiffness, and impact resistance, but have a high density and difficult formability.

Fiber composite faces offer many advantages and are therefore widely used for sandwich construction. They enable high strength and stiffness to be coupled with low weight, whilst the orientation of the fibers makes it possible to optimize the strength and stiffness of the skin as a function of stress direction. They can also easily adopt complex forms with double curvature. The three main types of fibers used are glass, Aramid, and carbon fibers. Glass fibers are the most widely used due to their relatively low price, but their stiffness is lower than the other reinforcements. Aramid fibers have high strength and stiffness coupled with low density. Since they have very high wear resistance they are often used to improve the impact resistance of sandwich panels. Carbon fibers offer high strength and stiffness. They are divided into two classes: high strength, and high modulus fibers. Due to its very high strength- and stiffness-to-weight ratio, this type of reinforcement is the most widely used in high-tech sandwich structures, especially in aerospace applications.

The matrix of the fiber composite face can be either a thermoplastic (Polypropylene, Polyamide, PolyEthylEtherKetone (Peek), etc) or thermoset polymer. For sandwich manufacturing, thermosets are preferred due to their easier processing and bonding to a core. For large low cost sandwich structures with glass fibers reinforcements, polyester resins are often used, while epoxy resins are preferred for advanced applications.

These fiber composites are commonly designed by GFRP and CFRP (Glass / Carbon fiber reinforced plastic).

### Core materials

The choice of the core is also determinant for the performance of the sandwich structure. The density of the core has to be as low as possible, but with sufficient shear modulus, and strength and stiffness in the direction normal to the faces. The three main different core types are light wood, such as balsa, cellular foam, and honeycomb. Balsa offers good mechanical properties, but its use is limited by its minimum density which is ~ 100 kg/m$^3$. Cellular foams have lower mechanical properties but offer a very wide range of densities. Due to their relatively low cost, foams are the most widely used cores for sandwich applications.

Honeycomb cores have the best strength- and stiffness-to-weight ratio and are therefore used in high-tech applications such as aerospace. The most commonly used honeycombs are made of aluminum, glass or Aramid fiber mats such as Nomex®. To manufacture the honeycomb, thin sheets of the web material are stacked and bonded along the node lines and then expanded to obtain the desired cell geometry. The direction parallel to the stacked sheets is commonly called the ribbon direction of the core, which is perpendicular to the expansion direction. Aluminum honeycombs retain their shape due to the plastic deformation, while the non-metallic honeycombs are dipped into polyester, phenolic or polyimide resins and cured in their final shape. Aluminum honeycombs have slightly better mechanical properties than Nomex® honeycombs, but are more difficult to bond to skins, and do not exist with densities as low as Nomex® honeycomb, or only with big cell size.

An interesting comparison between foam and honeycomb core was made by Alstädt and Bardenhagen [16]. They showed that the strength of the panel with a honeycomb core was higher, but that energy absorption was higher with a foam core. Also the skin surface quality is better with foam, avoiding the so-called telegraphic effect in skin on honeycomb due to discontinuous core material.

#### Adhesives

The adhesive used to bond the skin to the core has also to be considered carefully. In practice, a bonding failure will result in complete failure of the sandwich structure. The most often used adhesives are epoxy resins, phenolic resins, polyurethanes and polyesters. Adhesives for core-to-skin bonding are often different from the matrix resin of the composite face and are modified to increase their toughness [27, 28]. The choice of an adhesive is mainly a function of the type of core and skins to be bonded. Strength and toughness are the main factors influencing their choice.

### 2.1.3. Processing of sandwich structures

The most common processes for a sandwich structure with fiber composite skins are briefly described in this section. A detailed description of sandwich structure manufacture can be found in [29]. The basic principle of the manufacturing process is to bond the core to the skins in a mould by applying pressure on the part to ensure good quality. The process may differ in the way the skins are impregnated with the resin, by the number of steps to bond the core to the skins, and by the way the pressure is applied.

The easiest way to impregnate the fibers with resin is to use the so called wet lay-up technique, in which the fibers are impregnated by hand with liquid resin. This method does not allow a good control of the resin distribution and quantity, and the fibers-to-matrix ratio is quite low. To improve the quality and also to avoid contact of the operator with the resin, resin injection techniques are used. Therefore, the complete sandwich part is pressed into a mould and the resin is injected or sucked by vacuum to impregnate the fibers [30]. Of course, this method only works with closed-cell core in order to avoid filling the core with resin. To further improve the quality, pre-impregnated fibers (commonly named prepregs) are used. The use of prepregs enables a high fiber-to-resin fraction to be obtained and to accurately control the quantity of resin in the skin, ensuring high quality and good reproducibility, which is of primary importance in designing structural parts. The use of prepregs is also very convenient for composite manufacturing since it avoids the need of liquid resin. The disadvantages of the prepregs are their limited drapability, limited life-time and their higher price.

The number of steps involved in sandwich fabrication can have a significant impact on the final properties of the structure. If a sandwich with two prepreg skins and a honeycomb core is considered, the following different procedures can be used. The skins can be cured separately under pressure in a mould, and afterwards bonded to the core. This method has the advantage of producing very good quality skins which are well compacted under pressure. However, if the sandwich panel is not flat, two different moulds are necessary for the two skins, which dramatically increases the cost. Also, the skins have to be manipulated between the different steps, which can be delicate for large structures with thin skins. Another solution is to cure the skins and bond them to the core in one step, the so-called one-shot curing. The clear advantage of this process is its simplicity and lower cost, but the quality of the skins can be lower because pressure is applied on the honeycomb and is not continuously distributed on the skins. This can cause waviness of the skin thereby increasing the risk of local instability under compressive stresses [31]. The best compromise between these different possibilities has to be evaluated for each different case, depending on the type of core, thickness of skin, size of the panel, and of course cost limitations.

To obtain good core-to-skin bonding and a satisfactory compaction of the composite skins, pressure has to be applied on the sandwich part during curing. The choice of the pressure applied has to be adapted to the type of sandwich manufactured. In fact, ultralight structures can be damaged by too high pressure while low pressure will lead to high skin void content in structures with thick skins. The vacuum bag technique enables almost 1 bar pressure to be easily applied all over the sandwich panel, even when dealing with very large sized parts with complex shapes. The use of an autoclave allows pressure on the part to be increased, but limits the size of the structure to the size of the autoclave which can dramatically increase the costs for large parts. Another solution is to use a press which functions at a higher production rate, but necessitates a male and female mould, which, again, increases the basic investment.

### 2.1.4. Sandwich mechanics

Sandwich mechanics have been covered extensively in several books [18-21, 23]. Therefore only the main equations used in the present work are given in this section, without a complete development. All the equations given apply to homogenous skins. If composite faces are used, then the equivalent mean Young's moduli have to be used, which are calculated according to Classic Laminate Theory (CLT) [32]. In addition, the mean stresses calculated in the skins have to be used to calculate the stress state in each ply of the composite skin.

#### Flexural rigidity and stresses

Flexural rigidity is calculated using the classic Bernoulli hypothesis, i.e. a plane section of the beam before flexion is still plane after deformation. Figure 2-3 shows a cross-section of a sandwich structure with the nomenclature of the different dimensions and properties.

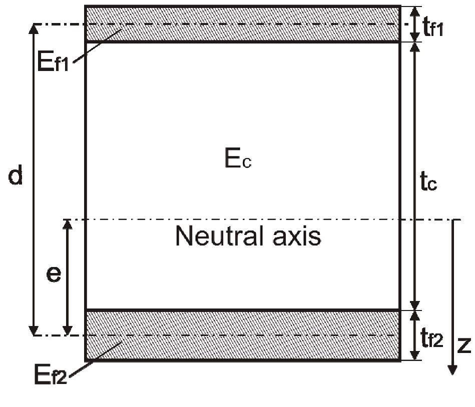

**Figure 2-3: definition of the neutral axis on a sandwich with different faces**

The position *e* of the neutral axis in the sandwich can be calculated with

$$e = \frac{E_{f1}t_{f1}\left(\frac{t_{f1}}{2} + t_c + \frac{t_{f2}}{2}\right) + E_c t_c\left(\frac{t_c}{2} + \frac{t_{f2}}{2}\right)}{E_{f1}t_{f1} + E_c t_c + E_{f2}t_{f2}} \tag{2.1}$$

and the flexural rigidity is then given by

$$D_B = B\left(\frac{E_{f1}t_{f1}^3}{12} + \frac{E_c t_c^3}{12} + \frac{E_{f2}t_{f2}^3}{12} + E_{f1}t_{f1}(d-e)^2 + E_{f2}t_{f2}e^2 + E_c t_c\left(\frac{t_c + t_2}{2} - e\right)^2\right) \tag{2.2}$$

with $E_f$ the elasticity modulus of the skins, $E_c$ the in-plane elasticity modulus of the core, $t_f$ the thickness of the skins, $t_c$ the thickness of the core and $B$ the width of the beam. $d$ is the distance between the centers of the two faces given by

$$d = t_c + \frac{t_{f1}}{2} + \frac{t_{f2}}{2} \tag{2.3}$$

When the faces are identical, the neutral axis is in the center of the beam and the flexural rigidity becomes

$$D_B = B\left(\frac{E_f t_f^3}{6} + \frac{E_c t_c^3}{12} + \frac{E_f t_f d^2}{2}\right) \tag{2.4}$$

Assuming that the in-plane Young’s modulus of the core is low, i.e. $E_c << E_f$, the in-plane tension and compression stresses in the core are negligible and the second term of equation (2.4) can be disregarded. This approximation is particularly justified with honeycomb cores which have a low in-plane Young’s modulus. Furthermore, if the faces are very thin, the first term, representing the bending stiffness of the skins alone, is also negligible. Changes in the stress state of the sandwich structure due to these approximations are represented in Figure 2-4. With these approximations, the flexural rigidity is

$$D_B = B\frac{E_f t_f d^2}{2} \tag{2.5}$$

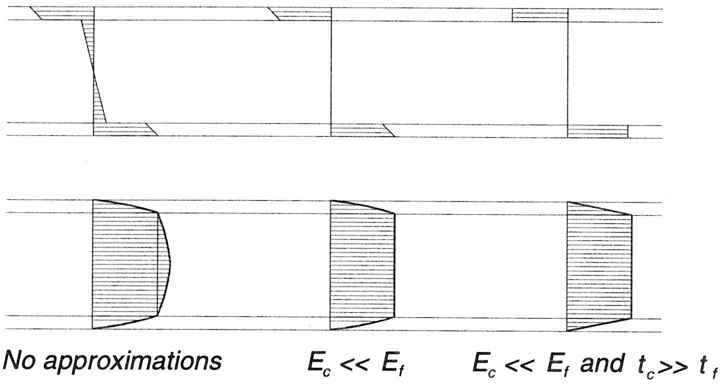

**Figure 2-4: direct and shear stresses in the skins and core of sandwich structures with approximations (figure from [20])**

Depending on the direction of bending, a skin can be either under tension or compression. As the stress calculation formulae are identical in both cases, the term of “direct stresses” is used to designate the stress in the skins, either tensile or compressive, in order to be more generic in the descriptions. Direct stresses in the faces caused by a bending moment *M* are given by

$$\sigma_{f1} = -\frac{M\left(d-e\right)E_{f1}}{D} \qquad \sigma_{f2} = \frac{MeE_{f2}}{D} \tag{2.6}$$

and this can be simplified with the weak core and thin faces approximation to

$$\sigma_{f1} = -\frac{M}{Bt_{f1}d} \qquad \sigma_{f2} = \frac{M}{Bt_{f2}d} \tag{2.7}$$

## Shear stiffness and stresses

Shear stresses have a parabolic profile through the thickness of the core. However, according to the weak core assumption, shear stresses in the core are constant and are given by

$$\tau_c = \frac{T}{Bd} \tag{2.8}$$

where *T* is the shear force. The shear stiffness of the sandwich then becomes

$$S_B = B\frac{G_{core}d^2}{t_c} \tag{2.9}$$

with $G_{core}$ the shear modulus of the core.

### 2.1.5. Failure modes

Sandwich structures composed of a combination of different materials present optimized mechanical properties but also complex mechanical behavior with many different types of failure [33, 34]. For the design of a sandwich structure to be coherent, each potential failure mode has to be considered. Therefore a brief description of the most usual failure modes is made in this section, with emphasis on the most critical ones for the light sandwich structures considered in this study. Figure 2-5 summarizes the most usual failure modes.

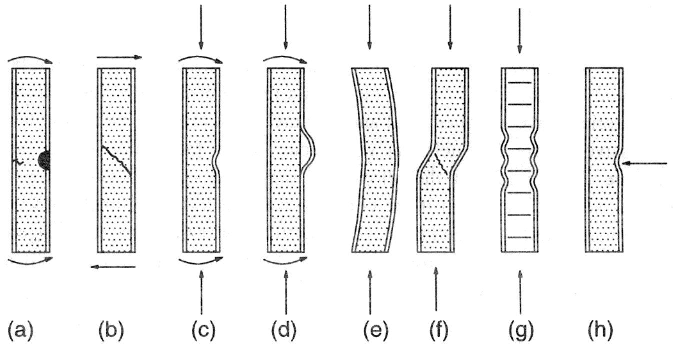

**Figure 2-5: The potential failure modes of sandwich beams: (a) Face yielding/fracture, (b) core shear failure, (c) wrinkling, (d) wrinkling and skin debonding, (e) global buckling, (f) shear crimping, (g) face dimpling, (h) local indentation (figure from [20])**

#### Face yielding or fracture

This failure mode occurs when the maximum stress in one face is higher than the yield or fracture strength of the skin either under tension or compression. This failure mode is easy to predict by calculating the maximum principal stresses in the face depending on loading case. In the case of a composite face, a ply-by-ply analysis has to be carried out using conventional failure criteria (for example Tsai-Hill [32]).

#### Core shear failure

This failure mode may occur when the shear stresses in the core calculated with equation (2.8) exceed the shear strength of the core. Attention has to be paid to the shear strength change according to the loading direction with honeycomb core.

## Face wrinkling

Wrinkling is a failure mode due to local face sheet instability. The skin buckles in the core and forms waves. This mode appears frequently in sandwich panels with thin skins and a low density core [35] and is therefore of primary importance for ultra-light sandwich structures. The prediction of the failure load in this mode is difficult, due to the very high sensitivity to imperfections, which are always present in composites. This mode can be interpreted as a beam or strut (the skin) resting on an elastic foundation (the core). Numerous studies have been made to model and predict the wrinkling load [17, 19, 35-51]. Ley *et al.* [52] made an extensive review of the most commonly used models, their advantages and disadvantages and their agreement with experimental data. Therefore, only the most commonly used models are presented in this section.

Wrinkling of the faces of a sandwich panel under compression can be either symmetric, or anti-symmetric, as depicted in the schematic cross-sections of sandwich beams in Figure 2-6. In this section, only symmetrical wrinkling is considered, because this phenomenon corresponds better to the wrinkling occurring in the face under compression during bending of the sandwich beam, which is especially investigated in this study.

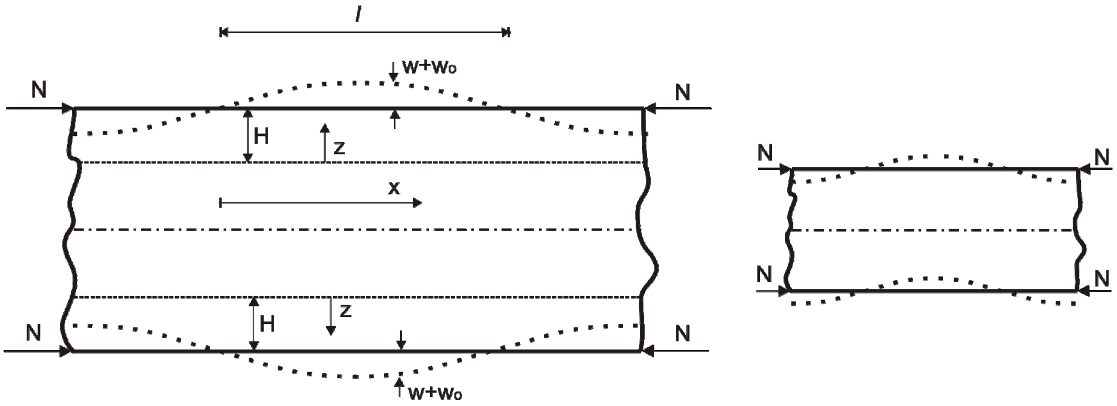

**Figure 2-6: symmetrical (left) and anti-symmetrical wrinkling of the faces of a sandwich panel under compression**

The wrinkling problem is usually represented as a face under compression laying on a continuous support. The corresponding equilibrium equation for this case is

$$D_f \frac{d^4 w}{dx^4} + N \frac{d^2 w}{dx^2} + kw = 0 \tag{2.10}$$

where $D_f$ is the bending stiffness of the face per unit width, $N$ the compressive force in the face per unit width, and $k$ the stiffness of the elastic foundation. The various wrinkling models are mainly based on the hypothesis that the wrinkled face has a sinusoidal shape so that the deflection perpendicular to the face is given by

$$w = W \sin\left(\frac{\pi x}{l}\right) \tag{2.11}$$

where W is the amplitude of the wrinkle, *l* the half-wavelength of the wrinkle, and x the coordinate parallel to beam length. By inserting equation (2.11) in (2.10), the load becomes

$$N = \pi^2 \frac{D_f}{l^2} + \frac{kl^2}{\pi^2} \tag{2.12}$$

The critical half-wavelength minimizing the load is found by setting $\partial N/\partial l$ equal to zero and is

$$l_{cr} = \pi \left(\frac{D_f}{k}\right)^{1/4} \tag{2.13}$$

and the corresponding critical load in the skin is then

$$N_{cr} = 2\sqrt{kD_f} \tag{2.14}$$

The choice of the stiffness *k* of the core depends on the assumptions made concerning the behavior of the core [19].

Hoff and Mautner [51] considered an isotropic homogenous core and a linear stress decay in the core and then calculated that the critical wrinkling stress in the skin was

$$\sigma_{Hoff} = 0.91\sqrt[3]{E_f E_c G_{core}} \tag{2.15}$$

where $E_f$ is the modulus of the isotropic facesheet and $E_c$ and $G_{core}$ are the normal and shear core moduli. Experiments showed that this formula was not conservative, i.e. that the predicted load was higher than the real failure load, so that the factor 0.91 was reduced to 0.5 to correlate with experimental results.

Plantema [18] considered an exponential stress decay in the core and took into account the possible anisotropy of the face sheets by keeping the bending stiffness of the face sheets in the formula, thereby obtaining the critical wrinkling load

$$N_{Plantema} = \frac{3}{2}\sqrt[3]{2D_f E_c G_{core}} \tag{2.16}$$

where $D_f$ is the face sheet bending stiffness calculated using laminate theory. Allen [19] developed a similar theory by considering that the stress in the core has to satisfy Airy's stress function and therefore obtained

$$N_{Allen} = 0.88\sqrt[3]{D_f\left(\frac{2\pi E_c}{(3-\nu_c)(1+\nu_c)}\right)^2} \tag{2.17}$$

where $\nu_c$ is the Poisson's ratio of the core. By considering isotropic face sheets, and a core Poisson's ratio $\nu_c = 0.3$ (for foam for example), equation (2.17) becomes

$$N_{Allen} = 0.58\sqrt[3]{E_f E_c^2} \tag{2.18}$$

These preceding formulae were established assuming a homogenous isotropic core. However, honeycomb core is not homogenous and corresponds better to the anti-plane stress assumption, i.e. that the core normal stresses in the plane of the sandwich panel are zero.

Hemp [41] developed a formula for wrinkling, assuming anti-plane stress in the core, which has shown relatively good agreement with experimental results [52], and provides a generally conservative prediction of the failure load. The critical line load in one skin when the panel is loaded under compression is given by

$$N_{Hemp} = 2\sqrt{\frac{2E_{cz}D_f}{t_c}} \tag{2.19}$$

where $E_{cz}$ is the compression modulus of the core normal to the panel. Yusuff [37] obtained the same formula by considering the elastic foundation stiffness in equation (2.14) to be

$$k = \frac{2E_{cz}}{t_c} \tag{2.20}$$

which means that the core behaves as linear springs on each side of the undeformed middle plane of the panel. The corresponding critical half-wavelength is then given by combining equations (2.13) and (2.20) and is

$$l_{cr} = \pi\left(\frac{D_f t_c}{2E_{cz}}\right)^{1/4} \tag{2.21}$$

He further developed the model by taking into account the shear deformations in the core caused by wrinkling. In this case, he postulated that the core was only affected by deformations to a depth $H$ on each side of the panel.

In this zone, the displacement of the core was given by

$$w = W\frac{z}{H}\sin\left(\frac{\pi x}{l}\right) \tag{2.22}$$

where *z* is the axis normal to the panel, with the zero placed at a depth H and pointing outward from the panel as illustrated in Figure 2-6. The normal and shear strain in the core could then be calculated as

$$\begin{aligned}\varepsilon_z &= \frac{\partial w}{\partial z} = \frac{W}{H}\sin\left(\frac{\pi x}{l}\right)\\ \gamma_{xz} &= \frac{\partial w}{\partial x} = \frac{W\pi}{l}\frac{z}{H}\cos\left(\frac{\pi x}{l}\right)\end{aligned} \qquad (2.23)$$

The normal stress is thus constant in the z direction over the height H, while the shear stress decreases linearly. The variation of the shear stress is not compatible with the anti-plane stress assumption, and therefore the model is not suitable for honeycomb cores. By setting the elastic energy caused by shear and normal strain equal to the elastic energy stored in an elastic foundation of stiffness k given by

$$k = \frac{2E_c}{H} \qquad (2.24)$$

the depth H is

$$H = 1.651\left[\frac{D_f E_{cz}}{G_{core}^2}\right]^{1/3} \qquad (2.25)$$

By combining equations (2.25) and (2.24) with (2.14) and (2.13), the critical load and corresponding wavelength are

$$\begin{aligned}N_{Yusuff} &= 2.201\left(D_f E_{cz} G_{core}\right)^{1/3}\\ l_{cr} &= 2.993\left(\frac{D_f}{\sqrt{E_{cz}G_{core}}}\right)^{1/3}\end{aligned} \qquad (2.26)$$

The load formula is similar to Plantema's and Hoff's models, however with a different coefficient. As deformation in the core vanished at a depth H in Yusuff's model, it is thus only valid if the sandwich panel has a thickness greater than 2H. Yusuff recommended using equation (2.19) when $t_c < 2H$, and equations (2.26) when $t_c > 2H$. He found satisfactory agreement between this theory and experimental work on sandwich panels with foam cores.

Pearce and Webber [46] developed a similar model, but especially for panels with orthotropic face-sheets. The experimental verification [47] with honeycomb core and laminated carbon faces showed that the predicted wrinkling load was 20 to 30% lower than experimental failure load. The model was then improved by Webber *et al.* [48] by taking into account the extension / bending coupling in unsymmetrical laminate facesheets. They compared their solutions with experiments made with sandwich panels with honeycomb cores and 0.3 mm carbon cross-ply face-sheets. They obtained good agreement with the experiments when they took into account a constant 0.25mm thick adhesive layer in the model.

All the equations developed previously in this section were derived for sandwich panels under compression and for symmetrical wrinkling. As in this case the middle plane of the panel is unchanged, the same equations can be used for wrinkling in bending using the following hypothesis:

- The bending deformations are small so that the induced compressive stresses in the core are small
- The tensile deformation of one skin does not affect the behavior of the core for the elastic foundation

In the case of bending, wrinkling occurs on one face only, so that the thickness of the elastic foundation is $t_c$, while for the symmetrical wrinkling case, it is $t_c/2$ for each face. Therefore, for bending the equations mentioned previously have to be corrected by replacing $t_c/2$ by $t_c$.

Gutierrez and Webber [39] extended the work of Webber *et al*. by considering the wrinkling of the face under compression when the sandwich panel is loaded in bending. They used the anti-plane stress assumption for the core and considered the behavior of laminated composite faces with tension / bending coupling. The equilibrium equations for the core then become

$$\sigma_z = -z \frac{d\tau_{xz}}{dx} + k_1 \tag{2.27}$$

$$w = -\frac{z^2}{2E_{cz}} \frac{d\tau_{xz}}{dx} + z \frac{k_1}{E_{cz}} \tag{2.28}$$

$$u = z \frac{\tau_{xz}}{G_{core}} + \frac{z^3}{6E_{cz}} \frac{d^2\tau_{xz}}{dx^2} - \frac{z^2}{2E_{cz}} \frac{dk_1}{dx} \tag{2.29}$$

where $\sigma_z$ is the normal stress in the core which decreases linearly through the thickness of the core, $\tau_{xz}$ is the shear stress in the core which is constant through the thickness, $k_1$ is the stress in the core at $z = 0$ function of $x$ only, $w$ is the vertical displacement, and $u$ the displacement in length direction. The axis $z$ is defined differently from symmetrical wrinkling. It is normal to the panel and the origin of the axis is in the middle of the face in tension, the middle of the face under compression being at $z = d$. Figure 2-7 illustrates the model used for the development of the equations. The skins are considered to be infinitely thin in the model, but separated from each other by the distance d corresponding to the distance between the skin centers in the real sandwich studied.

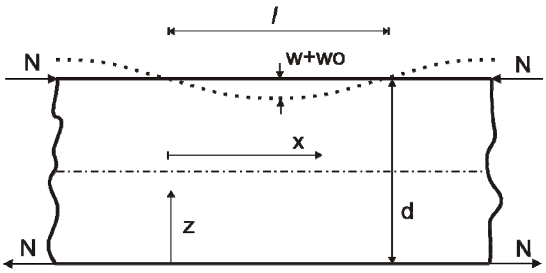

**Figure 2-7: wrinkling of the skin under compression in bending of the sandwich beam.**

To obtain equations (2.28) and (2.29), Gutierrez and Webber considered that the skin in tension stays flat and unstrained during wrinkling of the skin under compression, and so $u = w = 0$ at $z = 0$. The equilibrium equations for the face under compression at $z = d$ are

$$A_{ABD}\frac{d^2u}{dx^2} - B_{ABD}\frac{d^3w}{dx^3} = \left(\tau_{xz}\right)_{z=d} \tag{2.30}$$

$$B_{ABD}\frac{d^3u}{dx^3} - D_{ABD}\frac{d^4w}{dx^4} - N\frac{d^2w}{dx^2} = \left(\sigma_z\right)_{z=d} \tag{2.31}$$

where the coefficient $A_{ABD}$, $B_{ABD}$, $D_{ABD}$ are defined with the ABD matrix of the laminated face by Webber *et al*. [48] as

$$\begin{aligned}
A_{ABD} &= A_{11} + \frac{A_{12}B_{12}B_{22} - A_{12}^2 D_{22} - B_{12}^2 A_{22} + B_{12}A_{12}B_{22}}{A_{22}D_{22} - B_{22}^2}\\
B_{ABD} &= B_{11} + \frac{A_{12}D_{12}B_{22} - A_{12}B_{12}D_{22} - B_{12}D_{12}A_{22} + B_{12}^2 B_{22}}{A_{22}D_{22} - B_{22}^2}\\
D_{ABD} &= D_{11} + \frac{B_{12}D_{12}B_{22} - B_{12}^2 D_{22} - D_{12}^2 A_{22} + D_{12}B_{12}B_{22}}{A_{22}D_{22} - B_{22}^2}
\end{aligned} \tag{2.32}$$

At $z = d$, the displacement of the face-sheet and the core are equal, and so equations (2.27) to (2.29) can be combined into (2.30) and (2.31). Two differential equations in $\tau_{xz}$ and $k_1$ are obtained. By suitable differentiation and substitution, an eighth order differential equation is obtained for $\tau_{xz}$

$$q_1\frac{d^8\tau_{xz}}{dx^8} - q_2\frac{d^6\tau_{xz}}{dx^6} + q_3\frac{d^4\tau_{xz}}{dx^4} - q_4\frac{d^2\tau_{xz}}{dx^2} + q_5 = 0 \tag{2.33}$$

with

$$
\begin{aligned}
q_1 &= \frac{d^3}{6E_{cz}}\left[\frac{A_{ABD}D_{ABD}-B_{ABD}^2}{A_{ABD}d+2B_{ABD}}\right] \\
q_2 &= \frac{2d}{G_{core}}\left[\frac{A_{ABD}D_{ABD}-B_{ABD}^2}{A_{ABD}d+2B_{ABD}}\right]-\frac{NA_{ABD}d^3}{6E_{cz}\left(A_{ABD}d+2B_{ABD}\right)} \\
q_3 &= \left[\frac{B_{ABD}d+2D_{ABD}}{A_{ABD}d+2B_{ABD}}\right]+\frac{d}{3}\left[\frac{2A_{ABD}d+3B_{ABD}}{A_{ABD}d+2B_{ABD}}\right]-\frac{2A_{ABD}Nd}{G_{core}\left(A_{ABD}d+2B_{ABD}\right)} \\
q_4 &= \frac{2A_{ABD}E_{cz}}{G_{core}\left(A_{ABD}d+2B_{ABD}\right)}-\frac{2N}{A_{ABD}d+2B_{ABD}} \\
q_5 &= \frac{2E_{cz}}{d\left(A_{ABD}d+2B_{ABD}\right)}
\end{aligned}
\tag{2.34}
$$

By considering that the wrinkled face has a sinusoidal shape with a half wavelength *l* given by

$$w = W\sin\left(\frac{\pi x}{l}\right) \tag{2.35}$$

then to satisfy equation (2.28) the shear stress must have the form

$$\tau_{xz} = \mathrm{T}_{xz}\cos\left(\frac{\pi x}{l}\right) \tag{2.36}$$

By replacing $\tau_{\mathrm{xz}}$ in (2.33), the following equation is obtained, with the unknowns *N* (hidden in the coefficients $q_i$) and *l*:

$$q_1\left(\frac{\pi}{l}\right)^8+q_2\left(\frac{\pi}{l}\right)^6+q_3\left(\frac{\pi}{l}\right)^4+q_4\left(\frac{\pi}{l}\right)^2+q_5=0 \tag{2.37}$$

By solving this equation numerically, the wrinkling line load *N* in the face can be calculated as a function of *l*. The value of *l* giving the lowest load corresponds to the critical wavelength and gives the critical wrinkling load of the beam.

When using this model, Gutierrez and Webber noticed that taking into account the adhesive layer between core and skin in the calculation can have a significant influence on the wrinkling load when thin skins are considered. The model also confirmed than the wrinkling load was lower with thin faces and thick cores.

The wrinkling formulae were shown to be often non-conservative when compared to experimental results [53]. This is generally mainly due to initial imperfections in the skin, which induce significant pre-buckling deformations, which, in turn, can cause failure of the skin at a lower load level than the predicted wrinkling load. The effect of initial imperfections has been studied by different authors [44, 45, 52-54]. They calculated the local stresses induced in the core and the skin by the wavy deformation of the skin and compared it to the strength of the skin and core materials. The initial shape of the sandwich face sheet is described as

$$w_0 = W_0 \sin\left(\frac{\pi x}{l_0}\right) \tag{2.38}$$

where $W_0$ and $l_0$ are the initial amplitude and half-wavelength of the imperfection respectively. When a load $N$ is applied on the skin, the skin shape becomes

$$w + w_0 = \left(W_0 + W\right)\sin\left(\frac{\pi x}{l_0}\right) \tag{2.39}$$

and the equilibrium equation of the face is

$$D_f \frac{d^4 w}{dx^4} + N\frac{d^2 w}{dx^2} + kw = N\frac{d^2 w_0}{dx^2} \tag{2.40}$$

By solving this equation, the supplementary deformation of the face is obtained as

$$w = W \sin\left(\frac{\pi x}{l_0}\right) = \frac{W_0}{\frac{N_m}{N} - 1}\sin\left(\frac{\pi x}{l_0}\right) \tag{2.41}$$

with $N_m$ being the wrinkling load associated to the half-wavelength $l_0$ of the initial imperfection given as

$$N_m = \pi^2 \frac{D_f}{l_0^{\,2}} + \frac{k l_0^{\,2}}{\pi^2} \tag{2.42}$$

It can be seen in equation (2.41) that the amplitude of the deformation $W$ is maximum when $N_\mathrm{m}$ is minimum, i.e. when the wavelength of the initial imperfection is the same as the critical wavelength given by equation (2.13). It should be noted that if the applied load $N$ is near $N_\mathrm{m}$, the amplitude of the deformation tends to infinity. This confirms that if imperfections are present, the panel will not break due to instability at the wavelength of the imperfection, but either due to the stresses caused by high deformation of the face or due to instability at a more critical wavelength. High deformation of the face can lead to different types of failure. The core can break under compression, in tension or in shear, the bonding line can break in tension and the face can fail in bending.

With the elastic foundation model, the tensile or compressive stresses induced in the core can be written as

$$\sigma_z = wk = \frac{W_0 k}{\frac{N_m}{N} - 1}\sin\left(\frac{\pi x}{l_0}\right) \tag{2.43}$$

and the maximum local stress is then given by

$$\sigma_{zm} = \frac{W_0 k}{\frac{N_m}{N} - 1} \tag{2.44}$$

If Yusuff's model [50] with $t_c < 2H$ is used and the wavelength of the initial imperfection is considered to be identical to the critical wavelength, then by combining (2.19) and (2.20) and setting the maximum tensile or compressive stress equal to the core strength $Z_\mathrm{c}$, the limit load for core failure becomes

$$N_{comp\_t_c<2H} = \frac{2Z_c \left( \frac{2D_f E_{cz}}{t_c} \right)^{1/2}}{\frac{2E_{cz}W_0}{t_c} + Z_c} \tag{2.45}$$

If the model for $t_c > 2H$ is used, the maximum normal stress can be calculated with the strain in equation (2.23) which then becomes

$$\sigma_{zm} = E_{cz} \frac{W}{H} \tag{2.46}$$

Therefore, by considering that the wavelength of the initial imperfection is identical to the critical wavelength, and by combining (2.25), (2.26) and (2.41) and setting the maximum tensile or compressive stress equal to the core strength $Z_\mathrm{c}$, the limit load for core failure becomes

$$N_{comp\_t_c>2H} = \frac{2.201 Z_c \left( D_f E_{cz} G_{core} \right)^{1/3}}{0.606 W_0 \left( \frac{G_{core}^2 E_{cz}^2}{D_f} \right)^{1/3} + Z_c} \tag{2.47}$$

Similarly, the maximum shear stress in the core can be expressed with equation (2.23) as

$$\tau_{xzm} = G_{core} \frac{W\pi}{l} = G_{core} \frac{\pi}{l} \frac{W_0}{\frac{N_m}{N} - 1} \tag{2.48}$$

By setting the wavelength of the imperfection equal to the critical wavelength, and the maximum shear stress equal to core strength, the load causing shear failure of the core becomes

$$N_{fail\_shear} = \frac{2.201 S_c \left(D_f E_{cz} G_{\mathrm{core}}\right)^{1/3}}{1.049 W_0 G_{\mathrm{core}} \left(\frac{\sqrt{E_{cz} G_{\mathrm{core}}}}{D_f}\right)^{1/3} + S_c} \tag{2.49}$$

Note that all the formulae developed above consider a linear behavior of the core until failure. This may be corrected by using the secant modulus in the case of plastic deformation of the core.

Wrinkling deformation of the face can also cause failure of the face due to high local bending deformation as shown by Fagerberg and Zenkert [53]. As the critical part in bending is normally the part under compression, the maximum compressive strain in the face can be calculated by adding the part due to bending and the part due to compression as in

$$\varepsilon_m = \left(-\frac{d^2 w}{dx^2}\right)_m h + \frac{N}{A_{11}} = W\frac{\pi^2}{l^2}h + \frac{N}{A_{11}} = \frac{W_0}{\frac{N_m}{N} - 1}\frac{\pi^2}{l^2}h + \frac{N}{A_{11}} \tag{2.50}$$

where h is the distance from the neutral axis of the face to the surface under compression of the face ($t_f/2$ for isotropic faces), and $A_{11}$ is a coefficient of the ABD matrix of the laminated face. The strain can then be calculated with models for $t_c < 2H$ or $t_c > 2H$ and the corresponding critical wavelength, and then compared to the strength of the face in order to identify the load causing face failure.

Fagerberg and Zenkert [53] did compression tests on sandwich samples with foam cores and carbon faces and confirmed that the failure load prediction was good when assuming small initial imperfections in the skin between 0.01 mm and 0.25 mm.

A similar study was conducted by Kassapoglou *et al.* [17] in order to determine the compressive strength of a wavy facesheet. By considering an initial shape of the same form as that used in equation (2.38), they calculated the induced tensile, compressive and shear stresses in the core, the tensile and shear stresses in the adhesive layer, and finally the maximum local stresses in the skin with the models described previously, but considering Hoff’s model (equation (2.15))for the critical load $N_m$. The analytical models showed good agreement with the experimental results and an FE model.

These various models assume that wrinkling occurs at a particular critical wavelength. When honeycomb core is used, if the calculated wavelength is in the order of the cell size, there is not a continuous support to the skin and the accuracy of the models can be limited [39] because local instability changes to intracellular buckling (dimpling) of the skin. Large honeycomb cells, skins with low stiffness, and a stiff core will favor the transition from wrinkling to dimpling [49].

### Face dimpling (intracellular buckling)

Face dimpling is a local instability which occurs with discontinuous cores such as honeycomb or corrugated core. This type of instability is often observed in sandwiches with thin faces. It can be reversible, but may also lead to the instability and then failure of the skin. The critical stress in the skin leading to dimpling with a hexagonal honeycomb core is often calculated with the classic formula [43]

$$\sigma_{f,cr} = \frac{2E_f}{1-\nu_f^2}\left(\frac{t_f}{s}\right)^2 \tag{2.51}$$

where *s* is the inner diameter of the circle inscribed in honeycomb cells, i.e. the distance between two parallel faces. This formula was shown to be overly conservative and a new model better adapted to composite skins was developed by Thomsen and Banks [55]. They considered that the skin was clamped on two edges of the hexagonal cells and simply supported on the other edges and used a rectangular shape as approximation. Figure 2-8 shows the loading case used to solve the plate buckling problem.

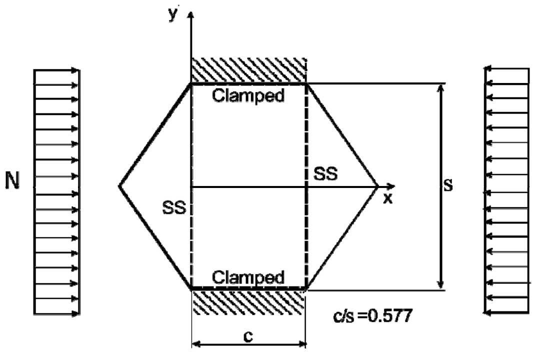

**Figure 2-8: loading case used to solve the dimpling problem. Two edges are clamped, the others are simply supported. Figure from [55]**

The critical line load obtained is

$$N_{\mathrm{dimp}} = \pi^2\left[\frac{D_{11}}{D_{22}}\left(\frac{s}{c}\right)^2 + \frac{8}{3}\frac{\left(D_{12}+2D_{66}\right)}{D_{22}} + \frac{16}{3}\left(\frac{c}{s}\right)^2\right]\frac{D_{22}}{s^2} \tag{2.52}$$

where the $D_{\mathrm{ij}}$ coefficients are the coefficients of the D-matrix of the skin obtained by classic laminate theory. A weakness of this model is that the nominal size of the honeycomb cell did not take into account the reduction of cell size caused by the formation of resin fillets along the cell walls with the adhesive used to bond the facesheet to the core. Also the choice of the length *c* as represented in Figure 2-8 is somehow arbitrary. In practice, *c* could be 1.5 times longer, which would correspond to the real wavelength from one row of honeycomb cells to the next.

### Skin debonding

Debonding of the skin can occur mainly due to two different loadings. Firstly, when out-of-plane loads are applied to the structure, shear stresses appear in the core / skin interface and can lead to debonding, if the bonding is insufficient. Secondly, when the skin is under compression, it can buckle and debond from the core. These two modes are often combined during loading and failure load is therefore difficult to predict. Debonding can also be favored by other parameters such as high internal pressure in the core in the case of honeycomb [11]. Furthermore debonding is very sensitive to pre-existing bonding defects [56], and the failure load is dramatically decreased even with small defects. In fact, failure criteria for this mode are lacking and each case has to be analyzed individually by taking into account the loading conditions, the materials, and the size of the potential defects which might be present in the interface but cannot be detected by non destructive testing (NDT) methods. Therefore this particular mode is especially studied in section 2.1.8.

### Global buckling and shear crimping

Buckling of the sandwich beams is very similar to ordinary Euler buckling theory. The difference is that instability may also occur due to shear in the sandwich beam. Therefore, the critical load is given by

$$\frac{1}{P_{cr}} = \frac{1}{P_b} + \frac{1}{P_s} \tag{2.53}$$

where $P_b$ is the critical load due to pure bending calculated with Euler theory and $P_s$ is the critical load due to shear, given by

$$P_b = \frac{\pi^2 D_B}{\eta L} \qquad\qquad P_s = S_B \tag{2.54}$$

where $L$ is the length of the beam and $\eta$ depends on the boundary conditions [57].

### Local indentation

Although the strength and stiffness of the sandwich structures are very high, they are highly sensitive to local loads which can easily indent the skins. This type of failure is favored by low compressive strength of the core and thin skins, but the exact failure load is difficult to predict [33].

## 2.1.6. Mechanical Testing

To validate the sandwich structure design for every potential failure mode, different mechanical tests have to be designed. The principal tests used to characterize the sandwich structures are described in this section.

### Bending tests

Bending tests are used to validate a structure in a loading mode, which might be similar to a loading situation during sandwich structure use. This test has the advantage of exposing the sandwich structure to several failure modes in a single test and can test simultaneously the tensile and compressive strength of the skins (including local instability) and the shear strength of the core.

The limitation of this test is the presence of transverse stresses in the bent sandwich structure pressing the skins against the core, so that the skins are not under pure tension and compression, even if no shear is present. Local loading of the sandwich parts can also lead to local indentation and failure of the skin, thus preventing measurements of the bending strength of the beam.

3-point and 4-point bending tests are the two main variants used. Figure 2-9 illustrates these tests schematically. The advantage of 4-point bending is that the central zone between the two inner loading points is free of shear, and also the load is applied through two loading points, thereby diminishing the risk of local indentation. 3-point bending is mainly used to measure the stiffness of the beam only, because failure usually occurs under the loading point, so with a mixity of local indentation and compressive failure of the skin, which gives no valuable information.

The requirements of the test are described in the ASTM standards [58]. The maximum deflection in the centre of the beam measured in 3-point bending is given by

$$w_3 = \frac{PL_3^{\ 3}}{48D_B} + \frac{PL_3}{4S_B} \tag{2.55}$$

The bending stiffness $D_B$ and shear stiffness $S_B$ can be calculated independently if the test is undertaken with two different spans. The use of a long span means that deflections due to shear can be disregarded.

The displacement of the loading points in 4-point bending is given by

$$w_4\left(\frac{L_2 - L_1}{2}\right) = \frac{P\left(L_2 - L_1\right)^2\left(L_2 + 2L_1\right)}{48D_B} + \frac{P\left(L_2 - L_1\right)}{4S_B} \tag{2.56}$$

and the relative displacement between the loading points and the center of the beam (measured by the Linear Variable Differential Transformer (LVDT) in Figure 2-9) is

$$w_{LVDT} = \frac{P\left(L_2 - L_1\right)L_1^2}{32D_B} \tag{2.57}$$

As the center part of the beam is free of shear, this last formula enables the bending stiffness $D_B$ to be calculated directly, and the shear stiffness can then be calculated with equation (2.56).

The direct stresses in the skins between the loading points are given by equation (2.7), that is

$$\sigma_f = \pm\frac{M}{Bt_f d} = \frac{P\left(L_2 - L_1\right)}{4Bt_f d} \tag{2.58}$$

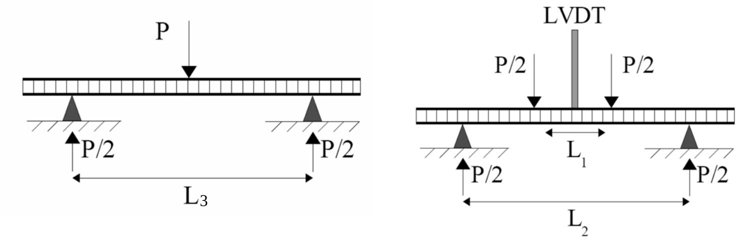

**Figure 2-9: 3-point and 4-point bending tests. The displacement of the loading point is measured, as well as the displacement of the centre of the beam in 4-point bending. The LVDT is fixed to the loading points and measures the difference between the deflection of the center point and the deflection of the loading points.**

During bending, when the sandwich deforms, a compressive load occurs in the core. This can be calculated by considering a portion of the sandwich beam submitted to pure bending, as illustrated in Figure 2-10. The equilibrium for the vertical component on the upper or lower skin separately is given by

$$\int_{-\theta}^{\theta} q\cos(\varphi) r d\varphi = 2N\sin\theta \tag{2.59}$$

where $\varphi$ is the angle between the vertical and the normal to the skin surface and q is the normal load per unit length exerted by the core on the skin. This gives

$$qr = N \tag{2.60}$$

and knowing that

$$\frac{1}{r} = \frac{M}{D_B} \qquad \text{and} \qquad Nd = M \tag{2.61}$$

we obtain finally

$$q = \frac{M^2}{Dd} \tag{2.62}$$

This load has to be taken in account for evaluating compressive failure of the core.

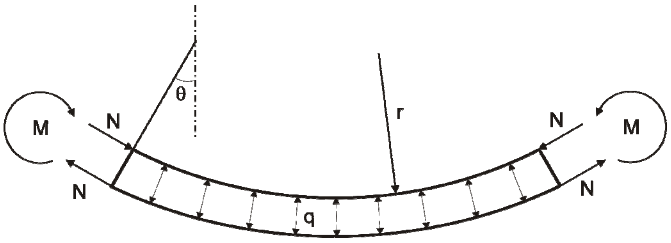

**Figure 2-10: sandwich beam in pure bending, with core replaced by load per unit length q**

### Compression test

Sandwich structures with thin skins are highly sensitive to local instabilities in compression and therefore failure modes under compression of the sandwich beam in a lengthwise direction have to be tested. This test has the advantage of loading the skins under pure compression without any out-of-plane loads. However several difficulties are encountered with this test. Firstly, failure often occurs at the load introduction points at the ends of the sandwich structure. The ends can be embedded in resin to avoid this problem. Secondly, the ends of the structure have to be perfectly parallel to the loading plates to avoid misalignment and dissymmetric loading. Equal loading of both faces of the sandwich is thus very difficult to obtain, and the real stress distribution in the skins is unknown, unless strain gages are placed on both sides of the sample, thus resulting in a wide scattering of the test results.

## Core-to-skin adhesion testing

As core-to-skin adhesion is difficult to predict by theory, numerous tests have been developed to evaluate the bonding. The Flatwise tensile test (FWT) [59] evaluates the tensile strength of the interface by pulling apart two blocks glued onto each face of a square sandwich sample. Figure 2-11 illustrates this test set-up. This simple test has often to be completed with more critical tests for the core / skin interface with pre-existing cracks. A modified double cantilever beam test (DCB) adapted to sandwich structures is often used to measure the strain energy release rate, or debonding energy, on sandwich structures [60]. A crack is propagated essentially in mode I (crack opening mode) by pulling apart the two skin tips of a sandwich beam. The main difficulty of this test is to measure the crack length, especially with honeycomb cores which are discontinuous. Therefore, Gunderson *et al.* [61] recently proposed a method to calculate the fracture toughness $J_C$ with the J-integral method [62] simply based on the load and the angular displacement of peel arms at the load application points during DCB test, thus avoiding measurement of the crack length. The measurements could then be carried out quickly with a simple transducer measuring peel arm angle. The DCB test is limited to sandwich structures with sufficiently thick skins to avoid too large bending of the skin during loading. Williams [63, 64] studied the potential errors due to large deflections of the peel arms during measurements with DCB tests for laminates, and introduced correction factors to obtain more accurate results. Different variations of this test were studied by Cantwell *et al.* [65-69] to measure the debonding energy either in mode I or mixed-mode (modes I and II). In particular, the single cantilever beam test illustrated in Figure 2-11 was often used. In this test, the sandwich sample is fixed onto a sliding carriage to allow self-alignment of the sample and to have mostly mode I crack propagation.

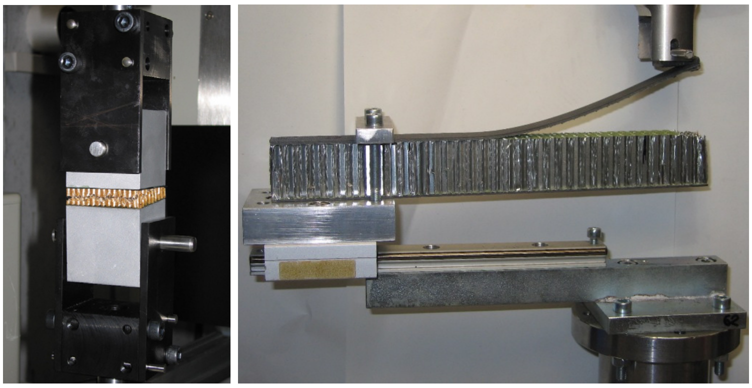

**Figure 2-11: Flatwise tensile test and single cantilever beam test on sandwich structures**

To measure the debonding energy for sandwich structures with very thin skins, either the skins have to be reinforced in order to use the DCB test or the climbing drum peel test can be used. The set-up used for this test is illustrated in Figure 2-12. The skin is rolled around a drum and progressively peeled from the core. By measuring the torque applied to the drum the debonding energy can be calculated. The crack is propagated principally in mode I and it was shown by Okada and Kortshot [70] that the strain energy release rate agreed well with that measured with the DCB test.

As the core / skin interface is often loaded in shear, it is also interesting to measure the strain energy release rate when a crack propagates in mode II (shearing mode). As no standards are available for such tests, various tests have been developed. The most current one is the cracked sandwich beam (CSB) test. It is based on classic bending test on a sandwich beam with a crack at the core / skin interface at one end of the beam. The crack propagates due to shear stresses in the interface during the bending test. This test only works when sufficient stiffness of the beam is maintained with partial core / skin debonding, i.e. with thick skins and a stiff core in in-plane direction. Therefore this test gives good results with foam cores [71-76], but is very difficult to use with honeycomb cores [77].

The tests described above are used to measure debonding energy in pure mode I or II. However, it is very difficult to identify the modes present in common loading cases. Charalambides [78] and Williams [79] have therefore developed analytical criteria to calculate the mode partition in laminates.

In order to better understand the mode partition and stress distribution at the core / skin interface, FE modeling is often used [69, 80-85]. The crack closure technique is often employed to calculate the mode partition of the strain energy release rate. In this method, a sandwich beam with an interfacial crack is modeled in the loading case studied. The forces that have to be applied on the nodes of the first element cracked at crack tip to close the crack are calculated in out-of-plane direction for mode I and in a lengthwise direction of the beam for mode II. With these loads and displacements of the nodes, the strain energy release rate in different modes can be directly calculated. These FE simulations enable the critical points and the most critical loading cases on the structure to be identified for debonding.

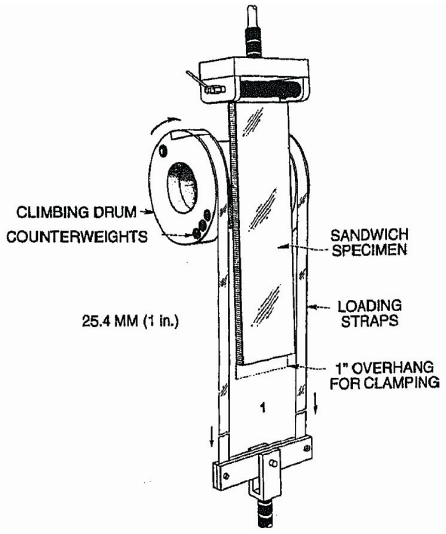

**Figure 2-12: Climbing drum peel test set-up (figure from [86])**

### 2.1.7. Design and optimization of sandwich structures

For optimal use of the high mechanical properties of the sandwich structures, all the different design variables have to be considered and the best compromise has to be found according to the loading cases during structure use. As the variation of each design variable affects all the others, a global optimization has to be carried out taking into account all the design variables at once in order to find the best sandwich structure for a given application. Such a global methodology for optimizing mechanical properties were described by Gibson and Ashby [87].

Froud [88] devised a simple analytical model to calculate the optimum ratio between skin weight and core weight for maximizing either the flexural rigidity or bending strength of sandwich beams. To calculate the flexural rigidity, the deflection due to shear of the core was not considered. With thin skins and weak core assumptions (see section 2.1.4), he found that maximal flexural rigidity was obtained when the core weight was 2/3 of the total weight. Similarly, by considering that failure of the beam occurred due to skin fracture, the maximum bending strength was obtained when the core weight was equal to the total weight of the skins.

These theoretical optima have been verified experimentally by Theulen and Peijs [89]. They produced sandwich panels consisting of foamed PVC core and glass/epoxy faces with various ratios of faces weight-to-core weight. The beams were tested under 4-point bending to measure their stiffness and strength. Every beam broke due to compressive failure of the face. Good correspondence was found between the experimental results and the theoretical model. More recently, a similar study was made by Murthy and

Munirudrappa [90]. They produced sandwich panels with GFRP skins and Nomex® honeycomb cores of various thicknesses and tested them with 4-point bending tests. They found an optimal core-to-skin weight ratio of 2.04 and 0.96 for stiffness and strength respectively, which correlates very well with theoretical models. However, they gave no details of the failure mode during tests evaluating the bending strength, which is vital to satisfy the basic hypothesis of face fracture for the model. For example, this model is not valid if face wrinkling occurs and is therefore not appropriate for the design of ultra-light structures.

Gibson [91] devised a similar optimization as Froud but concentrated on sandwiches with foam cores only. The basic hypothesis of the model was that, for foams, Young's modulus and shear modulus are proportional to the density squared. In his model, he calculated the bending stiffness, i.e. he considered the deflection due to pure bending and to shear of the core. He identified the optimal thickness for core and skins in order to reach the required bending stiffness by minimum weight. He found that the optimal ratio of the weight of the skins to that of the core is ¼.

Triantafillou and Gibson [92] studied the different failure modes in foam core sandwich beams with aluminum faces. They devised analytical models to predict the failure load due to face yielding, face wrinkling, core yield in shear, and core yield under tension or compression. They also considered possible debonding failure or core indentation, but this was not studied in detail. They developed failure maps predicting the failure type depending on core density and skin thickness for a given loading configuration. An example of such a map determining failure mode as a function of skin thickness to span ratio and core density is shown in Figure 2-13. They found that face yielding, face wrinkling, and core shear were the dominant failure modes.

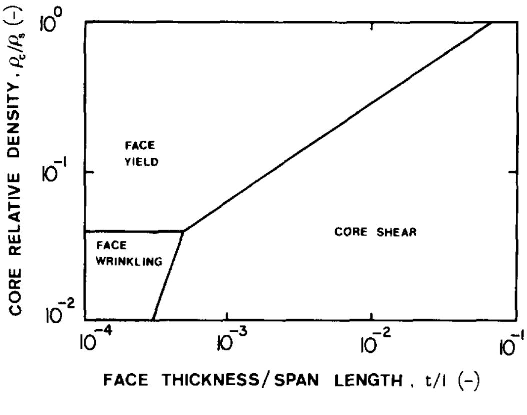

**Figure 2-13: typical failure mode map for sandwich plate with aluminum faces and foam core from reference [92]**

These maps were then verified experimentally by testing sandwich beams under 3-point bending and good agreement was found with the theory.

In a further study [93], they used the failure maps to find the minimum weight design for a given strength for foam core sandwich panels. The basic idea was that core and skin should break at the same time, otherwise one element is over designed. They found that the optimum design lies at the intersection of all three intersection lines on the failure map and that face yielding, wrinkling, and core shearing all occur simultaneously. The beam design variables are then fixed by the equations of the transition lines between failure modes. All these analyses assumed that the bond between the faces and the core did not fail. This has then to be further analyzed.

Petras and Sutcliffe [34] developed similar failure maps with honeycomb core sandwich panels. They investigated face yielding, intra-cell dimpling, face wrinkling, core shear failure, and indentation. They compared classic strength equations with 3-point bending measurements with various core densities, cell size, and span length. They found satisfactory agreement between the predicted failure loads and the measurements for face yielding, face wrinkling, and core crushing, but with significant scattering of the data. The prediction for face dimpling was poor. The limited quality of the results may be explained by the test chosen. In fact, the 3-points bending test caused failure under the loading point, making it difficult to separate the effect of core indentation from other failure types.

Ding [94] developed a methodology for optimizing the structure by taking into account the diverse global and local instabilities which can occur and gave a good overview of the buckling constraints.

The sandwich structures are often constructed symmetrically. Nevertheless, depending on the loading case, it may be advantageous to have skins of different thicknesses. For example, a sandwich with thin skins in bending will often break because of skin instability under compression, while the skin under tension is far from its tensile limit. Bending strength can then be improved by increasing the thickness of the skin under compression. Kim and Swanson [95] tested sandwich beams with foam cores and different face thicknesses. They did not obtain significant strength improvement because the failure was in the core. However they demonstrated the need to redesign every constituent when a change is made in order to improve the structure.

When the sandwich part is designed for commercial application, the cost has also to be part of the optimization process. To this end, Pflug and Verpoest [96] developed a methodology based on selection charts for sandwich structures in order to design structures with optimal cost / performance ratio.

All these different optimization procedures enable enhanced sandwich structures to be fabricated. However, as no design criteria exist for core to skin bonding, this potential failure mode was not taken into account for optimization. For classic sandwich structures weighing several kg per square meter, commercial adhesive films provide sufficient bonding, while increasing weight by only a few percent, whereas in ultra-light sandwich structures weighing less than 1 kg/m$^2$, an over-designed adhesive layer can significantly increase the weight. Therefore the influence of the adhesive joint on failure has to be taken into account and the debonding mechanisms understood in order to further optimize ultralight sandwich structures.

### 2.1.8. Core-to-skin bonding optimization

The study of bonding can be separated into two distinct scales of analysis: macroscopic scale by measuring debonding energy of the skin, and microscopic scale by observing the failure mechanisms. Many authors have measured the debonding energy of sandwich structures, principally with foam cores, but little attention has been paid to the microscopic mechanisms in skin debonding with honeycomb cores. A brief summary of the main conclusions of the papers studying core / skin adhesion with materials resembling those used in the present study is given in the present section.

#### Debonding energy measurements

To measure the debonding energy of a sandwich structure, every parameter during processing has to be carefully considered, since bonding can be highly sensitive to process variations. For example, using the DCB and FWT tests, Ural et al. [97] highlighted the fact that the debonding energy was lower for the skin on the bag side than on the tool side when the sandwich was cured in one shot, using the vacuum bag process. This showed that more resin flowed from the prepreg in the bonding line on the tool side than on the bag side, but no further analysis of the bonding line was made. This indicates that attention must be paid to the bonding of both sandwich faces, even if the materials and curing cycles are identical.

In addition, the geometry of the samples has to be chosen carefully, as this can also influence the measured strain energy release rate. Grau *et al*. [83] used the DCB test to measure fracture toughness with a honeycomb core and carbon skins. They especially studied the mode mixity at crack tip with FEM during a test. They observed that mode mixity and thus the strain energy release rate $G_c$ slightly changed with the thickness of the core and length of the crack in the DCB test. The interfaces subjected to a higher percentage of mode II stresses had a higher $G_c$ value. Using the DCB test, Avery and Sankar [98] also measured $G_c$ of sandwich beams with Aramid honeycomb cores and thin carbon skins, and observed the effect of varying core thickness, skin thickness, and core density. They measured higher values with low density cores and thick skins, but no significant effect of the thickness of the core was observed. As the sandwich was cured in one shot and the resin of the prepreg was used to bond the skin to the core, a larger amount of resin could flow in the bonding line when more layers of prepreg were used, thus explaining better bonding with thicker skins.

Berkowitz and Johnson [99] also used the DCB test to measure the fracture toughness of carbon skin to Nomex® honeycomb core bonding. They used the compliance calibration method [60] to avoid carrying out difficult crack length measurements. Once the equation correlating compliance to crack length was established, the toughness could be directly calculated, based on the force displacement curve, without measuring the crack length. They observed that with a light Nomex® honeycomb core (48 kg/m$^3$) bonded with commercial adhesive (Cytec Meltbond 1515-3M) film on the prepreg by co-curing, bonding was sufficiently high so that cracks propagated in the honeycomb core and not in the bonding line with a strain energy release rate of 1180 J/m$^2$ at ambient temperature. This shows that the core / skin bonding was oversized and needed to be optimized.

### Microscopic failure mechanisms

For honeycomb core-to-skin bonding, the formation of a resin fillet between honeycomb cell wall and the skin was shown to be determinant. Figure 2-14 shows a schema of a cross-section of such resin fillets. Okada and Kortschot [70] studied the importance of the resin fillet during core / skin delamination. They demonstrated that bigger resin fillets absorb more energy during delamination, due to energy dissipation phenomena by fillet breaking. In fact, because of the energy dissipation in the resin fillets, the strain energy release rate value of the honeycomb core-to-skin bonding could exceed that of a laminate made from the skin material and same resin as the fillet, even though the area of fractured resin was lower.

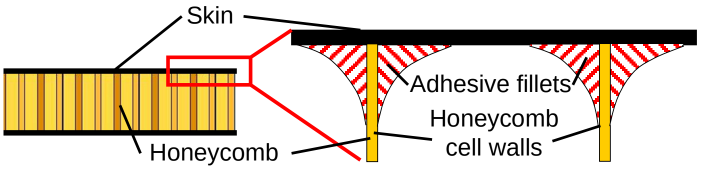

**Figure 2-14: schematic representation of the adhesive fillets forming between the skins and the honeycomb cell walls**

Grove *et al*. [100] studied the influence of cure cycle, vacuum pressure, temperature ramp rate, and vacuum application time on debonding energy. The temperature during the curing cycle and the temperature ramp rate had the most significant effect on the bonding. They found that high peel strengths were associated with the largest and most regular adhesive fillets between the skin and core cell walls. The same findings were made by Allegri *et al*. [101]. They used an interesting method to obtain a uniform geometric shaping of the menisci. They laid a thin adhesive film on the honeycomb core, perforated the film in the middle of each cell and then heated it with a heated air jet. The viscosity of the resin decreased and the adhesive film tore in the middle of the cells. The resin was pushed by the air jet close to the edges of every single cell and it was shaped into a bonding meniscus made of partially reticulated adhesive. The skin was then placed onto the core in direct contact with the menisci. This process enabled the whole adhesive film to be used in the regularly shaped adhesive menisci, thus obtaining better bonding than with classic adhesive film forming smaller and more irregular menisci.

The determinant effect of the meniscus size was also demonstrated by Chanteranne [102]. He studied the influence of the honeycomb cell size on meniscus size. He stated that the height of the fillets increased with the size of the honeycomb cells due to larger amount of adhesive available, and that the associated debonding energy was higher. He also observed that the humidity rate in the processing room, and primer treatment of the Aluminium honeycomb had important influences on meniscus height and thus on debonding strength, the highest strength being associated with high menisci.

The dominant influence of the resin menisci in bonding was further highlighted by Hayes *et al*. [103]. They showed that not only the size, but also the quality of the resin fillet played a role. They made sandwiches with commercial self-adhesive prepregs and a home-made model prepreg with less solvent content. They showed that the solvent led to porosity formation and then decreased debonding energy.

These different studies underline the need to control meniscus formation in core / skin bonding in order to achieve good bonding and to predict failure mechanisms during debonding.

### Debonding in sandwich structures under compression and bending

Measurement of the critical strain energy release rate $G_c$ and an understanding of failure mechanisms enables the debonding energy for the special loading case used for the measurement of $G_c$ to be predicted and improved, but gives no information for the design of a sandwich structure with optimized core-to-skin bonding for loading cases to which the structure will be subjected when functioning in reality. In actual practice, the debonding energy is often measured in opening mode by peeling, but debonding of a skin in fact often occurs when the skin buckles due to applied compressive stresses. Several authors have studied the so-called post-buckling behavior of sandwich structures with bonding defects, or composite plates with delamination, in order to predict further propagation of the defect [84, 85, 104-111]. This research field has often been studied in order to understand the behavior of structures exhibiting impact damage under compressive loading. However, this domain is too wide to be reviewed in the present work and only a few results of interest for the present study are considered here.

Models have often been developed using finite element simulation. One important conclusion to be drawn from these different studies is that post-buckling crack/defect propagation occurs mainly in mode I, and thus confirms the importance of determining the debonding energy in this mode [84, 85, 105, 106]. However, depending on the loading case, Grau *et al*. [83] demonstrated that ignoring mode-mixity at crack tip can lead to overestimation of the load carrying capacity of debonded sandwich panels by as much as 40%. This confirms the need to know precisely the distribution and the mode of the strain energy release rate at crack tip. To this end, Withcomb and Shivakumar [84], for example, described a virtual crack closure technique which enabled mode partition and the distribution of total strain energy release rate around the boundary of a rectangular delamination to be calculated in a laminated plate. Such a calculation made it possible to predict where and at which stress level the delamination propagated.

For a simpler loading case, such as compression or bending of a sandwich beam with partially debonded skin, prediction of the ultimate compressive stress can be made based directly on the strength of the bonding [109], or on the critical strain energy release rate measured in mode I. On the basis of the $G_{IC}$ value, Kim and Dharan [112, 113] developed an analytical model to predict the critical compressive load which causes skin buckling and debonding on beams with an initial debond. They therefore adapted the buckling model of Vizzini and Lagace [108, 109] in order to calculate the strain energy release rate. The model correlated well with experimental results and may be used to predict a skin buckling load, knowing the initial debond length and $G_{IC}$ value for core / skin bonding. However, the authors used a very low $G_c$ value, in the order of 5 J/m$^2$ to validate the model (usual $G_c$ values for such bonding are ~1000 J/m$^2$), which is questionable for the validity of the model and results.

On the basis of the core / skin debonding energy, Zenkert [114] developed a similar analytical and FE model to predict the failure load of sandwiches with foam cores and with interface debonds loaded in bending. He investigated the shear stresses at the interface, and measured the critical energy release rate in mode II using the CSB test, and obtained good agreement between tests and model predictions.

### 2.1.9. Process optimization

Once all the components of the sandwich structure are chosen in order to obtain an optimal structure, the processing method has also to be adapted and optimized to achieve the highest possible quality. The main parameters are the applied pressure, the curing cycle, the number of cures, and finally the consumable used (i.e. the films, peel ply, breather cloth, etc, placed on the sandwich panel during curing).

The easiest way to produce a sandwich panel with prepreg faces is to cure the skins directly on the core and bond them to the core at the same time, the so-called one-shot curing. The pressure required to press the skin against the core is usually applied by a vacuum bag. When honeycomb core is used, the skin on the vacuum bag side is pushed into the cells by the vacuum bag and a wavy surface results [16, 17]. This is often called the telegraphic effect. This was shown to decrease the compressive strength of the sandwich and to favor local instabilities. The skin cured on the mould side is of better quality, but with irregular compaction due to the local pressure applied only under honeycomb cell walls and not in the center of the cells. Furthermore, as thin uncured skins have almost no compressive stiffness, lateral crushing of the honeycomb core due to the applied pressure [13-15] has to be avoided by using a very stiff frame. This can be difficult when dealing with large panels with a curved shape.

The optimal quality of the skins is reached by curing them separately under high pressure in an autoclave prior to bonding onto the core [31, 33]. Perfectly flat skins with low porosity can be obtained with this process. However, this process is only suitable for flat panels, but not for curved sandwich panels, which will require two different moulds for the two skins. Furthermore, the secondary bonding will require more adhesive, i.e. more weight, to reach a bonding strength similar to that obtained with one-shot processing where the resin of the prepreg can participate in the bonding. A further disadvantage of this method is that the skins have to be manipulated after curing to bond them onto the core, which can be very difficult with large thin skins, especially if internal stresses deform the skin after curing. This process also precludes using combo prepregs, i.e. with the adhesive already deposited on the prepreg, so that adhesive films have to be used. This can be time consuming on large parts, especially with light adhesive films difficult to manipulate.

A compromise between these two processes is to bond the core to the skin on the tool side by co-curing, and to bond the second skin also on the tool side by a second co-curing. This is simple for flat panels which have simply to be turned down on the mould, but will necessitate two moulds for curved panels.

The curing cycle influences resin viscosity during curing and so changes the resin flow. Grove [100] showed that the curing temperature and cycle can influence the bonding of the skin. So the different curing cycles recommended by the adhesive manufacturer can give different qualities.

The consumables used during curing can also affect the sandwich quality. To be able to drain air through the prepreg to obtain a vacuum in the honeycomb cells [115] (in the case of a non-perforated honeycomb), the classic method is to put a peel ply, perforated non-adhesive film, and then a breather cloth on the surface. During curing, part of the prepreg resin may flow into the peel ply, thereby reducing the quality of the skin. The use of a non-perforated film on the surface solves this problem, but prevents good air circulation and the formation of a good vacuum in the cells. A compromise has then to be found to obtain sufficient vacuum without sucking too much resin out of the skin prepreg.

Finally, the process pressure also exerts a significant influence on the mechanical properties on the sandwich panel. High pressure causes a telegraphic effect and then reduces the compressive strength of the skin [17], while a too low pressure may lead to bad skin quality. The optimal process pressure has thus also to be calculated in order to attain the highest strength of the panel.

### 2.1.10. Conclusions

Sandwich structures are widely used in applications requiring lightweight and stiffness. The various failure modes have been intensively studied and have been shown to be highly interactive. Therefore the constituents cannot be optimized individually, but the sandwich structure has to be considered as a whole. To this end, optimization procedures have been developed taking into account most of the failure modes. However, no failure criteria are available for skin-to-core bonding design, especially for very light sandwich structures.

Core-to-skin bonding has been mainly studied by measuring the debonding energy with various core and skin designs, and many test methods have been developed to this end. In the case of a honeycomb core, it has been shown that the adhesive menisci forming between the core cell wall and the skin control core-to-skin bonding, and are most efficient when their size is large and their shape regular. The debonding energy measured with specific tests can be used for the prediction of strength of structures with preliminary core /skin debonding, but often requires FEM to know the stress state in the debonding area.

Many processes for making sandwich structures have been developed. Vacuum bag curing has been widely used and studied. It has been shown that the pressure can cause a surface waviness on the skin on the vacuum bag side when honeycomb core is used, thus decreasing the strength of the panel. However, little attention has been paid to the manufacture of ultra-light sandwich structures.

## *2.2. Solar cells mechanical analysis and encapsulation*

### 2.2.1. Introduction

For high-tech applications requiring high efficiency (defined as the ratio between the electrical output energy of the cell and the incoming solar energy, i.e. the energy of the photons coming on the cell), the solar cells used are either silicon solar cells which can reach an efficiency of 24 % [116-119] or multi junction solar cells with gallium arsenide (GaAs) and/or gallium indium phosphide (GaInP) junctions with an efficiency higher than 30 % [120]. In term of efficiency, the selection of multi junction solar cells is advantageous, but for large surfaces as for solar gliders [10, 121], the very high price of multi-junction cells is a limiting factor. Nowadays, therefore, the mono-crystalline silicon solar cells represent the best compromise for efficiency, weight, and cost for high-tech applications over large surfaces [122, 123].

Silicon is not only used for solar cells. It is in fact the basic material of the microelectronic industry for its semiconductor properties. It is also more and more used for Micro-Electro-Mechanical Systems (MEMS). A good knowledge of the mechanical properties of silicon is of primary importance in improving the reliability, and especially the process yield, i.e. avoid breaking the wafer (thin plates of silicon in the range of 100 to 500 μm thickness) during manipulation. For this reason, silicon failure properties have been already studied extensively, but particularly at the size-level of the MEMS (μm size order). Studies of mechanical behavior of complete wafers such as those used in solar cells technology are less common. In fact, most of solar panel producers avoid exposing wafers to the hazards of mechanical loading by gluing the wafer directly onto a glass substrate. This stiff substrate prevents deformations and stresses on the wafer. Therefore, only a limited amount of literature is available dealing with testing complete silicon solar cells in order to identify the mechanical properties.

### 2.2.2. Silicon for solar cell applications

Solar cell technology uses silicon in three possible forms: single crystal, semi-crystalline and amorphous [116, 117, 124, 125].

In single-crystal silicon, the molecular structure (the arrangement of atoms in the material) is uniform, because the entire structure is grown from the same crystal. This uniformity is ideal for transferring electrons efficiently through the material. Single-crystal silicon therefore enables the most efficient solar cells to be constructed with this material, and the following sections will concentrate on this type.

Semi-crystalline silicon, in contrast, consists of several smaller crystals or grains, which introduce boundaries. These boundaries impede the flow of electrons and encourage them to recombine with holes (place left by lacking electron on atoms) and thus reduces the power output of the solar cell. However, semi-crystalline silicon is much less expensive to produce than single-crystalline silicon. So researchers are working on other ways to minimize the effects of grain boundaries.

Amorphous solids, such as common glass, are materials whose atoms are not arranged in any particular order. They don't form crystalline structures at all, and they contain large numbers of structural and bonding defects. However, they have some economic advantages over other materials that make them attractive for use in solar electric or photovoltaic (PV) systems.

To create silicon in a single-crystal state, high-purity silicon has first to be molten. It is then solidified very slowly in contact with a single crystal "seed." The silicon adapts to the pattern of the single-crystal seed as it cools and gradually solidifies. One can say that this process is "growing" a new rod of single-crystal silicon out of molten silicon.

Several different processes can be used to grow a rod of single-crystal silicon. The most established and dependable processes are the Czochralski (Cz) method and the float-zone (FZ) technique. In the Czochralski process, a seed crystal is dipped into a crucible of molten silicon and withdrawn slowly, pulling a cylindrical single crystal as the silicon crystallizes on the seed. In the float-zone process, a silicon rod is set atop a seed crystal and then lowered through an electromagnetic coil. The coil's magnetic field induces an electric field in the rod, heating and melting the interface between the rod and the seed. Single-crystal silicon forms at the interface, growing upward as the coils are slowly raised. The float-zone process produces purer crystals than the Czochralski method, because they are not contaminated by the crucible used in growing Czochralski crystals.

Once the single-crystal rods are produced, by either the Cz or FZ method, they must be sliced or sawn to form thin wafers. Such sawing, however, wastes as much as 20% of the valuable silicon as sawdust.

The resulting thin wafers are then doped in order to produce the necessary electric field. In fact, in a crystalline silicon cell, p-type silicon contacts n-type silicon to create the built-in electrical field. P-type silicon is silicon with a lack of electrons (p = positive), and n-type silicon is silicon with to many electrons (n = negative).

The process of doping, which creates these materials, introduces an atom of another element into the silicon crystal to alter its electrical properties. The "dopant," which is the introduced element, has either three or five valence electrons (which is one less or one more that silicon's four). Phosphorus (five valence electrons) and boron (3 valence electrons) are the most often used dopants. Doping also slightly changes molecular structure, replacing some silicon atoms by others, a fact that should be taken into account in mechanical analysis.

The wafers are then treated with a coating to reduce reflection [126, 127] (for example with a thin layer of silicon or titanium oxide). A second technique is texturing the top surface [128-132]. Selective chemical etching for mono-crystalline cells or mechanical texturing for polycrystalline ones creates a pattern of inverted cones or pyramids, which capture light rays that might otherwise be reflected away from the cell.

The wafers are then coated with electrical contacts to form functioning PV cells.

### 2.2.3. Elastic properties

Single crystalline silicon has anisotropic mechanical properties. As the Young's modulus depends on the crystalline orientation, it is difficult to measure accurate values, and therefore the values vary according to different sources [133-135]. Well accepted values are those measured in [133] given in Table 2-1.

**Table 2-1: single crystal silicon Young's modulus**

| **Direction** | **<100>** | **<110>** | **<111>** | **Mean value** |
|---|---|---|---|---|
| **Young's modulus (GPa)** | 130.2 | 168.9 | 187.5 | 162.2 |

These high values of elastic modulus potentially make silicon suitable for mechanical application where high stiffness is required.

### 2.2.4. Mechanical strength

The mechanical strength of silicon is difficult to measure because the strength of a test probe is highly dependant on surface defects [135-140]. However, measurements of the intrinsic strength of silicon showed very high values. The tensile yield strength of silicon single crystals was measured at 6.9 GPa [134], which is at least 3 times higher than stainless steel. But the primary difference is that silicon yields by fracturing (at room temperature) while metals usually yield by deforming plastically. Therefore the intrinsic strength is almost never reached on a silicon part since it breaks (brittle fracture) at lower stress because of stress concentrations at defects. It is therefore of primary importance to reduce surface defects to get good mechanical strength for silicon parts. Mechanical processing such as sawing, grinding and polishing, which introduce surface defects, have to be avoided, or followed by further surface treatment such as chemical etching in order to remove the highly damaged regions.

The influence of defect size on the fracture strength of a silicon part is easy to understand by knowing the toughness value compared to that of other materials as summarized in Table 2-2. The fracture stress for a given surface defect size can be calculated as

$$\sigma = K_{IC} / [1.12(\pi a)^{1/2}] \qquad (2.63)$$

where *a* corresponds to the depth of vertical cracks at the surface of the material [141]. It means that for a given stress state, a steel surface will fail with a surface defect 10’000 times larger than on a silicon plate (the steel will thus fail by yielding before it fractures).

**Table 2-2: toughness of different materials**

| | **Toughness ($K_{IC}$) (MPa $m^{1/2}$)** |
|---|---|
| **Single crystal silicon** | 0.9 [137, 142] |
| **Windows glass** | 0.7-0.8 |
| **High strength steel** | 50-150 |

The effects of surface damage size on the fracture strength of silicon are well described by Ericson and Schweitz [137]. They showed the influence of diamond polishing of a silicon wafer on its fracture strength. They used diamond paste of three different grades (0.25, 1 and 3 μm) and also studied the effect of thermal oxidation. They measured strength almost as high as intrinsic strength. They were able to do this because of the small size of the cantilever beam tested (197 μm long and 17 μm thick) and the careful preparation and etching of the samples, removing almost all surface defects. They observed that the average fracture strengths diminished by 33%, 54% and 75% respectively for the three paste grades as reported in Table 2-3. Thermal oxidation of the polished silicon surface not only restored the original fracture strength, but actually resulted in fracture strength 15%-20% higher than the original. It was thought that most of the polishing damage on the silicon surfaces became incorporated in the oxide layer and that this oxide layer acted as a strengthening agent.

The calculation of the surface defect size *a* corresponding to the failure stress can be made with equation (2.63). It shows that defects of size in the order of 10 nm have already a significant influence on the strength. It explains why mechanical processing as sawing, grinding, etc, which introduce defects greater than this size should be avoided.

**Table 2-3: fracture strength characteristics measured by Ericson and Schweitz [137]. σ = fracture stress, m = Weibull modulus, a = depth of initiating surface cracks**

| | | **Polished 0.25µm** | | **Pol. 1 µm** | **Polished 3 µm** | |
|---|---|---|---|---|---|---|
| | **Reference** | | **+ oxidized** | | | **+ oxidized** |
| **σ (GPa)** | 6.1 | 4.1 | 7.2 | 2.8 | 1.5 | 7.0 |
| **m** | 10.1 | 6.3 | 32.4 | 8.0 | 9.1 | 6.7 |
| **a (nm)** | 6 | 12 | (4) | 26 | 91 | (4) |

For such a fracture type, it is interesting to use the Weibull failure probability distribution function [137]. For a body exposed to a stress field σ, the probability of failure is

$$P_f = 1 - e^{-\int_v \left(\frac{\sigma - \sigma_u}{\sigma_0}\right)^m dv} \qquad (2.64)$$

where

V = the volume of the stressed body

$\sigma_u$ = a lower stress limit which is usually equal to zero in brittle materials (N/mm$^2$)

$\sigma_0$ = a parameter related to the average fracture stress (N/mm$^2$)

m = the Weibull modulus, a measure of the statistical scatter displayed by fracture events

For simple geometry, it can be simplified into the two-parameter Weibull probability function [143]

$$P_f = 1 - e^{-\left(\frac{\sigma}{\sigma_0}\right)^m} \qquad (2.65)$$

The higher the Weibull modulus m, the smaller the spread of failure stress. The prediction of failure stress for materials with high m values is thus more reliable than for those with small m values.

When the failure stress of several samples is measured, the Weibull modulus m can be calculated. Equation (2.65) can be written

$$\ln\left[\ln\left(\frac{1}{1-P_f}\right)\right] = m\ln\sigma - m\ln\sigma_0 = m\ln\sigma + const \qquad (2.66)$$

By drawing the ln-ln plot, *m* is given by the slope of the curve. However, to obtain an accurate value for *m*, testing of many samples is necessary. To obtain an uncertainty of ±10 %, more than 120 samples are needed [143].

The measurements of Ericson and Schweitz showed that polishing slightly diminished the Weibull modulus *m* (Table 2-3), therefore increasing the spread in fracture strength.

Wang *et al*. [139] and Wilson and Beck [140] also showed the importance of defect size by comparing surface treatment (grinding, polishing, etc). They also studied the influence of crystal orientation on strength. They showed that the <111>-type fracture was the most frequent one. It was expected because the <111> planes of silicon, a diamond cubic structure, have the lowest surface energy to overcome as the crack propagates.

As already mentioned, one way to reduce surface defects is to etch the surface. Yi *et al*. [135] evaluated the strength of tensile test samples treated with different etchants. Due to the anisotropic structure of single crystal silicon, there was a directional etching by anisotropic etchants such as KOH. This caused the formation of “steps” with sharp corners in place of a smooth surface, resulting in low strength. Chemical etching should then be used carefully so as not to create further stress concentrations on the surface.

Similarly, Stefancich *et al*. [138] measured the effect of two different etching techniques on the strength of a silicon wafer with bending tests of clamped cantilever. Using alkaline etching, which creates a pyramidal textured surface due to the anisotropic etching, they obtained 150 % increase of the surface stress at failure compared to the “as cut” wafer. Using acidic etching which creates a smooth surface, the increase was 250 %. Table 2-4 summarizes their results. The stresses measured were still far from the intrinsic strength of honeycomb, showing that critical defects still remained on the sample surface or sides. The Weibull modulus showed, however, a higher dispersion of the measured values for the etched samples. The difference between the two etching process also showed that the texture of the surface diminished the stress at failure.

**Table 2-4: Maximum stresses and Weibull modulus measured in bending with different surface preparations (from [138])**

| Samples | Maximum stress (MPa) | Weibull modulus |
|---|---|---|
| **As sawn wafers** | 145 | 8.8 |
| **Alkaline etched** | 212 | 5.7 |
| **Acidic etched** | 338 | 5.4 |

Many studies have been dedicated to the effect of surface defects and surface treatments only, but the edges of the silicon parts are also likely to have micro-cracks and cause failure. Schoenfelder *et al*. [144] studied three different dicing techniques: sawing, dicing by chemical thinning with sawn groves and dicing by chemical thinning with dry-etched trenches. Using 3-point bending tests, they found that the sawing process induced edges with defects causing premature failure. The maximum stresses at failure could be increased by 500% with the third dicing process. The surface treatments have thus to be accompanied by edge treatments to really improve the strength of the silicon wafers.

### 2.2.5. Solar cells mechanical testing

As the strength of a silicon part is dependant on the presence, or not, of surface defects, it is necessary to test the solar cell itself to know its strength. Behnken *et al*. [142] described different testing configurations for a square 100 x 100 mm$^2$ wafer to assess the wafer strength. Some of them are illustrated in Figure 2-15:

- Point bending: the force is introduced at the center of the wafer top side; the three supports are positioned at the bottom side on a circle of radius 40mm.
- Biaxial point bending: the wafer is supported by a ring of radius 40 mm and the force acts at the wafer center.
- Double ring bending: the wafer is supported by a ring of radius 40 mm and the force is transmitted by a ring of half diameter.
- 3-line bending: the sample is supported by two parallel lines with distance d=80 mm. The force is applied by a third line centered between the supports.
- 4-line bending: the sample is supported by two parallel lines with distance d=80 mm. The force is applied by two parallel lines with distance 40mm centered between the supports.

- Twist test bending: the wafer is supported by two points on the wafer diagonal with 22 mm, 10 mm or 2 mm perpendicular distance to the wafer edges. The forces act on the other diagonal on the top side.

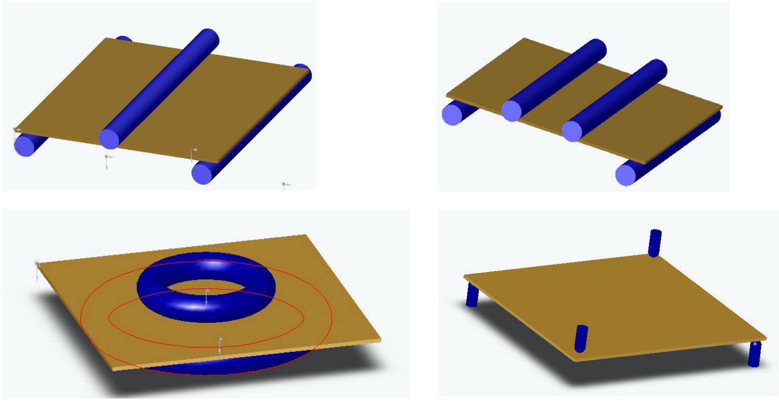

**Figure 2-15: different wafer-testing configurations: 3-line bending, 4-line bending, double ring bending, and twist bending.**

Point bending, biaxial point bending and double ring bending are efficient for testing the strength of the wafer without the edge effects, because the stresses are essentially concentrated at the center of the wafer. It is, however, difficult to correlate the failure loads with the failure stresses since the stresses distribution in the wafer is quite complicated and requires numerical analysis to be described accurately.

3-line, 4-line, and twist bending include the effect of the edges on the strength of the wafer. This is important in order to ascertain the real strength of the wafer, since crack growth often begins at edge flaws induced during sawing or laser cutting. 3-line bending produces a rather local loading of the edge and is therefore useful when studying local damage of the wafer edge, whereas 4-line bending enables extended sections of the edges to be tested. In both tests wafer anisotropy can be taken into account by testing the wafer in two different directions. Twist bending tests all wafer edges more or less simultaneously. It is useful for comparing the strength of different wafers, but it is difficult to correlate the failure load to the stresses, since the stress distribution is complicated.

Kray *et al*. [145] tested wafers of thickness from 70 µm to 500 µm to analyze the relation between thickness and strength, using the 4-line bending test. They observed that the breakage force increased monotonically with the thickness, but with an exponent of 1.66 as illustrated in Figure 2-16. If the surface stresses at failure were the same for the different thicknesses, the exponent would be 2. Surface stresses at failure were in fact smaller with thicker wafers. Supplementary fine polishing of the thin wafers removed some critical surface defects introduced by sawing, and explains the highest stresses at failure.

Similarly, the minimum radius of curvature of the wafer before cracking varied proportionally to $W^{0.73}$ (W is the wafer thickness), whereas it should be linear if the surface stresses at failure were the same for the various thickness.

These two curves show that it is advantageous to reduce the wafer thickness and thereby to remove surface defects to increase wafer flexibility, and increase the surface stress at failure.

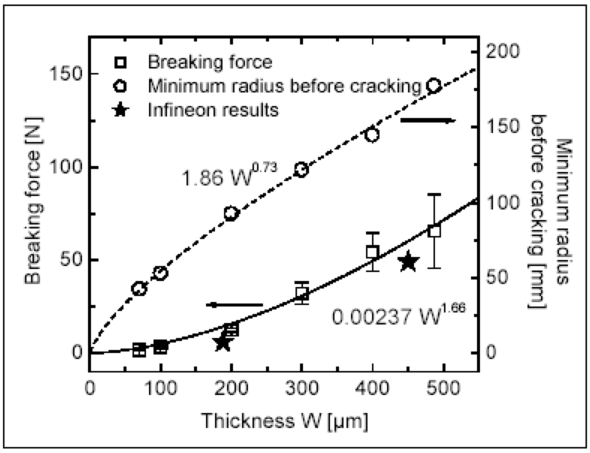

**Figure 2-16: measured breaking force and minimum radius before cracking as a function of wafer thickness. Stars represent measurements of Kröninger [146] (figure from [145])**

Using the twist bending test Schneider *et al.* [147] also measured an increase of wafer failure load with thickness with an exponent 1.85, which showed a slight increase of surface strength when the thickness was decreased. They also observed that alkaline etching improved the load at failure of the wafers by up to 30-50%.

Münzer *et al.* [148] studied the mechanical strength of wafers with different thicknesses and different surface texturations. The surface texturation was made of small pyramids (2-20µm) that covered the surface and thus improved the light trapping effect, especially at low incidence angles.

They therefore used the point bending test, which enabled the strength of the wafer to be measured with limited influence of the edges of the wafer. They also found a decrease in failure load and an increase in flexural deformation by reducing thickness. But they observed an even more pronounced dependence on the wafer surface preparation than on the wafer thickness. Figure 2-17 illustrates the failure load as a function of wafer thickness for different surface treatments. The highest fracture force was measured on a damage-etched wafer which presented a near "flaw-free" surface. The breaking force of textured wafers was significantly smaller. Texturation with the biggest pyramids had the most severe effect on the breaking force. Wafers with texturation on both sides had the lowest breaking force, but wafers with only texturation downside (side in tension) had nearly the same breaking force, while those textured only upside had almost twice as high breaking force. This means, as expected, that it was the side under tension which was critical for breaking and that the texturation created sufficient stress concentrations to decrease the strength of the cell.

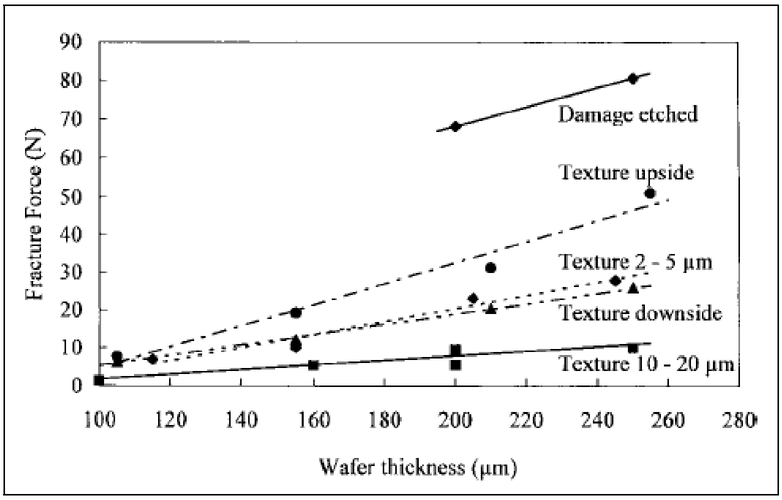

**Figure 2-17: fracture force of silicon wafers with different surface preparations as a function of the wafer thickness (figure from [148])**

Schneider *et al.* [149] studied the effect of the different fabrication steps on the wafer breaking force in twist bending tests. The process revealed several noticeable points. Firstly, they achieved about 10% strength increase by etching the wafer. Optimal etching depth was investigated [149, 150] and was located at about 15 µm. Less depth was not enough to remove sawing defects, greater depth caused step formation due to different crystallographic orientation in different grains (polycrystalline wafers were studied).

Secondly, edge isolation by sawing reduced the breaking force by about 20%. Edge analysis by SEM after sawing showed that sawing introduced notches on the edge, which favored crack growth. Finally, screen printing and contact firing process (deposition and fixation of the electric grid) yielded a 30 % strength reduction of the wafer. All these different parameters thus contribute to the low strength of solar cells in comparison to intrinsic strength of silicon.

### 2.2.6. Ultra-light encapsulation of solar cells

Silicon solar cells need to be encapsulated to obtain a protection against environmental attacks (moisture [151], dust, etc.) and to ensure sufficient mechanical support to avoid breaking. In most cases, a glass protection is used. Glass has many advantages: it is highly optically transparent in useful wavelengths, UV stable, it is a moisture barrier and is very stiff, which provides high mechanical stability and protection to the brittle silicon solar cells. But glass has to be thick enough to have sufficient strength and then becomes too heavy for applications requiring lightweight panels.

To obtain a lightweight encapsulation, thin polymeric materials should be used. As this ultra-light encapsulation is dedicated to very specific applications, such as solar planes, or racing solar cars, only a limited amount of literature is available on this topic.

Nowlan *et al.* [123] studied different combinations of cover films and encapsulants for photovoltaic modules on unmanned aerial vehicles (UAV). They used ethylene vinyl acetate (EVA) and silicone transfer adhesive as encapsulant, both of them in the form of 50 µm thick film. The tested cover films were 23µm thick DuPont Tefzel®, and 25µm thick DuPont Tedlar® with UV-screening additive. They developed a fabrication method to achieve the required quality. The cover film was pre-laminated on the encapsulant film to form a void-free and wrinkle-free film. Then it was assembled onto the solar cells by vacuum laminating. Further planned environmental tests have not yet been reported.

Snowdon *et al.* [152] investigated different material combinations to encapsulate the solar array of Sunswift II. They also tested EVA and silicone as encapsulants. The main problem with silicone was to remove bubbles from the silicone when working out of vacuum. EVA film was therefore used to encapsulate the cells. A disadvantage with EVA was the needy for heating (~100°C) during lamination as this caused small wrinkles in the polycarbonate cover film due to the CTE mismatch between the constituents.

They also attempted to use Teflon® or Tefzel® as cover film. But they were not able to produce wrinkle-free surfaces with very thin films. They finally used 0.38mm thick polycarbonate sheets. With this cover, the optical losses were about 4%.

Both sides of the cells were encapsulated in this way in order to obtain a symmetric structure, thus avoiding bending with temperature variations. It was then fixed on a carbon fiber structural substrate.

The company Photon Technologies proposed 3 different solutions for ultralight polymeric encapsulation. An EVA encapsulant with Tefzel® cover film may be used. The principal problem, as noted above, is the need to use heat-laminating, inducing internal stresses due to the CTE mismatch. To allow room-temperature laminating, two-part silicone may be used instead of EVA. Conformal coating encapsulation (for example Dow Corning 1-2577) offer “self-washing” surface and thus avoid using a cover film.

Accelerated exposure tests conducted by Pern and Glick [153] under high UV exposure showed that EVA tended to turn yellow-brown, which reduced the optical transmission and the efficiency of the solar panel. On the other hand, solar cells encapsulated with silicone and a UV-transmitting film (like Tefzel®) did not have this yellowing problem. Discoloration of the EVA encapsulant has also been demonstrated by Klemchuk *et al.* [154].

### 2.2.7. Conclusions

Mono-crystalline silicon presents high stiffness and high intrinsic strength, but very low toughness, making it highly sensitive to surface defects. Therefore the thin silicon wafers constituting the solar cells are very brittle and the surface requires very fine polishing and then chemical etching to remove as much as possible the defects created during wafer sawing. Attention has also to be paid to surface treatments and texturation in order to increase cell efficiency, as these can reduce the strength of the cells.

The use of polymer film as a lightweight encapsulation has proved successful. However, careful selection of the materials regarding long-time environmental stability is necessary. The use of fluorinated films having good optical properties in association with silicone adhesive has been shown to be a durable choice.

# CHAPTER 3. MATERIALS AND EXPERIMENTAL METHODS

The behavior of new composite materials is often difficult to predict accurately. Particularly in the present study, the combination of sandwich structures with very thin skins and light cores with brittle silicon solar cells is completely new, and therefore the behavior unknown. The optimization of such structures thus requires a lot of experimental testing in order to characterize the structure manufactured, and then be able to model it. To this end, many different experimental methods were used. Some of these methods are common and are only briefly mentioned, others needed special adaptations and developments and are thus described in details in the present chapter.

Also to avoid describing the materials used in every chapter, a description of the main materials composing the sandwich structures studied, and their properties is given.

## 3.1. Materials

### 3.1.1. Honeycomb core

The core used for the sandwich construction was a 29 kg/m$^3$ Nomex® hexagonal honeycomb of aerospace grade with a 3.2 mm cell size (distance between two parallel cell walls) and 8 mm thickness. In the first part of the study, concerning the core-to-skin bonding analysis, a core from Hexcel was used, while for all the sandwich panels tested in bending, the core came from Euro-composite. The two different types were used for availability reasons. The properties of the two cores are, however, very similar and are listed in Table 3-1 and Table 3-2. The data are taken from the suppliers datasheets. The modulus of the honeycomb from Euro-composite was not available and was therefore measured by compressing 50 x 50 mm$^2$ samples between two plates.

**Table 3-1: mechanical properties of the Nomex® honeycomb core from Hexcel. Under compression, the bare value corresponds to testing of honeycomb with simply supported boundary conditions for cell walls, while the stabilized value corresponds to clamped boundary conditions, i.e. with honeycomb bonded to loading plates**

| Compression [MPa] | | | | | Shear [MPa] | | | | | |
|---|---|---|---|---|---|---|---|---|---|---|
| Bare | | Stabilized | | | Ribbon direction | | | Perpendicular to ribbon | | |
| Strength | | Strength | | Modulus | Strength | | Modulus | Strength | | Modulus |
| min | typ | min | typ | typ | min | typ | typ | min | typ | typ |
| 0.59 | 0.72 | 0.66 | 0.79 | 55 | 0.52 | 0.62 | 26.21 | 0.28 | 0.34 | 10.34 |

**Table 3-2: mechanical properties of the Nomex® honeycomb core from Euro-Composite.**

| Compression [MPa] | | | Shear [MPa] | | | | | | | |
|---|---|---|---|---|---|---|---|---|---|---|
| Bare | | | Ribbon direction | | | | Perpendicular to ribbon | | | |
| Strength | | Modulus | Strength | | Modulus | | Strength | | Modulus | |
| min | typ | | min | typ | min | typ | min | typ | min | typ |
| 0.54 | 0.8 | 50 | 0.52 | 0.62 | 22 | 27 | 0.28 | 0.38 | 12 | 16 |

### 3.1.2. Skin material

The skins of the sandwich were made of carbon fibre prepregs. Two different prepregs were used. Carbon fibres were chosen because they offer the best strength and stiffness-to-weight ratio. The use of prepregs ensures a high fiber-to-resin fraction and enables the quantity of resin in the skin to be controlled accurately, thereby achieving high quality and good reproducibility of the results. In the first part of the study concerning core-to-skin bonding analysis, a unidirectional (UD) prepreg with 200 g/m$^2$ T700 fibres from Toray, and 34%wt VTM 264 epoxy matrix from Advanced Composite Group (ACG) was used. This resin could be cured with temperatures ranging from 60 to 130°C. This prepreg was chosen because the matrix resin offers good compatibility with VTA 260 adhesive from the same producer.

In the second part of the study concerning the bending strength of sandwich structures, a thinner prepreg was chosen. It was made of 70 g/m$^2$ UD high strength carbon fibers and 35%wt EH84 epoxy matrix from Hexcel. This resin could be cured with temperatures ranging from 100 to 140°C. The mechanical properties given by the supplier are displayed in Table 3-3.

**Table 3-3: mechanical properties of the UD prepreg used for bending tests samples. The nominal fiber volume is 56%, the thickness after polymerization 0.07mm**

| **Loading direction** | **0° (parallel)** | **90° (perpendicular)** |
|---|---|---|
| **Tensile modulus** | 120 GPa | 8.5 GPa |
| **Compressive modulus** | 100 GPa | 8.5 GPa |
| **Tensile strength** | 1700 MPa | - |
| **Compressive strength** | 1500 MPa | - |
| **Compressive strain** | 1.5 % | |
| **Shear modulus** | 5.4 GPa | 5.4 GPa |
| **Poisson’s coefficient** | 0.33 | 0.33 |

### 3.1.3. Adhesive

The adhesive used for skin-to-core bonding was mainly the rubber-toughened epoxy resin VTA 260 from ACG. This adhesive can be cured at temperatures ranging from 65 to 120°C. The adhesive was available as film weighing 50, 150 or 300 g/m$^2$. Some trials where also made using EH 84 resin as an adhesive or a 150 g/m$^2$ Redux 382H adhesive film from Hexcel.

### 3.1.4. Solar cells

The cells used in this project were high efficiency monocrystalline silicon solar cells. The main solar cells tested were the S32 model from RWE Space Solar Power GmbH (now AzurSpace Power GmbH) which have 16.9% efficiency. Figure 3-1 shows one solar cell of this type. These cells are 130 +/-10 µm thick. The dimensions are 74 x 31.9 mm. The edges of the cell correspond to [100] and [010] directions in silicon crystal.

The active face of the cell has an inverted pyramid surface texturation as depicted in Figure 3-2 to increase light absorption, especially for light rays with low incidence angle. The second type of cells used for mechanical testing only was RWE 2PR/200-6540. The dimensions are 65 x 40 mm$^2$ with a thickness of 200 +/- 40 µm. This type of cell does not have any surface texturation. The efficiency is 13.6%. Both types of cells have a 3-11 µm thick silver layer on the back surface acting as a current collector.

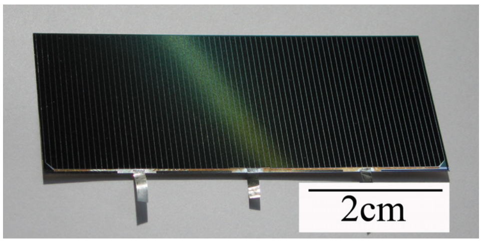

**Figure 3-1: RWE S32 monocrystalline silicon solar cell with three Ag electrical connectors**

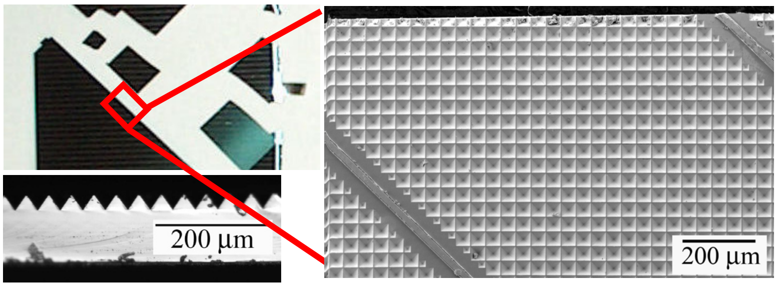

**Figure 3-2: Detailed view of the surface texturation of the solar cell from a broken part of the cell. The image on the right is a top view taken by scanning electronic microscopy (SEM). The square bases of the inverted pyramids are clearly visible. On the left, a cross-section of the same cell along the texture shows the saw teeth created by the texture.**

### 3.1.5. Silicone encapsulant

For the encapsulation of solar cells, a silicon adhesive was mainly used to glue encapsulation film onto the solar cell. The silicone Sylgard 184 from Dow Corning (DC) with service temperatures ranging from -45 to 200°C was used. It can be cured at room temperature or up to 150°C. The corresponding primer DC 1200 was applied by wiping on the cell and the encapsulation film.

### 3.1.6. Encapsulation film

A fluoropolymer (confidential grade) from Solvay-Solexis was used for the encapsulation of solar cells. Films with thicknesses between 30 and 70 µm were used. Some experimental trials were also made with 12 µm thick PET films coated with $SiO_2$.

## *3.2. Experimental methods*

### 3.2.1. Adhesive deposition on honeycomb

For the optimization of the sandwich structures developed here, the influence of the adhesive layer used for skin-to-honeycomb core bonding was particularly studied. As the commercial adhesive films offer only a few different areal weights (typically, 150 g/m$^2$, 300 g/m$^2$ and heavier), a method was developed allowing free choice of the amount of adhesive from around 0 g/m$^2$ to 100 g/m$^2$ (which is already heavy for the ultra light structures studied). Figure 3-3 illustrates the method used for controlling the amount of adhesive for skin-to-core bonding. A paper coated with a thin layer of heat-curable epoxy was placed onto the honeycomb and maintained under slight pressure by means of a steel block. The assembly was subsequently put in a temperature-controlled oven (between 45 and 70°C) for few minutes (0.5-15 minutes), long enough to allow a drop in resin viscosity, but short enough to avoid polymerization of the resin system. The paper was then removed immediately after taking the plate out of the oven, leaving an adhesive quantity on the honeycomb directly dependent on the time and temperature in the oven. This method was tested with 150 g/m$^2$ and 300 g/m$^2$ VTA 260 adhesive films from ACG, and also with 86 g/m$^2$ EH84 resin system from Hexcel.

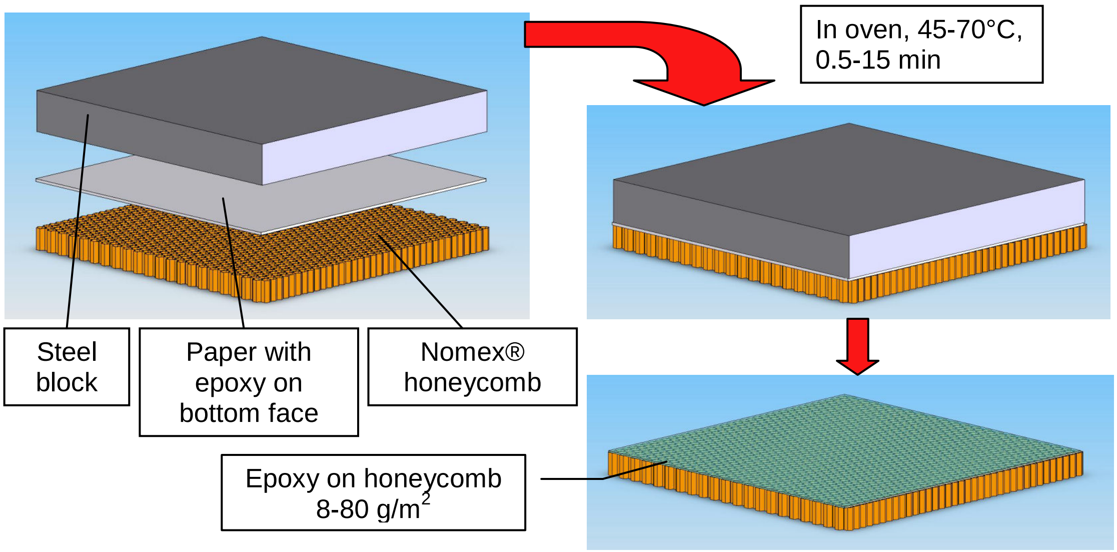
In oven, 45-70°C, 0.5-15 min
Steel block
Paper with epoxy on bottom face
Nomex® honeycomb
Epoxy on honeycomb 8-80 g/m$^2$

**Figure 3-3: Adhesive deposition method. The steel block was used to press the adhesive onto the honeycomb. After removing the paper, a thin controlled adhesive layer stayed on the honeycomb.**

By varying time and temperature in the oven, an adhesive weight ranging from 8 to 80 g/m$^2$ was obtained on honeycomb as depicted on Figure 3-4 and Figure 3-5. The type and viscosity of the adhesive, as well as the type of transfer paper on the film were crucial factors determining the quantity of adhesive transferring onto honeycomb. These results enabled an accurate choice to be made concerning the quantity of adhesive required for skin-to-core bonding; this is of great interest in studying resin meniscus shape as a function of adhesive weight. This method is not limited to the specific core and adhesives used in this study, but can be adapted to any other adhesive presenting viscosity drop with temperature. The temperature in the oven should be high enough to allow a viscosity drop, and the time should be short in comparison to the curing time to avoid crosslinking of the resin. As a guideline, the temperature used should be close to the curing temperature of the adhesive when it is cured for about 10 hours.

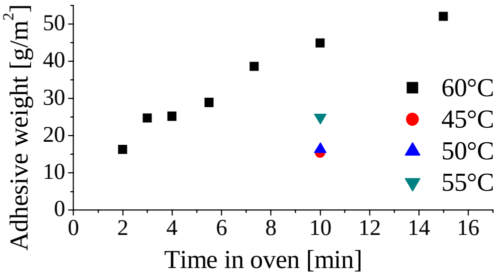

**Figure 3-4: Adhesive weight laid on honeycomb with 86 g/m$^2$ EH84 adhesive film**

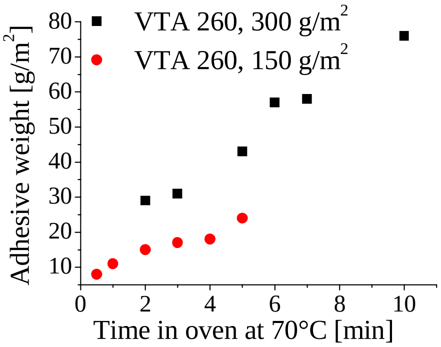

**Figure 3-5: Adhesive weight deposited on honeycomb with ACG VTA 260 adhesive films**

Another advantage of this method is that the adhesive is laid directly on top of the cell walls where the resin fillets form during bonding. No excess adhesive is used, (i.e. there was none on the skins in the centre of honeycomb cells), thereby allowing weight-saving without decreasing bonding capability. This method is therefore well suited and accurate to produce ultra-light sandwich panels, and could be adapted to automatically deposit adhesive on large panels (for example with adhesive passing on heated rolls pressing the film onto the honeycomb).

### 3.2.2. Optical microscopy

In order to understand the relation between the microstructure of the sandwich panels (particularly the adhesive menisci) and the mechanical properties measured on the panel, the microstructure was observed under optical microscope. Cross-sections of the sandwich panels were prepared in order to investigate the morphology of the adhesive menisci. Samples were cut from the sandwich panels, and the honeycomb was cut between the two skins, so that the honeycomb cells could be filled with embedding resin. Figure 3-6 shows a sandwich sample and the corresponding embedded cross-sections. The samples were fixed in acrylic resin Durofix-2 from Struers. The embedded samples were then polished with SiC paper with the following sequence: polishing to observation plan with grade 220, then 30 seconds with grades 500, 1000, 2400, and finally 4000. The depth of polishing was carefully controlled, so that the cross-section was in a zone perpendicular to the hexagonal cell wall as depicted in Figure 3-6. The cross-sections were then observed using an optical microscope Olympus BX-61 with motorized stage, allowing automatic surface scanning and reconstruction of large size pictures. The observation was done under bright field illumination with a magnification 50 to 500x.

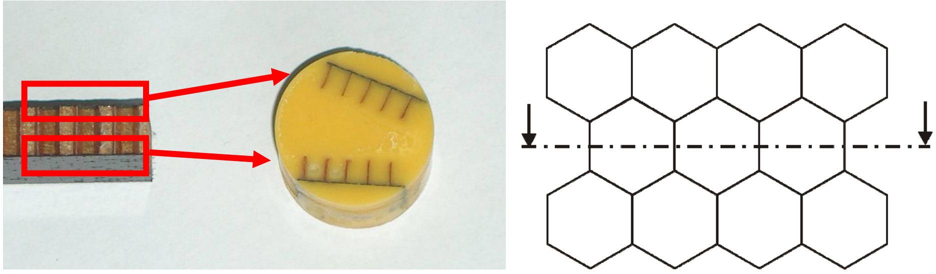

**Figure 3-6: (left) preparation and embedding of the sandwich cross-sections. The samples are polished up to selected observation plan (designated with the arrows on the right) for microscopic observation of menisci perpendicularly to honeycomb cell walls.**

### 3.2.3. Flatwise tensile test

This test was used to measure the core-to-skin bonding strength. It was carried out following ASTM standards [59]. 50 x 50 $mm^2$ sandwich samples were glued between two 50 x 50 x 50 $mm^3$ aluminium blocks and loaded in a self-aligning set-up in the tensile machine with a speed of 0.5 mm/min. The load and tensile machine crosshead displacements were recorded during the test.

### 3.2.4. Climbing drum peel test

This test was used to measure the core-to-skin debonding energy. It was achieved following ASTM standards [86]. The drum had an inner radius of 50 mm (rolling radius of the peeled skin) and an outer radius of 65mm (rolling radius of the loading tapes). The set-up designed and built for the present investigation was placed in the UTS tensile machine and loaded with a speed of 25 mm/min.

### 3.2.5. Four-point bending test on the sandwich beams

This test was used to assess strength and stiffness of the sandwich beams. ASTM standards [58] were used as guidelines. The set-up used was not self-aligning, i.e. the two loading points could not rotate relative to the two supporting points. Therefore, the parallelism of the loading points and supporting points was carefully verified, so that the load introduced was the same at each point. The set-up was fixed in the UTS tensile machine and the loading speed was 15 mm/min. The dimensions of the samples depended on the size of the panels produced. The span between supporting points was as long as possible (depending on sample size) to maximize the moment in the center of the beam, and reduce the risk of core shear failure or skin indentation under the loading points. Furthermore, small carbon plates of 18mm width and 1.5 mm thickness were placed under the 8 mm diameter loading pins to avoid local indentation.

### 3.2.6. Compression test of sandwich beams

This test was used to load sandwich beams under pure compression, parallel to the length of the beam. The main problem of this test was to introduce the loads in the sample without breaking the ends of the sample. Therefore, the samples were fixed in embedding acrylic resin. Figure 3-7 shows a compression sample with embedded ends being tested. A perfect alignment of the two ends had also to be ensured in order to have equal loading in the skins [31]. To this end, the embedding was effected directly on the plates of the UTS testing machine. They were then loaded at 1mm/min up to failure.

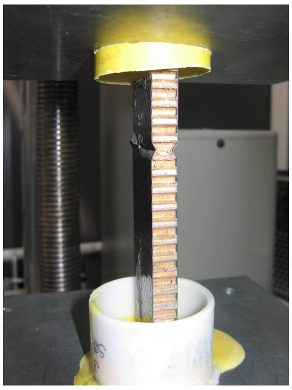

**Figure 3-7: Sandwich beam tested in compression with the two ends embedded in resin in order to introduce the load.**

### 3.2.7. Skin permeation measurements

During one-shot vacuum bag curing, as the honeycomb cells are closed on both sides by the skins, the absolute pressure in the cell can be significantly higher than under the vacuum bag. In order to ascertain the evolution of the pressure in the honeycomb cells when vacuum is applied under the vacuum bag, a set-up developed by Bonjour *et al*. [155] and Sequeira Tavares *et al*. [115] was used. It is represented schematically in Figure 3-8. Honeycomb was placed in a tight box. The top of the box was closed with the prepreg and the different consumables. A vacuum bag was then placed on the different layers and sealed around the prepreg. The vacuum was applied under the vacuum bag and the pressure was measured on both sides of the prepreg skin. The set-up could be put in the oven and the pressure monitored during resin curing. Changes in the pressure in the box under the prepreg corresponded to the pressure in the honeycomb cells during sandwich processing and were a function of the permeability of the prepregs and consumables. However, a main limitation of this system is that air can easily circulate from one honeycomb cell to another on the tool side. This is different from the one-shot curing of panels where the honeycomb is sealed on both sides by the skins. In fact, in the first case, a small leak through the skin will allow air to evacuate from all the cells, while in the second case, only the cell under the leak and few neighboring cells will be affected.

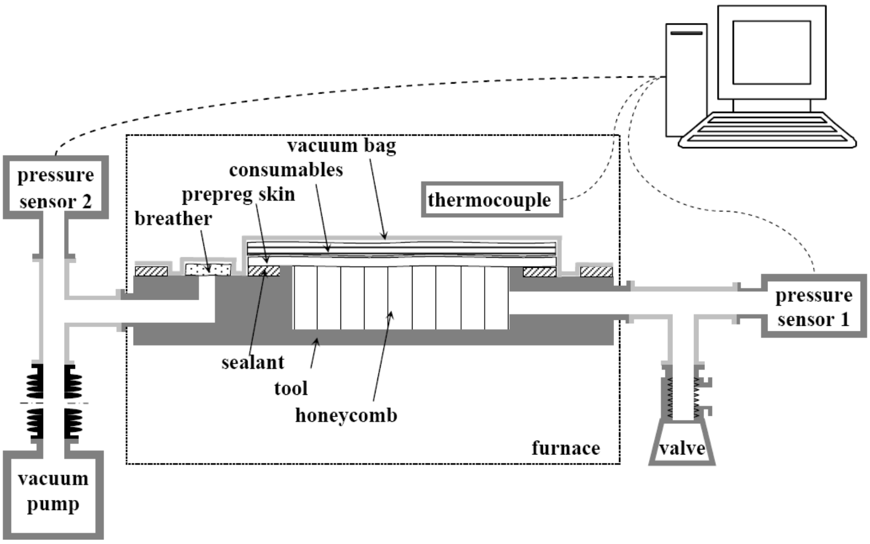
vacuum bag
consumables
prepreg skin
breather
thermocouple
pressure sensor 2
pressure sensor 1
sealant
tool
honeycomb
furnace
valve
vacuum pump

**Figure 3-8: Experimental set-up for through-thickness air permeability measurements during curing in processing conditions**

### 3.2.8. 3-point bending of solar cells

This test was used in order to determine solar cell strength. The initial span of 40 mm was reduced to 30 mm because the cells deformed too much without breaking. The support and loading pins were 8 mm in diameter and the loading speed was 15 mm/min.

### 3.2.9. Tensile test of solar cells

This test was used to determine the strength of the cells in tension. The major problem of this test was to introduce the force in the cell without breaking it too early. Therefore steel plates with a beveled edge were glued onto the cells. Figure 3-9 shows a broken cell with the steel plates glued onto it. The load was introduced in the plate with pins, allowing rotation and self aligning of the loaded cell, thus minimizing the edge effects on the solar cells. The loading rate was 0.2 mm/min. The cell was loaded until failure, and maximum load was recorded. As the strains were very small, they were not measured

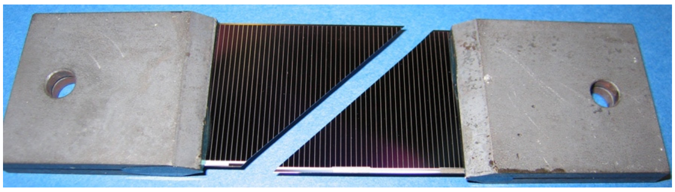

**Figure 3-9: Solar cell broken in a tensile test. Steel plates are glued on each side to introduce the loads. Failure along the [111] plane is evident**

## 3.3. *New video-based crack length measurement method in cantilever beam tests*

It was observed during peeling of the skin of sandwich samples that the core could be torn when core/skin bonding was sufficiently strong. Therefore, in order to characterize the core, the tearing energy of the core was measured. As such measurements have not been described in the literature, a modified version of the double cantilever beam test (DCB) described in the ASTM standards [60] was used to measure the tearing energy in mode I. Figure 3-10 shows a schema of this test. The measurements were carried out with Nomex® honeycomb from Hexcel and Euro-Composite. The specimens were made of 8mm thick, 20 mm wide and 200 mm long honeycomb samples, cut with the ribbon direction parallel to the length direction of the sample. The honeycomb was glued between 2 layers of 2 mm thick glass fibers / epoxy composite. The adhesive film used was a 150 g/m$^2$ ACG VTA 260 adhesive film. Two small aluminum blocks with a hole were glued onto the sample in order to introduce the load. A crack was initiated with a cutter in the middle of the honeycomb. The two arms were then pulled apart with a speed of 2 mm/min and the crack propagated in the honeycomb. The load and crosshead displacement were recorded during the test

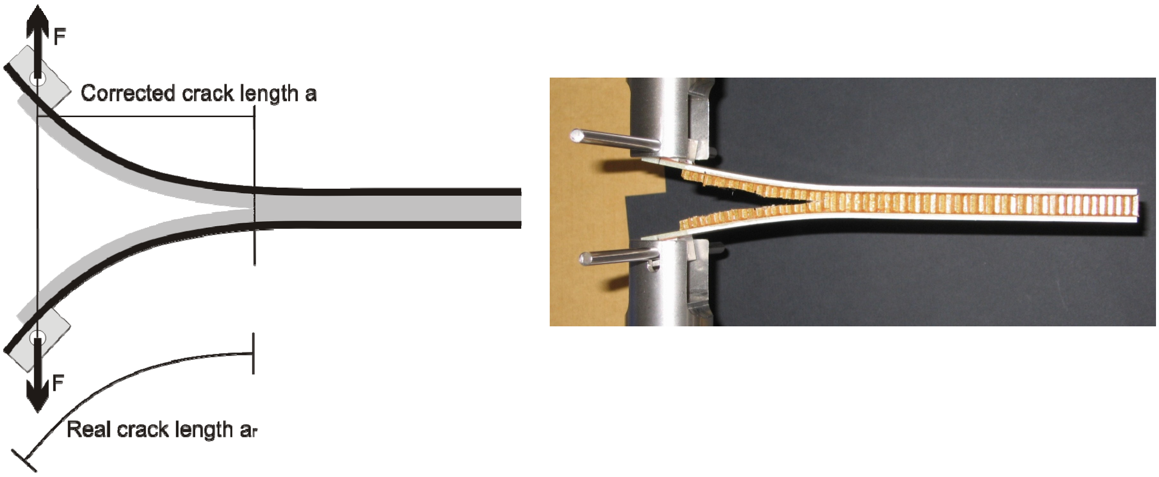

**Figure 3-10: Schema of the DCB test specimen. The corrected crack length represents the distance from loading line to crack tip.**

The critical point of this test was to measure crack length. In fact, as Nomex® honeycomb is tough, the honeycomb tore progressively and the crack tip could hardly be localized by visual observation. Therefore a new method based on video acquisition and analysis of the deformed sample was used to measure the crack and the results were confirmed with the more classic but time consuming compliance calibration (CC) method [65, 66, 99].

The video-based crack length measurement allows continuous recording of the crack length during the test. To this end, a video camera takes pictures of the sample being tested. A black background was used in order to provide a good contrast with the peel arms. Figure 3-11 shows a typical picture taken during the test. The images were treated in real time by a NI Labview program. This measures the vertical distance between the two peel arms. A mean distance in the uncracked region was calculated and according to classic beam theory, a third order polynomial was fitted to the vertical distance measured in the cracked zone. The intersection between the third order polynomial of the cracked zone, and the mean of the uncracked zone, indicates the location of the crack tip. By preliminary calibration of the pixel size in the program, and by defining the loading line, the corrected crack length was calculated by the program. This corrected crack length, represented in Figure 3-10, was smaller than the real length of the cracked zone. But it was shown by Williams [63] that by using the corrected length, no correction factors are necessary for large displacement, as it corresponds to the true distance for the calculation of the moment at crack tip. This video-based crack length measurement method was only used to measure the tearing energy of honeycomb in the present study, but it can be used for every cantilever beam tests, as soon as the deformation of the peel arm is sufficient to make an accurate fit.

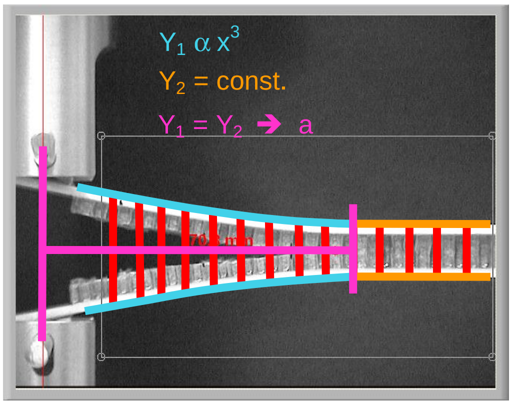

**Figure 3-11: image of the sample with the video camera. The program measures the vertical distance between the peel arms (red), makes a 3rd order polynomial fit in the cracked zone (cyan) and calculates a mean value in uncracked zone (orange). The intersection of the two fits shows the position of the crack tip.**

In the CC method, the relation between the compliance of the sample (ratio between loading point displacement and load) was measured with various controlled crack lengths prior to the test in order to identify the exact relation between compliance and crack length. To this end a crack of controlled length was cut in the honeycomb with a cutter. The tip of the crack was marked with a pen. The sample was loaded to the beginning of the crack propagation. The crosshead was stopped at that time and the corrected crack length between loading line and marked crack tip was measured. The slope of the load/deformation curve was measured and the compliance C was calculated for this crack length. This procedure was conducted for crack lengths between 40 and 120 mm. Five measurements were made on each of the six samples. The function correlating the compliance and crack length was then determined. It has to be remembered that determining the compliance with controlled crack length was useful only to verify the measurements made with the video-based crack length acquisition. In fact, as the force, displacement, and crack length were acquired continuously using the video-based method, the compliance could be calculated for each crack length.

Another solution to avoid measuring the compliance is to use an analytical model to predict compliance as a function of the properties of the materials constituting the sample. The basic idea is to consider that the two arms of the DCB sample are not perfectly clamped, but are laid on an elastic foundation. Figure 3-12 illustrates the loading case considered for elastic foundation model, which is similar to the Winkler model as described in [156], but specially adapted to the sandwich structure studied.

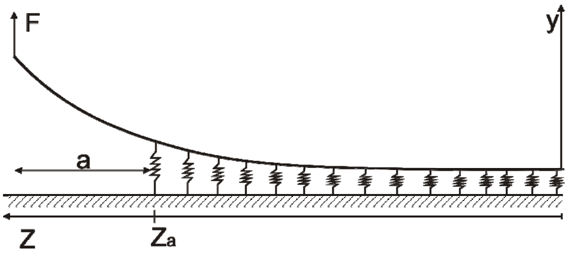

**Figure 3-12: basic scheme of a DCB arm on elastic foundation. At *z = 0*, the moment and the shear force is zero.**

The elastic foundation is considered as linear springs, so that the line load *q(z)* is

$$q(z) = -k \cdot y(z) \tag{3.1}$$

with

$$k = \frac{E_{czt} B}{t_c / 2} \tag{3.2}$$

where $E_{czt}$ is the tensile modulus of honeycomb, and $t_c$ the thickness of the core. For equilibrium for $0 < z < z_a$, we have

$$D_P \cdot y''(z) = \int_0^z -k \cdot (z-t) \cdot y(t)\, dt \tag{3.3}$$

where $D_P$ is the bending stiffness of the peel arm. The integral can be considered as a convolution product and Laplace Transform results in

$$Y(s) = \frac{s^3 \cdot y(0) + s^2 \cdot y'(0)}{s^4 + \kappa^4} \tag{3.4}$$

with

$$\kappa^4 = \frac{k}{D_P} \tag{3.5}$$

The inverse Laplace Transform then gives

$$y(z) = \frac{Cosh\left[\frac{\kappa z}{\sqrt{2}}\right]\left(2\kappa y(0) Cos\left[\frac{\kappa z}{\sqrt{2}}\right] + \sqrt{2} y'(0) Sin\left[\frac{\kappa z}{\sqrt{2}}\right]\right) + \sqrt{2} y'(0) Cos\left[\frac{\kappa z}{\sqrt{2}}\right] Sinh\left[\frac{\kappa z}{\sqrt{2}}\right]}{2\kappa} \tag{3.6}$$

The equilibrium conditions also give

$$\begin{gathered} \int_0^{z_a} K \cdot y(z) dz = F \\ \int_0^{z_a} K \cdot z \cdot y(z) dz = F(a + z_a) \end{gathered} \tag{3.7}$$

where $z_a$ is the length of the elastic foundation, i.e. the length of the uncracked part of the sample (see Figure 3-12). By solving the equations, the slope and displacement for $z = 0$ are

$$\begin{gathered} y(0) = \frac{2F\kappa\left(\sqrt{2} Cos\left[\frac{\kappa z_a}{\sqrt{2}}\right] Sinh\left[\frac{\kappa z_a}{\sqrt{2}}\right] - Sin\left[\frac{\kappa z_a}{\sqrt{2}}\right]\left(\sqrt{2} Cosh\left[\frac{\kappa z_a}{\sqrt{2}}\right] + 2a\kappa Sinh\left[\frac{\kappa z_a}{\sqrt{2}}\right]\right)\right)}{k\left(-2 + Cos\left[\sqrt{2} z_a \kappa\right] + Cosh\left[\sqrt{2} z_a \kappa\right]\right)} \\ y'(0) = \frac{2F\kappa^2\left(\sqrt{2} a\kappa Cosh\left[\frac{\kappa z_a}{\sqrt{2}}\right] Sin\left[\frac{\kappa z_a}{\sqrt{2}}\right] + Sinh\left[\frac{\kappa z_a}{\sqrt{2}}\right]\left(\sqrt{2} a\kappa Cos\left[\frac{\kappa z_a}{\sqrt{2}}\right] + 2 Sin\left[\frac{\kappa z_a}{\sqrt{2}}\right]\right)\right)}{k\left(-2 + Cos\left[\sqrt{2} z_a \kappa\right] + Cosh\left[\sqrt{2} z_a \kappa\right]\right)} \end{gathered} \tag{3.8}$$

With equations (3.8) and (3.6), the slope and displacement at $z = z_a$ can be calculated. Then for $z_a < z < z_a + a$, classic beam theory gives

$$y(z) = \frac{F}{2D_P}\left(a(z - z_a)^2 - \frac{1}{3}(z - z_a)^3\right) + y'(z_a)(z - z_a) + y(z_a) \tag{3.9}$$

and finally the compliance can be calculated as

$$C(a) = \frac{y(a + z_a)}{F} \tag{3.10}$$

For the numerical application, $D_P$ was measured using the 3-point bending test on a peel arm of a broken DCB sample. The Young's modulus $E_{czt}$ of the honeycomb was measured by pulling apart the honeycomb, as for the flatwise tensile test [59], and measuring the strain.

Honeycomb is a cellular material, but the tearing energy per unit surface was calculated as for a continuous material, i.e. by dividing the dissipated energy by the unit surface of the core, and not by the effective cell wall material surface. Various methods can be used to calculate the strain energy release rate at crack propagation $G_c$. With classic beam theory for a perfectly clamped beam with end load, the compliance is

$$C = \frac{\delta}{F} = Da^3 \tag{3.11}$$

where $\delta$ is the displacement of the loading point, $D$ a coefficient depending on beam geometry and material, $F$ the applied load and $a$ the distance between loading line and clamped end. In the DCB test the end cannot be considered to be perfectly clamped, due to honeycomb elasticity, so that a correction has to be established. The compliance calibration method (CC) and the modified beam theory (MBT) are the most often used corrections methods [60].

The compliance calibration method uses a correction factor considering that

$$C = \frac{\delta}{F} = Da^n \tag{3.12}$$

where $n$ is fitted to the experimental results. Therefore, a graph representing *log(C)* as a function of *log(a)* is constructed and the slope directly gives $n$. The tearing energy $G_c$ can then be directly calculated.

With Griffith theory [141], the strain energy release rate for an infinitesimal increase in crack length *da* under constant displacement is

$$G = -\frac{1}{B}\frac{dU}{da}\bigg|_{\delta = const.} \tag{3.13}$$

where $U$ is the total elastic strain energy in the test specimen and $B$ the sample width.

More generally, for crack length increase with variation of force and displacement of loading point, following Irwin theory [141],

$$G = -\frac{1}{B}\frac{dP}{da} \tag{3.14}$$

where $dP$ is the potential energy variation during infinitesimal crack growth, defined as

$$dP = dU - dW \tag{3.15}$$

where $W$ is the external work. It then follows that

$$\begin{aligned} dP &= \frac{1}{2}d\left(F\delta\right) - Fd\delta \\ &= \frac{1}{2}\left(\delta dF - Fd\delta\right) \\ &= -\frac{F^2}{2}d\frac{\delta}{F} \\ &= -\frac{F^2}{2}dC \end{aligned} \tag{3.16}$$

From (3.14) and (3.16), we have finally

$$G = \frac{F^2}{2B}\frac{dC}{da} \tag{3.17}$$

Using (3.12) and (3.17)

$$\begin{aligned} G &= \frac{F^2}{2B}nDa^{n-1} \\ &= \frac{F^2}{2B}nD\left(\frac{C}{D}\right)^{\frac{n-1}{n}} \end{aligned} \tag{3.18}$$

With equation (3.18), when the coefficient $D$ and $n$ are known, the strain energy release rate can be calculated without measuring $a$, but only with the load and displacement values, which is a great advantage when making tests. This method was, for example, successfully used by Berkowitz and Johnson [99]. Combining equations (3.12) and (3.17), the strain energy release rate can also be written as

$$G = \frac{nF\delta}{2aB} \tag{3.19}$$

which is a more classic form, but requires load, displacement, and crack length measurements.

In the MBT solution, correction is made by introducing a slightly longer crack length $a + \mathit{\Delta}$. From equation (3.11) and (3.17), the strain energy release rate is

$$G = \frac{3F\delta}{2Ba} \tag{3.20}$$

which becomes for MBT

$$G = \frac{3F\delta}{2B(a+\Delta)} \tag{3.21}$$

The calculation of the delta value can be made empirically, as described in the standards for the modified beam theory method [60], or by considering a beam on an elastic foundation similar to that described by Williams [64] for DCB testing on laminates. To calculate $\Delta$ empirically, $C^{1/3}$ is represented as a function of crack length, and the abscissa where $C^{1/3}$ is zero gives the value of $\Delta$ as shown in Figure 3-13.

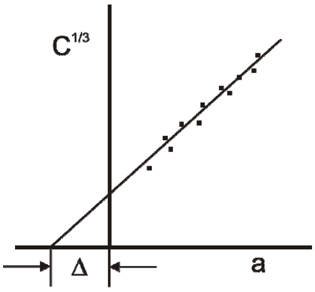

**Figure 3-13: calculation of the correction factor $\Delta$ for MBT method.**

Many different methods can be used to calculate the critical strain energy release rate by combining either the CC or the MBT method with either crack length measured by video-based method, with the compliance calibrated with crack of controlled length, or with the elastic foundation model. Four different solutions were considered.

Firstly, $G_c$ was calculated with equation (3.18) in which the coefficients $n$ and $D$ were measured by fitting the compliance determined with controlled crack lengths, and with the load $F$ recorded during test.

Secondly, equation (3.19) was used with the load $F$ and displacement $\delta$ recorded during the test and the crack length $a$ measured with the video-based method. The coefficient $n$ was determined by fitting linearly the measured compliance (recorded displacement / recorded load) as a function of recorded video-based crack length during test.

Thirdly, the MBT method was used coupled with the compliance calculated with elastic foundation model. The value of $\Delta$ was calculated so that the displacement of the ends of the peel arms was identical as calculated using classic beam theory with crack length $a + \Delta$, or with the elastic foundation model, i.e.

$$\frac{F\left(a+\Delta\right)^3}{3D_P} = y\left(a+z_a\right) \tag{3.22}$$

The strain energy release rate was then calculated with equation (3.21) with the load *F* and displacement $\delta$ recorded during the test and the crack length *a* measured with the video-based method.

Finally, the elastic foundation model was used to calculate *dC/da* for any crack length and equation (3.17) was used in which the load *F* was recorded during the test and the crack length *a* was measured with the video-based method.

For the measurement of *G*, the crack was propagated in 3 steps, from 50 mm to 70 mm, 70 mm to 90 mm and from 90 mm to 110 mm, to allow for adjustments to the camera zoom in order to obtain the most accurate crack length measurements. These successive loading cycles also allowed the energy used to propagate the crack to be calculated by integrating the area under the curve [65, 66, 83]. Figure 3-14 shows one loading unloading cycle and the corresponding dissipated energy. As all the deformations are elastic, all the energy dissipated during the loading cycle is due mainly to crack propagation, and eventually to some losses (for example friction of the loading pins in the holes of the aluminum blocks). The mean *G* value could then be calculated as

$$G = \frac{\Delta U}{\Delta a_r} \tag{3.23}$$

where $a_r$ is the real crack length as represented in Figure 3-10.

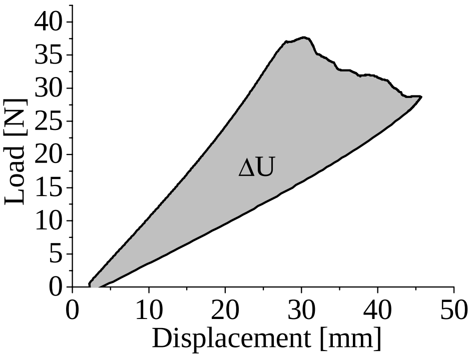

**Figure 3-14: Load displacement curve recorded during DCB crack propagation. The energy used for the crack propagation is *ΔU*.**

### 3.3.1. Results

This section presents mainly the results of the measurements on Nomex® honeycomb from Hexcel. The behavior of Euro-Composite honeycomb was similar and only the final results (i.e. tearing energy) are given for this type. Figure 3-15 shows the load displacement curves measured during successive loadings of a sample with cracks of various controlled length. The load-displacement curves confirmed the hypothesis of linear elastic behavior of the DCB sample until crack growth. When a sharp crack was created with a razor blade, the opening force did not decrease directly when the crack began to propagate. This was due to the toughness of the honeycomb. In reality, the process corresponded more to progressive tearing of the honeycomb than to real crack propagation. The force-displacement curve could then be separated into different regimes. Firstly, linear behavior, where no tearing took place, can be used to calculate compliance. Then the tearing zone formed between the non linearity point of the curve and maximum load. Finally, the tearing zone propagated and the force decreased. The tearing energy was calculated during this third regime.

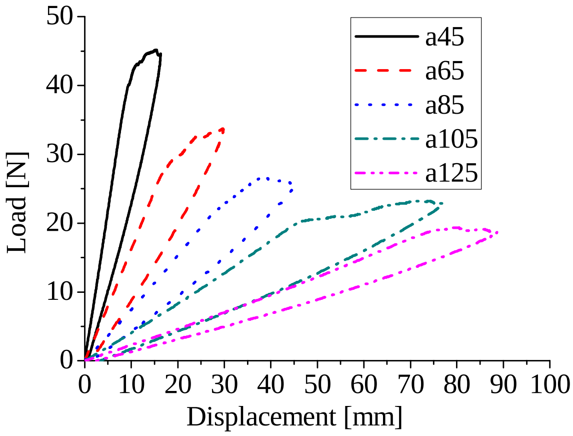

**Figure 3-15: measurement of compliance with different crack lengths from 45 to 125 mm. The DCB sample is loaded until the crack begins to propagate and then unloaded. The crack is then propagated artificially with a razor blade. The slope of the loading curve allows calculation of the compliance corresponding to the crack length.**

The compliance corresponding to cracks of controlled lengths was measured in the first linear zone of the curves and is depicted in Figure 3-16 with its fit following CC method. The compliance calculated by dividing the recorded displacement by the recorded load during crack propagation between 75 and 115 mm and represented as a function of crack length measured with the video-based method (“C video”) is also depicted. It corresponds very well to the measured compliance with controlled crack length. This confirms the high accuracy of the video-based crack length measurement method. The coefficients *D* and *n* used in the CC method were determined with the LN/LN plot represented in Figure 3-17. The curve fitting the compliance measured with controlled length has a slope n = 2.75, and D is 6.79 x $10^{-6}$. If the compliance is calculated by dividing the recorded displacement by the recorded load during crack propagation between 75 and 115 mm, and represented as a function of crack length measured with the video-based method, the slope of the fitting curve is n = 2.81 for the sample tested in this case. The mean value of the n calculated during crack propagation in all the different samples was 2.79 which is close to the n value with controlled crack length.

With the coefficients determined, *G* can be calculated only by measuring the force during crack propagation, using equation (3.18), or by measuring the load, displacement, and crack length and using equation (3.19).

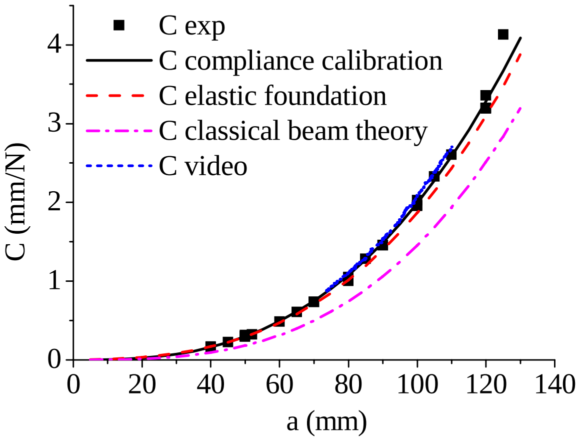

**Figure 3-16: Compliance of the DCB samples as a function of crack length. "C exp" corresponds to measurements of the compliance with controlled crack length, "C compliance calibration" to the corresponding fitting curve, "C elastic foundation" to the compliance predicted by elastic foundation model, "C classic beam theory" to the compliance predicted with third order polynomial deformation and "C video" to the ratio displacement/load measured during testing as a function of crack length measured by video-based method.**

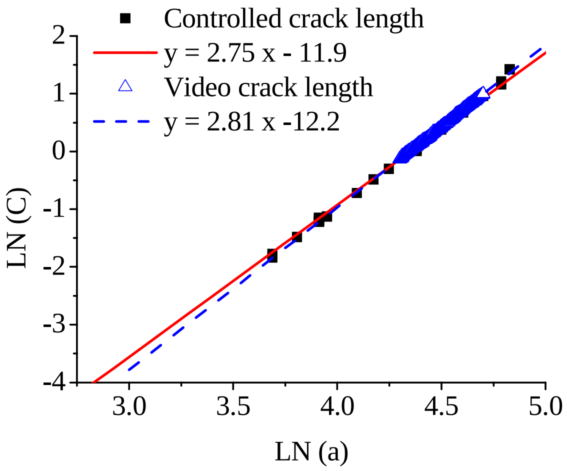

**Figure 3-17: Compliance of the DCB sample as a function of crack length measured either as a function of controlled crack length or crack length measured with video-based method.**

For the elastic foundation model, the following measured values were used:

Sample length $L$: 200 mm
Sample width: 20 mm
Peel arm bending stiffness $D_P$: 458582 Nmm$^2$
Tensile modulus of honeycomb $E_{czt}$: 64 MPa

The calculated shape of the peel arm on elastic foundation is represented in Figure 3-18. As $y(x)$ is negative on part of the foundation, it means that the honeycomb is under compression in this area. The Young's modulus of honeycomb in compression is 60 MPa according to the suppliers datasheet (Hexcel). This is very close to the measured tensile modulus, so the error made by considering the tensile modulus $E_{czt}$ = 64 MPa on the whole beam is very small. In fact, if the Young's modulus is considered to be 60 MPa, the compliance changes by less than 1%.

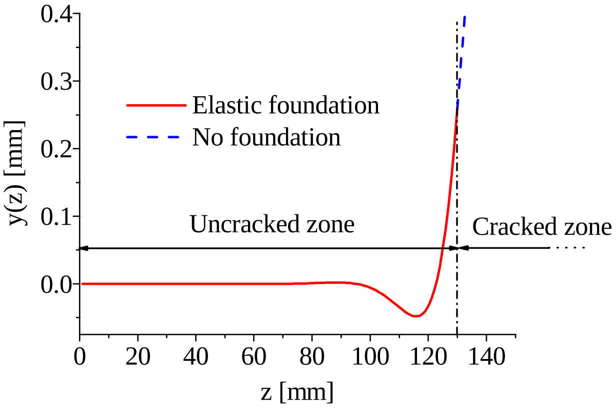

**Figure 3-18: shape of the deformed peel arm on elastic foundation of 130 mm length, i.e. with a crack length of 70 mm. The free end is at $z$ = 0, and the force is applied at $z$ = 200 mm. $y(z)$ is positive at the end of the elastic foundation, but is negative on part of the elastic foundation.**

The compliance predicted with the model is represented in Figure 3-16. It corresponds well to the compliance measured with controlled crack length, with a slight underestimation when crack length was large. As the calculation of $G$ was made with crack lengths smaller than 110 mm to avoid too much deformation of the peel arms, the model corresponds well in the targeted range. Compliance calculated according to classic beam theory, in which the peel arm was clamped at crack tip, is also represented. It underestimates significantly the real compliance, confirming the need to of take into account the deformations of the very light core.

The $\Delta$ value calculated with this compliance model in order to use the MBT method ($\Delta$ has to satisfy equation (3.22)) varied only slightly with crack length, between 8.74 mm for $a$ = 40 mm, and 8.70 mm for $a$ = 100 mm.

For the measurement of $G$, the crack was propagated in 3 steps, from 50 to 70 mm, from 70 to 90 mm, and finally from 90 to 110 mm. Figure 3-19 shows the load, displacement, and crack length measured during the second propagation. The crack was 70 mm length at the beginning of the test. As the crack was created by loading the DCB sample, the tearing zone was already created (in contrast to the crack created with a cutter). Therefore propagation of the tearing zone began almost directly after the linear regime, and maximum force was obtained at the end of the linear regime and corresponded well to the beginning of the measured crack growth.

Measurements of the crack length with the video system corresponded very well to the crack length calculated from the recorded load and displacement using the compliance calibration method. The video system allowed fast and accurate crack length acquisition without the time consuming compliance calibration procedure.

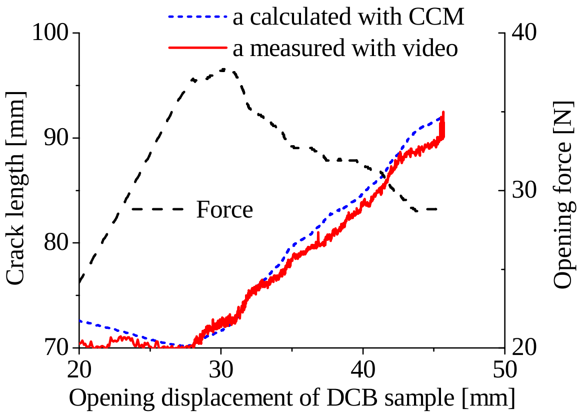

**Figure 3-19: crack length *a* measured with video system and calculated with CC method. Crack length before loading was 70 mm. In contrary to Figure 3-15, the crack before this test was created by loading the DCB sample and propagating the crack to 70 mm, but not with a razor blade.**

For each sample, the $G$ value was calculated during propagation of the tearing zone, i.e. from maximum load up to unloading. A mean value was calculated then for each measurement. In many papers (see for example [65-67, 70, 97, 99]), the so called R-curve representing the value of $G_C$ as a function of crack length is represented. In the present study, by considering all the samples, no clear tendency can be identified and the measured $G_C$ value can be considered as being constant for crack length between 50 and 110 mm. Table 3-4 summarizes the debonding energy calculated according to the different methods described in section 3.3 for Nomex® honeycomb from Hexcel and Euro-Composite respectively. The different calculation methods give very similar results with a maximum difference smaller than 3%. According to the standards [60], the MBT method provides the most conservative result. The direct use of the compliance calculated with the elastic foundation model gives an intermediate value between the MBT and CC methods. The use of the elastic foundation model coupled with the video system measurement thus enables the $G_C$ to be calculated quickly and accurately. Integration of the energy dissipated gives a slightly higher value, but the small difference may be due to other energy dissipation mechanisms, as for example, the friction of the loading pins in the holes. The tearing energy of honeycomb from Euro-Composite was significantly higher than for honeycomb from Hexcel. This is probably due to different Aramid fibers mats and impregnation resin used to make the Nomex® paper and settle the honeycomb in its final shape. However, for the design of sandwich structures, this property should not be determinant, as peeling loads are usually avoided. The shear and compressive stiffness and strength of the core have a much greater influence, for example in bending (see sections Chapter 5 and 6.3).

**Table 3-4: critical strain energy release rate $G_C$ for cracks propagating in honeycomb from Hexcel calculated with various methods.**

| **Honeycomb type** | ***Hexcel*** | ***Euro-Composite*** |
|---|---|---|
| **Calculation method** | **G [J/m$^2$]** | **G [J/m$^2$]** |
| CC method (equation (3.18)) with controlled crack length | 1009 +/- 71 | 1393 +/- 41 |
| CC method (equation (3.19)) with video-based crack length | 1005 +/- 74 | 1380 +/- 76 |
| Modified beam theory (equation (3.21)), Δ from elastic foundation model | 996 +/- 69 | 1370 +/- 83 |
| Definition formula (equation (3.17), C from elastic foundation model | 998 +/- 71 | 1374 +/- 73 |
| Crack propagation energy measurement (equation (3.23)) | 1025 +/- 66 | 1407 +/- 68 |

### 3.3.2. Summary

The tearing energy of the honeycomb core was measured to predict the maximum core/skin debonding energy attainable. A modified DCB test was used to this end and a new method was developed to measure the crack length, based on deformation analysis of the peeling arms. Coupled with the elastic foundation model developed in this work, the tearing energy was measured quickly and accurately and found to be equal to ~1000 J/m$^2$ and ~1380 J/m$^2$ respectively for honeycomb from Hexcel and Euro-Composite, as confirmed using the more classic but time consuming compliance calibration method.

## 3.4. Toughness measurement of epoxy

The properties of the adhesive are determinant for skin-to-core bonding. If the adhesive is too brittle, the meniscus breaks early and the debonding energy is small. The adhesive has to be tough to resist crack propagation in the core/skin interface. The toughness of the adhesive was measured in order to ascertain the limits of the adhesive for cohesive failure. Therefore, compact tension (CT) probes were fabricated and tested. In a second step, DCB samples with a thick layer of adhesive were produced to measure the toughness of the adhesive film.

The adhesive measured was the VTA 260 adhesive from ACG. A major difficulty in measuring the bulk properties of adhesive was to produce samples without air bubbles. As the adhesive was not available commercially in a liquid form, attempts were made to fabricate a plate with several layers of adhesive films. Many bubbles were entrapped in the plate and it was not usable for testing. Therefore, a 4-mm thick plate was produced directly by ACG based on a liquid resin. CT samples were cut from the plate to the shape described in Figure 3-20, and then tested according to the ASTM standard [157]. The specimens were machined and the crack was initiated with a razor blade. After failure, on the broken surface of the sample, the crack length and exact thickness of the sample were measured using an optical microscope. A CT sample without a notch was also produced to measure the compliance of the machine and loading points as described in the standard. The critical strain energy release rate was then calculated as

$$G_C = \frac{U}{BW_{CT}\phi} \tag{3.24}$$

where $U$ is the difference between the elastic energy stored in the CT probe at failure load, $U_Q$, and the elastic energy stored in the uncracked probe at same load level, $U_I$, as illustrated on the load/ displacement curves in Figure 3-20, $B$ is the probe thickness, and $W_{CT}$ the specimen width. The energy-calibration factor $\phi$ is defined in the ASTM standards as

$$\phi=\frac{\left(1.9118+19.118x-2.5122x^2-23.226x^3+20.54x^4\right)\left(1-x\right)}{\left(19.118-5.0244x-69.678x^2+82.16x^3\right)\left(1-x\right)+2\left(1.9118+19.118x-2.5122x^2-23.226x^3+20.54x^4\right)} \qquad (3.25)$$

where $x=\frac{a}{W_{CT}}$ with $a$ representing the crack length.

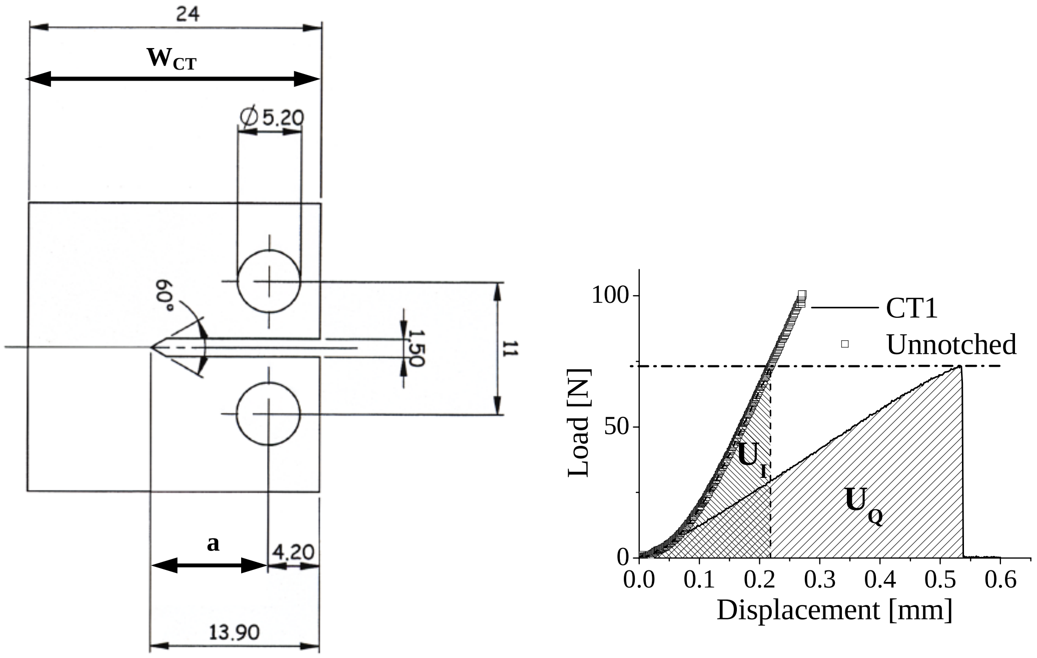

**Figure 3-20: (Left) CT probe dimensions. (Right) Load-displacement curves of Ct probe and unnotched probe. The stored elastic energy was measured for the CT probe at failure load and also for the unnotched probe at same load level.**

To confirm the results obtained with the CT probes (only 3 specimens due to the size of the plate manufactured by ACG), DCB tests were made on samples with a thick layer of adhesive, thus allowing the critical strain energy release rate to be calculated. Two GFRP plates were glued together with 4 layers of 300 g/m$^2$ adhesive film. On one edge of the plate, a Teflon film was put between the two center adhesive layers to initiate the crack. To remove as many air bubbles as possible, intermediate compactions with a vacuum bag were made after each adhesive layer was laid on the plate. To prevent the two plates touching each other and resin flowing away during curing under a vacuum bag, 0.8mm thick steel ribbons were put at the edges to ensure minimum spacing between GFRP plates and to control the adhesive thickness. The edges of the plate (GFRP / adhesive / GFRP) were closed with a semi-permeable membrane in order to suck out the air without the adhesive. The plate was then cured under vacuum bag at 80°C for 5 hours. It was cut into two centimeters wide beams. Aluminum blocks were glued at the pre-cracked end to introduce the load.

The crack was then opened at a rate of 0.2 mm/s and propagated. Crack length was measured by visual observation.

The critical strain energy release rate was calculated by the standard method as

$$G_C = \frac{3P_C\delta}{2Ba} \tag{3.26}$$

where $P_C$ is the peak load at crack propagation, $\delta$ the opening displacement of the DCB sample, $B$ the width of the sample and $a$ the crack length before each crack propagation.

The 3 CT probes broke at a similar load level as illustrated on the load / displacement curves reported in Figure 3-21. The critical strain energy release rate was calculated as $G_C$ = 878 +/- 73 J/m$^2$.

Figure 3-21 shows the typical load-deformation curves of the DCB test with the crack advancing step by step. The $G_C$ value was calculated for each peak load. However, crack propagation was not always cohesive and some parts of the samples contained many air bubbles. The measurements corresponding to these zones were thus not taken into account. The strain energy release rate obtained was $G_C$ = 898 +/- 120 J/m$^2$.

This value is similar to the one obtained with the CT probes and thus confirms the validity of the measurements. This value can then be used to evaluate the energy required to crack the bonding joint between the core and skin of sandwich structures.

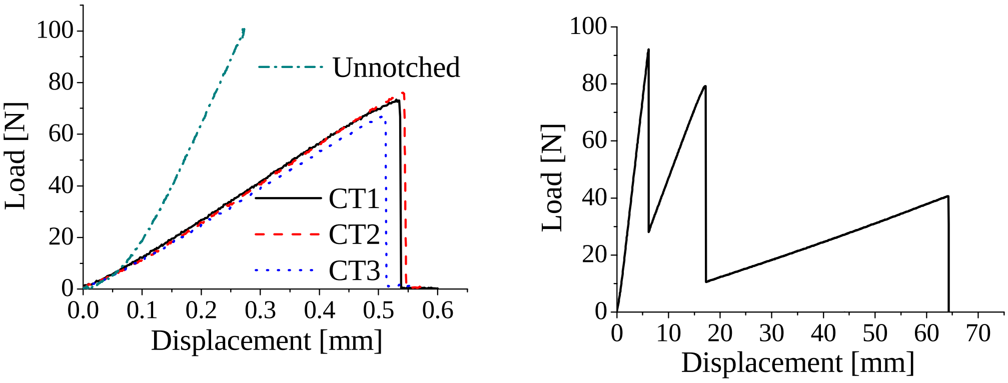

**Figure 3-21: load-displacement curve obtained with CT probes (left) and by propagating the crack in DCB samples (right).**

# CHAPTER 4. CORE TO SKIN BONDING OPTIMIZATION IN ULTRA-LIGHT SANDWICH STRUCTURES

When designing ultralight sandwich structures, the criteria and methods used for traditional sandwich structures are not sufficient to ensure an optimal strength to weight ratio. As shown in section 2.1.8, bonding of the skin to the core requires special attention because the reduction of adhesive for bonding can lead to a significant relative weight saving. Therefore this chapter concentrates mainly on optimizing of the bonding layer, i.e. reducing the weight of adhesive by keeping sufficient bonding. The first step of the study was devoted to understanding and predicting the formation of the adhesive menisci which was shown to control the bonding [70]. In the second step, the debonding energy of the skin measured with various meniscus sizes was studied in relation to the microscopic failure mechanisms. The correlation between the debonding energy and the properties of the different constituents was then established.

## *4.1. Prediction of the adhesive fillet size*

The considerable influence of the microscopic failure process on debonding energy has already been highlighted in section 2.1.8. To understand these mechanisms, it is vital to know precisely the size and the shape of the menisci. A model allowing accurate prediction of the fillet size as a function of the properties of the different sandwich constituents was developed as detailed in the following. The model was validated with sandwich panels fabricated using various adhesive quantities for core-to-skin bonding.

### 4.1.1. Sandwich processing

The skins were fabricated with 200 g/m$^2$ T700 UD carbon fibre prepregs, Nomex$^®$ honeycomb from Hexcel, and VTA 260 adhesive. The contact angle of adhesive was measured on both Nomex$^®$ honeycombs from Hexcel and from Euro-Composite.

As a first step, and in order to control exactly the amount of glue in the resin menisci forming between the skins and the honeycomb cell walls, the skins were cured separately under vacuum on an aluminium plate, so that the prepreg resin did not participate in the bonding process. The vacuum applied created a relative pressure of -0.9 bar under the vacuum bag. The skin was cured at 120°C for 70 min and the heating rate was 1°C/min. During this process, a peel ply was placed on the skin to create surface roughness in order to improve subsequent bonding with the core [158]. Figure 4-1 depicts a typical roughness obtained after peel-ply removal. It is essential to use a peel ply which does not transfer any silicone or fluorinated elements onto the prepreg surface, otherwise adhesion can be reduced dramatically (see section 4.2 and [159]). The peel-ply used in this study was a nylon fabric producing a medium texture (A100 PS from Aerovac).

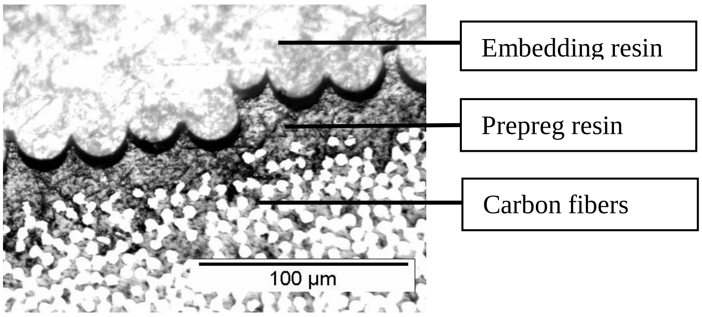

**Figure 4-1: Cross-section of the carbon-fibre skin after peel-ply removal. The surface texture enables improved subsequent bonding, with increased adhesive surface and mechanical anchoring of the resin.**

The adhesive for core-to-skin bonding was deposited on honeycomb using the method described in section 3.2.1. The honeycomb, with the controlled amount of glue, was finally placed on the cured carbon skin on an aluminium plate, and the panel was cured under vacuum at 120°C during 70 min with a heating ramp of 1°C/min. The same process was used for bonding the second skin.

The shape and size of the adhesive menisci between skin and cell wall were measured on micrographs of sandwich cross-sections.

### 4.1.2. Apparent contact angle measurements

The shape of the resin fillets is essentially a function of the contact angles of the adhesive on the skin and core material. This contact angle is defined in Figure 4-2 which shows a sessile drop in equilibrium on a surface. The contact angles were measured on the cured prepreg surface (after removal of the peel ply), and on the honeycomb cell walls. In the latter case, bands of Nomex® were peeled from the honeycomb panel and fixed onto a plate in order to have a flat surface.

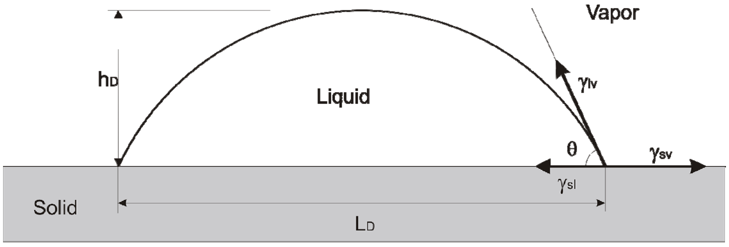

**Figure 4-2: sessile drop in equilibrium on a surface.**

The sessile drop technique [160-162] was used to measure the contact angle. Small pieces of adhesive film were cut and deposited on the carbon or Nomex® surface, and cured at 80 or 120°C in order to observe the effect of the processing temperature. Shrinkage of the resin during curing may slightly change the shape of the drop, and so the contact angles measured in the solid state are not the true contact angles of the resin, but apparent contact angles. Furthermore, the pronounced roughness of the surfaces, especially the prepreg surface after peel-ply removal, has a significant influence on the contact angle. In fact, the free energy of the surface is increased as a result of an increase of the effective surface, and thus changes the contact angle. The theory of Wenzel enables the real contact angle on a smooth surface to be calculated, based on the contact angle measured on the rough surface, and a roughness parameter [163-165]. This shows that the contact angle will be decreased on a rough surface when the liquid wets the surface, and will be increased when the angle is larger than 90°. The improved wetting of the prepreg surface treated with peel-ply has been highlighted by Bénard *et al.* [166] and it is particularly interesting to have good adhesion on the surface. The contact angle measured in the present study was the apparent contact angle on the rough surface. As the modeling of the meniscus formation only required the contact angles with the real rough surface, the corresponding contact angle on a smooth surface was not calculated.

A significant contact angle hysteresis was observed, and the advancing and receding angles were measured. This effect is usually attributed to surface roughness and heterogeneities[160] For the advancing angle, small balls of adhesive were laid on the surface and these then spread spontaneously over the surface during curing. For the receding angle, small pieces of 50 μm thick adhesive film were laid on the surface and these retracted, due to surface tension during curing, to form sessile drops.

The size of the drop usable for angle measurements is limited by gravity effects. The influence of gravity on the shape of the drop is characterized by the Bond number [160]

$$\mathrm{B}_o = \frac{g r^2 \Delta\rho}{\gamma} \tag{4.1}$$

where $g$ is the acceleration due to gravity, $\Delta\rho$ the difference of density between air and the liquid forming the drop, $r$ is the radius of a sphere with the same volume as the sessile drop, and $\gamma$ is the surface tension of the liquid. When the Bond number is zero, the drop is a truncated sphere. To estimate the Bond number in the present case, in which the surface tension of the adhesive is not known, values of surface tension of an epoxy resin system as measured according to the Wilhelmy slide method [160, 162] by Page *et al.* [167] were used. They ascertained a surface tension of about 35 mJ/m$^2$ for the uncured resin at room temperature. They showed that surface tension decreases slightly when temperature increases, and increases with the rate of conversion during curing.

Considering $g$ = 9.81 m/s$^2$, $\Delta\rho$ =1189 kg/m$^3$, and $r$ = 0.4 mm which corresponds to the drops considered in the measurements, the Bond number is 0.05. According to the work of Smith and Van de Ven [168], using this Bond number, associated with the small value of the contact angles measured, the error in angle measurement due to gravity (considering that the drop has a spherical shape) is less than 0.5°, which is smaller than the standard deviation of the measurements.

As the viscosity of the adhesive is a function of temperature, the drops were cured at 80 and 120°C, in order to determine the influence of temperature on the contact angle. Curing was carried out at atmospheric pressure as well as under vacuum.

After curing, the drops were cross-sectioned and polished to the center with SiC paper of grade 1000. The advance of the polishing was controlled with an optical microscope in order to stop polishing at the centre of the drop. The height, $h_D$, of the drop and the diameter, $L_D$, of the contact line circle were measured under microscope in order to calculate the contact angle $\theta$:

$$\tan\left(\frac{\theta}{2}\right)=\frac{2h_D}{L_D} \tag{4.2}$$

The contact angle measured will satisfy Young's equation

$$\gamma_{sv}=\gamma_{sl}+\gamma_{lv}\cos\left(\theta\right) \tag{4.3}$$

where the $\gamma$ values represent the surface tension of the interface solid/vapor, solid/liquid and liquid/vapor respectively, as represented in Figure 4-2.

### 4.1.3. Fillet shape modeling

Resin fillets are 3D structures with hexagonal symmetry. Their cross-section is, however, independent of position along most of the honeycomb cell wall, with only a small change noticeable in the corner of the hexagonal cell. Therefore, to predict the shape of the resin fillet, a 2D model was designed with two perpendicular planes and a resin fillet, as depicted in Figure 4-3. The two contact angles $\theta_1$ and $\theta_2$ were defined by the different surface tensions, and the area under the meniscus $A$ was fixed by the volume of adhesive, considered to be incompressible.

By using the Young-Laplace equation [160]

$$\Delta P=\gamma_{lv}\left(\frac{1}{r_1}+\frac{1}{r_2}\right) \tag{4.4}$$

where $r_1$ and $r_2$ are the two radii of curvature of the meniscus surface, $\Delta P$ is the pressure difference between the inside and outside of the meniscus, and, considering that for the 2D case $r_2$ is infinite, we have

$$\Delta P=\frac{\gamma_{lv}}{r} \tag{4.5}$$

If the effect of gravity is disregarded, $\Delta P$ is constant and thus $r$ is also constant [169]. The free surface of the meniscus is circular, with radius and center determined by the contact angles and the area of the meniscus.

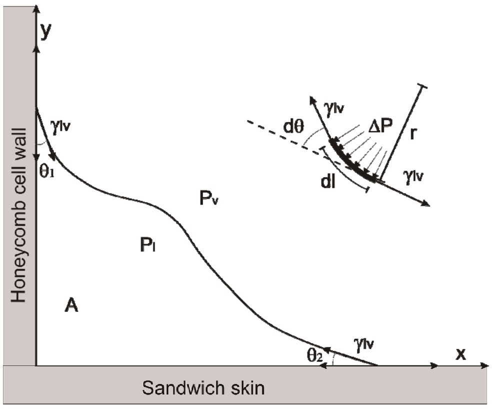

**Figure 4-3: Calculation of the shape of the meniscus. The contact angles are determined by the surface tension, and the area *A* is fixed by the fillet volume. The forces involved in achieving equilibrium are the surface tension and the pressure difference.**

This result was also obtained by considering equilibrium equations, as represented in Figure 4-3:

$$\gamma_{lv} d\theta \cong \Delta P dl \tag{4.6}$$

with

$$dl = \sqrt{dx^2 + dy^2} = dx\sqrt{1 + \left(\frac{dy}{dx}\right)^2} = dx\sqrt{1 + y'(x)^2} \tag{4.7}$$

As

$$\theta = \arctan\left(y'(x)\right) \tag{4.8}$$

we have

$$\frac{d\theta}{dx} = \frac{y''(x)}{1 + y'(x)^2} \tag{4.9}$$

and thus

$$\frac{d\theta}{dl} = \frac{y''(x)dx}{dx\left(1 + y'(x)^2\right)\sqrt{1 + y'(x)^2}} = \frac{y''(x)}{\left(1 + y'(x)^2\right)^{3/2}} \cong \frac{\Delta P}{\gamma_{lv}} \tag{4.10}$$

By introducing in (4.10) a circle equation of center ($X_c\,;\,Y_c$) and radius $r$

$$y(x) = Y_c - \sqrt{r^2 - x^2 + 2xX_c - X_c^{\,2}} \tag{4.11}$$

we obtain

$$\frac{\Delta P}{\gamma_{lv}} = \frac{1}{r} \tag{4.12}$$

which is exactly the Young-Laplace equation for the 2D case. It should be noted that by considering the segment in equilibrium in Figure 4-3, it can be shown that:

$$\frac{d\theta}{dl} = \frac{1}{r} \tag{4.13}$$

The center of the circle can be determined as:

$$\begin{aligned} X_c &= r\cos(\theta_1) \\ Y_c &= r\cos(\theta_2) \end{aligned} \tag{4.14}$$

The fillet should thus have a concave shape if the contact angles are smaller than 90°, i.e. if the adhesive wets the surfaces. In the schematic representation of the fillet in Figure 4-4, the radius of the circle is determined by the area of the resin fillet using following equations:

$$\begin{aligned} H_m &= r\cos(\theta_2) - r\sin(\theta_1) \\ W_m &= r\cos(\theta_1) - r\sin(\theta_2) \end{aligned} \tag{4.15}$$

and

$$A = \frac{W_m r\cos(\theta_2) + H_m r\cos(\theta_1) - r^2\left(\frac{\pi}{2} - \theta_1 - \theta_2\right)}{2} \tag{4.16}$$

However, the area of the meniscus depends of the quantity of adhesive available for its formation. This was well-controlled when the adhesive forming the meniscus was directly put onto the honeycomb, as described in Figure 3-3, and the skin was already cured, but in cases where adhesive film, or one-shot processing were used, the amount of resin from the adhesive film and from the prepreg forming the meniscus was unknown and depended on the processing conditions, i.e. mainly the temperature and the level of vacuum applied. The effect of pressure on meniscus formation in the case of one-shot curing is discussed in section 6.3.

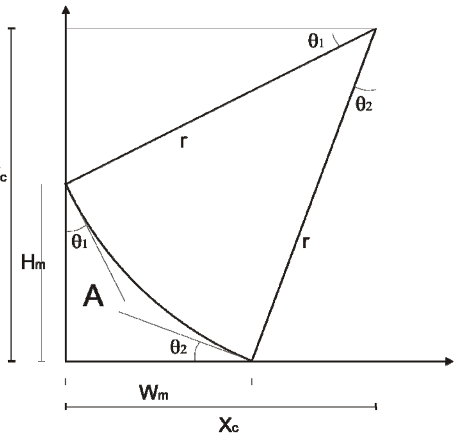

**Figure 4-4: Fillet with constant radius of curvature. The radius r is determined by the area of the fillet**

The relation between the height of the meniscus $H_m$ and the weight per unit area of adhesive could be easily calculated for a honeycomb with hexagonal cells, working on the hypothesis that the 2D model is valid for the entire honeycomb cell. Actually, in the cell corners between two adjacent cell walls, the meniscus presents a double curvature which changes the geometry. Nevertheless, in the case of small menisci ($W_m/s$ ~ 0.1), the deviation is only located in the cell corners and the 2D model is valid for the greater part of the cells. By assuming a triangular meniscus of height $H_m$ and width $W_m$, the volume of adhesive contained in one hexagonal cell is

$$V = 6\left(\frac{2cW_m H_m}{4} - \frac{H_m W_m^2 \tan(\pi/6)}{3}\right) \tag{4.17}$$

where *2c* is the outer diameter of the honeycomb cell. As the surface of one honeycomb cell is

$$S = \frac{3\sqrt{3}c^2}{2} \tag{4.18}$$

the relation between the size of the fillet and the adhesive areal weight is

$$M_A = \alpha\left(\frac{2H_m W_m}{\sqrt{3}c} - \frac{4H_m \tan(\pi/6)W_m^2}{3\sqrt{3}c^2}\right)\rho \tag{4.19}$$

where $\rho$ is the density of the adhesive, and $\alpha$ is the ratio between the area of the real meniscus and the triangular shape approximation. Figure 4-5 illustrates the meaning of the coefficient $\alpha$ on a meniscus cross-section, given by

$$\alpha = \frac{2A}{H_m W_m} = \frac{H_m r\cos(\theta_2) + W_m r\cos(\theta_1) - r^2\left(\frac{\pi}{2} - \theta_1 - \theta_2\right)}{H_m W_m} \tag{4.20}$$

Knowing the contact angles of the adhesive with the skin and honeycomb, the shape and size of the meniscus could then be predicted with equations (4.15) to (4.20).

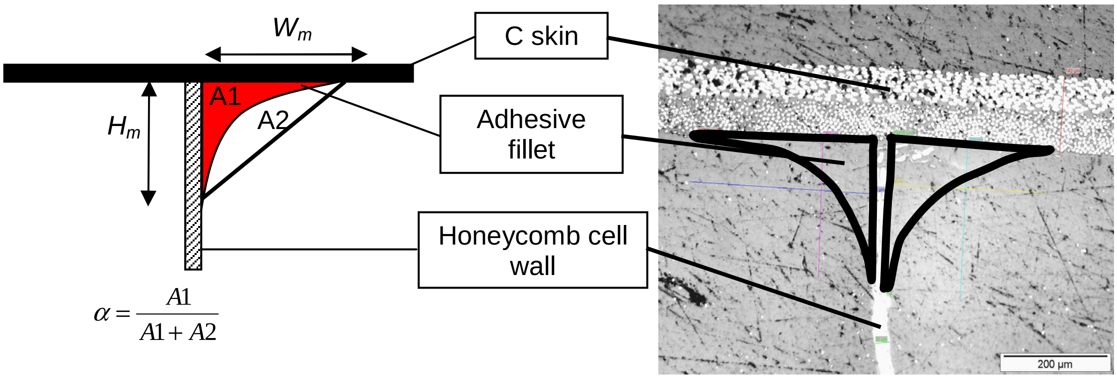

**Figure 4-5: Fillet shape, triangular approximation, and ratio α determining the real shape**

In the Young-Laplace equation (4.5), if the meniscus forms with a concave shape (as in Figure 4-4), $r$ is positive and thus $\Delta P$ is positive. This means that the pressure in the meniscus is lower than the ambient pressure. This explains why the resin flowed into the meniscus. If the meniscus is convex, $\Delta P$ is negative and the meniscus cannot form. Furthermore, $\Delta P$ decreases when r increases. As the system will automatically tend to equilibrium, the radius tends to be as big as possible, as a function of the adhesive available, and as long as gravity can be disregarded. So when equilibrium is reached, the quantity of adhesive in the meniscus is only determined by the amount of adhesive in contact with the meniscus, and the geometry by the contact angles. If highly viscous adhesive is used, polymerization may occur before the adhesive has completely flowed into the meniscus. In this case, the size of the meniscus will also be controlled by the temperature-dependant chemo-rheological properties of the adhesive. These complex transient phenomena were disregarded in the present study, since the highest recommended curing temperature of the adhesive (120°C) given by the supplier was chosen in order to have the lowest resin viscosity.

### 4.1.4. Results and discussion

#### Fillet size prediction and measurements

The apparent contact angle of the adhesive deposited on the prepreg and Nomex® was calculated from the width and height of the sessile drops. Due to the roughness of the honeycomb surface and of the carbon prepreg after peel-ply removal, the adhesive drops did not systematically adopt a regular sessile drop shape. When vacuum was applied, bubbles occasionally formed in the drop and then changed its form. In calculating the contact angle, only the drops with a regular shape were considered such as those represented in Figure 4-6 and Figure 4-7. The contact angles measured are summarized in Table 4-1. The advancing angles were smaller when the adhesive was cured at 120°C rather than at 80°C. This was due to the lower viscosity of the adhesive at 120°C, thereby enabling the resin to spread more easily than it did at 80°C. The effect of resin viscosity was confirmed by the fact that the difference between advancing and receding angles was more pronounced at 80°C than at 120°C.

The receding angles changed only slightly under the different curing conditions. Actually, the pieces of adhesive film laid on the surface did not really retract to form sessile drops, and this caused errors in the measurements. The receding angles were too small to be measured accurately with this method. The advancing contact angles measured when the adhesive was cured under vacuum were slightly lower than those under atmospheric pressure, but the difference was in the order of the standard deviation and was thus not significant.

**Table 4-1: Contact angles measured with adhesive VTA 260 on carbon prepreg and Nomex® honeycomb, with adhesive cured at 80° or 120° either under vacuum or at ambient pressure.**

| | **Carbon prepreg:** | | **Hexcel Nomex®:** | | **Euro-Comp. Nomex®:** | |
|---|---|---|---|---|---|---|
| | **mean angle [°]** | **S.D.** | **mean angle [°]** | **S.D.** | **mean angle [°]** | **S.D.** |
| **80°C advancing angle** | 24.0 | 3.5 | 23.1 | 4.9 | 25.4 | 4.5 |
| **80°C receding angle** | 8.9 | 2.2 | 6.3 | 2.0 | 5.7 | 1.2 |
| **120°C advancing angle** | 15.3 | 2.3 | 16.6 | 1.0 | 17.5 | 0.8 |
| **120°C receding angle** | 8.5 | 2.6 | 9.4 | 0.5 | 9.8 | 0.7 |
| **120°C advancing angle with vacuum** | 12.5 | 1.9 | 13.9 | 3.3 | 14.9 | 3 |
| **120°C receding angle with vacuum** | 7.7 | 2.7 | 11.1 | 5.7 | 12.7 | 6.3 |

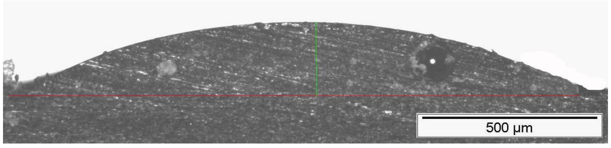

**Figure 4-6: Adhesive sessile drop on carbon prepreg. The adhesive was cured at 80°.**

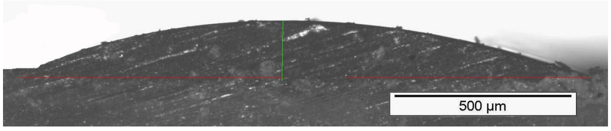

**Figure 4-7: Adhesive sessile drop on Nomex® honeycomb. The adhesive was cured at 80°.**

The shape factor of the meniscus was then calculated with equation (4.20), and the weight per unit area of adhesive as a function of the contact angles and height of meniscus could be determined with equation (4.19).

### Meniscus size with adhesive deposition method

When the adhesive deposition method was used, the adhesive stayed at the top of the honeycomb cell wall. Figure 4-8 shows adhesive on the top of the cell wall after the deposition process. During skin bonding, the adhesive had to spread onto the carbon surface as well as onto the honeycomb surface. Therefore, the advancing angles for both surfaces were taken into account in predicting fillet size.

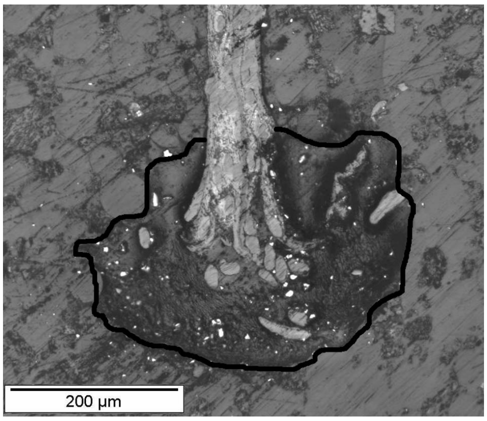

**Figure 4-8: Adhesive on the top of a honeycomb cell wall after adhesive deposition of 22 g/m$^2$. The adhesive surface has been highlighted with a black line for clarity**

The changing size and shape of the meniscus is illustrated in the micrographs of sandwich cross-sections in Figure 4-9 and confirms its predicted circular shape, especially in the case of a large meniscus. However, the adhesive menisci sometimes have an irregular shape due to the rough surface of the Nomex® and prepreg. In fact, small Aramid fibres pointing out of the honeycomb cell wall surface can completely change the meniscus shape, and thus the height of the meniscus differs from that with a circular shape. Figure 4-10 shows an example of such an irregular meniscus. These irregularities explain the large standard deviation of the measurements.

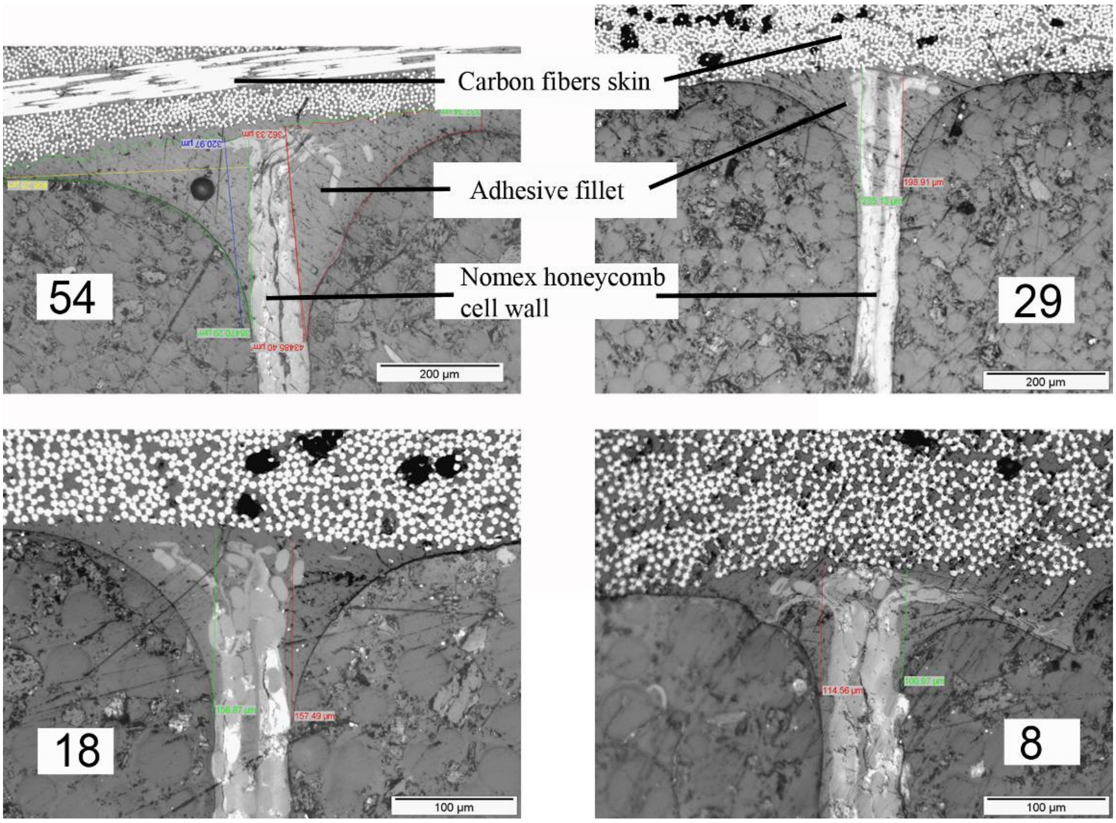

**Figure 4-9: Resin fillet with 54, 29, 18 and 8 g/m$^2$ adhesive. The size increases with adhesive weight. The end of the honeycomb cell walls is crushed (by pressure and the sawing process), and this distorts the shape of the meniscus, especially at low adhesive weights. Note that the scale is different on the two lower micrographs.**

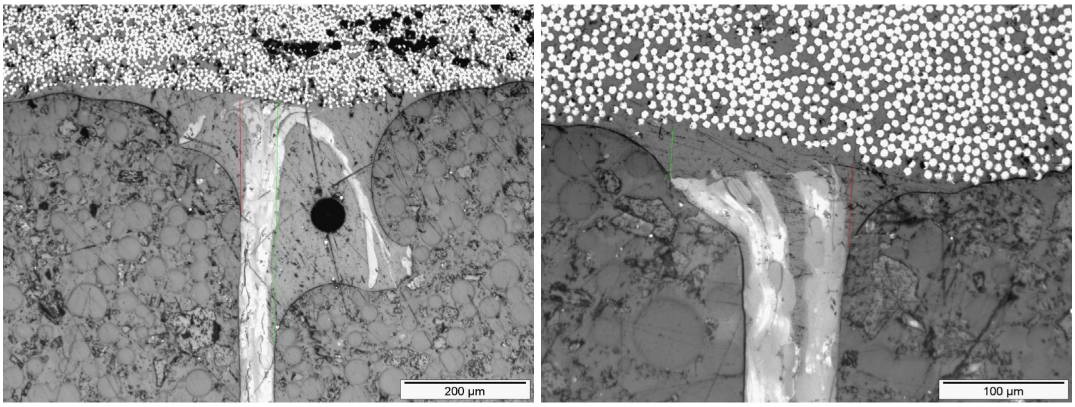

**Figure 4-10: (Left) Adhesive meniscus forming between the honeycomb cell wall and carbon fiber skin, with 25 g/m$^2$ adhesive. Aramid fibers from the Nomex® honeycomb cell wall completely change the shape of the meniscus. (Right) Adhesive meniscus with 12 g/m$^2$ adhesive. Some of the adhesive is in the resin meniscus, but some remains between the cell wall and the prepreg.**

The predicted fillet size as a function of adhesive weight is represented in Figure 4-11 with the height $H_m$ of resin fillet measured on sandwich samples produced with various adhesive quantities. When comparing the predictions to the actual measurements, it is noticeable that the average size of the meniscus is overestimated by the model. In fact the model considers that all the resin is used to form a meniscus between two perfectly smooth surfaces. Actually, as the prepreg and the Nomex® are rough, some resin remains between the prepreg and the honeycomb cell wall, instead of forming the meniscus, as illustrated in the meniscus cross-section in Figure 4-10. This is accounted for with the following modification of equation (4.19):

$$M_A = \alpha\left(\frac{2H_m W_m}{\sqrt{3}c} - \frac{4H_m \tan(\pi/6) W_m^2}{3\sqrt{3}c^2}\right)\rho + M_{A0} \tag{4.21}$$

where $M_{A0}$ is the weight per unit area of adhesive not involved in forming the meniscus. The value $M_{A0}$ minimizing the difference between the measured height and the predicted height with the least squares method is 4.85 g/m$^2$. Allowing for this correction, the model describes very well the average size of the meniscus. This model can thus be used for any combination of core, skin and adhesive materials, providing that the contact angles of the adhesive on the core and skin materials are known at the curing temperature. The value of $M_{A0}$ has to be adapted according to the roughness of the cured skin.

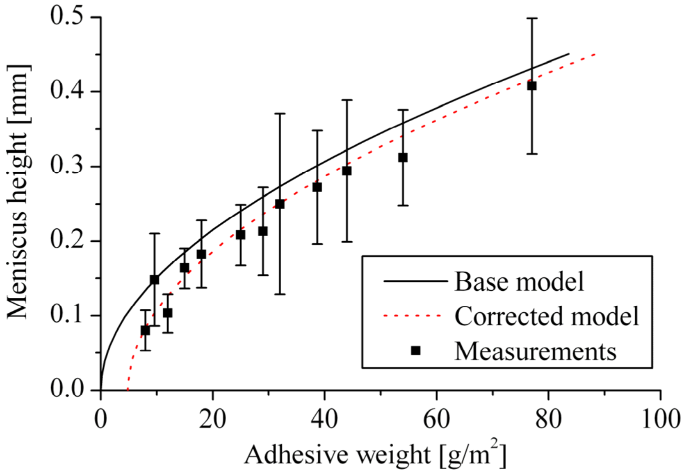

**Figure 4-11: Meniscus height predicted as a function of adhesive weight and contact angles. The contact angles were 13° on carbon and 14° on Nomex®. The corresponding shape factor was $\alpha$ = 0.60. For the corrected model, the adhesive weight $M_{A0}$ was 4.85 g/m$^2$.**

Furthermore, with the known meniscus size, the assumption that gravity could be disregarded in calculating meniscus shape could be verified. By considering a fillet radius of 0.5 mm, and with the epoxy surface tension according to Page *et al.* [167], the Young-Laplace equation (4.12) gives $\Delta P$ = 70 Pa. In comparison, the pressure exerted by gravity with a 0.5 mm epoxy column is

$$\rho g h = 1190 \times 9.81 \times 0.5 = 5.8 \text{ Pa} \qquad (4.22)$$

which is small in comparison, and further confirms the hypothesis of disregarding gravity effects.

### Meniscus size with commercial adhesive films

When continuous commercial adhesive films were used for skin-to-core bonding, it was assumed that the contact angle with the prepreg was 0°, as the film completely covered the surface. On the honeycomb, the advancing angle should be considered as for the preceding case. However in the present case a large amount of adhesive remained on the surface of the prepreg in the honeycomb cell instead of forming the meniscus. This was mainly due to the high roughness of the carbon prepreg surface after removing the peel ply. The mean thickness of the adhesive left on the surface was measured on micrographs. As the surface was very rough, a mean thickness was calculated on each micrograph as shown in Figure 4-12. The mean thickness measured was 21 μm, which corresponds to 25 g/m$^2$ adhesive. The amount of resin which was not in the meniscus was then set to 25 g/m$^2$ in the model. Figure 4-13 shows the predicted meniscus height which corresponds well to the size of the meniscus measured with 3 different adhesive films, thus confirming the validity of the model.

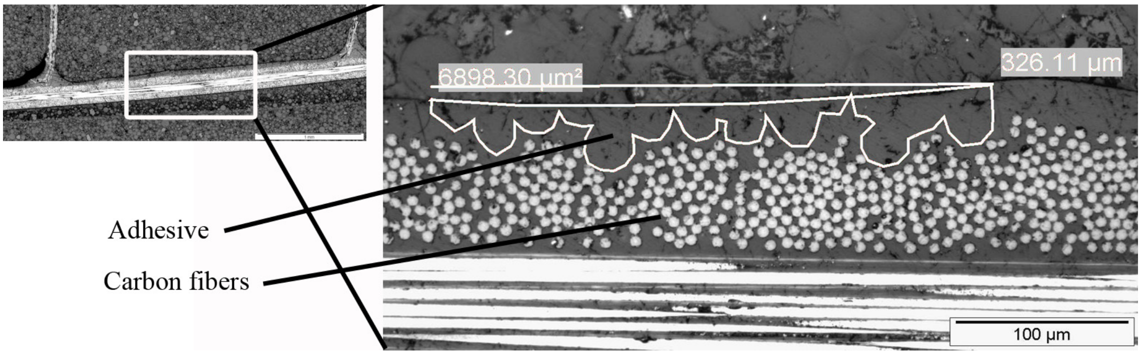

**Figure 4-12: Measurement of the mean thickness of adhesive left on the surface of the prepreg by the adhesive film. The area delimited by the white contour is adhesive on top of the rough prepreg surface. The mean thickness, calculated by dividing the area by the length of the zone considered, was 21 μm in the present case, which represents 25 g/m$^2$ adhesive.**

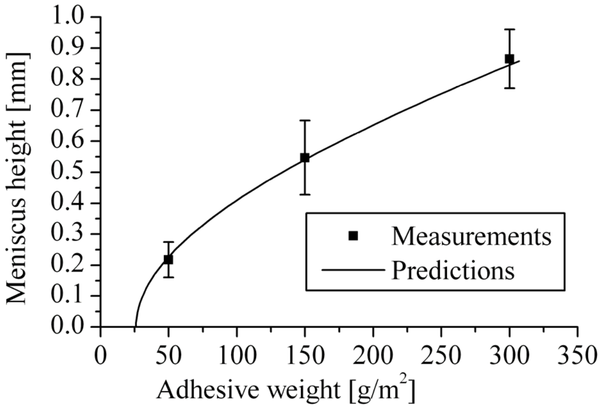

**Figure 4-13: Meniscus height predicted as a function of adhesive weight and contact angle. The contact angles were 0° on carbon and 14° on Nomex®. The corresponding shape factor was $\alpha$ = 0.52. The adhesive weight $M_{A0}$, which is not in the meniscus, was considered as 25 g/m$^2$.**

It was also interesting to observe that in the case of a 50 g/m$^2$ adhesive film on already cured prepreg, half of the resin was not used to bond the core to the skin and merely constituted supplementary weight. This shows the advantage of the adhesive deposition method when small quantities of adhesive are used. An alternative is to use one-shot curing of the skin panel, so that part of the prepreg resin can be used to form the meniscus. However this method has the clear disadvantage of producing skin of reduced quality, especially when thin skins are used (see section 6.3). The adhesive deposition method associated with the meniscus size prediction model is thus an efficient tool for producing high quality ultra-light sandwich panels.

### 4.1.5. Summary

In this section the formation and size of the adhesive fillet between honeycomb cell walls and the skins of sandwich structures was studied. The adhesive deposition method described in chapter 0 was useful to study the size and shape of the menisci with controlled adhesive quantities as low as 8 g/m$^2$ and up to 80 g/m$^2$.

To predict the shape of the adhesive meniscus, the contact angles between the adhesive and the Nomex® and carbon skin were measured. A pronounced contact angle hysteresis was highlighted, due to rough surfaces.

A model was developed to predict the shape and size of the menisci on the basis of the contact angles. It was shown that the meniscus surface adopts a circular shape at equilibrium when the menisci are small enough to be unaffected by gravity. This was confirmed on the micrographs of sandwich panel cross-sections.

The model predicting the height of the meniscus showed very good agreement with the measurements on sandwich cross-sections, providing that the residual layer of adhesive on the skin surface was taken into account. Prediction of adhesive fillet size and geometry is now used to predict the microscopic failure mechanisms, and thus the bonding quality, between honeycomb core and skin.

## *4.2. Core-to-skin debonding energy and mechanisms*

The value of debonding energy as well as debonding mechanisms are of vital importance in achieving an optimal design of the bonding joint. Therefore, the debonding energy was measured with various quantities of adhesive and the corresponding failure mode was identified.

The final goal of this section is to establish a relation between the properties of the honeycomb, the adhesive, the adhesive fillet formation mechanisms, and the measured debonding energy.

### 4.2.1. Flatwise tensile test

The flatwise tensile test was used to measure the bonding strength [59]. This test is convenient when comparing the bonding strength in different sandwich structures, but can lead to core failure when light cores are used, thus giving no information on the bonding strength [16].

The skins were made of 70 g/m$^2$ carbon prepreg with an EH84 matrix, and bonded to the core with EH84 epoxy resin. The core was a Nomex® honeycomb from Hexcel. The sandwich panels were manufactured in two steps. For each panel, the skin was first cured under vacuum on an Al plate. Figure 4-14 shows schematically the stacking of the different layers. During curing, a peel ply (Airtech Release ply B) was placed on the skin to create surface roughness to improve subsequent bonding with the core.

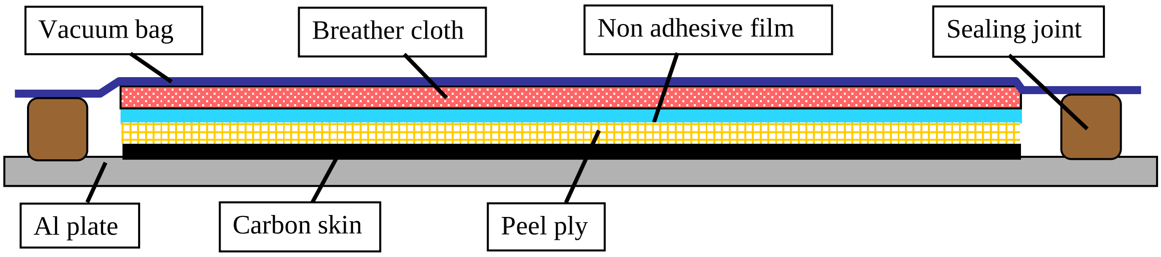

**Figure 4-14: curing process of the skin. The skin was cured at 120 °C. The temperature was increased by 1°C/min. The relative vacuum pressure was -0.9 bar.**

A selected amount of adhesive was laid on the honeycomb using the adhesive deposition method (see section 3.2.1) and the first skin was then glued onto the honeycomb core under vacuum with the stacking represented in Figure 4-15. As the processing parameters can have high influence on the debonding energy [100], the curing parameters were carefully kept unchanged for the different samples with same materials in order to measure only the variability due to different adhesive quantities. The second skin of each sample was glued using the same process.

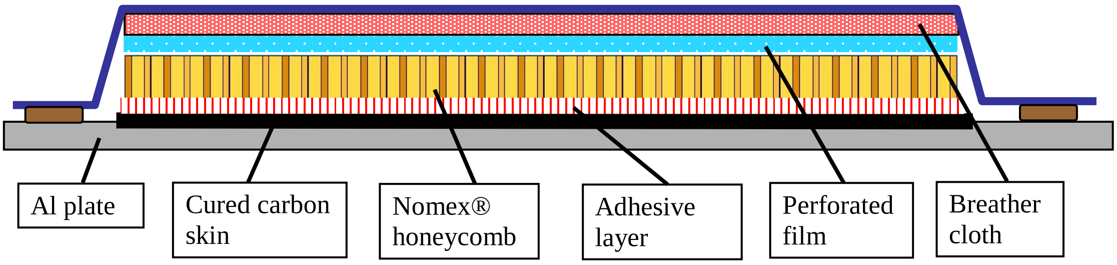

**Figure 4-15: core-to-skin bonding process. The adhesive was cured at 120 °C. The temperature was increased by 1 °C/min. The relative vacuum pressure was -0.9 bar.**

50 x 50 $mm^2$ square samples were cut from the sandwich panels and glued onto Al blocks. The two blocks were then pulled apart on the UTS testing machine until the sandwich sample broke. All the samples tested broke due to honeycomb core tearing, at a mean tensile stress of 1.45 MPa, even with only 15 $g/m^2$ adhesive. Figure 4-16 depicts the core tearing during testing, and the failure stresses as a function of adhesive weight. When the amount of adhesive was greater than 15 $g/m^2$, the variation of the quantity had no effect on the failure load. For these materials, this test was therefore not adequate to measure debonding strength, and another test measuring crack propagation energy had to be used to characterize skin-to-core bonding.

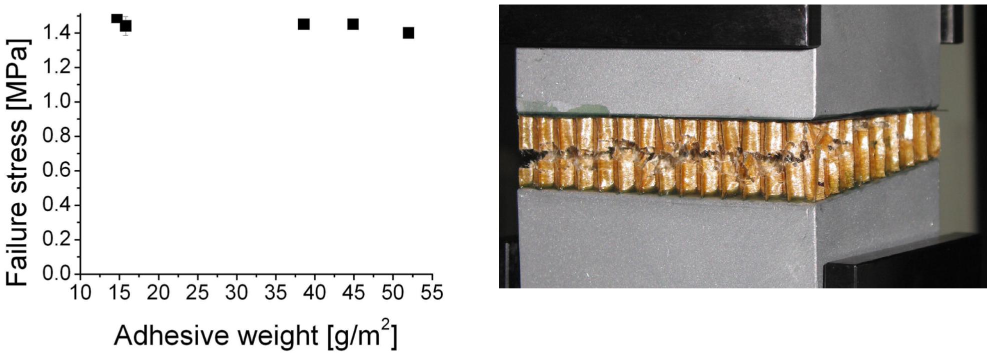

**Figure 4-16: flatwise tensile test results. The honeycomb core tore before skin / core debonding occurred.**

### 4.2.2. Climbing drum peel test

As the skins of the sandwich structure were very thin, the most suitable testing method for measuring debonding energy was the climbing drum peel test [86]. This method allowed the critical strain energy release rate to be calculated in mode I [70]. In a first step, the same materials were employed as those used in the flatwise tensile test, and in a second step, the skins were made of 200 g/m$^2$ carbon prepreg with a VTM 264 matrix and VTA 260 adhesive was used for core-to-skin bonding. However, the second skin of the samples was made with a 3-mm thick Al plate glued on honeycomb to avoid bending of the debonded part of the sandwich structure during peeling. As the material of the peel-ply as well as the degree of roughness have a strong influence on the adhesion [158, 159], various types of peel-ply were tested, and the one providing the better bonding was selected. Table 4-2 summarizes the different peel-plies used. Fine peel-plies were first used in order to avoid taking too much resin out of the prepreg. In a second step, a peel-ply with a larger thread was used to get better adhesion.

**Table 4-2: list of peel plies tested**

| | | |
|---|---|---|
| 1 | Airtech Release Ply B | Tightly woven nylon fabric, produces a fine texture |
| 2 | Airtech Bleeder Lease B | Silicone coated version of 1 |
| 3 | Airtech Release Ease 234 TF NP | PTFE coated glass fabric |
| 4 | Aerovac A100 PS | Nylon fabric, produces a medium texture |

The samples were cut into 70 mm widths. The peel direction was the ribbon direction of honeycomb, i.e. parallel to the cell walls of double thickness. The test was conducted in two steps. Firstly, the carbon skin was peeled off the sandwich during a first climb of the drum and the force-displacement curve was recorded. Figure 4-17 illustrates the peeling process. Immediately after this first climb, a second climb was carried out with the same structure, but with debonded skin. The force recorded during this second step corresponds to that needed to make the drum climb and to bend the skin, which was subtracted from the total force measured in first step. The debonding energy of the skin was subsequently calculated.

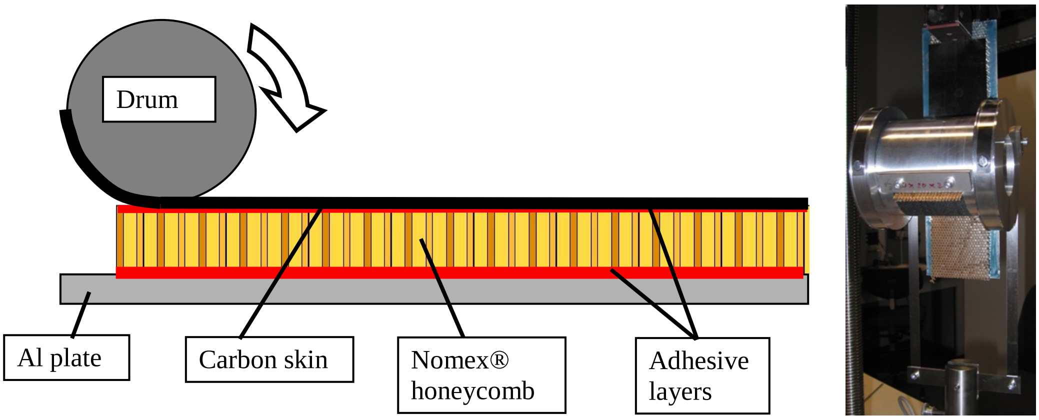

**Figure 4-17: climbing drum peel test setup**

Figure 4-18 shows a typical load / displacement curve recorded during climbing drum peel test which presents a saw-tooth shape. This is due to the discontinuity of the honeycomb core. Each tooth corresponds to a crack propagation of length $\delta_1$ as depicted in the schematic representation of the core in Figure 4-18. The measured average crosshead displacement between the peaks was $\delta_2 = 0.841$ mm. The corresponding peeled distance is given as

$$\delta_{1\exp} = \delta_2 \frac{r_i}{r_o - r_i} = 2.78\ mm \qquad (4.23)$$

where $r_o$ is the outer diameter of the drum plus half of the loading ribbon thickness, and $r_i$ is the inner diameter of the drum, respectively 65.1 mm and 50 mm. As the cell diameter $s$ of the honeycomb is 3.2 mm, the outer diameter $2c$ of the cell is 3.7 mm, and the theoretical distance between two periodic honeycomb structures is

$$\delta_1 = \frac{3c}{2} = 2.78\ mm \qquad (4.24)$$

which corresponds exactly to the measured distance between peaks.

For the calculation of the critical strain energy release rate $G_{IC}$, the average of the peak loads was considered. The work done by the load $F$ exerted by the tensile machine to rotate the drum by an angle $d\theta$ is given by

$$dW = F\left(r_o - r_i\right)d\theta \qquad (4.25)$$

The $G_{IC}$ value was calculated by subtracting the work done to make the drum climb from the work done at peak load and dividing it by the surface peeled and is

$$G_{IC} = \frac{F_{peak}(r_o - r_i)d\theta - F_o(r_o - r_i)d\theta}{Br_i d\theta} = \frac{(F_{peak} - F_o)(r_o - r_i)}{Br_i} \qquad (4.26)$$

where $F_{peak}$ is the average peak load, $F_o$ is the force to make the drum climb and to bend the skin and B is the sample width.

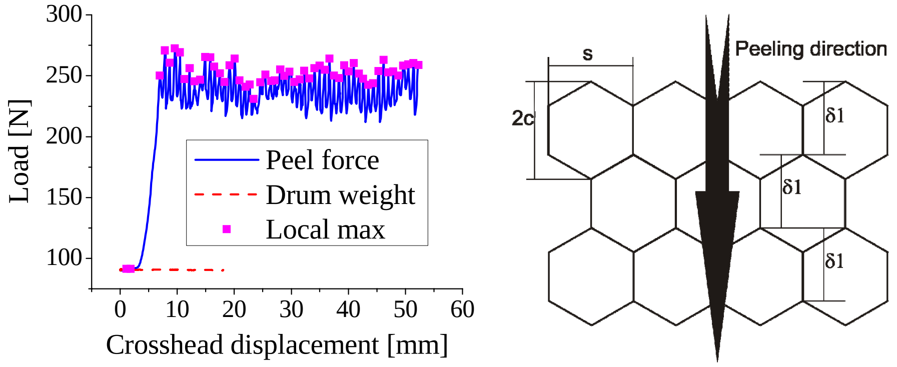

**Figure 4-18: (left) force displacement curve recorded during skin peeling. The force needed to peel the skin is the difference between peel force recorded and the force needed to make the drum climb and to bend the skin. (Right) schematic representation of the honeycomb core and of the different dimensions considered. $\delta_1$ represents the distance between two fronts for crack propagation.**

In a first step, the different peel-plies were compared; the corresponding debonding energies are given in Table 4-3. The fine nylon peel-ply produced quite good adhesion, but with a high standard deviation, which made reproducible tests difficult. The resin absorption in the peel-ply was low.

The silicone-coated version gave very high standard deviation values, making it unsuitable for studying the variation of $G_{IC}$ due to adhesive quantity variations. This large scatter probably arose from various coating transfers from the peel-ply to the prepreg.

The PTFE-coated peel-ply presented the advantage of not sucking any resin out the prepreg, but there was then almost no adhesion to the skin surface, probably because of PTFE transferring onto the surface of the skin.

Finally the peel-ply producing a medium texture gave higher and reproducible values of $G_{IC}$. This was not only due to the selected peel-ply, but also to the adhesive used (VTA 260) which was tougher than for the other tests (EH84). Furthermore, despite the larger thread, the resin absorption was similar to that of the fine peel-ply, which made it suitable for our study.

**Table 4-3: average value and standard deviation of $G_{IC}$ measured with 30 g/m$^2$ adhesive. The values for the 3 first peel-plies were measured with EH84 adhesive and the 4th with VTA260.**

| Type | $G_{IC}$ [J/m$^2$] | S.D. [J/m$^2$] | Prepreg resin sucked in peel-ply [g/m$^2$] |
|---|---|---|---|
| **1. Nylon, fine texture** | 173 | 47 | 12.1 |
| **2. Silicone coated** | 297 | 193 | 8 |
| **3. PTFE coated** | 8 | 4.4 | 0 |
| **4. Nylon, medium texture** | 668 | 26 | 13.5 |

Figure 4-19 represents the debonding energy measured with various adhesive weights. The energy values measured with various quantities of EH84 adhesive and peel-ply number 1 were rather low, and reproducibility was poor. This was presumably due to the chosen peel-ply which did not provide good adhesion, and also to the brittle behavior of the EH84 adhesive. In fact, this resin is primarily designed for use as a prepreg matrix and is stiff but not very tough. The brittle behavior induced a low debonding energy and also scatter in the results.

The curve representing the peeling energy as a function of VTA 260 adhesive weight clearly presents two different slopes. A rapid increase of $G_{IC}$ from 0 to 40 g/m$^2$ adhesive was followed by a slower increase above this value.

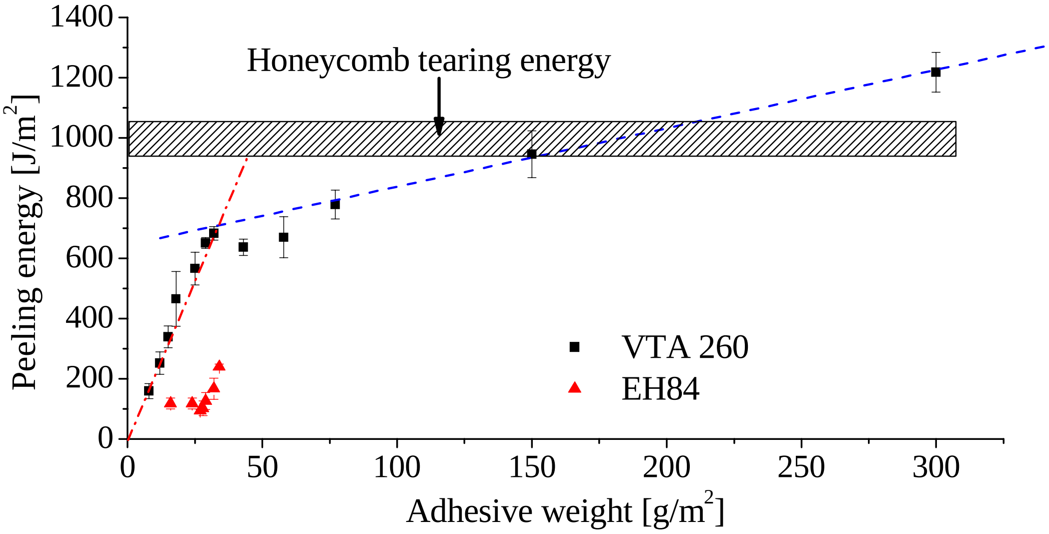

**Figure 4-19: Peeling energy values measured by the climbing drum peel test as a function of quantity of adhesive EH84 or VTA260. The dotted lines are guides for the eye and the cross-hatched zone represents the honeycomb tearing energy reported in section 3.3**

### 4.2.3. Failure micro-mechanisms

The micrographs taken from the samples after the peel test allowed different failure modes to be identified. Firstly failure with EH84 was often due to adhesive failure between the resin meniscus and the skin. Figure 4-20 illustrates a meniscus which debonded adhesively from the skin. Secondly with VTA 260 adhesive failure mode changed depending on the adhesive quantity. Figure 4-21 illustrates the failure modes with various adhesive weights on meniscus cross-sections. With low adhesive weight, failure was mainly due to cohesive failure of the adhesive fillet. There were also areas where adhesive failure between the honeycomb cell wall and the adhesive fillet occurred. Above 25 g/m$^2$, honeycomb cell wall tearing began to appear, as honeycomb pieces stayed in the resin meniscus on the skin. This phenomenon was more pronounced with 43 g/m$^2$. At 77 g/m$^2$ and more, the unique failure mode was honeycomb cell walls tearing above the resin fillet.

The two mean failure regimes causing the two different slopes in Figure 4-19 can be explained. From 0 to 40 g/m$^2$, cohesive failure of the adhesive fillet is the dominant mode. As the fracture energy is proportional to the fracture surface, the $G_{IC}$ value increases quickly with adhesive weight.

Above 40 g/m$^2$ adhesive, the dominant failure mode is honeycomb tearing. As the adhesive quantity increases, small adhesive amounts move along the honeycomb cell walls in the corners of the hexagonal cell due to capillarity forces; this slightly reinforces the core and accounts for the slow increase in $G_{IC}$ with adhesive amounts above 40 g/m$^2$.

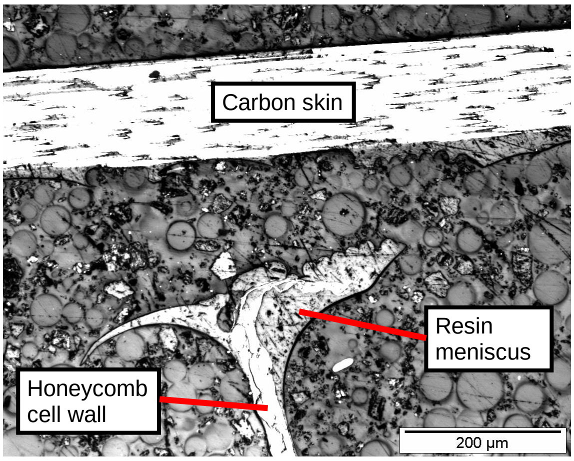

**Figure 4-20: Honeycomb cell wall debonded from the skin after the peel test. The texture of the peel-ply is visible on the fillet, showing that this was an adhesive failure. The fillet was made of 35 g/m$^2$ EH84 adhesive and the peel-ply was of type 1.**

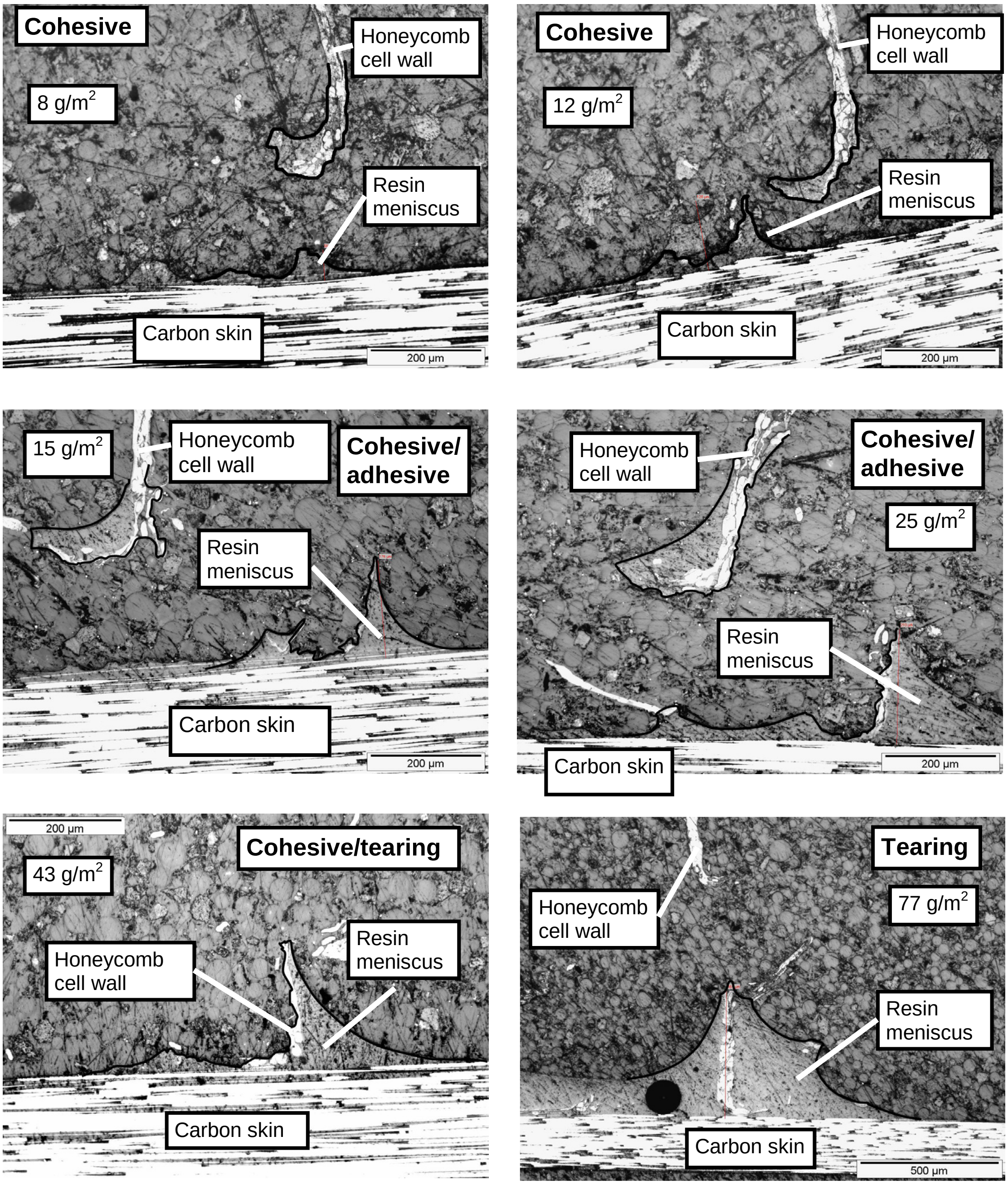
Cohesive
8 g/m2
Honeycomb cell wall
Resin meniscus
Carbon skin
200 µm
Cohesive
12 g/m2
Honeycomb cell wall
Resin meniscus
Carbon skin
200 µm
15 g/m2
Honeycomb cell wall
Cohesive/ adhesive
Resin meniscus
Carbon skin
200 µm
Honeycomb cell wall
Cohesive/ adhesive
25 g/m2
Resin meniscus
Carbon skin
200 µm
200 µm
Cohesive/tearing
43 g/m2
Honeycomb cell wall
Resin meniscus
Carbon skin
Tearing
Honeycomb cell wall
77 g/m2
Resin meniscus
Carbon skin
500 µm

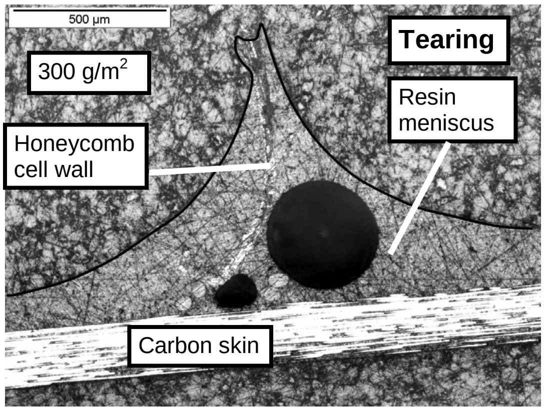
500 µm
Tearing
300 g/m2
Resin meniscus
Honeycomb cell wall
Carbon skin

**Figure 4-21: Micrographs of cross-sections of sandwich samples after peeling of the skin. The failure mode changed progressively from cohesive failure of the adhesive, and adhesive failure between honeycomb cell walls and adhesive fillet, to tearing of the honeycomb cell wall**

The debonding energy measured with 150 g/m$^2$ of adhesive agrees well to the tearing energy of the honeycomb reported in section 3.3 (see Figure 4-19). This confirms that the tearing energy of the honeycomb is the limiting factor in core-to-skin debonding energy when large amounts of adhesive were used with light cores.

However, when honeycomb tearing already occurred with 40 g/m$^2$ of adhesive during peeling, the debonding energy was smaller than the tearing energy reported in section 3.3. This can be explained by slightly different stress states and tearing mechanisms. In fact, during tearing energy measurements using the modified DCB test, a tearing zone formed before the crack propagated, while during the climbing drum peel test the stresses were concentrated above the adhesive meniscus, so that the energy dissipation zone was smaller, and thus the measured tearing energy was smaller too.

Failure mechanisms involved in the first regime (i.e. cohesive failure of the meniscus) are very complex due to the intricate geometry of the honeycomb and menisci and cannot be described precisely, and then predicted. The failure path was examined on micrographs after peeling. Two principal types of failures were present. In the first one, the meniscus broke at its base across its complete width, as depicted in the cross-sections in Figure 4-22, while in the second one, the meniscus broke first vertically along the honeycomb cell wall and then horizontally in the meniscus, as can be observed in the cross-sections in Figure 4-23.

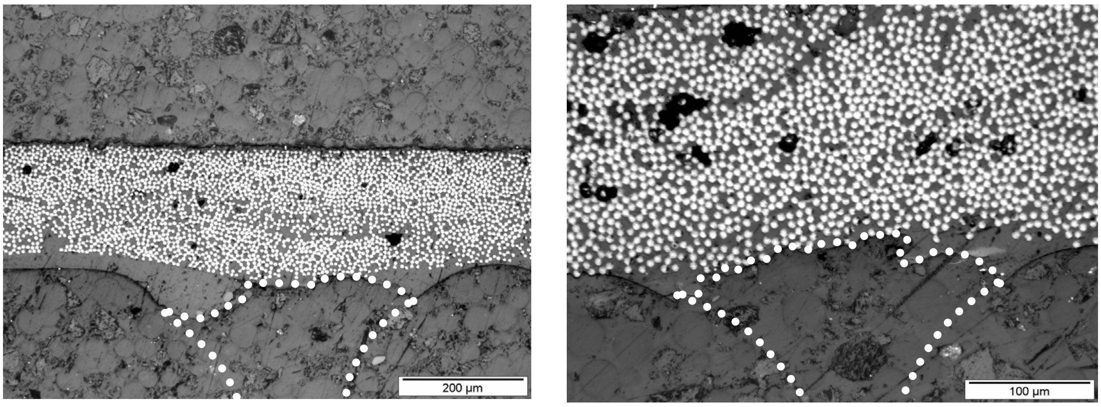

**Figure 4-22: Meniscus failure during the climbing drum peel test with crack propagation from the right side. The crack propagated horizontally at the base of the meniscus. The broken menisci were formed with 18 g/m$^2$ (left) and 8 g/m$^2$ (right). The white dots show the missing part of the meniscus**

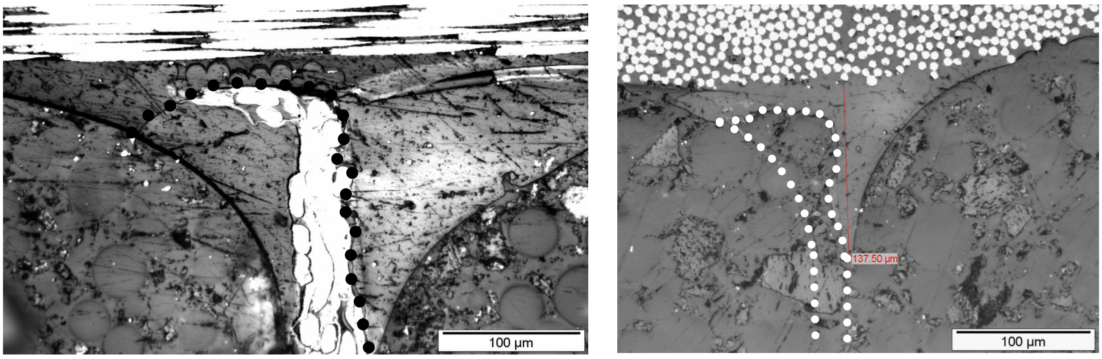

**Figure 4-23: Meniscus failure during the climbing drum peel test with crack propagation from the right side. The crack propagated first vertically along the honeycomb cell wall and then horizontally at the base of the meniscus. The left-hand picture shows the path of the crack on an intact meniscus (black dots) and right-hand picture on a broken meniscus with 18 g/m$^2$ adhesive. The white dots show the missing part of the meniscus**

In both cases, the failure area is similar and as a first approximation can be considered as the length of the base of the meniscus $W_m$ for one side. The broken area in each honeycomb cell is then approximately

$$S_{broken} = 6cW_m \tag{4.27}$$

By dividing this broken area by the surface of one cell, we obtain the broken area fraction in comparison to a continuous failure surface

$$\Phi = \frac{6cW_m}{3c^2 \cos(\pi/6)} = 4\frac{W_m}{s} \tag{4.28}$$

As the length $W_m$ can be calculated as a function of adhesive weight, as described in section 4.1, the broken area fraction can also be expressed as a function of adhesive weight. By multiplying the broken area fraction by the toughness of the adhesive measured in section 3.4, the breaking energy corresponding to mode I crack propagation in the menisci is obtained and represented as a function of adhesive weight in Figure 4-24. This prediction significantly underestimates the peeling energy measured in the peel test. This is in agreement with the results obtained by Okada and Kortshot [70], who obtained a higher debonding energy with discontinuous adhesive fillets than with a continuous adhesive layer. This shows that debonding cannot be considered as a crack propagation in mode I through the resin menisci. The high peeling energy measured is thus dissipated by other mechanisms. Firstly, the menisci break partly along the honeycomb cell walls, thus not in mode I but rather in mode II. As the critical strain energy release rate in mode II is usually greater than in mode I, this means that more energy is dissipated in this mode during peel testing. Secondly, the toughness of the bulk adhesive is measured by propagating a sharp crack, while in the case of the resin menisci, the crack is stopped in front of each honeycomb cell (see Figure 4-18), and the crack has then to be initiated again. The amount of energy required to initiate the crack can be high on a smooth meniscus surface. Furthermore, a little plastic deformation may also occur before the crack initiates, and this also dissipates some energy. Finally, even with very small amounts of adhesive, some small pieces of Nomex® are sometimes torn, which further dissipates energy.

By considering that all these mechanisms are proportional to the broken area, the calculated debonding energy can be multiplied by a coefficient in order to minimize the difference with the experimental results, using the least squares method. With a coefficient 2.31, the theoretical curve approximately fits the experimental results. This means that the dissipation mechanisms involved during debonding dissipate more than twice the energy required to propagate the crack in mode I through the menisci.

However, it can be seen that a linear fit matches the experimental results very well. This indicates that the peeling energy is directly proportional to the adhesive quantity when the meniscus is fractured. This may be the case for energy dissipation due to plastic deformation of the menisci, but this energy dissipation mode cannot be dominant, because the epoxy resin is brittle.

So, as the energy dissipation mechanisms are multiple, some of them dependant on the broken area and others dependant of the volume of adhesive, the exact dependency between peeling energy and adhesive weight can only be predicted theoretically with great difficulty.

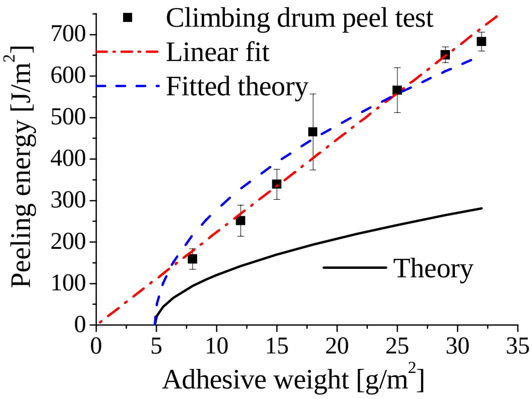

**Figure 4-24: peeling energy as a function of adhesive weight in the domain where failure is due to fracture of adhesive menisci. The model predicting the energy proportional to the fracture area significantly underestimates the experimental data and was multiplied with a fit coefficient**

The optimal adhesive weight for this loading case is the one providing the highest debonding energy-to-weight ratio. Figure 4-25 represents the $G_{IC}$ value divided by adhesive plus skin weight calculated as a function of adhesive weight with the experimental data. The curve presents a maximum at about 35-40 g/m$^2$. This is then the optimum adhesive quantity required in order to achieve the best strength-to-weight ratio for this loading case, i.e. peeling of the skin. This optimum is only valid for this specific loading case, but as peeling of the skin is usually the most critical loading case for debonding, this is the maximum adhesive weight to consider for other loading cases in order to avoid debonding of the skins. Of course, this value is directly related to the materials used, particularly the adhesive and honeycomb, and has thus to be adapted to other materials. Also, the optimal amount of adhesive determined corresponds to the quantity of adhesive forming the menisci on a pre-cured skin. If adhesive films or one-shot curing is used, the real amount of adhesive in the menisci has to be calculated in order to use this result.

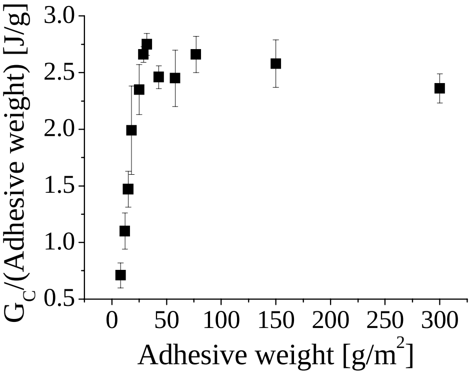

**Figure 4-25: $G_{IC}$-to-weight ratio, as a function of adhesive weight. The maximum value is in the range of 35 - 40 g/m$^2$.**

## 4.3. Conclusions

The influence of the amount of adhesive on the formation of resin menisci between the honeycomb core and the carbon skin, and the resulting debonding energy was investigated. The deposition method (section 3.2.1) was used, and the experimental values of debonding energy were modeled using predicted geometry of the menisci, leading to following conclusions:

- In contrast to the flatwise tensile test found to be inappropriate due to core failure, the climbing drum peel test enabled the optimum strength-to-weight ratio to be identified in the range of 35-40 g/m$^2$.

- At adhesive quantities higher than 40g/m$^2$, failure was due to honeycomb tearing and the debonding energy corresponded well to the measured honeycomb tearing energy. With lower adhesive quantities, the failure was due to menisci fracture.

# CHAPTER 5. INFLUENCE OF ADHESIVE QUANTITY AND BONDING DEFECTS ON THE STRENGTH OF SANDWICH STRUCTURES

During their use, sandwich structures are usually not exposed to peel loading of the skin, which is the worst case for core / skin debonding. Debonding may occur due to shear stresses at the core / skin interface or after skin buckling under compression. In these cases, the optimal adhesive quantity reported in Chapter 4 (~40 g/m$^2$) gives an indication of the maximum amount of adhesive to use when designing a sandwich structure specifically to avoid debonding. However, this amount may be too much for the targeted loading case resulting in an overdesigned bonding joint, whereas weight could be saved by reducing the adhesive amount. In addition, the adhesive layer may also have functions other than only core-to-skin bonding. For example, Webber *et al*. [48] observed that the adhesive layer increased the stability of the skin against wrinkling, which can be advantageous on sandwich with very thin skins. Therefore, in order to observe the influence of the adhesive quantity on the strength of sandwich structures in a common loading case, the strength of sandwich beams with different amounts of adhesive was investigated in 4-point bending and under compression. The effect of bonding defects which could be present in use was also studied.

## 5.1. Materials and methods

The skins of the sandwich structures were made of 70 g/m$^2$ UD carbon prepregs. The core was Nomex® honeycomb from Euro-Composite. The adhesive used was VTA260. Two different types of samples were prepared in order to evaluate the bending strength as a function of adhesive weight. Firstly, samples with very thin pre-cured skins were fabricated. The skins were made each of one UD layer at 0° (beam-length direction) cured at 120°C during 100 min., with a heating rate of 1°/min, under vacuum (-0.9 bar relative pressure), with the peel-ply A100 PS on the surface, as described in Figure 4-14. Various amounts of adhesive were deposited on the honeycomb using the method described in section 3.2.1. The core was bonded to the first skin under vacuum (-0.9 bar relative pressure), as described in Figure 4-15. The second skin was bonded to the core in a second step with a 50 g/m$^2$ adhesive film under vacuum (-0.9 bar relative pressure). During this second cure, the first skin was on an Aluminum mould to avoid damaging the skin or creating waviness due to the pressure applied by the vacuum bag. Each panel was cut in samples of 350 mm length and 30 mm width. The span between the outer supports in 4-point loading was 300 mm and 100 mm between the loading points. Since during bending it was always the skin under compression which failed, the samples were tested with the first fabricated skin with controlled adhesive weight under compression.

The second type of sandwich samples was fabricated in one shot with skins made of two prepreg layers at 0° and 90°. This kind of structure with a cross-ply skin corresponds better to structures found in real applications than those with a UD skin. However, these skins could not easily be cured separately and then bonded to the core, because the asymmetry of the 0°/90° layers caused a pronounced bending of the skin due to internal stresses, and the skin was then difficult to manipulate. Since during one-shot curing the skin on the vacuum bag side had a lower quality due to waviness, the study concentrated on the smooth skin on the mould side. The effect of waviness of the skin on the vacuum bag side is considered in section 6.3. The 0° prepreg layer was placed first on the Al plate to ensure maximum flatness of this layer which supports a much greater load than the 90° layer. Five different adhesive weights were used on the smooth side. In a first case, no supplementary adhesive was used, and bonding was carried out with the prepreg resin. In a second case, the adhesive deposition method was used and 25 respectively 85g/m$^2$ of adhesive were deposited on the honeycomb. In a third case a 50 g/m$^2$ adhesive film was used and one or two layers of film were laid on the skin. As the panels were cured in one shot, the amount of resin from the prepreg participating in meniscus formation was unknown. Therefore, in order to ascertain precisely the adhesive quantity in the menisci for core-to-skin bonding, the size of the menisci was measured on micrographs of cross-sections and the corresponding amount of adhesive was calculated accordingly to section 4.1.3. The second skin was always bonded with a 50 g/m$^2$ adhesive film.

The complete panel was cured under vacuum (-0.9 bar relative pressure) at 120°C during 100 min. An Al frame avoided lateral crushing when the vacuum was applied. Figure 5-1 illustrates the stacking of the different layers for curing. A non-perforated film was placed on the top prepreg to prevent resin flowing out of the prepreg. Fiber rovings were placed between the Al frame and the non-perforated film to allow air to circulate. As the film prevented air circulation through the thickness of the skin, the vacuum was only applied from the sides of the panels, and a good vacuum could not be ensured in the honeycomb cells. This phenomenon is further discussed in section 6.2. The panels were then cut into 7 samples of 30 mm width and 450 mm length. The span between the outer supports in 4-point loading was 400 mm, and 100 mm between the loading points. The panels were tested with the smooth skin under compression.

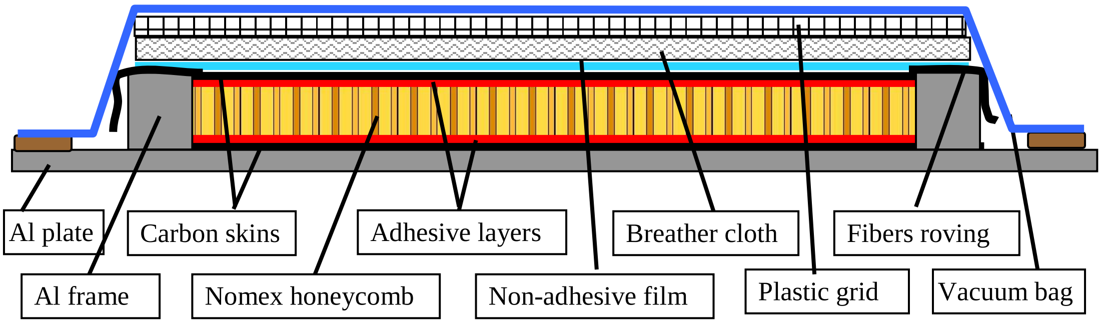

**Figure 5-1: Stacking of the different layers during one-shot vacuum bag curing. The breather cloth and plastic grid allowed better air circulation and a more uniform vacuum under the vacuum bag.**

The stresses in the skin were calculated from the load applied in bending, as explained in section 2.1.6. For the pre-cured UD skin, the stress was directly given by equation (2.58). When the skin was a cross-ply, the highest load would be in the ply at 0°. Using the CLT, it could be calculated that under compression the ply at 0° supported 93% of the load in the skin. The stress in the 0° ply was calculated as

$$\sigma_{p0} = \frac{0.93N}{t_p} = 0.93\frac{M}{Bdt_p} \tag{5.1}$$

where $N$ is the load per unit width in the beam and $t_p$ the ply thickness.
Since, during the 4-point bending, the sandwich had out-of-plane deformations, the skin under compression was bent and loaded the core under compression, as explained in section 2.1.6, which might then favor local instability of the skin. In order to have pure compression, 120mm beams were also cut from the second type of beams tested in 4-point bending and these were loaded under compression as described in section 3.2.6. A clear disadvantage of this test was that the two skins were loaded at the same time. As the quality of the skins was different, it was difficult to identify the influence of the parameters modified on one skin only.

When using models calculating the wrinkling load of the skin under compression, either during bending or compression tests, the bending stiffness of the facesheet with the adhesive menisci on its surface has to be known accurately. Therefore, after testing the sandwich beams, a 90 mm long section of the skin was cut from the beams. The honeycomb was removed from the skin by cutting it with a cutter at the top of the adhesive menisci, as shown in Figure 5-2. The stiffness of the skin was measured in 3-point bending, with a span of 50mm. The measurement was made with the menisci side either in tension or under compression and the mean value was calculated.

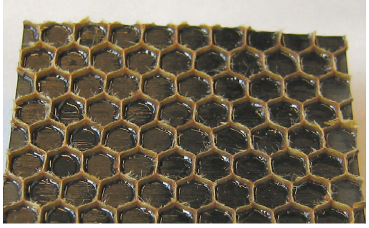

**Figure 5-2: skin of a sandwich structure with honeycomb core cut at the top of the resin fillets**

## 5.2. Modeling of skin instability phenomena

The failure of the sandwich beams with thin skins was mainly due to local instability of the skins. Therefore adequate models had to be chosen so as to be able to describe and predict the failure with best accuracy.

### 5.2.1. Dimpling

The first instability to consider with honeycomb is intra-cell buckling of the skin (dimpling). As the UD skin was highly anisotropic, the model developed by Thomsen and Banks [55] and described in section 2.1.5, which takes into account the different bending stiffness of the skin in different directions, was used as basis. The wavelength chosen in the model, however, does not correspond to the periodic structure of the core. It was therefore changed by considering the length of the rectangle used for buckling calculation as the periodic distance between honeycomb rows, corresponding to $\delta_1$ in Figure 4-18, i.e. *1.5c* with *c* being the length of a cell wall. This should in fact better correspond to the periodical waviness developing when dimpling occurs. To further improve the model, the presence of the adhesive fillet between the honeycomb cell walls and the face-sheets was taken into account. If the meniscus is infinitely stiff, it prevents bending of the face-sheet on the meniscus, and the width of the meniscus has to be subtracted at each edge of the rectangle considered for the buckling model. However, as the meniscus is not infinitely stiff, some bending of the face is still possible on the meniscus. This was taken into account in the model by subtracting not the complete meniscus width, but only a part of the width. Finally, the following model gave the critical compressive load per unit width in the skin for dimpling

$$N_{\mathrm{dimp}} = \pi^2 \left[ \frac{D_{11}}{D_{22}} \left( \frac{s - 2\xi W_m}{1.5c - 2\xi W_m} \right)^2 + \frac{8}{3} \frac{\left( D_{12} + 2D_{66} \right)}{D_{22}} + \frac{16}{3} \left( \frac{1.5c - 2\xi W_m}{s - 2\xi W_m} \right)^2 \right] \frac{D_{22}}{\left( s - 2\xi W_m \right)^2} \quad (5.2)$$

where s is the cell size, i.e. the distance between two opposite cell walls, *1.5c* the distance between two rows of cells, i.e. $s\sqrt{3}/2$, $W_m$ the width of the meniscus as represented in Figure 4-4 and $\xi$ a coefficient varying between 0 (no meniscus) and 1 (infinitely stiff meniscus).

### 5.2.2. Wrinkling

The second type of instability is wrinkling of the skin, i.e. local buckling of the skin which can debond from the core or crush the core locally. As described in section 2.1.5, many models have been developed. The model developed by Gutierrez and Webber [39] is the one which corresponded the best to the case studied here. Firstly, it was developed for a bending loading case, so no adaptations were necessary. Secondly, the anti-plane stress assumption in the core was used, which corresponded very well to the very light honeycomb core used. Finally, both compressive and shear stresses were considered in the core, giving the best accuracy. The critical line load and the corresponding critical half-wavelength for wrinkling were calculated by solving equation (2.37).

The critical wrinkling stress is highly dependent on the bending stiffness of the skin and core out-of-plane and shear modulus. The adhesive used to bond the skin to the core formed resin fillets which significantly increased the wrinkling load. This effect could be taken into account in the model in two different ways. On one hand, the skin in the model could be replaced by the skin plus adhesive fillets, i.e. by a skin with increased bending stiffness lying on an unchanged honeycomb core. On the other hand, the skin could be considered as unchanged, but lying on a core locally reinforced on its surface by adhesive fillets. The first solution was considered in this model because the bending stiffness increase was easier to quantify.

The first hypothesis of the model is that only the bending stiffness of the skin is changed by the presence of adhesive fillets, and not tensile or compressive stiffness. In fact, as the modulus of the adhesive is 2 orders of magnitude smaller than that of carbon fibers, the tensile modulus of the skin will be only slightly changed by the fillets. However, due to their geometry, the menisci act as local stiffeners of the skin in bending, and can significantly increase the bending stiffness despite their low modulus.

The second hypothesis is that the coupling between tensile and bending deformations of the faces can be disregarded. In fact, as the skins are very thin, the bending force created by tension or compression in the skin due to the asymmetric stacking of the ply are very low, and the coupling effect has only a marginal influence on the wrinkling loads. This was verified with the model. This second hypothesis is used in the model of Gutierrez by setting $B_{ABD} = 0$, $A_{ABD} = A_{11}$ and $D_{ABD} = D_f$ in equations (2.34), with $A_{11}$ being the first coefficient of the ABD matrix, and $D_f$ the bending stiffness of the skin. The value of $D_f$ can be calculated with CLT as

$$D_f = D_{11} - \frac{B_{11}^2}{A_{11}} \tag{5.3}$$

However, as the bending stiffness with the adhesive menisci is difficult to calculate, because the adhesive layer is not continuous, $D_f$ was measured with different adhesive quantities, as described previously, and a fitting function was used in the model.

The classic wrinkling solutions assume a perfectly flat face sheet. If this hypothesis is more or less satisfied for the skin cured on the mould side, it is certainly not for the wavy skin cured on the vacuum bag side. In order to obtain a general model, the effect of initial waviness was included, and an arbitrary small waviness was used for the smooth face of the sandwich.

The model of Gutierrez and Webber [39] can be adapted to take into account the initial deformations in a similar way to the models described in section 2.1.5. Equation (2.31), giving equilibrium of the face, has to be modified and written as

$$B_{ABD}\frac{d^3u}{dx^3} - D_{ABD}\frac{d^4w}{dx^4} - N\frac{d^2w}{dx^2} - N\frac{d^2w_0}{dx^2} = \left(\sigma_z\right)_{z=d} \tag{5.4}$$

where $w_0$ and $w$ are respectively the initial deformation and the deformation due to the load $N$. These deformations are represented by a sinusoidal function as described by equation (2.39). By combining equation (5.4) and equation (2.30) with the core equations (2.27) to (2.29), and taking into account the sinusoidal forms of $w$, $w_0$ and $\tau_{xz}$, the amplitude of the shear stress can be obtained as

$$\mathrm{T}_{xz} = \frac{NW_0\left(\frac{\pi}{l_0}\right)^5}{q_1\left(\frac{\pi}{l_0}\right)^8 + q_2\left(\frac{\pi}{l_0}\right)^6 + q_3\left(\frac{\pi}{l_0}\right)^4 + q_4\left(\frac{\pi}{l_0}\right)^2 + q_5} \tag{5.5}$$

Then as $w$ has a sinusoidal shape, the coefficient $k_1$, and the normal stress in the core $\sigma_z$ have also a sinusoidal shape of the type

$$\begin{gathered} k_1 = K_1 \sin\left(\frac{\pi x}{l_0}\right) \\ \sigma_z = \Sigma_z \sin\left(\frac{\pi x}{l_0}\right) \end{gathered} \tag{5.6}$$

Thus, by inserting the calculated shape of $\tau_{xz}$ in the differential equation obtained by combining the core equilibrium equations into (2.30), the value of $K_1$ can be determined as

$$K_1 = \frac{2E_{cz}\mathrm{T}_{xz}}{A_{ABD}d^2 + 2B_{ABD}d}\left(\frac{l_0}{\pi}\right)^3\left(\frac{A_{ABD}d}{G_{core}}\left(\frac{\pi}{l}\right)^2 - \frac{A_{ABD}d^3 + 3B_{ABD}d^2}{6E_{cz}}\left(\frac{\pi}{l_0}\right)^4 + 1\right) \tag{5.7}$$

The amplitude of normal stress in the core, and of displacement $w$ can then be calculated using equations (2.27) and (2.28)

$$\Sigma_z = \mathrm{T}_{xz} d \frac{\pi}{l_0} + K_1 \tag{5.8}$$

$$W = \frac{\mathrm{T}_{xz} d^2}{2E_{cz}} \frac{\pi}{l_0} + \frac{d}{E_{cz}} K_1 \tag{5.9}$$

The maximum local compressive strain in the skin due to local bending and to compression of the face can be calculated as in equation (2.50)

$$\varepsilon_m = \left( -\frac{d^2 w}{dx^2} \right)_m h + \frac{N}{A_{11}} = W \frac{\pi^2}{l_0^2} h + \frac{N}{A_{11}} \tag{5.10}$$

where h is the distance from the neutral axis of the face to the surface of the skin under compression.

When the bending deformation of the sandwich beam increases, a supplementary compressive load rises in the core as shown in section 2.1.6. Equation (5.8) can then be corrected by adding this load resulting in

$$\Sigma_z = \mathrm{T}_{xz} d \frac{\pi}{l_0} + K_1 + \frac{N^2 d}{D_B} \tag{5.11}$$

where $D_B$ is the bending stiffness of the sandwich beam.

To identify the critical load for a sandwich structure with initial skin waviness of wavelength $l_0$ and amplitude $W_0$, the critical load for core compressive strength, core shear strength, and skin compressive strength have to be calculated by setting the stress or strain, as calculated with equations (5.5), (5.10) and (5.11), equal to the core strength or to the critical strain of the skin material and solving the corresponding equations numerically. The lowest of the critical loads will determine the type of failure. Of course, none of these different critical loads can be greater than the critical wrinkling load corresponding to the wavelength of the initial imperfection considered, because the wrinkling load is calculated for a perfectly smooth skin.

To take into account the adhesive weight in the model, the same approach was used as for the wrinkling model, i.e. replacing the coefficient $A_{\mathrm{ABD}}$, $B_{\mathrm{ABD}}$ and $D_{\mathrm{ABD}}$ by $A_{11}$, 0 and $D_{\mathrm{f}}$, measured as a function of adhesive weight.

## 5.3. *Failure analysis of sandwiches with thin pre-cured UD skins*

During 4-point bending tests, the samples exhibited a non-linear behavior. Figure 5-3 shows the load displacement curve recorded during 4-point bending tests on beams with different adhesive weights. After a linear part, corresponding to the pure compression and tension of the skins, the slope of the curve decreased. As carbon skins are elastic, the non-linearity is due only to geometrical non-linearity. In fact, during loading of the sandwich beams, a clear buckling of the skin in the cells (dimpling) could be observed. This dimpling created a misalignment of the fibers, and thus the stiffness of the skin was reduced. The force and displacement corresponding to the beginning of the non-linearity was fixed where the difference between the linear fit and the measured curve was 1% as depicted in Figure 5-3. Unfortunately, the force-displacement curves were not recorded for all the samples and are available for only four different adhesive weights.

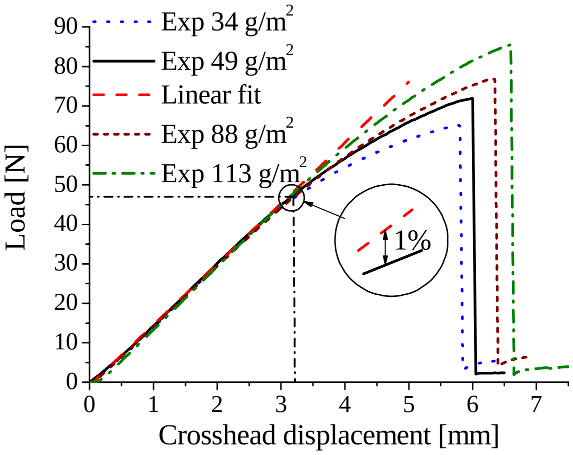

**Figure 5-3: Load-displacement curve measured in a 4-point bending test for samples with a single prepreg layer as skins, and various adhesive weights. The linear fit of the first part of the curve for 49 g/m$^2$ adhesive, and the corresponding definition of the non-linearity point is also shown**

To calculate the dimpling load by taking into account the effect of the adhesive menisci, the size of menisci was calculated for each adhesive weight by using the model described in section 4.1. The critical load was then calculated using equation (5.2) and the numerical values given in Table 5-1. In this model, it is interesting to observe that the stiffness in the width direction considerably influences the calculated dimpling load. Low stiffness of the UD skin perpendicular to the fibers is thus the main reason for the low dimpling load. The coefficient $\xi$ was then adjusted so that the model fit the results.

**Table 5-1: properties of the skin made of one layer UD prepreg calculated with CLT and dimensions of honeycomb considered for dimpling calculation**

| $D_{11}$ | $D_{22}$ | $D_{12}$ | $D_{66}$ | *1.5c* | *s* |
|---|---|---|---|---|---|
| 2.885 | 0.2452 | 0.0809 | 0.1544 | 2.77 | 3.2 |
| Nmm | | | | mm | |

Figure 5-4 depicts the dimpling load calculated with the model and the experimental data as a function of adhesive weight. The dimpling load increased with adhesive weight, confirming the stabilizing effect of the resin menisci. With $\xi = 0.6$, the correspondence between the calculated dimpling load and the non-linearity point on the curves is very good for the four different adhesive weights considered. This means that the meniscus is replaced in the model by an infinitely stiff support of about half the width of the meniscus. This hypothesis is very reasonable and this dimpling model can then be used with the coefficient $\xi = 0.6$ to predict the dimpling load. Of course, the value of this coefficient could change when considering other materials, because it depends on the stiffness of the adhesive used, and on the shape of the meniscus, but it does provide a good approximation.

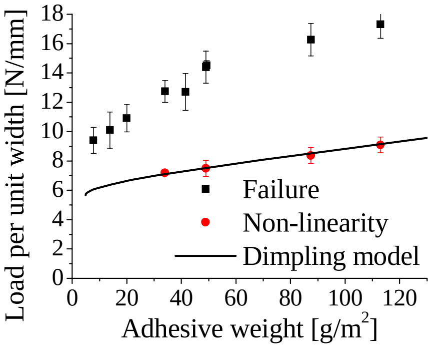

**Figure 5-4: Load per unit width in the skin under compression in sandwich beams under bending as a function of adhesive weight.**

Dimpling instability was elastic and reversible and did not cause failure of the beam. In fact, at dimpling load, the fibers in the middle of the honeycomb cells buckled, but the fibers on the cell walls and menisci were maintained flat. Therefore, above dimpling load, the load continued to increase in the fibers maintained flat, but not in the buckled fibers. The mean load in the skin continued thus to increase but with reduced stiffness until failure occurred. As more fibers were maintained flat when the menisci were bigger, the stiffness after dimpling was higher with greater adhesive weight as depicted in Figure 5-3. All the samples broke due to compressive failure of the skin between the loading points. Figure 5-4 depicts the load per unit width at failure in the skin, which increased with adhesive weight. The increase was more pronounced with low adhesive weights and a change of slope seemed to occur at about 40-50 g/m$^2$ adhesive. However, the failure mode of the samples changed with the adhesive quantity at ~15-20 g/m$^2$, so that the change of slope can hardly be related to the observed failure mechanisms, and should be confirmed by further testing. Figure 5-5 shows the two different types of failure. The samples broke mainly due to debonding of the skin when the adhesive quantity was smaller than 15 g/m$^2$. As the core-to-skin debonding energy increases with adhesive weight, as observed in section 4.2, thus, logically, the stress at failure increased with adhesive quantity. Above 20 g/m$^2$, failure of the skin was mainly due to local instability and compressive failure of the skin. The stress at failure also increased with adhesive weight greater than 20 g/m$^2$. This confirms that the adhesive not only prevented skin debonding, but also reinforced and stabilized the skin.

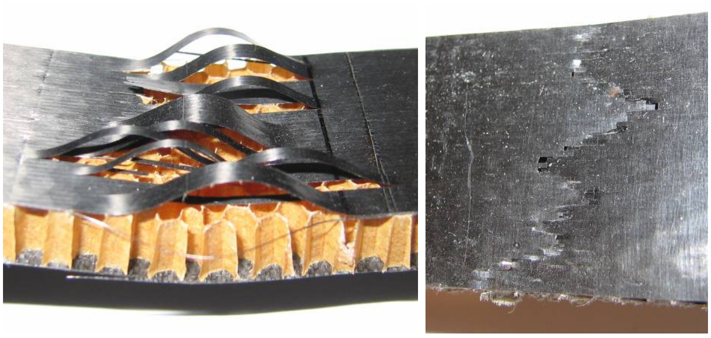

**Figure 5-5: Failure of the skin under compression when the sandwich beam was loaded in 4-point bending. The failure was due to debonding with 8 g/m$^2$ (left) and to compressive failure with 113 g/m$^2$ (right)**

Above the dimpling load, the stresses and deformations in the skin are no longer constant in the skin because some fibers buckle, others stay straight. Also, among the buckled fibers, the stress level is not the same depending on their position over the honeycomb cell. Therefore, the failure mechanism and loads are difficult to predict. By observing carefully the compressive failure in the samples with more than 20 g/m$^2$ of adhesive as illustrated in Figure 5-5, it can be seen that the fibers are always broken at about the middle of the honeycomb cell. It is thus the buckled fibers which break and not those staying flat on the adhesive menisci. A typical failure pattern is represented in Figure 5-6. This type of failure does not correspond to a wrinkling failure, and this is confirmed by calculating the wrinkling load with the Gutierrez [39] model, which is two times greater than the experimental data. A possible failure mechanism is as follows:

after dimpling, most of the load is supported by the fibers maintained flat by the menisci. However, the honeycomb cell walls oriented in the direction of the fibers are not continuous, but are shifted by half the cell size from one row to the next. To transmit normal stress from one row to the next, shear stresses appear in the flat zone over the cell walls oriented at 60° to the fiber direction. These zones with normal and shear stresses are depicted in Figure 5-6. As the skin is made of only one UD skin, shear stresses appear between fibers in the matrix. When shear strength is reached, shear failure occurs along the fine dotted lines of the failure path represented in Figure 5-6. The buckled fibers are then no longer supported along the side edges and so fail along the thin plain lines represented in Figure 5-6. As the area of skin supporting the shear is directly proportional to the meniscus size, this explains the dependence between failure load and adhesive weight. However, the complex failure mechanism makes analytical modeling and prediction of failure very difficult to achieve, and was not further investigated in the present work.

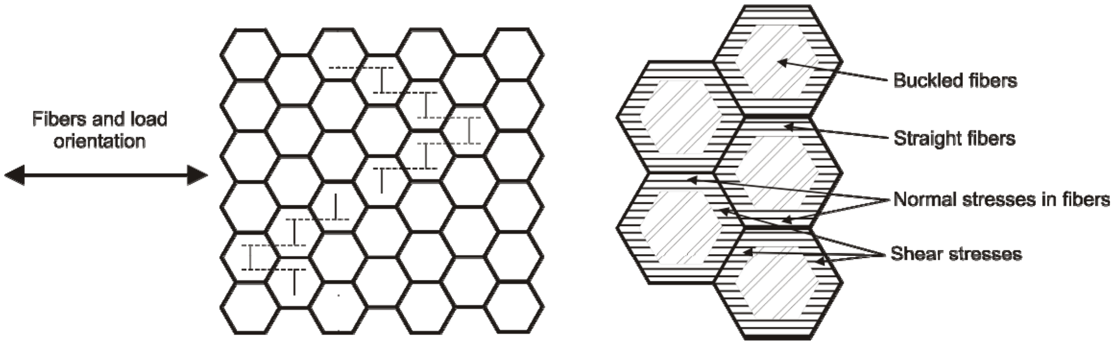

**Figure 5-6: (Left) Schematic representation of an example of a failure path in the skin under compression. The fine dotted lines represent failure between fibers, and the thin plain line the failure of the fibers. (Right) Representation of the buckled area (center of the cells) and the area maintained flat by the menisci.**

## 5.4. Failure analysis of sandwiches with cross-ply skins

All the samples with 0/90° fibers in the skins tested in 4-point bending broke due to compressive failure of the skin between the two central loading points. The skin broke due to wrinkling of the skin in the core, as illustrated in Figure 5-7. The skin became locally unstable and crushed the core. No debonding occurred, even when no supplementary adhesive was used. However, the strength of the sandwich beam increased with adhesive weight, even though no debonding occurred, as illustrated in Figure 5-8, which depicts the failure load as a function of adhesive weight. So, as stated with the pre-cured skin, the adhesive not only ensured core / skin bonding, but also stabilized the skin and reinforced the core, thus increasing the wrinkling load.

Interestingly, despite the fact that the amount of fibers oriented at 0° (length direction of the beam) and carrying 93% of the load in the cross-ply is the same as for the UD skins studied in the preceding section, the strength is significantly higher with the cross-ply (23-35 N/mm instead of 9-15 N/mm). Thus, this underlines how important is the stabilizing effect of the 90° ply.

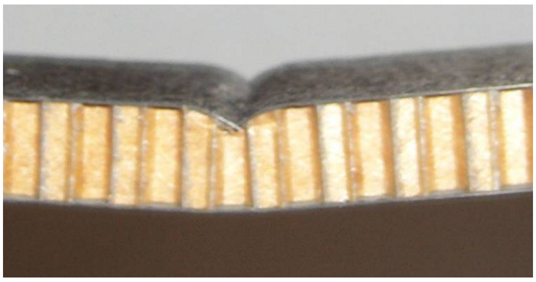

**Figure 5-7: failure mode of the skin under compression without bonding defects. The skin became locally unstable and crushed the core.**

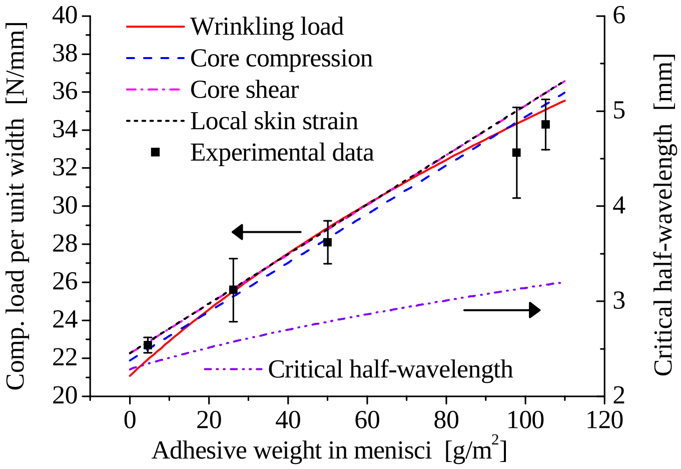

**Figure 5-8: compressive load per unit width in the skin at failure during 4-point bending test as a function of adhesive weight in the menisci for core-to-skin bonding. The critical loads predicted by the models for the different types of failure are represented.**

The bending stiffness of the skin was measured in order to evaluate the stiffening effect of the adhesive meniscus on the skin. It is represented in Figure 5-9 as a function of the adhesive quantity in the resin meniscus. For the range of adhesive quantity studied, the bending stiffness rose linearly with adhesive weight. Bending stiffness is also represented, as calculated with CLT and assuming an even layer of adhesive on the surface of the skin. The reinforcing effect is much more pronounced with the adhesive menisci due to the stiffener geometry, and also due to the small fragments of Nomex® honeycomb fixed in the menisci.

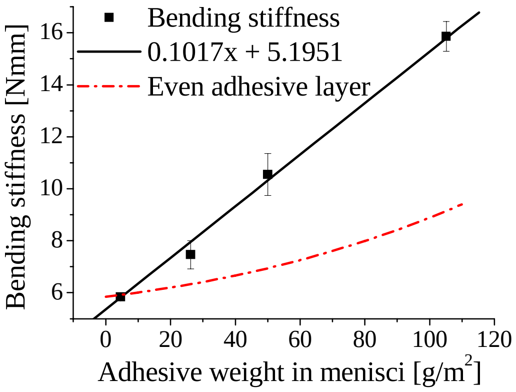

**Figure 5-9: Bending stiffness of the skin measured by the 3-point bending test as a function of adhesive weight in the menisci for skin-to-core bonding. The theoretical stiffness calculated with CLT for an even adhesive layer is also represented.**

Once the relation between the bending stiffness of the skin and the adhesive quantity was established, the critical load could be calculated with the different models described.

Firstly, the ABD matrix of the 0/90° skin without any adhesive layer was calculated as

$$\begin{pmatrix} A_{3x3} & B_{3x3} \\ B_{3x3} & D_{3x3} \end{pmatrix} = \begin{pmatrix} 7666 & 396 & 0 & -226 & 0 & 0 \\ 396 & 766 & 0 & 0 & 226 & 0 \\ 0 & 0 & 756 & 0 & 0 & 0 \\ -226 & 0 & 0 & 12.52 & 0.647 & 0 \\ 0 & 226 & 0 & 0.647 & 12.52 & 0 \\ 0 & 0 & 0 & 0 & 0 & 1.23 \end{pmatrix} \tag{5.12}$$

As the skins are thin and the core is cellular, the critical dimpling load was calculated with equation (5.2). The cell size *s* being 3.2 mm, the critical dimpling load without any adhesive meniscus ($W_m$ = 0) is 65.7 N/m. This is about three times higher than experimental failure loads, implying that this mode is not critical in this case. Therefore, wrinkling models were used to predict the failure load. In order to use the model of Gutierrez and Webber [39], the minimal properties of honeycomb given in Table 3-2 were considered and the ribbon direction was used. With these values, the critical load per unit width in the skin for wrinkling is 22.1 N/m and the corresponding critical half-wavelength is 2.37 mm. As the half-wavelength is smaller than the honeycomb cell size, the validity of the formula seems to be questionable, because the model considers a continuous support of the skin. However, failure occurs always on a line perpendicular to the beam direction, i.e. perpendicular to the ribbon direction of the honeycomb. This line always crosses the same number of honeycomb ribbons, wherever it is placed. Therefore, the support provided by the honeycomb on a line perpendicular to the ribbon direction is more or less continuous in the lengthwise direction of the beam, so that the elastic foundation can be regarded as being constant and the model is still valid.

If the coupling effect between tension and bending of the skin is discounted, i.e. by replacing the coefficient $A_{ABD}$, $B_{ABD}$ and $D_{ABD}$ by respectively $A_{11}$, 0, and the skin bending stiffness calculated with CLT as 5.842 Nmm, then the critical wrinkling load is 22.25 N/m and the critical half wavelength 2.36 mm. The difference between this result and the complete model is then less than 1%, and the coupling effect can thus be disregarded in this case.

By inserting into the model the bending stiffness of the skin as a function of adhesive weight as measured in Figure 5-9, the critical wrinkling load and half-wavelength can be calculated as a function of adhesive weight in the menisci. This curve, represented in Figure 5-8 correlated well with the experimental data, underestimating the value by 3.5% when no supplementary adhesive is used, and overestimating by 3% when 100 g/m$^2$ of adhesive film was used.

To use the models with preliminary deformation of the skin, the half-wavelength $l_0$ was chosen, as for the dimpling model, i.e. by considering the distance between two honeycomb cells rows, which is 2.77 mm. This length is close to the critical wrinkling wavelength calculated, so that the deformations and the stresses caused by initial waviness can be significant. However, the model was developed for a sinusoidal shape of the skin across the whole width of the beam, which is not the case with honeycomb, where the skin is maintained more or less flat on each honeycomb ribbon. This will then reduce sensitivity to waviness, and will be studied more in-depth in section 6.3. An arbitrary small waviness, $W_0 = 0.5$ µm, was used to calculate the critical loads for core compressive and shear stresses as well as local strains in the skin. Sensitivity to the changes in this arbitrarily fixed parameter was also studied. The numerical values used for these models are summarized in Table 5-2.

**Table 5-2: numerical data used in the models with initial deformations**

| $l$ [mm] | $W_0$ [µm] | $h$ [µm] | $D_{beam}$ [Nmm] |
|---|---|---|---|
| 2.77 | 0.5 | 40.5 | 279328 |

With this small initial deformation, the failure loads for all three models are very close to the wrinkling load calculated. It can be observed in Figure 5-8 that predicted loads for shear failure of the core, and local compressive skin failure are the highest for all adhesive weights. The predicted failure load for core compressive failure is smaller and very similar to the wrinkling load. The failure mode is thus a coupling between local skin instability and core crushing. This is confirmed by observation of the broken sample illustrated in Figure 5-7. If the initial imperfection is considered to be 10 times smaller, the curves for core shear failure and skin compressive failure are nearly unchanged, and the curve for core compressive failure merges with the two other curves. The three curves tend, in fact, towards the wrinkling failure corresponding to the half-wavelength $l_0$. If the initial waviness is considered to be 10 times larger, the predicted loads for core shear failure and skin compressive failure are decreased by 3% and the one for core compressive failure by 14%, thus confirms that this mode is the most sensitive to initial imperfections. This also shows that in the case of a smooth skin, the initial imperfection has to be assumed small enough in order to not under-evaluate the failure load. The choice of the size of initial imperfection is further discussed in section 6.3.

So when the skin under compression is very smooth, failure load can be predicted accurately either by the wrinkling model or by considering a small initial imperfection causing compressive failure of the core, always taking into account the stiffening effect of the adhesive menisci on the skins.

## 5.5. Influence of bonding defects on sandwich failure

In some panels with 0/90° skins, bonding defects were simulated by introducing small non-adhesive film bands between the smooth skin and the core. The defects were either 1.6, 2.5 or 5 mm long and extended across the complete width of the panel. They were placed in the middle zone of the beam, where the moment is maximum, and also in the zone between supporting point and loading point, where the shear force is present. Figure 5-10 shows the position of the defects during testing. In bending, 4 samples were tested for each panel with the smooth skin (with defects) under compression, and 3 with the smooth skin in tension.

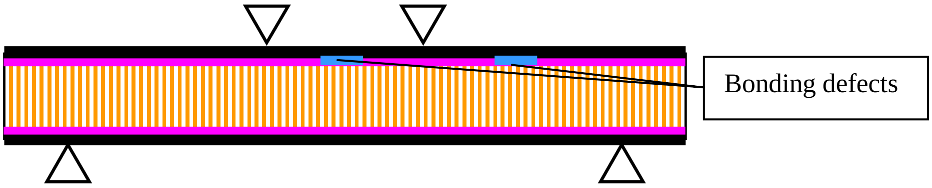

**Figure 5-10: sandwich beam in 4-point bending with the smooth skin with bonding defects under compression. The defects extended across the entire width of the beams**

All the samples broke in the skin under compression. The skin buckled over the defect between the two loading points and debonded from the core or delaminated between the plies as depicted in Figure 5-11. In the case of 1.6 mm long defects, the total delaminated length after buckling was 6, 8 and 10 mm with respectively 0, 21 and 50 g/m$^2$ adhesive. With 0 g/m$^2$ adhesive, the defect propagated at the core / skin interface, whereas it propagated between the plies when more adhesive was used. The defect could easily move from the core / skin interface to the plane between the plies because the fibers bonded onto the core were at 90° (i.e. parallel to crack front), so that the crack could propagate in the matrix between the fibers. With 100 g/m$^2$ adhesive, the failure was partly buckling and debonding, and partly wrinkling of the skin. With 2.5 mm defect and 100 g/m$^2$ adhesive, the skin buckled and delaminated between the plies so that the total debonded length was ~12 mm. In the case of the 5 mm defects, buckling of the skin occurred with little debonding so, when no supplementary adhesive was used, the total debonded length was about 6 mm.

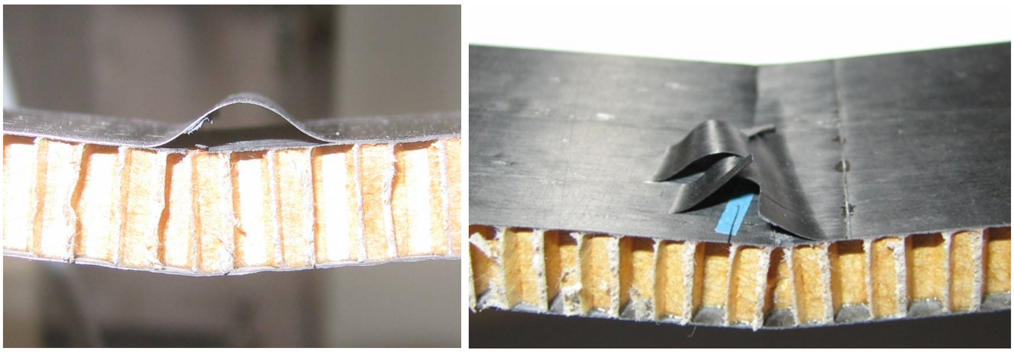

**Figure 5-11: failure of the skin with bonding defect under compression. With adhesive weight less than 100 g/m$^2$, the skin buckled over the bonding defect and delaminated between the plies (left). With 100 g/m$^2$ adhesive and a 1.6mm defect, the failure was partly buckling and delamination, and partly wrinkling (right)**

When the skin with defects was in tension the failure always occurred due to wrinkling of the skin under compression between the two loading points. The defect in the zone where shear stresses were present never caused any failure or debonding. Also the variation of adhesive weight on the face in tension did not change the failure load of the beam which is only controlled by the skin under compression.

Figure 5-12 shows the compressive load in the skin at failure as a function of adhesive weight and with different defect sizes, as well as the load measured without defects. The 5 mm long defects severely decreased the strength of the beam, and the load-carrying capacity was only 25% of that without defects, when no supplementary adhesive was used. With 1.6 mm defects, the strength was reduced to 70% of the one without defects, when no supplementary adhesive was used. By increasing the adhesive weight, the strength increased almost linearly, and the strength difference with the beams without defects was reduced. With 100 g/m$^2$ the strength of the beam with 1.6mm defects was close to the one without defects. This is in complete agreement with the observed failure mode, which was partly wrinkling, i.e. the same mode as in the sample without defects. With 100 g/m$^2$ adhesive, the 1.6 mm defects had thus almost no impact on strength. However, when the defect was 2.5 mm long, the strength was reduced to 70% of the strength without defects, thus showing a high sensitivity to defect size.

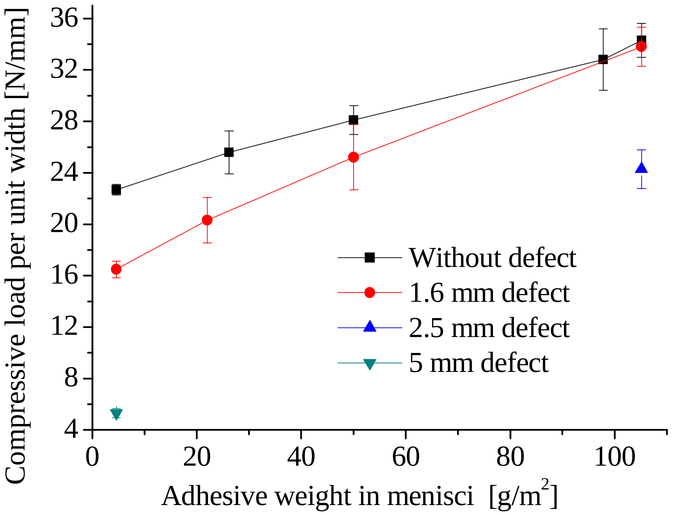

**Figure 5-12: Compressive load per unit width in the skin at failure as a function of adhesive weight and with various debonding size.**

During the compression tests on the samples, the same failure modes were observed as occurred in bending. This confirmed that the out-of-plane loads introduced during bending tests did not change the type of failure of the skin under compression. However, the strength measured could hardly be used as misalignment problems disturbed the measurements and the scattering was very high.

As already mentioned, the strength of the beam with 1.6 mm defects increased almost linearly as a function of adhesive weight up to 100 g/m$^2$. However, it was observed in section 4.2 that the debonding energy increased quickly up to 40 g/m$^2$ and then increased slowly. There is thus no direct relation between debonding energy and the strength of the beams with bonding defects. Furthermore, as the defects propagated between the plies when more than 21 g/m$^2$ adhesive was used, the core /skin debonding energy should not influence the failure load. Therefore, the increase of failure load of the beams with adhesive weight is not related to debonding energy but is controlled by other mechanisms. As for wrinkling, the skin bending stiffness was increased by the adhesive menisci, and the buckling load of the skin was increased. To confirm this hypothesis, a buckling model of the skin with debonding was developed.

A skin with localized debonding could consist of a beam laying on an elastic foundation loaded under compression, as represented in Figure 5-13. When the compressive load in the skin is sufficient, the skin buckles. High tensile stresses then appear at the core/skin interface at the edges of the defects, and the crack propagates either in the core/skin interface or between the plies of the skin, if the energy required is lower. Buckling may be reversible, but this represents the limit load for the sandwich beam. The buckling load is controlled by the size of the debonded zone, by stiffness of the core, and by the flexural stiffness of the skin in the debonded zone as well as in the bonded zone represented by the elastic foundation. Therefore, as the adhesive menisci may have a significant influence on the flexural stiffness of the skin, and thus on local instability, the failure load of beams with bonding defects increases with adhesive weight.

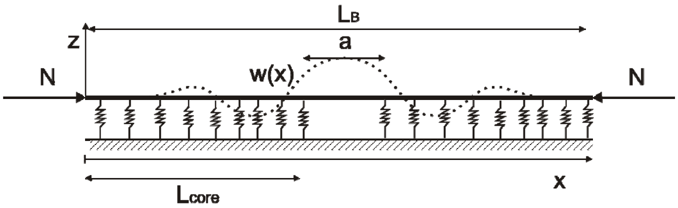

**Figure 5-13: schematic representation of the skin under compression lying on an elastic foundation and with a bonding defect of length a. A possible buckled shape is also represented.**

Hansen [107] solved the equations analytically for the buckling problem with an elastic foundation, as described in Figure 5-13. They are

$$w(x)=\begin{cases} w_1''''+k_3w_1''+k_2w_1=0 & \text{for elastic foundation}\\ w_2''''+k_3w_2''=0 & \text{for debonded zone}\end{cases} \qquad (5.13)$$

where *w(x)* is the deflection of the skin and $k_1$ and $k_2$ are given by

$$k_3 = \frac{N}{D_f} \text{ and } k_2 = \frac{k}{D_f} \tag{5.14}$$

where $D_f$ is the flexural rigidity of the skin and *k* the stiffness of the elastic foundation. The continuity of displacement, slope, transverse load, and moment between the two zones is obtained by setting equally $w_1$and $w_2$ and their three first derivatives at the beginning of the debonded zone. The solution provided by Hansen [107] for skin deflection was a complex number and thus had no physical meaning. In fact, the analytical solution separates into two distinct solutions at $k_3^2 = 4k_2$ depending on the ratio between core stiffness and skin bending stiffness, and the authors used the solution valid for ($k_3^2 < 4k_2$) in the domain ($k_3^2 > 4k_2$). An exact solution was therefore derived for the present case, and slightly modified in order to take into account the influence of adhesive weight.

As the problem is symmetrical, only half of the beam was considered. At $x = 0$, the beam was considered to be clamped, which is realistic if the length of the zone considered, $L_B$, is sufficiently large in comparison to the defect. The boundary conditions are thus

$$\begin{aligned} w(0) &= 0 \quad w'\left(\frac{L_B}{2}\right) = 0 \\ w'(0) &= 0 \quad w'''\left(\frac{L_B}{2}\right) = 0 \end{aligned} \tag{5.15}$$

The stiffness of the core *k* is given by

$$k = \frac{E_{cz}}{H_{def}} \tag{5.16}$$

where $E_{cz}$ is the Young’s modulus of the core. The compressive modulus measured for the honeycomb used was considered despite the fact that the foundation was mainly under tension because the tensile modulus was not known. However, it was noted in section 3.3.1 that tensile and compressive moduli were very similar for the honeycomb from Hexcel, which should also be the case for honeycomb from Euro-Composite. $H_{def}$ is the equivalent length of the linear spring representing the foundation so that the stiffness of the core is the same as the elastic foundation. If the shear stresses in the core are disregarded, then $H_{def}$ is equal to the thickness of the core $t_c$, the normal stresses being constant throughout the thickness of the core. If the shear stresses are taken into account, the core is stiffer and $H_{def} < t_c$. This equivalent length is dependent on the core shear modulus, and on the deformed shape of the face. As a first approximation, one can consider the equivalent length $H$ calculated by Yusuff [37] (see section 2.1.5) for symmetrical wrinkling with a thick core

$$H = 1.651\left[\frac{D_f E_{cz}}{G_{core}^2}\right]^{1/3} \tag{5.17}$$

However, the development of this equation did not include the anti-plane stress hypothesis in the core and is thus not exact for the honeycomb core. Moreover, the shape of the face was assumed to be sinusoidal with the wavelength corresponding to the critical wavelength for wrinkling. This equation therefore gives only an approximation of the real foundation depth in this case.

The bending stiffness of the skin can be significantly increased with adhesive menisci due to their geometry. In the beams with defects, two distinct stiffnesses have to be considered, one for the bonded and another for the unbonded zone. For the bonded zone, the measurements of skin bending stiffness with adhesive fillets were used. For the unbonded zone, two different cases were considered depending on the bonding method used. If the adhesive deposition method was used, the adhesive was laid on the core and the thin non-adhesive film creating the defect was situated between the adhesive and the skin, so that the stiffness of the skin in the unbonded zone was not affected by the adhesive weight. If adhesive films were laid on the faces, the non-adhesive film was placed between the adhesive film and the core, so that the skin was locally reinforced by an even adhesive layer. In this case, the bending stiffness of the skin was calculated with an even adhesive layer, using CLT.

With these adaptations, equation (5.13) becomes

$$w(x) = \begin{cases} w_1'''' + k_3 w_1'' + k_2 w_1 = 0 & \text{for } 0 < x < L_{core} \\ w_2'''' + k_{3b} w_2'' = 0 & \text{for } L_{core} < x < \dfrac{L_B}{2} \end{cases} \tag{5.18}$$

with

$$k_3 = \frac{N}{D_{f1}} \qquad k_2 = \frac{k}{D_{f1}} \qquad k_{3b} = \frac{N}{D_{f2}} \tag{5.19}$$

where $D_{f1}$ is the bending stiffness of the skin in the elastic foundation as a function of adhesive weight, and $D_{f2}$ is the bending stiffness of the skin in the debonded zone. The continuity of displacement, slope, transverse load, and moment between the two zones is obtained by setting

$$\begin{aligned} w_1\left(L_{core}\right) &= w_2\left(L_{core}\right) & D_{f1}w_1''\left(L_{core}\right) &= D_{f2}w_2''\left(L_{core}\right) \\ w_1'\left(L_{core}\right) &= w_2'\left(L_{core}\right) & D_{f1}w_1'''\left(L_{core}\right) &= D_{f2}w_2'''\left(L_{core}\right) \end{aligned} \tag{5.20}$$

Using the Laplace Transform, the first part of equation (5.18) becomes

$$W_1(s) = \frac{sw''(0) + w'''(0)}{k_2 + k_1 s^2 + s^4} \tag{5.21}$$

where s is the variable in the Laplace domain. The inverse Laplace Transform gives

$$\begin{aligned} w_1(x) = \frac{1}{\sqrt{\mathrm{k}_3^2 - 4k_2}} \Bigg[ & w''(0)\left( Cosh\left[\frac{\sqrt{-k_3 + \sqrt{\mathrm{k}_3^2 - 4k_2}}}{\sqrt{2}}\right] - Cosh\left[\frac{\sqrt{-k_3 - \sqrt{\mathrm{k}_3^2 - 4k_2}}}{\sqrt{2}}\right]\right) + \\ & \sqrt{2}w'''(0)\left( \frac{Sinh\left[\frac{\sqrt{-k_3 + \sqrt{\mathrm{k}_3^2 - 4k_2}}}{\sqrt{2}}\right]}{\sqrt{-k_3 + \sqrt{\mathrm{k}_3^2 - 4k_2}}} - \frac{Sinh\left[\frac{\sqrt{-k_3 - \sqrt{\mathrm{k}_3^2 - 4k_2}}}{\sqrt{2}}\right]}{\sqrt{-k_3 - \sqrt{\mathrm{k}_3^2 - 4k_2}}} \right)\Bigg] \end{aligned} \tag{5.22}$$

If $k_3^2 < 4k_2$, it can be simplified as

$$\begin{aligned} w_1(x) = \frac{1}{\sqrt{-\mathrm{k}_3^2 + 4k_2}} \Big[ & 2w_1''(0)\,Sinh[\zeta x]Sin[\omega x] + \\ & \frac{w_1'''(0)}{\zeta^2 + \omega^2}\left(2\zeta Cosh[\zeta x]Sin[\omega x] - 2\omega Sinh[\zeta x]Cos[\omega x]\right)\Big] \end{aligned} \tag{5.23}$$

with

$$\psi = \pi + ArcTan\left[\frac{-\sqrt{-k_3^2 + 4k_2}}{-k_3}\right] \quad \omega = \sqrt[4]{k_2}\,Sin\left[\frac{\psi}{2}\right] \quad \zeta = \sqrt[4]{k_2}\,Cos\left[\frac{\psi}{2}\right] \tag{5.24}$$

where *ArcTan* gives values between -π/2 and π/2. As illustrated later, this function corresponds well to the expected shape represented in Figure 5-13.

If $k_3^2 < 4k_2$, the solution becomes

$$\begin{aligned} w_1(x) = \frac{1}{\sqrt{\mathrm{k}_3^2 - 4k_2}} \Bigg[ & w_1''(0)\left( Cos\left[\frac{\sqrt{k_3 - \sqrt{\mathrm{k}_3^2 - 4k_2}}}{\sqrt{2}}\right] - Cos\left[\frac{\sqrt{k_3 + \sqrt{\mathrm{k}_3^2 - 4k_2}}}{\sqrt{2}}\right]\right) + \\ & \sqrt{2}w_1'''(0)\left( \frac{Sin\left[\frac{\sqrt{k_3 - \sqrt{\mathrm{k}_3^2 - 4k_2}}}{\sqrt{2}}\right]}{\sqrt{k_3 - \sqrt{\mathrm{k}_3^2 - 4k_2}}} - \frac{Sin\left[\frac{\sqrt{k_3 + \sqrt{\mathrm{k}_3^2 - 4k_2}}}{\sqrt{2}}\right]}{\sqrt{k_3 + \sqrt{\mathrm{k}_3^2 - 4k_2}}} \right)\Bigg] \end{aligned} \tag{5.25}$$

This solution is sinusoidal and periodic, meaning that the skin has the same deformation far from the defect as near the defect, but this does not correspond to observations made during the test.

The solution for the debonded zone is

$$w_2(x) = c_3 + c_4\left(Cos\left[\sqrt{k_{3b}}\,x\right]Cot\left[\frac{\sqrt{k_{3b}}L_B}{2}\right] - Sin\left[\sqrt{k_{3b}}\,x\right]\right) \tag{5.26}$$

where $c_3$ and $c_4$ are integration constants. To determine $c_3$ and $c_4$, and the integration constants $w_1''(0)$ and $w_1'''(0)$ in equation (5.23), the boundary conditions given in equations (5.20) are used. A system of four homogenous equations with four variables is obtained and a solution different from zero is obtained only if the determinant of the system is zero. The lowest positive value of $N$, setting the determinant to zero, thus corresponds to the buckling load. Once $N$ is determined, the corresponding deformation mode of the skin $w(x)$ can be calculated by solving a set of three of the 4 equations with 4 variables.

To calculate the depth of the elastic foundation, the minimum value of the shear modulus in ribbon direction in Table 3-2, and the skin bending stiffness calculated with CLT $D_f = 5.84$ Nmm$^2$, were used, giving $H_{\mathrm{def}} = 1.4$ mm. Provided that there is no supplementary adhesive on the skin, and the total length of the elastic foundation and defect $L_B = 20$ mm, the buckling load with 1.6 mm defects is $N = 17.2$ N/mm, whereas the experimental load was 16.5 N/mm. This means that the model, coupled with the foundation depth predicted by Yusuff’s model, gives a good approximation for the buckling load. However, it should be remembered that this foundation depth was calculated without taking into account the anti-plane stress state in the core, and the wavelength considered was the wrinkling wavelength, which differs from the wavelength with bonding defects. Therefore, this foundation depth should only be used as an approximate guideline for selecting the depth in the present case. A more complex model, corresponding more accurately to the present case, has to be developed to calculate the real foundation depth. As for the wrinkling model, the hypothesis of continuous support of the core at the wavelength of the defect is questionable for defects smaller than the cell size. But as explained for wrinkling, since the support of a line perpendicular to the beam length is almost constant on beam length, and as buckling occurs on a line perpendicular to the beam length, this hypothesis can be considered to be realistic.

Figure 5-14 shows the deformed shape of the skin at maximum deflection in the center of the debond, and deflection vanishing quickly with distance from the debond. The use of a greater value for $L_B$ in the model resulted in the same buckling load and deformed shape. An increase in defect size significantly decreased the buckling load. The predicted load with 5 mm debond was 4.9 N/mm, while the measured load was 4.65 N/mm. Oscillations of the skin near the defect were smaller when the debond was larger, and the buckled shape became closer to the cantilever beam. Thus, when debond size increased, the buckling load predicted by the model was close to the buckling load predicted by Euler's model for a cantilever beam given as

$$N_{Euler} = \frac{\pi^2 D_{f2}}{(a/2)^2} \tag{5.27}$$

The buckling load for both models is represented in Figure 5-15 and confirms the similar predictions of both models with large debonds, while the Euler model diverges with small debonds. When debond size decreases, the elastic foundation model tends toward the critical value for $k_3^2 = 4k_2$, i.e. N = 28.5 N/mm. Above this value, the deformed shape becomes sinusoidal and the model becomes a wrinkling model. However, as the wrinkling load measured without defects was 22.3 N/mm, wrinkling will occur prior to buckling on the debond with defects smaller than ~1 mm.

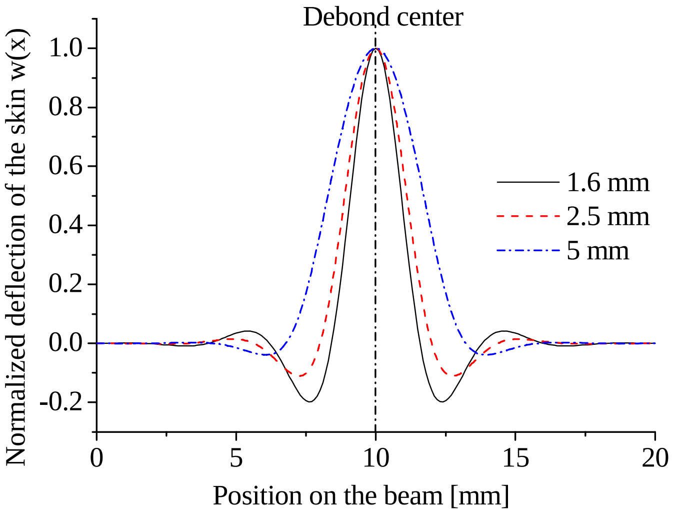

**Figure 5-14: deformed shape of the skin when buckling occurs with different debond sizes.**

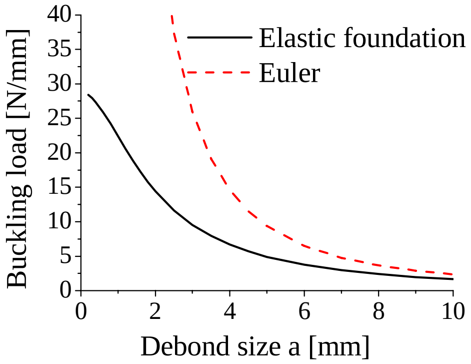

**Figure 5-15: buckling load per unit width in the skin as a function of debond size predicted by the elastic foundation, model when no supplementary adhesive is used, or by the Euler model.**

Figure 5-16 shows the buckling load predicted by the model as a function of adhesive weight. The two different cases, corresponding to the two possible choices for the bending stiffness of the skin over the debond $D_{f2}$, are represented. When adhesive films were used (50 and 100 g/m$^2$), an even adhesive layer reinforced the debonded part of the skin (case “a”), while when the adhesive deposition method was used (25 g/m$^2$), no adhesive was on the skin over the debond, and its stiffness was unchanged (case “b”). Therefore, the buckling load increased faster in case “a”. However, the increase in the model is less pronounced than the actual measurements, and the model significantly underestimates the buckling load with large adhesive quantities. This means that the skin stiffening effect of the adhesive was not the only phenomenon that could explain the increase of buckling load. Actually, the model considers the skin with menisci as a skin of unchanged thickness, with increased bending stiffness, and lying on an unchanged elastic foundation. Due to the small size of the debond and the short wavelength of the solution, then disregarding the adhesive fillet size with 100 g/m$^2$ adhesive (~0.5 mm) may lead to an underestimation of elastic foundation stiffness and consequently buckling load. A more complex model, taking into account the real shape of the menisci, should be used to evaluate the effect of menisci on elastic foundation, and the effect on the depth of the foundation $H_{def}$.

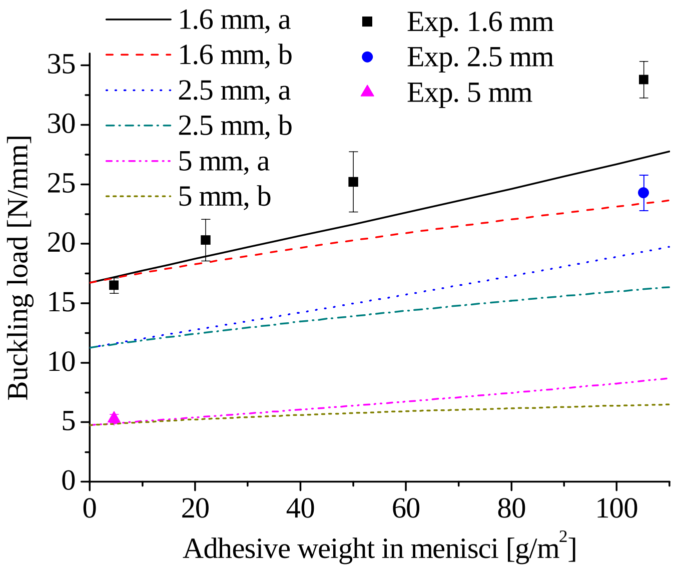

**Figure 5-16: experimental and theoretical buckling load per unit width in the skin with various debond lengths as a function of adhesive weight in the menisci. The case “a” of the model corresponds to a skin reinforced by an even adhesive layer over the debond, case “b” to unchanged skin properties over the debond.**

The increase in buckling load with adhesive weight was less pronounced with large defects. This is explained by the larger skin oscillations and stresses in the foundation with small debonds, whereas with large debonds (see Figure 5-14) skin deformations tend towards the cantilever beam deformations. This means that the reduced failure load with small debonds can be improved by adding adhesive, while this has very little effect with large debonds.

## 5.6. Optimization of the strength to weight ratio in symmetric sandwiches

The results of the 4-point bending tests have shown the high influence of the type of skins and adhesive weight on the failure mechanisms and load. The use of only one layer of prepreg at 0° results in a structure presenting dimpling at a low load, due to the very thin skin and low stiffness of the skin in width direction. This instability does not allow full advantage to be taken of the intrinsic strength of the core and skin. With the 0/90° skin, the load is mainly in the 0° ply, so that this configuration is not optimal for the bending loading case. But as a sandwich panel is often loaded in various directions in different applications, this lay-up is more realistic. Therefore, the present optimization of the sandwich structure concentrates on this lay-up.

It was shown in the precedent section that bending strength increased with adhesive weight used for core-to-skin bonding, but the adhesive weight providing the best strength-to-weight ratio has still to be identified. Furthermore, an increase in the load-carrying capacity of the sandwich due to supplementary adhesive needs to be compared to the increased load-carrying capacity by increasing skin thickness or core thickness. Three different cases were considered for the sandwich beams:

1. carbon skin = 0.14 mm thick, 8 mm thick honeycomb, adhesive 0-100 $g/m^2$
2. carbon skin = 0.14-0.22 mm thick, 8 mm thick honeycomb, 0 $g/m^2$ adhesive
3. carbon skin = 0.14 mm thick, 8-16 mm thick honeycomb, 0 $g/m^2$ adhesive

Based on the compressive load per unit width at failure $N_{max}$, calculated with the models already developed, the critical bending moment per unit width is

$$M_{\max} = dN_{\max} \tag{5.28}$$

where $d$ is the distance between the centers of the two faces. The total weight of the beam was calculated by considering two identical faces. However, it should be noted that, in the case of bending in one direction only, unsymmetrical faces would be advantageous. In fact, as all the failures observed in this work occurred in the face under compression, reinforcement of this face only is recommended in terms of strength-to-weight ratio.

Figure 5-17 illustrates changes in the bending stiffness of the skin by varying either the adhesive weight or carbon weight as a function of the total weight of carbon and adhesive. Changes in bending stiffness with an even adhesive layer, and with varying carbon thickness, was calculated with CLT. The reinforcing effect of adhesive menisci on the skin was similar to that obtained by increasing carbon thickness up to ~40 $g/m^2$ supplementary weight. Above this weight, the increase of bending stiffness by increasing skin thickness was more pronounced, and thus the strength of the beam is higher if the failure mode stays the same.

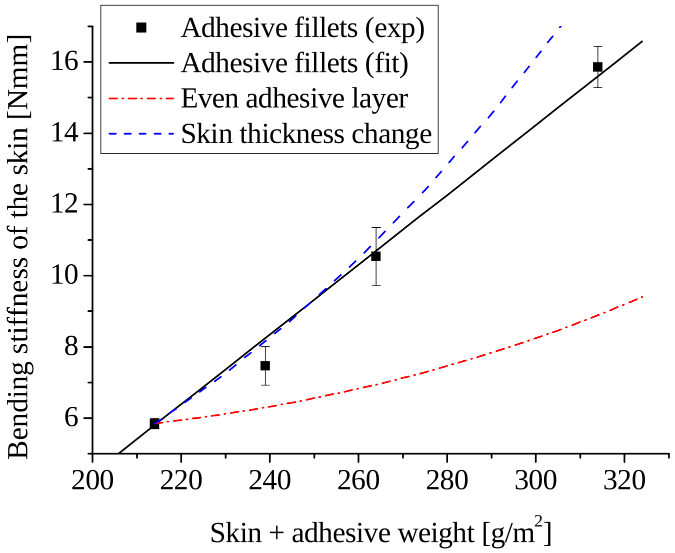

**Figure 5-17: changes in skin bending stiffness with: (Adhesive fillets) variation in adhesive fillet size and constant carbon thickness; (Even adhesive layer) variation of the thickness of even adhesive layer and constant carbon thickness; (Skin thickness) no adhesive and variation of carbon thickness.**

To calculate the moment causing failure of the sandwich beams without debonds, the wrinkling model for a smooth face described in section 5.2 was used. The other failure models for core compression, core shear, or local skin compression, with small preliminary waviness of the skin resulted in exactly the same tendencies and are therefore not represented here. Skin stiffness as a function of adhesive fillet size or carbon thickness, as represented in Figure 5-17, was used in the model to calculate the change of wrinkling load as a function of these two parameters. The change of core thickness was also inserted into the wrinkling model by varying the distance *d* between the faces. Increased elastic foundation thickness induced a decreased wrinkling load. However, the increased distance *d* between the faces increased the failure moment. Figure 5-18 shows changes in the failure moment for various adhesive weights and carbon and core thicknesses. The highest reinforcing effect was obtained by increasing the thickness of the carbon skin. The reinforcement obtained by increasing adhesive quantity was similar up to ~40 g/m$^2$ supplementary weight per face, but was smaller at higher weights. The reinforcing effect obtained by increasing core thickness was lower and thus not interesting in this case. The ratio between failure moment and total weight of the beam increased by increasing all three parameters considered. This means that the increase of the failure moment was higher than the increase in weight. The increase of honeycomb thickness induced only a small increase of the ratio, and the maximum was reached when the core thickness was ~16mm (890 g/m$^2$). It was therefore preferable to increase either adhesive weight or carbon thickness, which caused a more pronounced increase of the ratio. Of course, these predictions were only valid if the failure mode stayed the same, i.e. wrinkling of the skin. This was certainly the case when the parameters were slightly changed, but may differ when the change is more significant. For example, significantly increasing the skin thickness without adding supplementary adhesive for skin-to-core bonding may lead to skin debonding. All the failure modes have thus to be considered in order to verify the validity of parameters choices.

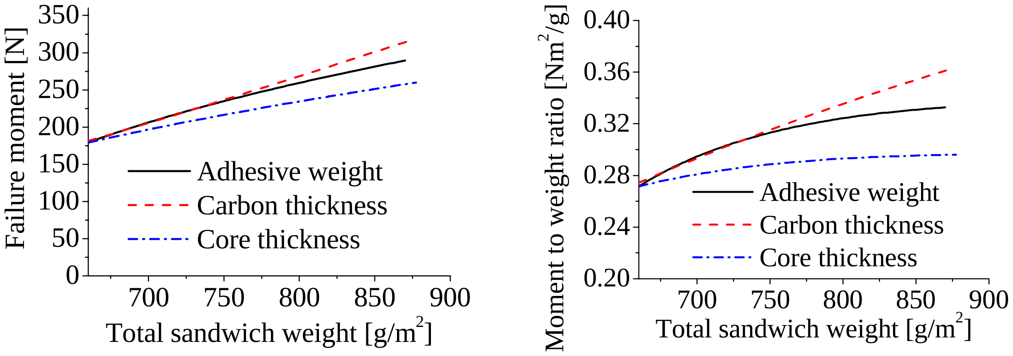

**Figure 5-18: moment per unit width causing wrinkling of the face under compression as a function of total sandwich weight, by varying either adhesive quantity, carbon thickness, or core thickness. The ratio between failure moment and total weight is represented on the right.**

The moment-to-weight ratio increased by increasing the adhesive weight between 0 to 100 g/m$^2$, the optimal adhesive weight giving maximum strength-to-weight ratio being in fact 160 g/m$^2$ of adhesive on each face. However, above ~40 g/m$^2$ supplementary weight by face, the increase in carbon thickness caused a more pronounced increase of the ratio and was therefore advantageous. This means that 40 g/m$^2$ adhesive on each face is the most pertinent choice for the bending or compressive loading case, since a lower adhesive weight provides a lower strength-to-weight ratio, and a higher adhesive weight provides less reinforcement than by increasing carbon skin thickness. Furthermore, adding 40 g/m$^2$ of adhesive provides, on one hand, the same reinforcing effect as adding 40 g/m$^2$ of carbon prepregs, and, on the other hand, also improves the core-to-skin bonding, since 35-40 g/m$^2$ of adhesive provided the best debonding energy-to-weight ratio, as shown in section 4.2. It is thus preferable to add 40 g/m$^2$ of adhesive rather than 40 g/m$^2$ of carbon prepreg. However, this is only valid for a structure design based on strength. If bending stiffness of the beam is considered, the tensile and compressive stiffness of the skin have to be considered and the conclusions would be different.

For the beams with debonds, the model developed was used despite the fact that it underestimated the reinforcing effect of the adhesive. Calculation of the buckling load as a function of adhesive weight was made assuming an even adhesive layer on the face over the debond. The buckling load for various carbon thicknesses was calculated by inserting the stiffness of the skin as a function of carbon thickness in the elastic foundation model, both for $D_{f1}$ and $D_{f2}$. For the various honeycomb core thicknesses, the change of failure moment was due to the change of distance between the faces, with the buckling load in the skin being considered as constant. This hypothesis may however lead to inaccurate prediction, because the core thickness will affect the elastic foundation which is actually constant in the model.

Figure 5-19 shows changes in the failure moment of a beam with a 1.6 mm debond, as a function of the total weight of the sandwich structure, by varying the three parameters mentioned above. The reinforcing effect was most pronounced by increasing carbon thickness. This case had the advantage that the skin stiffening effect was the same over the whole beam, while the skin stiffening due to adhesive menisci was only present on the bonded area, and not over the debond. In terms of moment-to-weight ratio, the increase of carbon thickness was also most effective. The optimal weight providing maximal ratio was higher than 100 g/m$^2$ supplementary weight for all cases. However, as the prediction model is not accurate, the tendencies shown by the curves should be considered rather than the quantitative values. The main conclusion is that the best way to avoid skin buckling and debonding over a preliminary debond is to increase carbon thickness in the skin instead of adding adhesive.

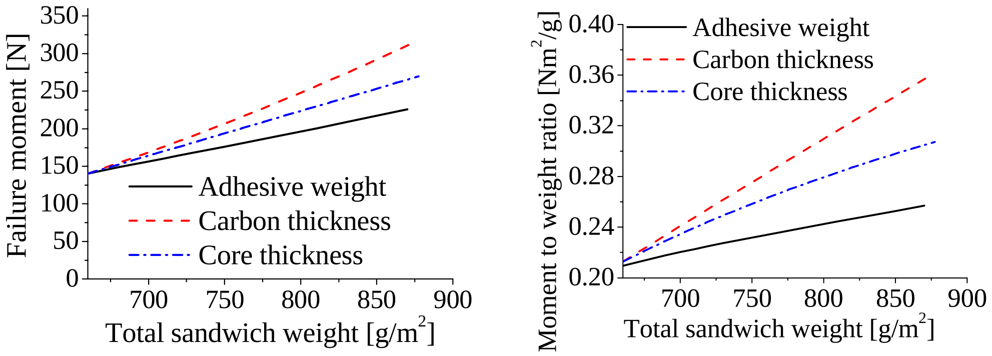

**Figure 5-19: moment causing buckling of the face under compression with 1.6 mm debond as a function of total sandwich weight, by varying either adhesive quantity, carbon thickness, or core thickness. The ratio between buckling moment and total weight is represented on the right.**

## 5.7. Conclusions

- Ultralight sandwich structures with thin skins broke under bending due to local instability of the skin under compression. Local instability was either dimpling with skins with only one 0.07 mm thick UD prepreg layer, wrinkling of the skin in the core with two prepreg layers at 0 and 90°, or buckling and delamination of the skin when preliminary debonds were present.

- The strength of sandwich structures with 0/90° fibers in the skin was twice as high as in those without 90° fibers. This showed the important stabilizing effect of the 90° layer on thin skins.

- Bonding defects induced a significant strength reduction (75 % reduction with 5 mm defect); great care is thus necessary to avoid defects during processing.

- An increased adhesive quantity for core-to-skin bonding increased the strength of the beam. However, the strength increase was not due to the better core-to-skin bonding, but rather to the stabilizing effect of the adhesive menisci on the skin. The models taking into account the stabilizing effect of the adhesive menisci on the skin gave a good prediction of the instability load and confirmed the observed strength increase with adhesive weight.

- With the models developed, for beams with 0/90° skins, it was calculated that ~40 g/m$^2$ adhesive per skin can be considered as the optimal choice to optimize the strength-to-weight ratio in bending of this particular sandwich structure.

# CHAPTER 6. PROCESS OPTIMIZATION OF ULTRALIGHT SANDWICH STRUCTURES

As explained in section 2.1.9, the optimal choice in terms of process pressure, temperature, temperature ramp, consumables used, or number of curing steps is difficult to find and optimal processing is often a compromise between several solutions. The present chapter concentrated essentially on the relation between microstructure, strength and process pressure, defined as the pressure exerted on the panel, i.e. the difference between pressures outside the vacuum bag and in the vacuum bag. It should be high enough to ensure good bonding and skin compaction, but must be adjusted to avoid pronounced skin waviness and core damage.

Preliminary experiments were realized in order to identify suitable consumables and to investigate the changes in actual pressure in honeycomb cells during curing.

## 6.1. Influence of the consumables on sandwich failure

In a first step, the influence of the consumables used was studied in order to define the option giving the highest quality and ensuring reproducibility of the results.

The skin and core materials were identical as in chapter Chapter 5. Skins comprising two prepreg layers at 0 and 90° and 50 g/m$^2$ of adhesive films were used on both faces. Two different methods were used in processing the structure. The first one was similar to the one described in Figure 5-1, but replacing the non-perforated film by a peel-ply (A100 PS from Aerovac) and a perforated film, thus allowing air circulation through the skin, and better vacuum formation in the honeycomb cells. The second process was identical to the one described in Figure 5-1. The panels were cut into samples of 30 mm width and 450mm length and tested in 4-point bending. The inner and outer span were respectively 100 and 400 mm.

In both processing options, the skin on the vacuum bag side had a wavy aspect due to the vacuum pressure applied. During curing, the peel-ply absorbed a lot of resin, and some resin flowed through the perforated film into the breather cloth. By weighing the peel-ply before and after processing, it was calculated that 27 g/m$^2$ of resin flowed into the peel-ply. As the two prepreg layers contained 74 g/m$^2$ adhesive, 36% of the resin was removed from the skin on the vacuum bag side during processing.

During the 4-point bending tests, the skin under compression broke between the loading points due to wrinkling. The compressive strength of the skin cured with peel-ply was reduced by 15%. Stresses at failure in the 0° ply of the skin for the two sides of the panels are represented in Figure 6-1. The use of peel-ply with such thin skins should therefore be avoided in order to have good skin quality. Other methods could be used to allow air circulation through the skin without sucking out too much resin. Pre-impregnated peel-ply could be used, but an accurate choice of the resin amount in the peel-ply would have to be made so that resin was neither sucked out of the prepreg nor added to the skin. Alternatively, a perforated film could be placed directly on the prepreg under the peel-ply and breather cloth, so that air could be evacuated from the core by sucking resin out of the prepreg only locally at the perforations. The size and spacing of the perforations would have to be optimized to allow good air circulation through the skin without reducing skin properties. These solutions were, however, not further investigated here.

The presence of peel-ply on the vacuum bag side did not, however, influence the strength when the smooth side (cured on an Al plate) was loaded under compression. When comparing the compressive strength of the skin cured on the vacuum bag side without peel ply to the strength of the skin on the smooth side, a strength reduction of 7% was observed, due to the waviness of the skin. This effect is studied in more details in section 6.3.

Finally, as the strength was higher when using non-perforated film without peel-plies, this solution was chosen for a study of sandwich strength, by varying other parameters. It has the additional advantage of sucking no resin out of the prepreg, thus ensuring thus good reproducibility.

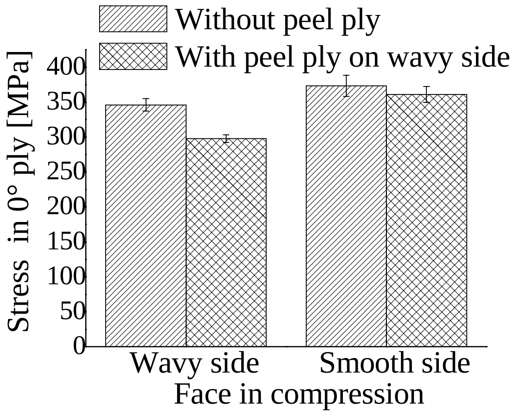

**Figure 6-1: Stress at failure in the 0° ply of the skin in a 4-point bending test. The wavy skin was cured with and without peel-ply on the surface, while the corresponding smooth face was cured on the Al plate in both cases.**

## 6.2. Permeation measurement of the skin and consumables

During vacuum bag processing, the pressure under the vacuum bag is measured by a pressure sensor and controlled by the vacuum pump. However, if the sandwich is cured with both skins at once, the honeycomb cells are closed and the pressure in the honeycomb is unknown, and can neither be measured nor controlled. In fact, the absolute pressure in the cells can be significantly higher than that under the vacuum bag. Using various consumables, the changes in pressure were thus measured by applying vacuum through the prepreg skin, in order to correlate the pressure measured in the vacuum bag during processing to the pressure in honeycomb cells, thereby ascertaining the real pressure in the honeycomb cells and the effective pressure applied on the skin, i.e. the difference between the atmospheric pressure and internal pressure in the cells.

### 6.2.1. Materials and methods

The set-up described in section 3.2.7 was used in order to measure the permeability of the skin and consumables. During this entire thesis project, the sandwich panels were mainly processed with a non-perforated film on the surface of the prepreg to avoid resin flowing out of the prepreg, as observed in the previous section. To allow circulation of the air under the non-perforated film, dry fiber rovings were placed on the side of the panel under the film, as described previously in Figure 5-1. The first pressure measurement was thus made with the following lay-up:

- Honeycomb 29 kg/m$^3$
- Adhesive film VTA 260 50 g/m$^2$
- UD prepreg 70 g/m$^2$, 0 and 90°
- Non-perforated non-adhesive film, with fiber tows to drain air on the sides
- Breather cloth
- Plastic grid for better air circulation
- Vacuum bag

In a second step, pressure changes were measured with a peel-ply and perforated film allowing air circulation through the skin. The following lay-up was used:

- Honeycomb 29 kg/m$^3$
- Adhesive film VTA 260 50 g/m$^2$
- UD prepreg 70 g/m$^2$, 0 and 90°
- Peel-ply
- Perforated film
- Breather cloth
- Plastic grid for better air circulation
- Vacuum bag

This solution ensured a better vacuum in the honeycomb, but some resin from the prepreg flowed into the peel-ply, and this decreased the strength of the skin (see section 6.1). In order to avoid the resin flow, a test was made by using a semi-permeable membrane to pump air without resin. The following lay-up was used:

- Honeycomb 29 kg/m$^3$
- Adhesive film VTA 260 50 g/m$^2$
- UD prepreg 70 g/m$^2$, 0 and 90°
- Semi-permeable membrane

- Perforated film
- Breather cloth
- Plastic grid for better air circulation
- Vacuum bag

### 6.2.2. Results

Figure 6-2 and Figure 6-3 show changes in pressure in the honeycomb and the temperature during curing cycle. In the case of non-perforated film, vacuum was applied during 60h before the curing cycle at 120°C began. The absolute pressure under the vacuum bag was ~0.02 mbar. The pressure in the honeycomb cell decreased only slowly, showing that air circulation between the honeycomb cell and the space under the vacuum bag was low. After 12 hours of applied vacuum, the pressure in the honeycomb was still at 350 mbar, decreasing to 230 mbar after 60h. In addition, during curing, pressure in the cells increased to 0.4 bar due to arise in temperature causing air dilatation and resin degassing. After curing, the vacuum in the honeycomb cells was released voluntary using the valve, and then applied again, but the pressure in the honeycomb decreased very slowly, which means that the lay-up was almost air-tight.

These results indicate that the pressure measured under the vacuum bag during processing of the panels does not match the pressure in the honeycomb cells, even after long vacuum application. Furthermore, the pressure in the honeycomb during sandwich panel processing cannot be predicted by using the present set-up, because the air is drained from the sides through the tows, and the surface to drain is much larger in the real panels fabricated. Also, air could circulate between the cells on the tool side in the permeation set-up, which is not the case when the panels were fabricated with both skins in one shot. A small air path through the skin in the permeation set-up would allow pressure to be decreased in all the cells, whereas it would only affect a few cells in a sandwich panel closed by both skins. The vacuum in the cells in the centre of a large sandwich panel will therefore never be better than that measured using the present set-up and the relative pressure exerted on the skin at 120°C will be, at a maximum, 0.6 bar if full vacuum is applied under the vacuum bag.

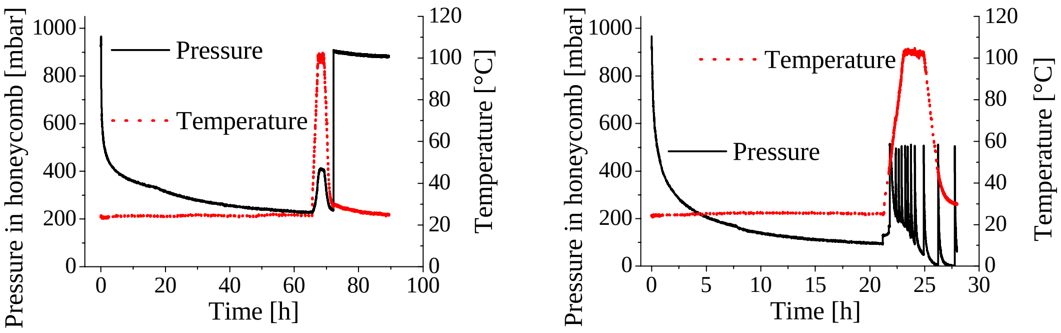

**Figure 6-2: changes in pressure in the honeycomb with an absolute pressure of 0.02 mbar under the vacuum bag. For the panel with non-perforated film (left), the curing cycle began after 64 h. The vacuum was released in honeycomb cells after curing, and then applied again. For the panel with peel-ply and perforated film (right), the curing cycle began after 20 h. The vacuum was partially released in honeycomb cells during curing, and then applied again (pressure peaks on the graph) in order to observe changes in permeability.**

When a perforated film and peel-ply was used, the pressure in the cells decreased rapidly and stabilized around 100 mbar. During curing, the vacuum was partially released and then applied again in order to observe changes in permeability. The pressure decreased rapidly each time showing good air circulation during and after curing. The use of peel-ply and perforated film ensured good pressure control in the honeycomb cells, but a large amount of the prepreg resin (up to 40%) flowed into the peel-ply and bleeder, and this decreased the mechanical properties of the skin.

The use of a semi-permeable membrane to avoid resin flowing out of the prepreg did not improve the control of the vacuum in the honeycomb cells. After 16h applied vacuum, the pressure was still at 300 mbar (Figure 6-3). When the vacuum was released and applied again during curing, the pressure did not decrease, but, on the contrary, increased due to temperature rise. The pressure only decreased during cooling. After curing, vacuum was released and applied again, but the pressure did not decrease, showing that the membrane became completely air tight, probably due to the presence of resin which filled the microscopic porosities.

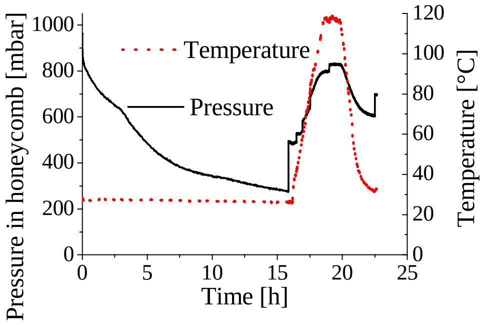

**Figure 6-3: changes in pressure in the honeycomb with a pressure of 0.02 mbar under the vacuum bag for the panel with a semi-permeable membrane. The curing cycle began after 16 h. The vacuum was partially released in honeycomb cells during curing (shown by the vertical segment in the pressure curve) and then applied again in order to observe the permeability.**

These different tests showed that there is no easy solution to the problem of controlling pressure in the honeycomb cells without taking out some prepreg resin in one-shot vacuum curing. On one hand, with non-perforated film, no prepreg resin is lost, but the pressure in the cell is not well controlled. On the other hand the use of peel-ply ensures better control of the pressure, but takes lot of resin out of the prepreg. A potential solution is to use perforated honeycomb (however, not available with Nomex®), but with the potential problem of humidity uptake in the honeycomb during use, unless the panel sides are sealed after processing.

## 6.3. Influence of pressure on skin waviness and fillet size

Sandwich structures with thin skins usually break due to failure of the skin under compression. As observed previously (sections Chapter 5 and 6.1), the wrinkling phenomenon, i.e. local buckling of the skin into the core (represented in Figure 6-4) is often the dominant failure mode. Sensitivity to this particular mode is increased by local defects of the skin. In particular, skin waviness, resulting from one-shot curing under vacuum also known as telegraphic effect [16] as illustrated in Figure 6-4, reduces the compression strength of the skin. Therefore, the relation between skin waviness and its strength was investigated. As applied pressure was responsible for the waviness, the relation between pressure applied during processing, waviness, and strength was investigated.

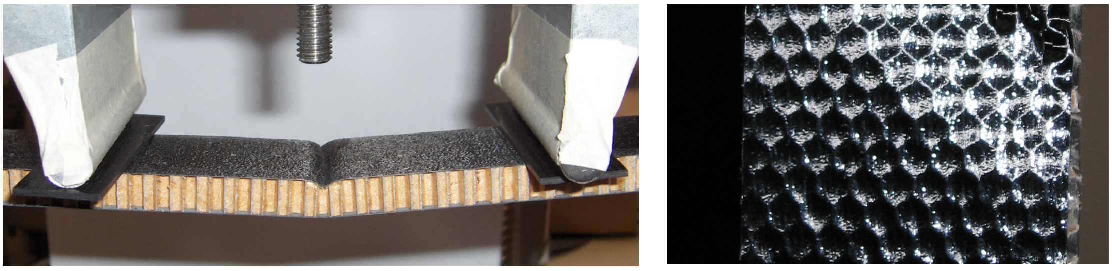

**Figure 6-4: (Left) wrinkling phenomenon in 4-point bending tests. (Right) skin waviness due to one-shot vacuum bag curing.**

To measure the effect of skin waviness, beams with one smooth face and one wavy face were fabricated. Three different kinds of samples were fabricated. In all cases, the skins were made of 70 g/m$^2$ of carbon prepreg, and the core was Nomex® honeycomb from Euro-Composite. For the first type of sample the adhesive used to bond the skin to the core was a 150 g/m$^2$ Redux 382H adhesive film from Hexcel, while the other samples were produced with 50 g/m$^2$ VTA 260 adhesive film.

The first samples were designed to create maximum waviness in order to observe clearly its effect. To this end, the skin comprised a single layer of UD prepreg and a thick adhesive layer in order to favor fiber sliding, a prerequisite for wave formation. To ensure a well pronounced and regular waviness of the skin, without using the autoclave technique, it was necessary to ensure a good vacuum in the honeycomb cells. Therefore, the panels were fabricated in two steps. The wavy skin was fabricated first. The honeycomb was laid onto a plate with a breather cloth in-between channeling the air under the honeycomb. The adhesive film and carbon prepreg were then laid onto the honeycomb. A non-perforated film was laid directly onto the carbon to avoid leakage of resin, and to allow the resin percentage in the skin to be controlled, and finally the vacuum bag was placed in position. The panel was cured with a relative vacuum pressure of -0.9 bar. Another panel was fabricated with only a -0.1 bar vacuum (for curing both the first and second skin) in order to observe the effect of reduced vacuum pressure.

For the second skin, the carbon prepreg and adhesive film were laid directly onto the flat Al plate, ensuring a flat surface. Honeycomb was laid on top of it and cured under vacuum. Table 6-1 summarizes the stacking of the different layers during curing.

Samples of the second type were produced to study the influence of processing pressure on the strength of a panel of a more conventional type. The skins were made with two plies of prepregs at 0° and 90°. To allow the vacuum level in the honeycomb cells to be controlled during curing, the panels were processed in two steps as in the case of the first type of samples; the stacking is described in Table 6-2. The breather cloth and plastic grid on top of the panel were not useful for draining air during the first cure because the air was drained below the honeycomb, but it was nevertheless included in order to have the same stacking on the surface as for conventional one-shot vacuum processing. Five different relative vacuum pressures were used: -0.1; -0.3; -0.5; -0.7; -0.9 bar. The second skin was cured on the Al plate using -0.9 bar vacuum pressure. The vacuum was applied during 5 hours before the second curing cycle began.

**Table 6-1: stacking of the different layers during the two cures of the first type of sample**

| First cure | Second cure |
|---|---|
| Al plate | Al plate |
| Breather Cloth | 0° UD prepreg |
| Honeycomb | 150 g/m$^2$ adhesive |
| 150 g/m$^2$ adhesive | Honeycomb |
| 0° UD prepreg | Cured carbon skin |
| Non-adhesive film | Non-adhesive film |
| Vacuum bag | Breather cloth |
|  | Plastic grid |
|  | Vacuum bag |

**Table 6-2: stacking of the different components during the two cures of the second type of sample**

| First cure | Second cure |
|---|---|
| Al plate | Al plate |
| Breather Cloth | 0/90° UD prepreg |
| Honeycomb | 50 g/m$^2$ adhesive |
| 50 g/m$^2$ adhesive | Honeycomb |
| 90/0° UD prepreg | Cured carbon skin |
| Non-adhesive film | Non-adhesive film |
| Breather cloth | Breather cloth |
| Plastic grid | Plastic grid |
| Vacuum bag | Vacuum bag |

The third type of sample was fabricated with the same lay-up as the second type, but in one shot, as described in Figure 5-1. Various vacuum pressures (-0.1, -0.5, -0.7, -0.9 relative pressure) were used, as for the second type of sample, but as explained in section 6.2, the absolute pressure in the honeycomb cells could be considerably higher than that under the vacuum bag because the cells were closed by the skins. The vacuum was applied during 12h before the curing cycle began.

The waviness of the skin was measured either on micrographs of cross-sections of the sandwich structures prepared as explained in section 3.2.2, or with a laser scanning profilometer. This second technique could only be used with the first type of sample because only the skin surface which was cured directly against plastic vacuum bag was sufficiently smooth. For the two other types of sample, the breather cloth between the skin and the vacuum bag created roughness on the skin which made the use of a laser profilometer inaccurate. The height measured for the waviness was the height difference between the top of honeycomb cells and the lower point of the skin in the middle of the honeycomb cell, as represented in Figure 6-5. The size of the adhesive menisci was also measured on the samples of the second and third type, and the weight of adhesive in the meniscus calculated accordingly to section 4.1.

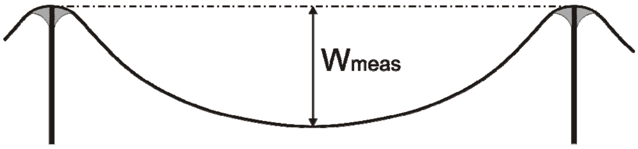

**Figure 6-5: measurement of the amplitude of the waves on the micrographs of cross-sections**

A significant difference in the quality of the wavy and smooth skins can be observed in Figure 6-6 which shows micrographs of cross-sections of the skins of the first type of sample. Bending of the honeycomb cell walls due to applied pressure can also be observed. This phenomenon can decrease the compressive strength and modulus of the core, and this then decreases the wrinkling strength of the skin.

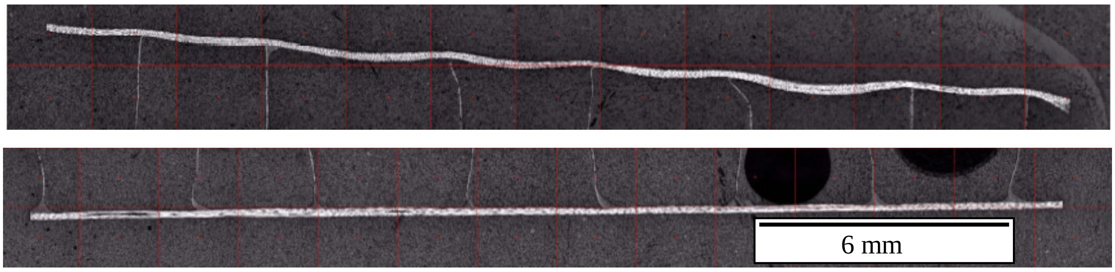

**Figure 6-6: Cross-section of the first type of sample. The upper skin is wavy, the lower is smooth. Some honeycomb cell walls are clearly bent due to the pressure applied during curing.**

The use of a laser scanning profilometer allowed the waviness of the skin to be quantified by measuring the depth of the wave and thus obtaining a 3D surface image, as illustrated in Figure 6-7. The maximum depth of the wave measured with -0.9 bar relative vacuum pressure was 370 μm, whereas it was only 160 μm with -0.1 bar. Furthermore, surface scanning also shows that some honeycomb cell walls collapsed due to the pressure. In fact, the cell walls in the ribbon direction, which are of double thickness, are clearly visible (pink color), while some single cell walls are crushed and therefore not visible. This indicates that -0.9 bar vacuum pressure, coupled with a curing temperature of 120°C, can damage the core even though its compressive strength is theoretically 10 times higher than the applied pressure at room temperature (see section 5.1).

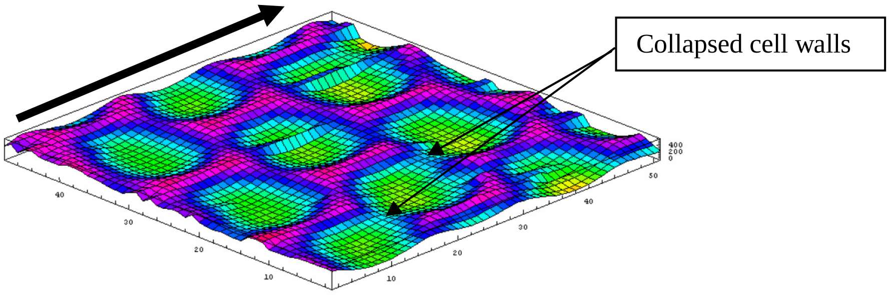

**Figure 6-7: scanning of the skin surface of a sample of the first type cured with -0.9bar relative pressure in order to measure the shape of the waviness. The arrow indicates the ribbon direction of the honeycomb.**

Figure 6-8 shows micrographs of cross-sections of the second type of sample cured using various pressures in two steps, and Figure 6-9 and Figure 6-10 are micrographs of the wavy and smooth skins of the third type of sample cured in one shot. A clear dependence between process pressure, skin waviness, and fillet height can be observed. Waviness and fillet size both increased with pressure exerted on the panel. As scattering of the measurements of waviness shown in Figure 6-11 was quite high, about 30 measurements were made for each pressure in order to obtain reliable data. The waviness of the samples cured in two steps was always higher than measured on the samples cured in one shot. This is due to the higher pressure difference between the inside of honeycomb cells and atmospheric pressure in the case of two-step curing. It is important to remember that the pressure represented in the figures is the relative pressure in the vacuum bag. The actual absolute pressure in the honeycomb cells may, however, be significantly higher that the absolute pressure in the vacuum bag during one-shot vacuum bag curing, due to the low permeability of the skins and the consumables closing the cells on both sides. On the samples cured in two steps, waviness increased rapidly with mounting pressure and was already about 40 µm with -0.1 bar of relative vacuum pressure. As waviness should be 0 when no pressure is applied, the data were fitted with a power law of the pressure applied. For the samples cured in one shot, a linear fit going through the origin was chosen. The fits for both one-shot and two-step curing represented in Figure 6-11, correlate well with the experimental data, so that the functions giving skin waviness as a function of process pressure were used in a model for the prediction of failure load as a function of process pressure.

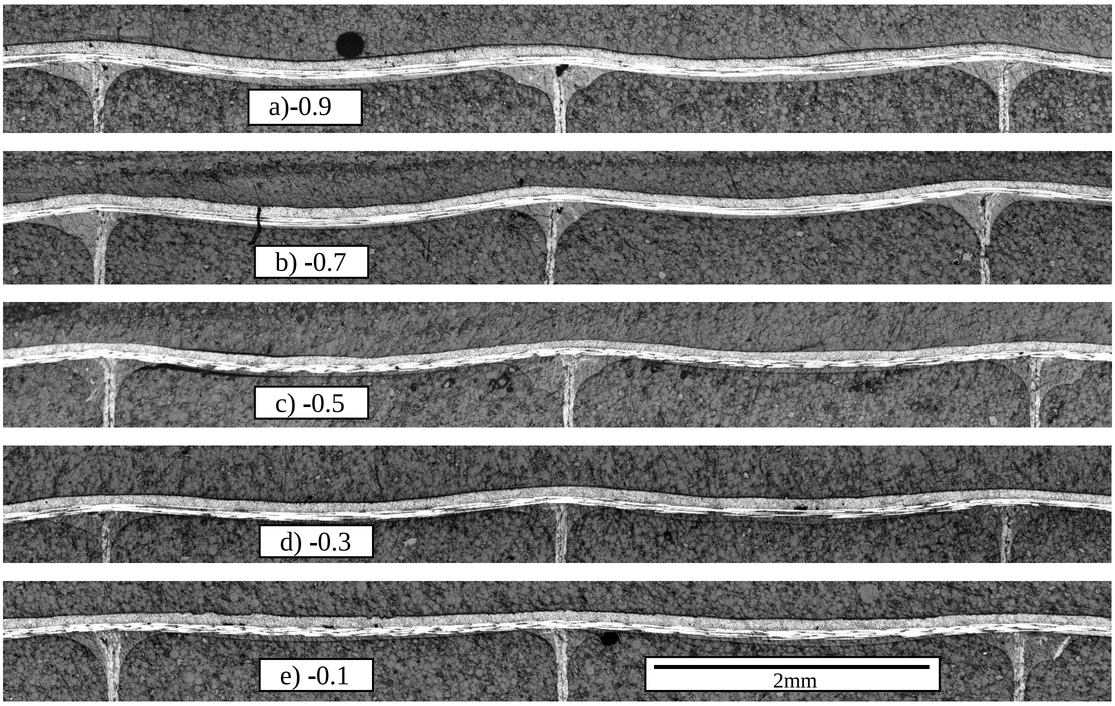

**Figure 6-8: Micrographs of cross-sections of the wavy skin of sandwich panels cured in two steps. The wavy skin was cured with relative pressures ranging from -0.9 to -0.1bar in the vacuum bag.**

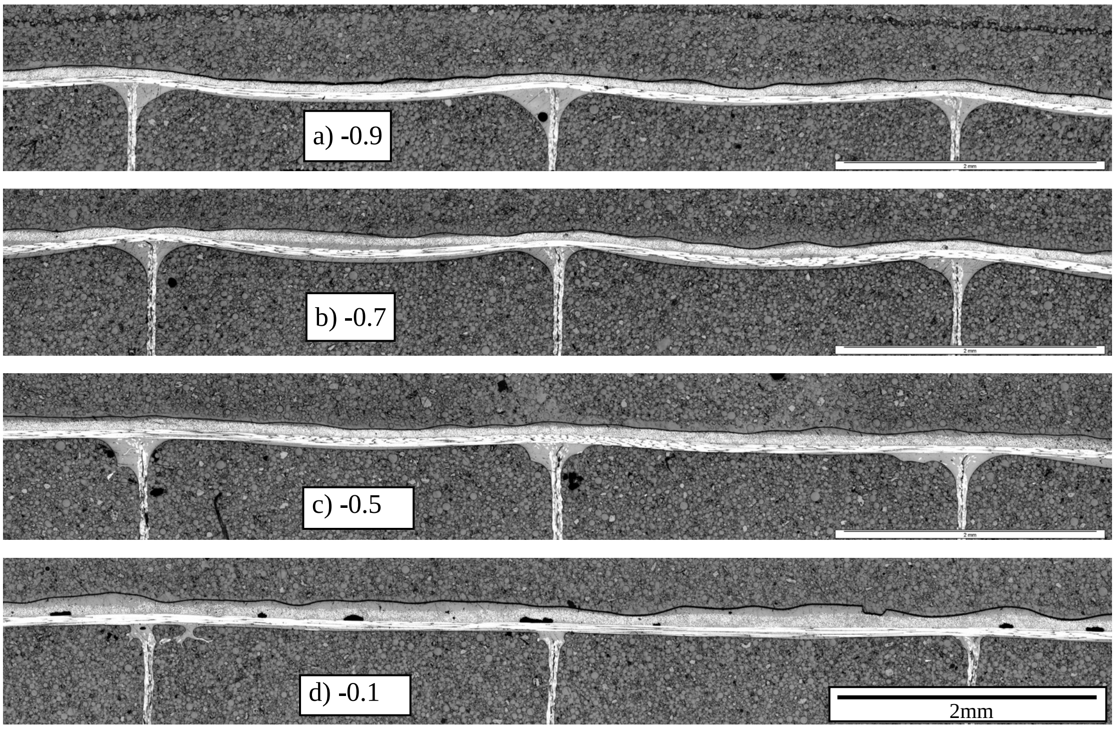

**Figure 6-9: Micrographs of cross sections of the wavy side of sandwich panels cured in one shot. The relative pressure applied during vacuum curing is indicated in bar on the pictures**

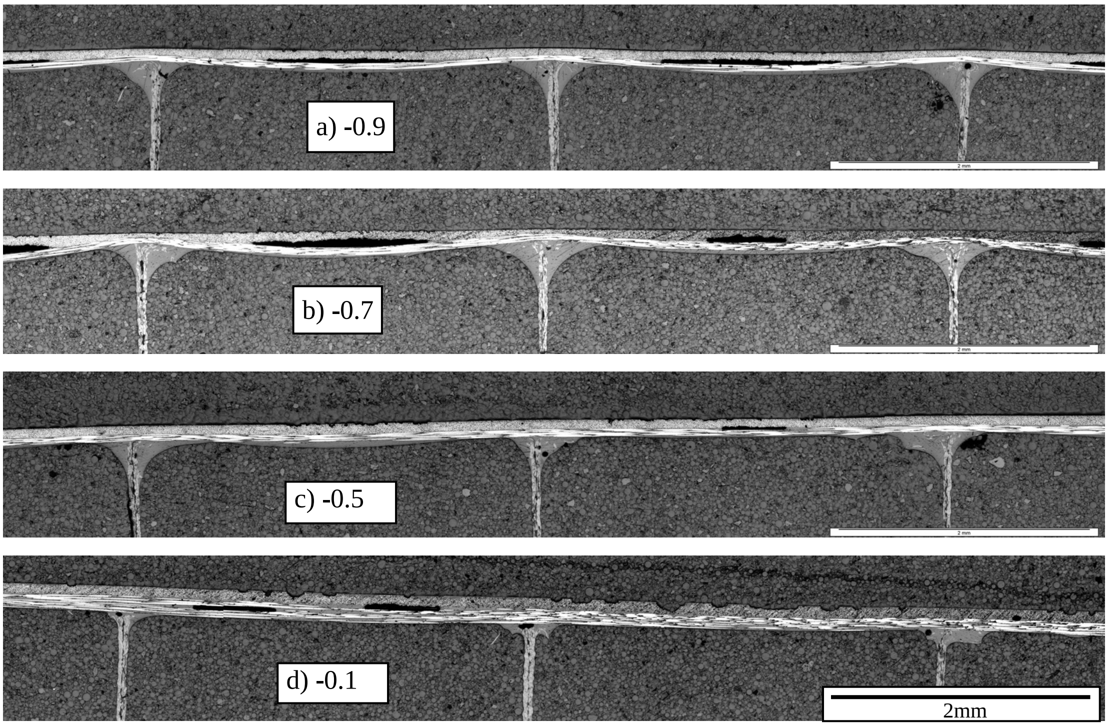

**Figure 6-10: Micrographs of cross sections of the smooth side of sandwich panels cured in one shot. The relative pressure applied during vacuum curing is indicated in bar on the pictures**

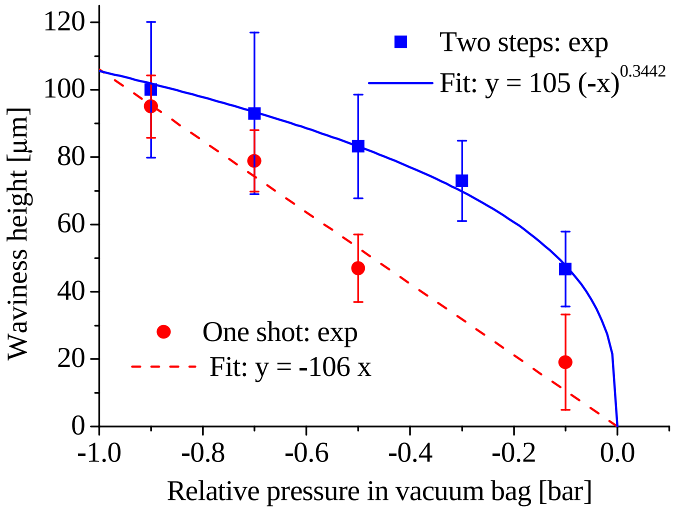

**Figure 6-11: Amplitude of skin waviness measured on cross-sections as a function of process pressure for the samples cured in one shot and in two steps**

On the samples cured in one shot, the face on the vacuum bag side had pronounced waviness of the two prepreg layers, while in the face on the mould side, the outer layer was flat but the inner layer was wavy, especially with high process pressure. The face was well-compacted under the honeycomb cell walls, but not in the middle of the honeycomb cell where a gap remained between the layers. The process pressure has thus also an influence on the quality of the smooth skin.

Figure 6-12 shows the adhesive weight in the menisci calculated with the measured menisci height for samples cured in two steps and in one shot. The size of the menisci was always higher in the samples cured in two steps due to the lower relative pressure in the honeycomb cells (better vacuum) as explained previously. For the samples cured in two steps the size of the adhesive menisci forming between core and skin increased between -0.1 and -0.3 bar pressure in the vacuum bag and then stabilized. In fact, when a sufficient pressure level is exerted by the honeycomb cell walls, the skin is compacted under the honeycomb cell walls and prepreg resin in addition to the 50 g/m$^2$ adhesive film flows into the menisci. This explains why the adhesive weight in the menisci was greater than 50 g/m$^2$. Of course the amount of resin is limited, and therefore the meniscus size does not change any more once a sufficient pressure level is reached. When low pressure is applied, the menisci form only with the adhesive film near the cell walls, while a certain amount stays on the prepreg in the center of the honeycomb cell. To fit the data by taking into account these phenomena, a function was chosen that started with a finite adhesive weight and then grew asymptotically to the limit adhesive quantity. A first order exponential decay was thus fitted to the experimental data.

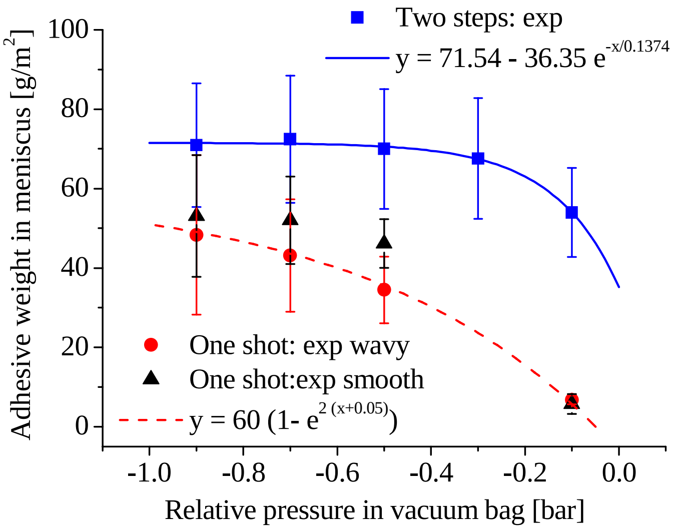

**Figure 6-12: Adhesive weight in the menisci as a function of process pressure for the samples cured in one shot and in two steps.**

For the samples cured in one shot, the increased fillet size linked to low relative pressure in the vacuum bag is due to several phenomena. Firstly, as for the samples cured in two steps, increased pressure pushes the cell walls against the prepreg, and the resin of the prepreg flows out and participates in fillet formation. Secondly, as the vacuum is not good in the honeycomb cells, due to low permeability of the-lay up, as explained in section 6.2, the pressure in the cells increases when temperature increases. Some air flows out of the cells through the skin and this forces adhesive and prepreg resin to flow out too. This can be seen in Figure 6-9 d) where a layer of resin is on the top of the prepregs of the panel cured with -0.1 bar relative pressure in the vacuum bag. This flowing effect was more pronounced on the vacuum bag side that on the Al mould, which explains why the resin fillets were greater on the mould side than on the vacuum bag side, as shown in Figure 6-12. As the amount of adhesive available for meniscus formation is limited, an asymptotic function was chosen to fit the experimental data, as for the samples cured in two steps. The functions fitting the measurements for both one-shot and two-step curing are represented in Figure 6-12. The exponential decay function used to fit the data obtained with the samples cured in one shot is negative, and has no physical meaning at pressure between -0.05 and 0. However, as this pressure range has no interest for processing, the function is valid in the useful range.

To further demonstrate the mechanisms increasing meniscus size with pressure exerted on the panel, it was shown that the vacuum quality has no effect on the meniscus size when the honeycomb cells are open and the pressure applied on the panel is constant. To this end, two layers of prepreg and a 50 g/m$^2$ of adhesive film were laid on an Al plate. Honeycomb was laid onto it and pressed with a weight. The samples were cured at 120°C, once in a vacuum oven, once with atmospheric pressure. The height of the menisci was the same in both cases, as illustrated on the micrographs of cross-sections in Figure 6-13. This demonstrates that vacuum quality has no effect when the cells are open. So only the difference of pressure between inside the honeycomb cells and outside the vacuum bag has an effect on meniscus size.

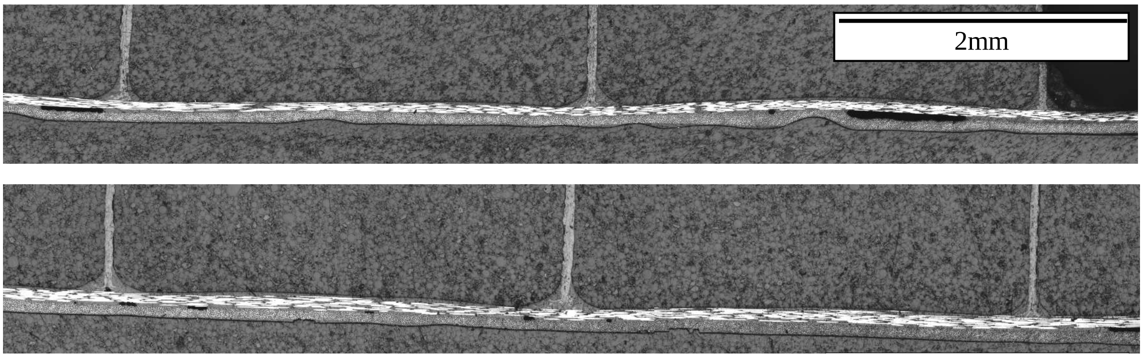

**Figure 6-13: cross sections of sandwich samples cured at atmospheric pressure (upper picture) and under vacuum atmosphere (lower picture), with open honeycomb cells allowing air circulation.**

It was also observed that the menisci were smaller when curing was carried out under pressure exerted by a small weight instead of under a good vacuum. This confirms that the squeezing of the prepreg under the honeycomb cell walls under high pressure forces the resin to flow out of the fiber bed and to go partly into the resin fillets.

The production of the sandwich panels in two steps also highlighted the need to create sufficient vacuum in the honeycomb cells to have good core-to-skin bonding. In fact on three of the 8 panels fabricated, a large area of the second skin was debonded in the center of the panel (10-15 cm diameter) right after processing. This was due to a very bad vacuum in the honeycomb cells during second curing, confirming that the first cured skin was air tight. The -0.9 bar relative vacuum pressure during 5 h was not sufficient to remove air from the cells enclosed between the cured and the uncured skin on the Al mould. The air entrapped in the cells expanded during curing and the degassing resin created supplementary pressure so that it almost prevented the contact between the skin and the core. Thus, if such a two-step process is used with non-perforated honeycomb, the first cured skin would have to be sufficiently permeable to allow air to drain out of the honeycomb cells for the second cure in order to avoid potential early debonding.

## 6.4. Influence of process pressure on stiffness

The sandwich beams underwent 4-point bending tests to evaluate the influence of waviness of the skin, and thus pressure, on the strength and stiffness of the structure. Stiffness of the second type of sample was measured. Deflection in the center of the beam was recorded with an LVDT fixed on the loading points, enabling the bending stiffness to be directly calculated with equation (2.57). Figure 6-14 shows that the bending stiffness decreased when process pressure increased. This can be explained by the increased waviness of the skin, which reduced the tensile and compressive stiffness due to misalignment of the fibers. However, the variations were small and the standard deviation was high, so that it is difficult to evaluate quantitatively the effect of waviness on the stiffness. The bending stiffness predicted by CLT is 8.4 Nm$^2$, which is close to the measured value with low waviness of the skin, and thus corresponds well to the sandwich with perfectly flat skins.

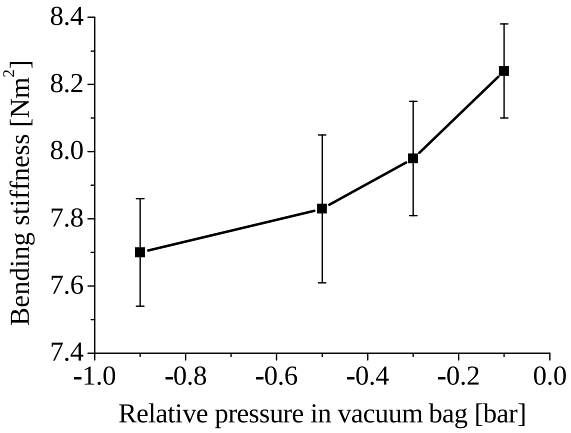

**Figure 6-14: Changes in bending stiffness as a function of process pressure**

## 6.5. Influence of process pressure on strength

As the face under compression usually broke first during 4-point bending tests, some of the beams were tested with the smooth side under compression, others with the wavy skin under compression. The samples broke mainly due to wrinkling failure of the skin under compression. Some samples of the third type, cured in one shot with -0.1 bar relative pressure in the bag, broke due to debonding of the faces, either on the upper or lower side of the structure. Therefore in order to compare the influence of waviness and meniscus size on local instabilities, the mean failure load was measured taking into account only failure due to wrinkling between the loading points.

Reduction of the compressive strength of the skin due to skin waviness was significant in the first type of sample. The reduction in strength for the samples cured with -0.9 bar relative pressure was 24%, while the reduction was only 3%, i.e. smaller than the standard deviation, when the panel was cured with -0.1 bar relative pressure, as illustrated in Figure 6-15. In addition, a reduction of the pressure for the second cure decreased the strength of the smooth face, probably due to bad compaction of the skin. It can be observed that stresses at failure of the skins were high in comparison to those occurring in similar samples in section Chapter 5, but this is easily explained by the very thick adhesive film (150% of the prepreg thickness) which reinforced and stabilized the skin, as explained in section Chapter 5, but was not taken into account in stress calculation.

This type of samples, manufactured on purpose to create an exaggerated waviness, thus illustrated well that curing under full vacuum pressure is not optimal for such light sandwich structures, and that optimal pressure has to be found.

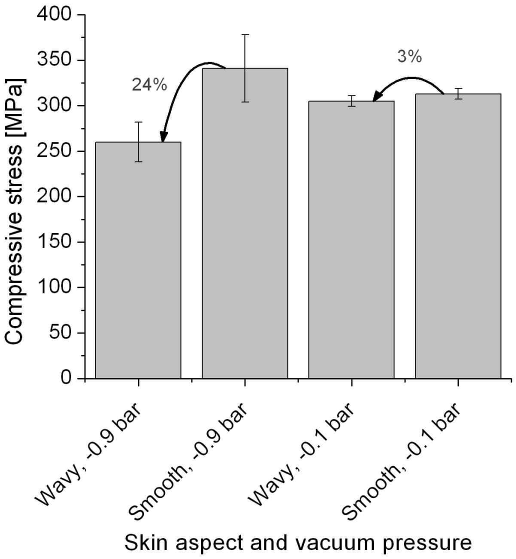

**Figure 6-15: effect of skin waviness on the compressive strength of the skin for the first type of sample. The pressure indicated is the relative vacuum pressure during processing.**

The two competing factors, namely waviness and meniscus size, both have a direct influence on bending strength. Figure 6-16 represents the compressive load at failure in the skin as a function of relative pressure in the vacuum bag for the samples cured in two steps and in one shot. On the samples cured in two steps, the strength of the beams increased between -0.1 and -0.3 bar and then decreased from -0.3 to -0.9 bar. The strength increase was due to the quick increase of adhesive quantity in menisci between -0.1 and -0.3 bar. The adhesive quantity then stabilized and the increasing waviness of the skin decreased the strength of the face between -0.3 and -0.9 bar. For the samples cured in one shot, the strength of the wavy skin was low at low process pressure (-0.1 bar relative pressure in the vacuum bag) due to very small adhesive fillets, poor skin-to-core bonding and also bad skin compaction. The strength increased by increasing the processing pressure (-0.1 to -0.7 bar relative pressure in the vacuum bag) because adhesive fillet size increased, but it then decreased due to more pronounced skin waviness (-0.7 to -0.9 bar relative pressure in the vacuum bag). An optimal process pressure giving the best compromise between these two competing factors could thus be determined. The optimal relative pressure in the vacuum bag identified experimentally was -0.3 bar for the samples cured in two steps and -0.7 bar for the wavy skin of the samples cured in one shot.

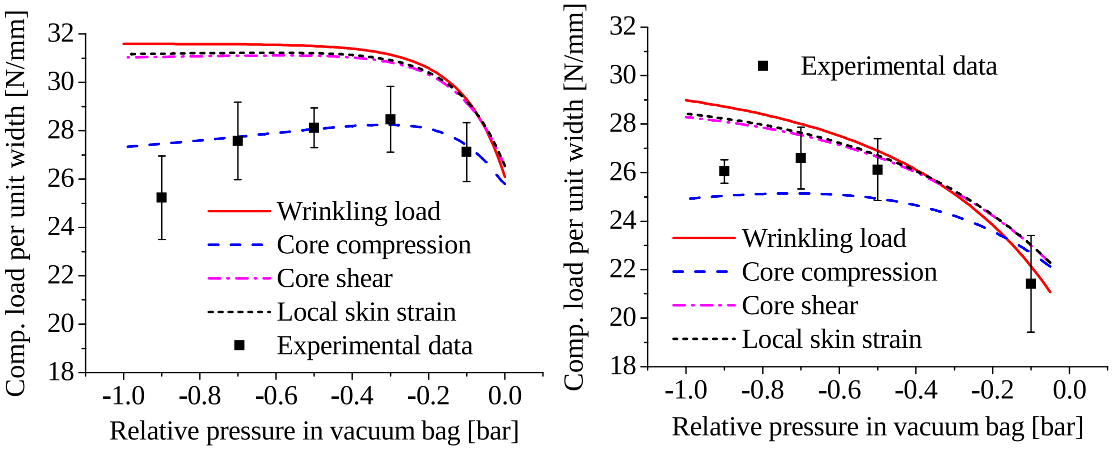

**Figure 6-16: Changes in the compressive load per unit width of the face at failure during a 4-point bending test as a function of process pressure for the samples cured in two steps (left) and in one shot (right), with the wavy face under compression. The failure loads predicted by the different models are represented.**

The analytical model based on the model of Gutierrez and Webber [39] for wrinkling load prediction, which was adapted in section 5.2 to take into account the amount of adhesive in menisci and the preliminary deformation of the skin, was used to predict the failure load of the skin as a function of the processing pressure. To this end, the fitting function relating pressure and adhesive quantity in the menisci was firstly integrated into the model in order to predict skin bending stiffness as a function of process pressure. Secondly, the function relating process pressure and skin waviness was integrated to determine the value of the parameter $W_0$. However, the amplitude of the waviness measured in the panels, $W_{meas}$, could not be used directly for $W_0$, because the wave measured had a width limited to the cell size, since the skin was maintained flat on the cell walls, while the wave extended across the full width of the beam in the model. This discontinuity of the wave in the width direction significantly reduced the sensitivity to waviness of the structure, and a reduction factor was determined so that the theoretical strength correlated well to the experimental data of the samples cured in two steps (second type of samples) expressed by

$$\chi = \frac{W_{meas}}{W_0} = 25 \qquad (6.1)$$

Figure 6-16 shows changes in the critical compressive load per unit width in the skin calculated according to the models for the different types of failure as a function of the process pressure. Among the models predicting the different possible failure types of the skin under compression, the one considering compressive failure of the core predicts the lowest failure load. In fact, this mode is the most sensitive to the initial imperfections of the skin and therefore determines the failure load of the beam. Only with low process pressure for one-shot curing (-0.1 to -0.2 bar relative pressure in vacuum bag) is the wrinkling load lower. With the parameter $\chi$ defined in equation (6.1) , the model giving the critical load for core compressive failure is in good agreement with the experimental data for both the 2nd and 3rd types of sample. For the samples cured in two steps, only the critical load measured for the panel cured with -0.9 relative vacuum pressure shows 8% deviation. However, the significant decrease of the measured strength between the panels cured at -0.7 and -0.9 bar is not well understood, as the adhesive weight in menisci is almost the same and the waviness only slightly more pronounced.

For the samples cured in one shot the model slightly overestimates the failure load at -0.1 bar relative vacuum pressure, but as the models do not take into account bad compaction of the skin due to low pressure, this is understandable. It slightly underestimates the failure load for the other processing pressures, but the error is in the order of 5%, which is very reasonable.

Furthermore, the curves showing the critical load for core compressive failure depict exactly the same tendencies as the experimental data for both curing processes. In fact, the load increases first when the relative vacuum pressure is decreased, then reaches a maximum and finally decreases. As for the experimental data, the optimal pressure in the vacuum bag for the sandwich panels cured in two steps is -0.3 bar, whereas it is ~-0.7 bar for the panels cured in one shot. However, for the panels cured in one shot, the strength variation between -0.5 and -0.9 bar relative vacuum pressure is small, so that this pressure zone can be considered as optimal.

Finally, the critical failure mode predicted by the model as the compressive failure of the core is confirmed by observing the broken samples where the skin crushed the core, as illustrated in Figure 6-17.

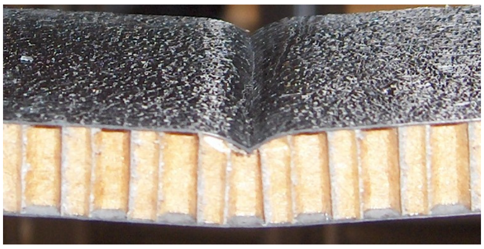

**Figure 6-17: failure mode observed in 4-point bending. The skin crushed the core as a result of the compressive stresses caused by initial waviness of the skin.**

As the predictions of the model correlate well to the experimental data, these can then be used to predict what happens if supplementary pressure is added during one-shot curing by using an autoclave. The predicted failure load is represented in Figure 6-18 as a function of the process pressure, i.e. the pressure difference between outside and inside the vacuum bag. At two-bar pressure (-0.9 bar relative pressure in the vacuum bag and 1.1 bar relative pressure in the autoclave), the strength of the beam is reduced by 10% compared with optimal pressure. Also the model does not take into account any damage caused to the honeycomb by high processing pressure, as stated with the first type of sample. Therefore, the model confirms that the use of supplementary pressure with such sandwich structures with light cores and thin skins decreases the properties and should be avoided.

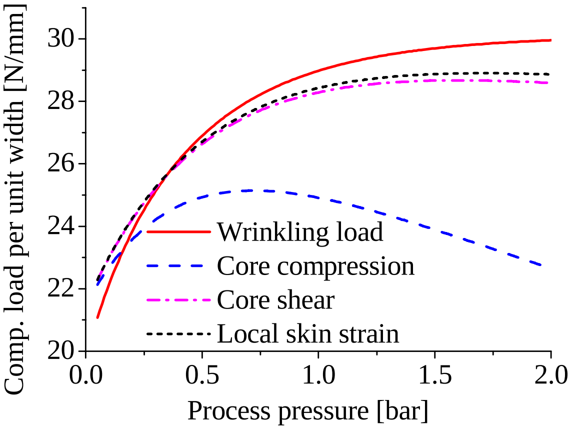

**Figure 6-18: Changes in the compressive load per unit width in the face at failure for a sandwich cured in one shot, during a 4-point bending test with the wavy face under compression, as a function of process pressure.**

As observed in Figure 6-10, the variation of process pressure also has an influence on the quality of the smooth skin. The measured strength under 4-point bending is represented in Figure 6-19 when either the smooth or wavy face was under compression. During the bending test, the smooth skin had a higher strength under compression than the way skin for every process pressure. Decreased fillet size decreased the strength at low process pressure. In addition, bad core-to-skin bonding and bad skin compaction at low pressure reduced the strength and caused high scattering of the results. Waviness of the inner ply and bad compaction of the plies in the center of the cells, as observed in Figure 6-10, decreased the strength with high process pressure. Optimal pressure was observed at -0.5 bar relative pressure in the vacuum bag, but as the strength of the wavy skin was lower, the process pressure has to be selected for the wavy skin.

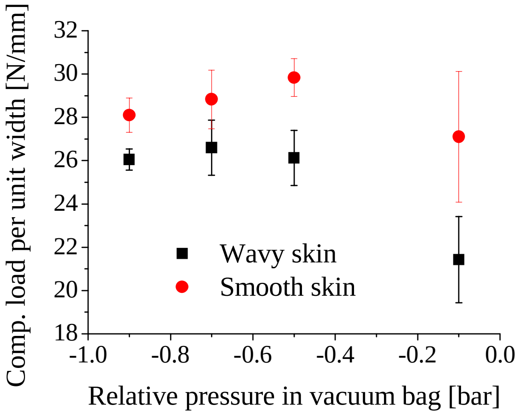

**Figure 6-19: compressive load at failure in the face as a function of relative pressure in the vacuum bag during curing. Sandwich beams were tested with either the smooth or wavy face under compression.**

## *6.6. Influence of core properties on strength*

The models used to predict the failure load as a function of process pressure can also be used to evaluate the influence of core properties on the strength of the panel. To this end, various properties were varied in the model and the corresponding strength was calculated. Four different cases were evaluated. Firstly, the core out-of-plane compressive modulus was varied. Secondly, the core out-of-plane compressive strength was changed. Then, as in practice the different properties of the core are related, the compressive modulus $E_{cz}$, shear modulus $G_{core}$, compressive strength $Z_c$ and shear strength $S_c$ of the core were varied with a linear relationship as follows

$$E_{cz} = E_{cz0}(1+\eta) \quad G_{core} = G_{core0}(1+\eta) \quad Z_c = Z_{c0}(1+\eta) \quad S_c = S_{c0}(1+\eta) \quad (6.2)$$

where the 0 indices indicate the properties of the core used in this study and $\eta$ varies between -1 and 3. Finally, the influence of core cell size $s$ was studied by varying the wavelength of the initial waviness $l_0$, corresponding to the distance between two cell rows, which is related to cell size by

$$l_0 = \frac{\sqrt{3}}{2} s \quad (6.3)$$

For all four cases, one-shot curing with -0.7 bar relative vacuum pressure was considered in the model.

Figure 6-20 shows changes in the compressive stress at failure in the skin predicted with the different models for the four different changes of core properties mentioned. For all cases, only failure modes due to local instability of the skin are considered. The change of out-of-plane compressive Young's modulus of the core has a high influence on the compressive failure load of the skin. When core modulus is doubled, the strength increases by 30%. As the failure cases studied are instability cases which are closely related to the stiffness this explains the pronounced effect of compressive modulus. When the modulus increases, the critical mode is the local compressive failure of the core caused by compressive stresses induced by the waviness of the skin. With a small compressive modulus, wrinkling of the skin becomes the critical loading case, and the preliminary waviness no longer has any effect.

Any change of core compressive strength only affects the failure load for local compressive failure of the core. This mode thus remains the critical failure mode for any core strength. The load at failure decreases significantly when the strength of the core is decreased, but only slightly increases with a stronger core. Actually, the maximum possible load for this failure mode is the wrinkling load, corresponding to the half wavelength of the preliminary waviness (2.77 mm), which is in fact very close to the critical half wavelength providing the lowest wrinkling load (2.79 mm for $E_{cz}$ = 50 MPa and with 50 g/m$^2$ adhesive, see Figure 5-8). Therefore, since the wrinkling load is unchanged by increasing core strength, the potential failure load improvement is very limited.

When the strength and modulus of the core are varied, the failure load for core compression changes almost linearly. The failure load increases by 55% when the core properties are doubled. However, with low and high core strength and modulus, the wrinkling load becomes the critical failure mode and the strength increase is no longer linear. This means that when the properties of the core are sufficient, the preliminary waviness of the skin does not change the failure load (considering that the waviness corresponds to -0.7 bar process pressure). The use of a stiffer and stronger core therefore facilitates processing, by causing the sandwich structure to be less sensitive to waviness.

As mentioned previously, the wavelength of preliminary waviness is very close to critical wrinkling wavelength. Therefore the failure load is significantly influenced by preliminary waviness. By slightly increasing or decreasing the cell size, the preliminary wavelength moves away from critical wavelength, so that sensitivity to the preliminary waviness is decreased and the failure load is increased. However, the wrinkling load does not change with cell size (the core being considered as a continuous elastic foundation), and thus this limits the gain in strength. Furthermore, by modifying the size of the cells, the reduction factor $\chi$, relating the measured waviness and the amplitude in the model, may also change, and thist could significantly influence the results. Moreover, when cell size is increased, intra-cell buckling may become critical and should be considered.

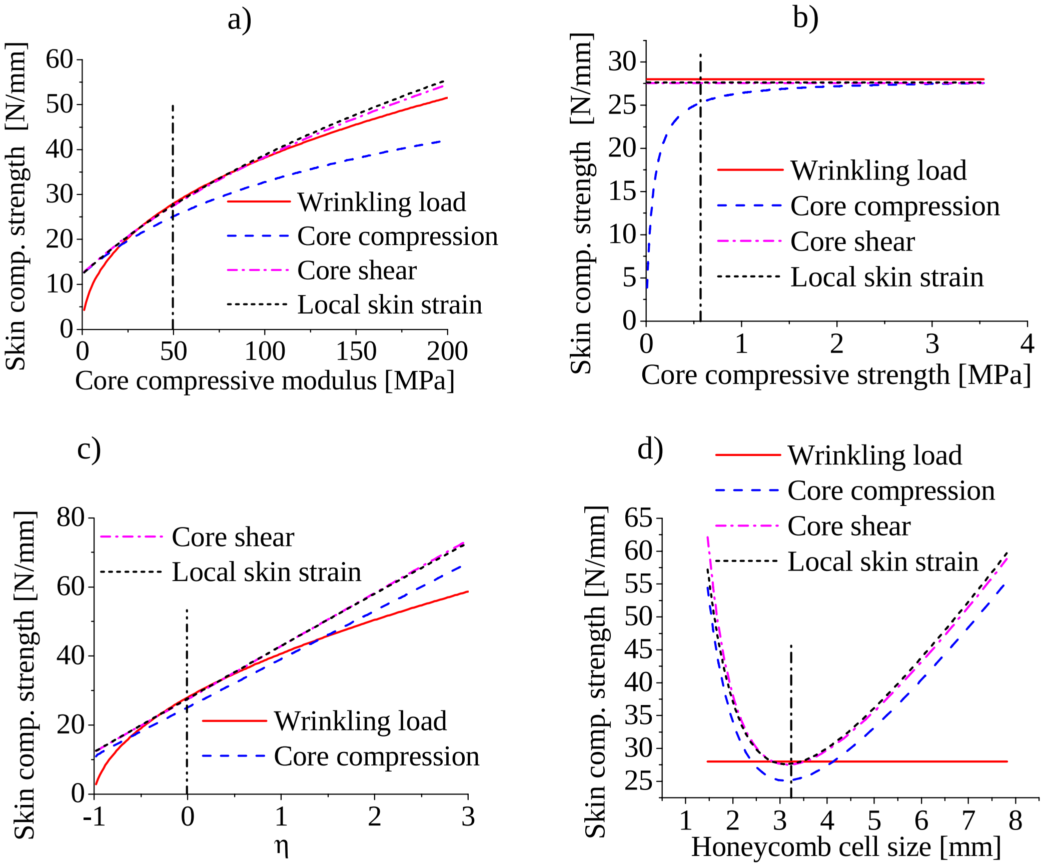

**Figure 6-20: Compressive load per unit width in the skin at failure as a function of: a) out-of-plane compressive modulus of the core, b) out-of-plane compressive strength of the core, c) linear variation of compressive strength and modulus, and shear strength and modulus, d) honeycomb cell size. The vertical dash/dot lines show the actual properties of the core used.**

## 6.7. Conclusions

- Varying process pressure has two distinct effects on the microstructure of sandwich panels. An increased process pressure increases waviness but also increases the adhesive fillet size between honeycomb cell walls and skin. These two different phenomena have conflicting effects on the flexural strength of the sandwich beams. Pronounced skin waviness decreases the strength and stiffness, while greater menisci increase the strength. An optimum pressure giving the best compromise between these two effects, and thus the highest strength, has been identified. For traditional one-shot vacuum bag curing, the highest strength was obtained with a relative pressure in the vacuum bag between -0.5 and -0.9 bar.

- The analytical models developed correlates well with the experimental results and show that curing with a higher processing pressure than full vacuum pressure leads to a decrease in strength and should be avoided with these ultralight structures. The models also show that an increase of core strength and stiffness significantly increases the failure load of the skin under compression. Moreover, a stronger and stiffer core reduces sensitivity to initial waviness of the skin.
- During one-shot vacuum bag curing the two faces closing both sides of honeycomb core prevented the air from being sufficiently evacuated from the honeycomb cells. If pressure in the vacuum bag was not sufficiently low, the increase of pressure inside the honeycomb cells during curing forced the adhesive to flow out at the surface of the skin, and in the worth case almost prevented contact between core and skin, thereby creating debonds in the sandwich panels.

# CHAPTER 7. ASYMMETRIC SOLAR SANDWICH STRUCTURE

In applications requiring light solar panels such as solar aircraft, solar cars or satellites, the solar cells are often glued onto very light sandwich panels which provide sufficient stiffness [177-183]. To save more weight, the possible use of the solar cells to form the skin of the sandwich structure was investigated. The high elasticity modulus of silicon (130-190 GPa depending on direction) can provide very high stiffness to the sandwich structure. Furthermore, the low thickness of the cell makes it compatible with classic CFRP skins. However, the brittleness of silicon, and thus the low strength of the cells, limits the load-carrying capacity of this structure.

In usual applications, solar cells are protected against mechanical loading by the encapsulation with a glass panel. Therefore, the only mechanical prerequisite of the cells is to survive the manufacturing process. In the concept of the solar sandwich structure the solar cells are, however, load-carrying elements and it is thus necessary to know precisely the strength of the cells. The mechanical properties of high efficiency silicon mono-crystalline cells, which may be used for such a sandwich design, were therefore studied. The influence of texturation of the surface of solar cells on their strength, and the potential reinforcement provided by a polymer encapsulation were also investigated.

The integration of the cells as structural skin element of the sandwich was then carefully studied, following four main steps. Firstly, the bonding of Ag back-contact of the solar cells onto a Nomex® honeycomb core was investigated. Secondly, the tensile strength of solar cells integrated into the sandwich was evaluated in order to detect eventual strength loss during sandwich manufacturing. In a third step, a stress transfer device between cells was developed. Finally, curved panels were fabricated to demonstrate the feasibility of producing curve-shaped panels to fit, for example, wing profiles.

In addition, a potential lightweight polymer encapsulation was investigated in order to protect the cells against environmental attacks.

## *7.1. Mechanical analysis of solar cells*

The solar cells tested were mainly the S32 type with an inverted pyramidal surface texture, as described in section 3.1.4. Cells without a texture of the type 2PR/200-6540 were also tested in bending to evaluate the influence of texture on strength. To observe the effect of the encapsulation on their strength, solar cells were encapsulated on the front active side of the cell at room temperature with 12 μm PET film and silicone adhesive Sylgard 184, as described in section 7.6, and tested.

The cells were firstly tested in 3-point bending, as described in section 3.2.8. Figure 7-1 shows a bent cell with high deformation due to the thinness of the cell. The cells were tested with the silicon active side, as well as the silver coated side, in tension in order to observe the quality of both front and rear surface. As cracks propagate mainly under tension, the cell should fail due to defects on the face under tension or on the edges. So the bending test enabled the strength of the two faces to be measured separately. 40 textured cells and 10 smooth cells were tested on each side. Three encapsulated cells were tested with the active side in tension.

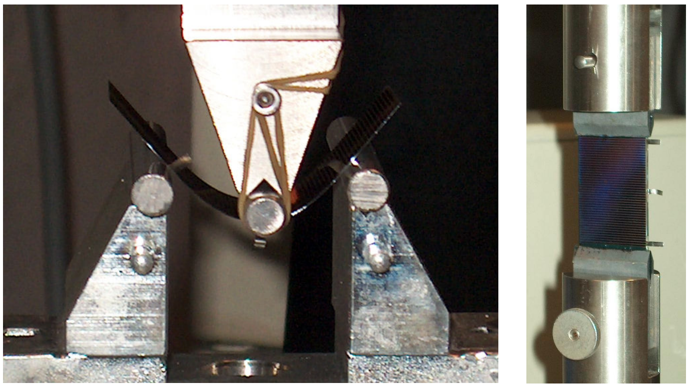

**Figure 7-1: (left) 3-point bending test on solar cells, (right) tensile test on solar cell. Two steel plates with beveled edges were glued onto each side of the solar cell.**

As the solar cells underwent high deformation during the bending test, simple linear beam theory was not sufficient to calculate the stress on the cells. A model similar to the one developed by Schoenfelder *et al*. [144] was used to take the large deflections into account. With the classic linear beam theory, the maximum moment in the centre of the cell is

$$M_{\max} = \frac{PL_3}{4} \tag{7.1}$$

where $P$ is the load applied, and $L_3$ the span. The maximum stress at the surface of the cell is then

$$\sigma_{\max} = \frac{M_{\max}}{I}\frac{t}{2} = \frac{6M_{\max}}{Bt^2} \tag{7.2}$$

where $I$ is the inertia moment of the cell in flexion, $B$ the width, and $t$ the thickness of the cell.

When the deformations are larger, the orientation of the reaction forces, the effective span and the effective displacement change. Figure 7-2 illustrates the difference between small displacements approximation and large displacements model. The reaction force becomes

$$R = \frac{P}{2\cos(\phi)} \tag{7.3}$$

In order to approximate the angle $\phi$, the deformed shape of the cell is assumed to follow linear beam theory and is expressed as

$$y(x) = \frac{4\delta}{L_3^3}\left(\frac{3L_3}{2}x^2 - x^3\right) \tag{7.4}$$

where $\delta$ is the deflection at the centre, and the axes are defined in Figure 7-2. The angle $\phi$ is then defined by

$$\tan(\phi) = y'\left(\frac{L_3}{2}\right) = \frac{3\delta}{L_3} \tag{7.5}$$

The moment under the loading point can then be calculated as

$$M_{\max} = \frac{PL_{cor}}{4} + R\sin(\phi)\,\delta_{cor} = \frac{PL_{cor}}{4} + \frac{P\sin(\phi)\,\delta_{cor}}{2\cos(\phi)} = \frac{PL_{cor}}{4} + \frac{3P\delta_{cor}^2}{2L_{cor}} \tag{7.6}$$

with

$$L_{cor} = L_3 - 2r\sin(\phi) \quad \text{and} \quad \delta_{cor} = \delta - r\left(1-\cos(\phi)\right) \tag{7.7}$$

If the friction on the supporting pins is disregarded, the maximum stress can then be calculated with equation (7.2). Using an FE simulation, Schoenfelder *et al.* [144] showed that the influence of friction on stress is very small and can be ignored.

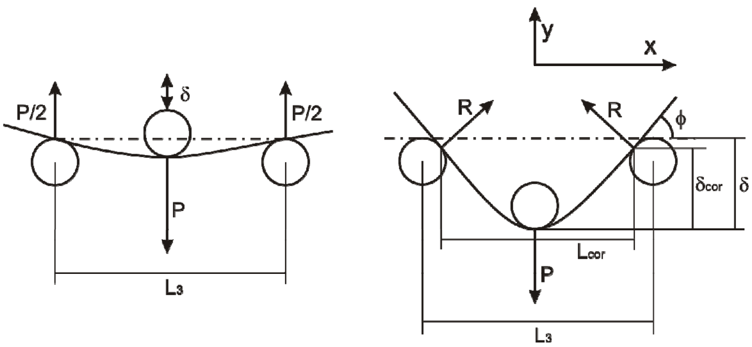

**Figure 7-2: 3-point bending test on a flexible solar cell. With small deformations (left), the supporting points are fixed, while with large deformations (right) the supporting points rotate around the loading pin, and the reaction forces, R, change the orientation.**

In order to calculate the stresses, an accurate measurement of the thickness was necessary. The thickness was therefore measured with a micrometer. However, the thickness measured comprises the back silver layer, the texture height, and the front silver grid, as illustrated on the schematic cross-section in Figure 7-3. To find an adequate mean value for the thickness, the slope $\beta$ of the load-displacement curve during the 3-point bending test was measured in the linear part (i.e. at small displacements). Using linear beam theory, this slope can be calculated as

$$\frac{\delta}{P} = \frac{1}{\beta} = \frac{L_3^{\;3}}{48E_{Si}I} = \frac{L_3^{\;3}}{4E_{Si}Bt_{th}^3} \tag{7.8}$$

with $t_{th}$ the thickness of an equivalent homogenous silicon rectangular section. Knowing that the Young's modulus in the [100] direction (length direction of the cell) of the silicon is 130 GPa, the equivalent thickness is

$$t_{th} = \sqrt[3]{\frac{\beta}{4E_{Si}B}}L_3 \tag{7.9}$$

The mean stress on the cell surface can then be calculated with this equivalent thickness. Of course, this does not take into account the local stress concentrations due to texture, but this is analyzed in detail in the next section. Moreover, the silver layer on the back side is not taken into account, but its influence is negligible, as explained in appendix 9.2.

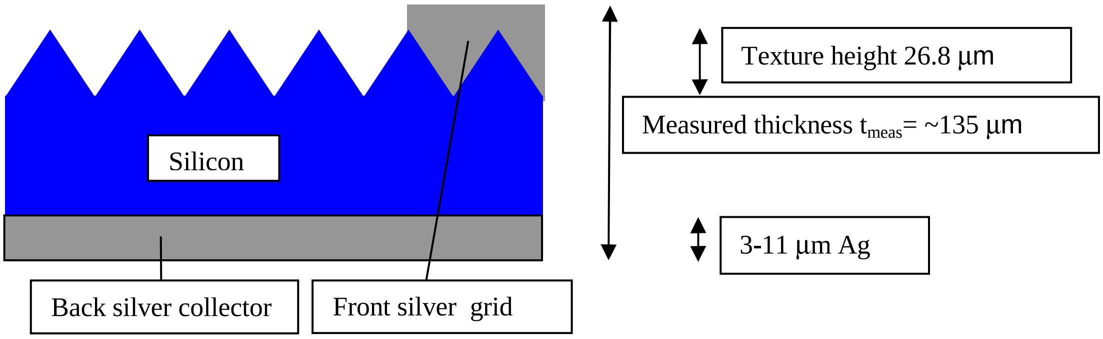

**Figure 7-3: schematic cross-section of a solar cell. The choice of the thickness used for stress calculation has a significant influence on the strength value.**

A typical non-linear load-displacement curve is illustrated in Figure 7-4, as well as the difference in stress calculation between small and large displacements models. As silicon is a linear-elastic material, the non-linearity of the curve was only due to the geometrical non-linearity at high displacements. The stresses calculated using the corrected model were significantly higher than those calculated according to linear beam theory, especially at high displacements, thereby confirming the need to use the corrected model.

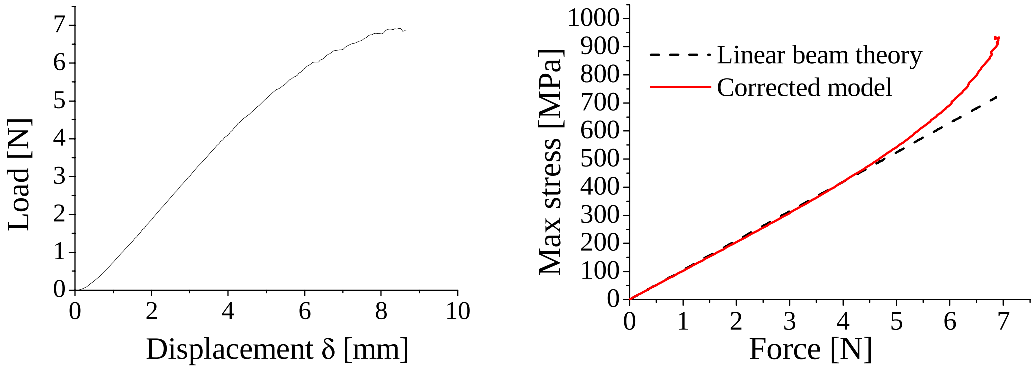

**Figure 7-4: (left) Load-displacement curve measured during 3-points bending of solar cells. (Right) Maximum stress in the cell corresponding to the measured load**

Measured with a micrometer, the mean thickness of the textured cells was 133 µm, while the equivalent thickness, calculated to match the measured bending stiffness, was 16 µm smaller. The equivalent thickness was then well located between the total thickness and the thickness without the texturation height. For smooth cells, the mean measured thickness was 240 µm, while the equivalent thickness calculated was 5 µm smaller. As the behavior of the cells was very brittle, a probabilistic approach was adopted in order to analyze the failure data of the solar cells. A Weibull distribution seemed to be adequate to match the failure strength distribution. The Weibull parameters could be calculated from the linear fit of the measured failure data given in Figure 7-5 and these are summarized in Table 7-1. The corresponding failure probabilities are given by

$$P_f = 1 - e^{-\left(\frac{\sigma}{\sigma_0}\right)^m} \tag{7.10}$$

and are represented in Figure 7-6.

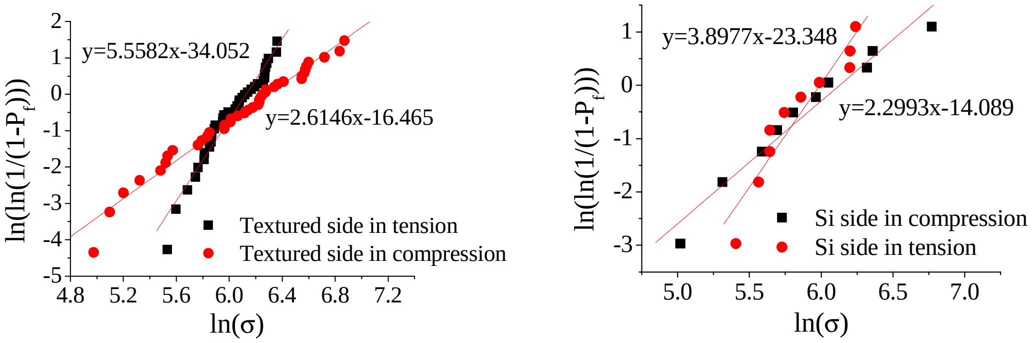

**Figure 7-5: Weibull analysis with the stress measured in bending for the textured cells (left) and smooth cells (right)**

**Table 7-1: Weibull parameters and mean stress at failure calculated from the failure data of the textured and smooth cells in bending**

| Type of cell, side in tension | Weibull modulus m | $\sigma_0$ [MPa] | $\sigma_{mean}$ [MPa] |
|---|---|---|---|
| **Textured, textured front side** | 5.5582 | 458 | 423 |
| **Textured, silver-coated back side** | 2.6146 | 543 | 483 |
| **Smooth, Si active front side** | 3.8977 | 399 | 361 |
| **Smooth, silver-coated back side** | 2.2993 | 458 | 407 |

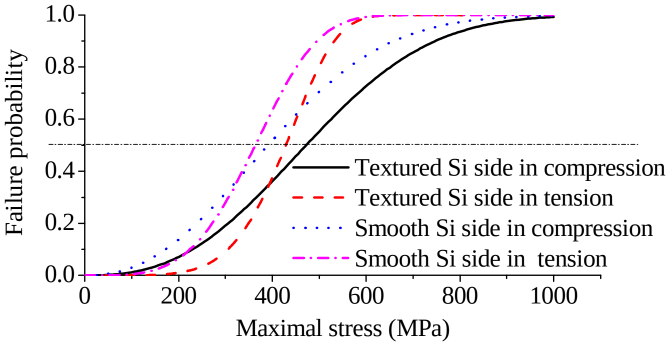

**Figure 7-6: Failure probability of smooth and textured solar cells in bending with either front or back side in tension.**

The textured solar cells broke at a slightly higher stress when the textured side was under compression rather than when it was in tension. There was no dramatic reduction of strength due to stress concentrations caused by the texture. The slightly higher strength when the silver-coated back side was in tension was partly due to the fact that the silver layer also carried part of the tensile stresses. In fact, when the silver layer was taken into account for the S32 type (see appendix 9.2), the stress in the silicon under a 3 µm silver layer was reduced by 3% compared to the case without taking silver into account, and by 12% with an 11 µm silver layer. These values were calculated by considering an elastic behavior of the silver, which was no longer the case when the bending deformations of the cell were high. If the silver deformed plastically, the stress reduction in the Si was thus less pronounced. Stress in the silicon on the textured side was scarcely changed by taking the silver layer into account (less than 0.2% difference). But as the thickness of silver is not precisely known for each cell, the exact contribution cannot be calculated. Another explanation for the very similar strength of both surfaces despite different treatments is that the critical defects could be created on the edges of the cell during dicing [144]. The similar strength of textured and untextured sides is contrary to the measurements of Münzer *et al*. [148], but as they measured the strength by point-loading (see section 2.2.4), they did not take into account edge defects which are not influenced by surface treatment. Moreover, they used different texturations which could create more severe stress concentrations.

The Weibull modulus was higher, i.e. the scatter of the results was smaller when the texture was in tension. This can be explained by the very regular etching of the textured face, removing most of the defects up to a given size. The size of the defects on the back side was less controlled and varied more, causing higher scatter.

Even though the surface was not textured, similar behavior was measured on the smooth cells. The strength was slightly higher with the silver-coated back side in tension, but the scatter was also more pronounced. This may also be explained by a more careful etching of the front surface, thereby reducing scattering on the front side, and also by the reinforcing effect of the silver layer on the back side. The reduction of strength when the front face is in tension may also be partly due to the stresses caused by the front silver grid deposition, as reported by Schneider *et al*. [149] who observed up to 30% strength reduction.

The strength of the smooth cells was less than the strength of the textured cells. As the textured cells were thinner, they were more polished and etched, thereby removing more defects and increasing the strength. This was in accordance with the results of Kray *et al*. [145]. This also confirms that the texturing process was not responsible for the low strength of the cells compared to the intrinsic strength of silicon, but that more critical defects were present in the solar cell.

The mean strength measured on encapsulated solar cells with textured side in tension was 350MPa. As only four cells were tested, no definitive conclusion could be made due to the brittle behavior, but it showed that no reinforcing effect was obtained with encapsulation.

When integrated as a skin in a sandwich structure, the solar cells are loaded mainly under tension and compression. Therefore, in order to determine the tensile strength, cells were tested in tension as described in section 3.2.9. Figure 7-1 illustrates a cell in the loading set-up. 40 naked and 2 encapsulated solar cells were tested.

From the failure load $F_{\max}$ measured, the tensile strength was calculated as

$$\sigma = \frac{F_{\max}}{Bt_{tens}} \tag{7.11}$$

with $t_{tens}$ the thickness of the cell. As the solar cells did not have a homogenous square section, the thickness used for the calculation was the thickness measured with a micrometer minus the height of the pyramids. This furnished a mean strength value which was certainly slightly overestimated, but gave a better estimation of the stresses in the most loaded zones. In actual fact, due to the shape of the texture pyramids, there were stress concentrations which are calculated in more detail in section 7.2.

All the cells broke at a 45° angle to the loading direction, as observed on the broken sample in Figure 7-7. This is explained by two reasons. Firstly, this is the maximum shear direction, and secondly the usual breaking plan for mono-crystalline Si is the (111) plan. As the solar cells were cut in the (001) plane, with the two edges in the directions [100] and [010], the 111 plan was oriented with a 45° angle to the edges.

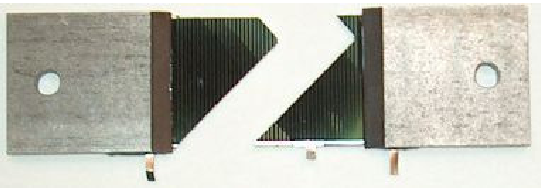

**Figure 7-7: broken solar cells after the tensile test**

Figure 7-8 illustrates the Weibull failure distribution calculated on the basis of the strength measured. The mean measured tensile strength was 221 MPa. This was almost two times lower than that measured in bending, but there was less scatter in the tensile test results. This lower strength could be due to several factors. Firstly, an inexact alignment of the loading set-up can induce stress concentrations on one edge and reduce the load carrying capacity. Secondly, in this test, a large zone of the solar cell was loaded, while in bending only a small zone supported the high bending stresses. As the probability to load critical surface defects increases with the area tested, this explains the lower strength measured in the tensile test. Lower scatter is also explained by this phenomenon. In fact, as a larger zone is loaded, the probability of loading similar critical defects in two different cells becomes higher.

The 95% survival level, calculated with the Weibull probability curve in tension, was 136 MPa. This value can be considered as a basic design value for the asymmetric sandwich structure.

The mean strength measured on two encapsulated cells was 230 MPa, showing no significant change in strength due to encapsulation.

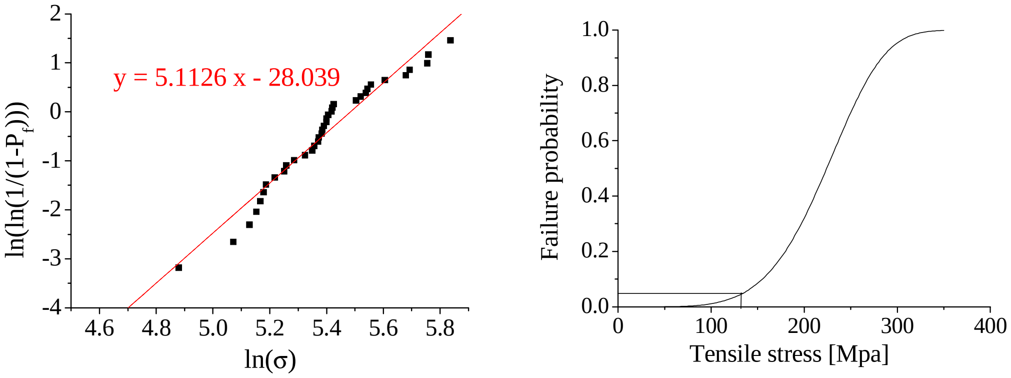

**Figure 7-8: Weibull analysis of the tensile strength of the solar cells. The Weibull modulus calculated in the left hand figure is 5.11, and $\sigma_0$ is 240 MPa. The probability of failure as a function of the tensile stress is plotted in the right hand figure.**

## 7.2. Numerical analysis of stress concentrations in textured solar cells

### 7.2.1. Stress concentration factor in pyramidal texture

Texturation of solar cells is likely to reduce the tensile strength of the textured surface. This is a well known phenomenon already studied in [148]. This effect is, however, dependent on the texturation geometry, since different geometries can cause various stress concentration factors. The exact geometry of the texturation was used in order to predict the stress concentration factor that was possibly responsible for low global cell strength.

The texture produced by photolithography and selective etching [170] of the silicon had a very regular pattern (see Figure 3-2). This regularity allowed the cell to be represented by only one texture unit in the simulation. The exact geometry of the surface texturation was measured with scanning electronic microscopy (SEM). In particular, the radius of curvature of the sharp corner of the texturation was measured on SEM views from a section of broken cells. Figure 7-9 shows a typical cross-section of the cell parallel to the texture axis. The mean measured curvature radius of the pyramid tips was 357 nm. This value was used for the fillet radius of all the sharp edges in the model of the textured surface. To observe the sensitivity to the fillet radius dimensions, simulations were also conducted with double and half size radii.

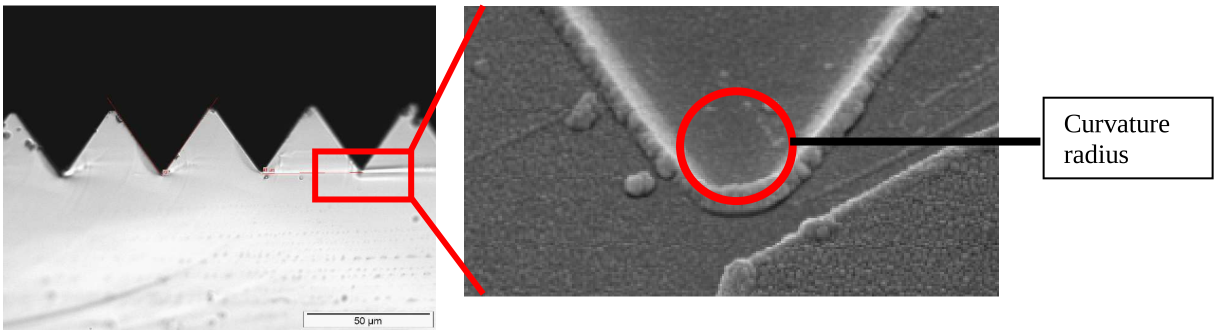

**Figure 7-9: Cross-section of a broken solar cell. The breaking line is aligned with the texture. The radius of curvature of texture pyramid tips was measured on 10 different pictures. The mean value was 357 nm.**

From these measurements, a CAD model was constructed, as depicted in Figure 7-10, and finite element simulation was conducted. In this simulation, the problem had to be solved in two different scales, because the cell thickness was in the order of 100 µm while the curvature radius at the tip of the pyramidal texturation was in the order of 100 nm. A sub-modeling technique was therefore used. A first model was built with element sizes adapted to the global cell scale. This was used to calculate stresses near the region of interest, i.e. the sharp edges in texturation, when the cell was under tensile loading or cylindrical bending. A second model, representing only the region of interest, was then constructed, with very fine elements allowing accurate stress calculation at the sharp edges. The loads applied in this second model were defined with the stresses calculated in the first global model. For the silicon material, an orthotropic material with diamond symmetry was used with the following elastic constants:

C11 =166 GPa
C12 = 64 GPa
C44 = 79.6 GPa

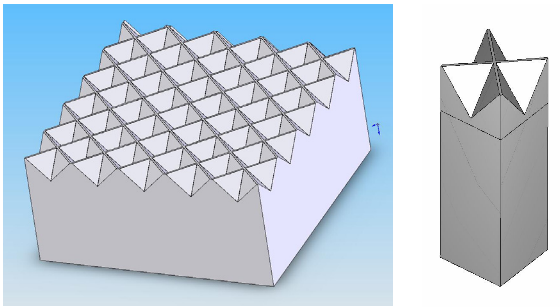

**Figure 7-10: CAD model of the pyramidal texture of the solar cell. The surface texture unit represented on the right was studied.**

Maximal stresses were identified in the stress concentration area at the sharp edges of the texture, and the stress concentration factor is given in Table 7-2 by the ratio $\lambda$ between the maximal stress and the mean stress without texture.

**Table 7-2: stress concentration factor $\lambda$ due to the texture of the surface with different fillet radii in the texture.**

| **Fillet radius** | **No texture** | **714 nm** | **357 nm** | **179 nm** |
|---|---|---|---|---|
| **$\lambda$ tensile loading** | 1 | 6.4 | 7.8 | 12.4 |
| **$\lambda$ bending** | 1 | 5.6 | 6.8 | 10.7 |

The stress concentration factors were similar in bending and tensile loading. It did not change linearly with the fillet radius, but increased rapidly when the radius became smaller. Considering a fillet radius of 357 nm and an intrinsic strength of 6.9 GPa for the silicon, and providing no other defects were present, then due to the stress concentration factor the cell would break at a mean stress of 885 MPa in tensile loading, and 1015 MPa in bending. As the mean measured tensile and bending stresses were smaller (221 MPa and 423 MPa)), this implies that other, more critical, defects were present in the cells, causing early failure. This confirms the results of the bending tests, showing little difference between the strength of the textured and untextured faces.

### 7.2.2. Effect of encapsulation on stress concentrations

To examine the potential reinforcing effect of encapsulation, a 2D simulation of the texture filled with polymer was made. Figure 7-11 represents the 2D model considered for the calculation. Three different valley angles of 0°, 70° (texture of S32 cells) and 110° were used, and a filet radius of 200 nm was considered at pyramid tip. When the

0° angle was used, representing a micro-crack in the material, the crack was filled either at 0 % (only a cover layer), 50 % or 100% by the polymer (from the top of the crack).

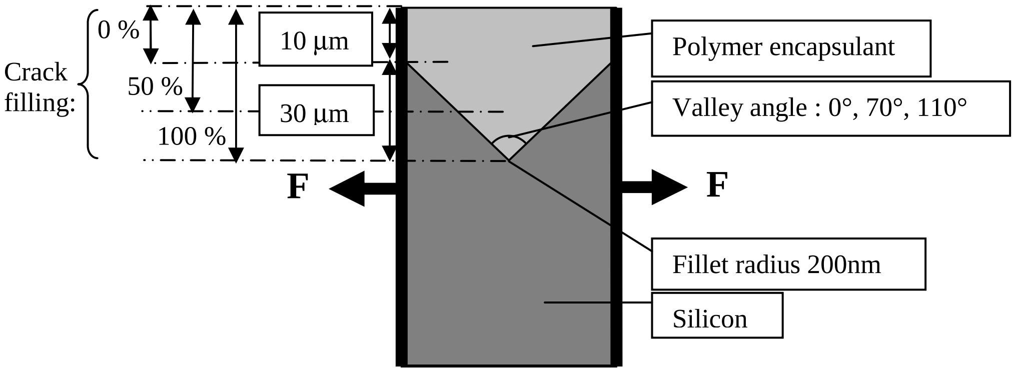

**Figure 7-11: 2D simulation of texture filled with a polymer encapsulant. A displacement was imposed to one edge, while the other was fixed and the stress intensity in the 200 nm fillet in silicon was calculated.**

The effect of the polymer encapsulation can be observed in Figure 7-12, which illustrates the stress reduction at the tip of pyramid texture as a function of the encapsulant modulus. For angles of the same order as those in the texture (70°), polymers with a Young's modulus less than 1 GPa had almost no effect on stresses. The stress was only reduced by 35 % with a Young's modulus of 10 GPa. Therefore, no reinforcing effect can be expected with a silicone encapsulant (0.01GPa).

For sharp cracks (0° valley angle), a 40% reduction could be obtained with a polymer of 1 GPa Young's modulus. However, the crack had to be filled up to the crack tip in order to achieve an efficient stress reduction. When the crack was only filled at 50%, the reduction was only 15 % with a 100 GPa encapsulant, while the coating (0% filling) did not reduce stresses even with a 100 GPa modulus.

Theses results showed that a high modulus encapsulant, with very low viscosity to fill the texturation or the crack, is necessary in order to reduce the stress concentrations at the tip of the texturation or crack; this is hardly attainable using polymer encapsulants.

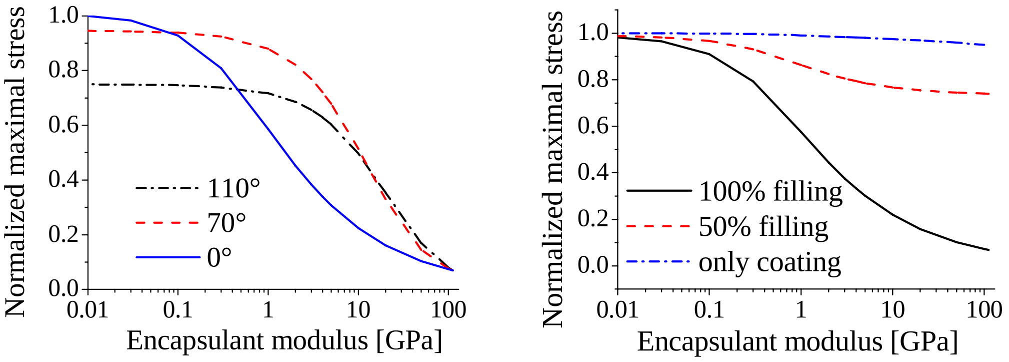

**Figure 7-12: Changes in stress at the sharp tip of the texturation, as a function of the Young's modulus of the polymer filling the texture, for three different valley angles (left) and for different amounts of filling of the 0° crack (right). The stresses are normalized by the maximum stress with 0° angle and no encapsulation.**

The same 2D model was used in order to evaluate the thermo-mechanical stresses in the surface texture caused by the encapsulation, i.e. with a valley angle of 70°. A supplementary 50 µm thick layer of fluoropolymer film was added at the top of the model, as represented in Figure 7-11. Two different process temperatures (stress-free state) were used at 20 and 120°C. Maximum thermo-mechanical stresses at the pyramid tip were calculated at -60°C and 100°C. Two different loading cases were studied: no load applied, and a tensile load causing 0.17% deformation, i.e. the mean strain at failure calculated from tensile tests on solar cells. The thermo-mechanical properties of the encapsulation materials used in the simulation are given in appendix 9.3. The CTE of silicon was approximated linearly between 1.65 ppm/K at -60°C to 3.1 ppm/K at 100°C, following the CTE model of Okada [171]. The simulation was conducted assuming a plane stress state. The real case will, however, be between plane stress and plane strain state.

Thermo-mechanical stresses caused by encapsulation are low. Table 7-3 summarizes the thermo-mechanical stresses calculated for the various process and service temperatures and various loading cases. At a low temperature (-60°C), the contraction of the encapsulant causes compression stresses at the pyramid tip. With a process temperature of 120°C, this reduces the tensile stress at the pyramid tip by 11.5 % when tensile strain is imposed. This could therefore slightly reinforce the cell in a case where all critical defects are filled with encapsulant. It is thus advantageous to encapsulate at high temperature to generate compressive stresses in the cell, even though the effect is very limited. At high service temperatures (100°C), if encapsulation is made at room temperature, the tensile stresses generated at the pyramid tip by the dilatation of the encapsulant are negligible, due to the low modulus of the polymer used at this temperature. Thermo-mechanical stresses in the surface texture of silicon, caused by encapsulation, can thus be disregarded for the design of structures integrating solar cells.

**Table 7-3: Normalized thermo-mechanical principal stresses at the tip of a pyramidal texturation (70° angle) for two different process temperatures, two service temperatures, and two loading cases. The stresses were normalized with the maximum principal stress at the pyramid tip without encapsulation at 0.17 % tensile strain of the cell (i.e. measured mean failure strain of cells in tension).**

| Processing temperature [°C] | Normalized stress [%] | | | |
|---|---|---|---|---|
| | T = -60°C Free | T = -60°C Tension | T = 100°C Free | T = 100°C Tension |
| **20** | -3.93 | 95.4 | 0.18 | 100.2 |
| **120** | -11 | 88.5 | -0.26 | 99.9 |

## *7.3. Honeycomb core-to-silver back-contact bonding*

To obtain good bonding of a honeycomb core onto the Ag back-contact of the solar cell, the formation of adhesive menisci between honeycomb cell walls and the Ag surface is a basic condition. In order to predict the shape of the menisci, the contact angle forming between VTA 260 adhesive and the silver backside of the S32 type cell was measured, as described in section 4.1. The sessile drops were cured at 120°C at atmospheric pressure.

Due to the relatively high surface energy of silver (1.25 J/m$^2$ [184]), good wetting of the silver surface by the adhesive was observed. Figure 7-13 shows a sessile drop of adhesive which formed from a small adhesive ball which spread on the cell during curing. The mean advancing angle measured was 21.6 +/- 4.4°, and the mean receding angle was 11.8 +/- 3.6°. The angles were not measured under vacuum, but, as stated in section 4.1, pressure had only a small influence on contact angle in the order of the standard deviation of the measurements. These angles were slightly bigger than those on a carbon prepreg (15.3° and 8.5° for advancing and receding angles). This was due to the roughness of the prepreg, which increased the effective surface and thus improved wetting, as explained in section 4.1.2. The adhesive menisci forming between the solar cell skin and Nomex® were therefore slightly higher (i.e. the adhesive spreads further on honeycomb cell walls) than with carbon skin. The ratio of height over width calculated according to section 4.1 and considering the advancing angles at atmospheric pressure, were 1.07 with solar cells instead of 0.93 in the case of carbon. As it was observed in section 4.2 that during skin peeling from the honeycomb core, the failure initiated in the adhesive meniscus along the honeycomb cell wall (see Figure 4-23), it may be advantageous to have higher menisci to improve bonding. However, as the difference of contact angle is small, this effect should be limited.

Good formation of the resin menisci was verified in the cross-sections of the samples tested in the next section.

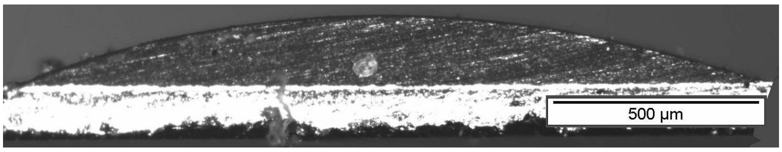

**Figure 7-13: Advancing sessile drop of adhesive on the silver side of solar cells**

Core-to-solar cell bonding was then evaluated. The classic tests for measuring skin debonding energy (DCB, or climbing drum peel test, for example) are difficult to use with solar cells because of their brittleness. Two different tests were thus tried. Firstly, a modified climbing drum peel test was used in order to evaluate the debonding energy. Figure 7-14 illustrates the test used. It was very similar to the test used to measure the debonding energy of the carbon skin, but in the present case, the crack was initiated between the honeycomb and the silicon solar cell fixed onto an Al plate. The honeycomb core was thus peeled with the skin and therefore the stress state at crack tip could differ significantly from the case where the crack propagated at core / carbon skin interface. The debonding energy measured could not be considered as pure mode I and could therefore not be compared directly to the energy measured in section 4.2.

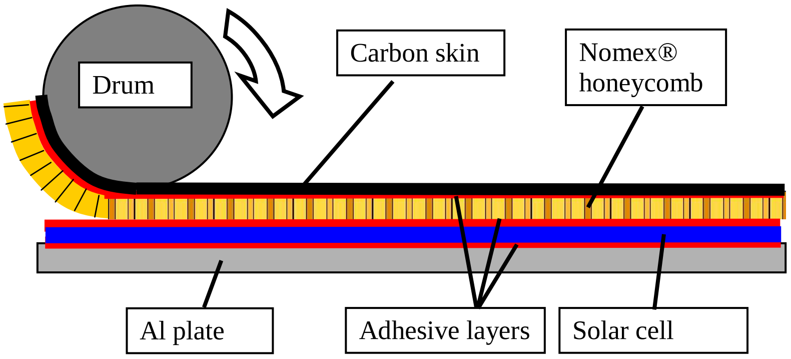

**Figure 7-14: Modified climbing drum peel test to measure solar cell / honeycomb core debonding energy.**

The core used was a Nomex® honeycomb from Euro-Composite. In order to minimize the distance between the drum and the crack tip, it was only 2 mm thick. The carbon skin was made of two plies of 70 $g/m^2$ prepreg at 0° and was bonded with 150 $g/m^2$ VTA 260 adhesive film. The core was bonded to the silver side of S32 solar cells with various adhesive weights deposited on the honeycomb, using the adhesive deposition method. The crack was initiated with a thin non-adhesive film placed between core and solar cell.

During the climbing drum peel test, even with only 15 $g/m^2$ of adhesive, the crack did not propagate at the interface between solar cell and honeycomb; instead, the honeycomb tore and the crack moved to the carbon skin / honeycomb interface. At this interface, the honeycomb tore above the resin menisci formed with the 150 $g/m^2$ adhesive film, as observed in section 4.2. Figure 7-15 shows the debonding energy measured in the climbing drum peel test, which was thus independent of the adhesive weight at the solar cell / honeycomb interface. Only one sample was measured for each adhesive weight, which explains the variations in the measurements. The debonding energy compares well with the tearing energy of Euro-Composite honeycomb as measured in section 3.3.

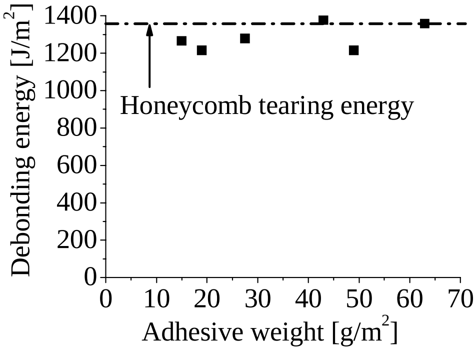

**Figure 7-15: Debonding energy measured with climbing drum peel test**

As mentioned previously, during the climbing drum peel test, the stress state at solar cell / honeycomb interface did not correspond exactly to mode I crack propagation. So, even though no debonding occurred at this interface, it could not be concluded that the $G_{IC}$ of this interface was higher than the tearing energy of honeycomb. However this did show, qualitatively, very good bonding of the honeycomb onto the cell with only 15 g/m$^2$ adhesive.

The second test was a single cantilever beam (SCB) test as described by Cantwell and Davies [65]. Figure 7-16 illustrates the single cantilever beam test set-up. The samples were fixed on a sliding carriage allowing lateral displacement but avoiding rotation of the sample. This self-aligning set-up ensured a mainly mode I crack propagation. The solar cell was bonded onto 2 mm thick GFRP used as a peel arm. The end of the peel arm was loaded in the UTS tensile machine at a speed of 5 mm/min. The core used was 8mm thick Nomex® honeycomb from Euro-Composite, and Hexcel (2 samples of each type).

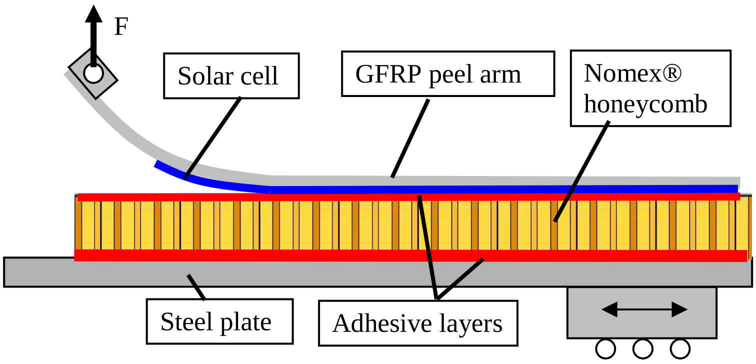

**Figure 7-16: single cantilever beam test to measure solar cell / honeycomb core debonding energy.**

The SCB test confirmed this very good bonding. Figure 7-17 shows an SCB sample after complete debonding. With only 5 +/- 0.5 g/m$^2$ adhesive, failure occurred mainly due to honeycomb tearing above the adhesive menisci. However, during bending of the peel arm, the solar cell cracked and the crack propagated in some places between the solar cell and the GFRP peel arm. Therefore, a quantitative measurement of the debonding energy was hardly feasible.

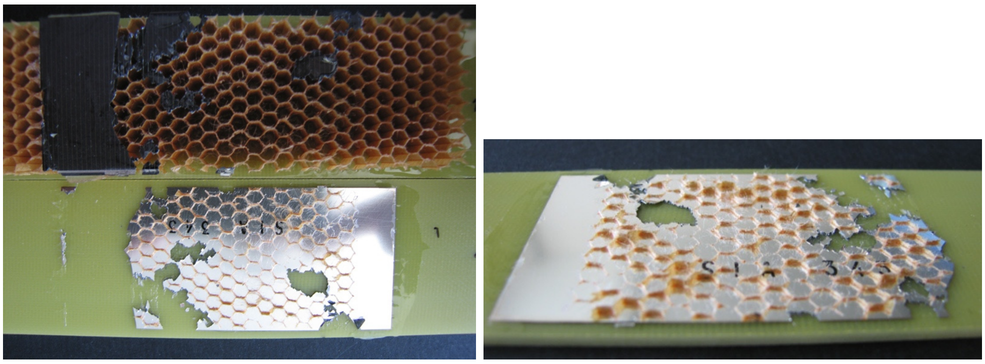

**Figure 7-17: SCB sample after complete debonding. Some parts of the solar cell debonded from the peel arm and stayed on the honeycomb (left). Honeycomb separated from the silver surface mainly by tearing (right)**

The measurement of solar cell / honeycomb core debonding energy was thus difficult due to the brittle behavior of the solar cells, and an accurate calculation of the $G_{IC}$ value of the interface was not possible. However, it was observed that as little as 5 g/m$^2$ of adhesive was sufficient to ensure very good adhesion and cause tearing of the honeycomb during debonding. This observation is thus sufficient for the design of an asymmetric sandwich structure.

## 7.4. Tensile strength of solar cell skin

As silicon cells are very brittle, the critical loading mode of the face is tensile loading, which causes crack opening and propagation in the cells. Compressive forces are less critical because the cracks do not tend to propagate. Therefore, sandwich samples were fabricated with one solar cell as face, and tested in 4-point bending with the solar cell in tension.

The materials used were the same as those used in the symmetric sandwich study. Although 5 g/m$^2$ adhesive was shown to be sufficient to ensure good bonding, a 50 g/m$^2$ adhesive film VTA260 was in fact used in order to allow quicker sample preparation.

The sandwich samples were 32 mm wide (width of one cell) by 460 mm long. One skin was made of 3 layers of carbon prepreg at 0/90/0°. This skin was thicker compared to those used in the symmetric sandwiches studied, but was chosen to avoid potential compressive failure of the skin and to ensure the failure of the solar cell. The other skin was composed of a solar cell in the middle of the beam and 3 layers of prepregs (0/90/0°) on each side of the cell. An overlap of 5 mm was made by the 0° ply on the cell in order to have good stress transfer. Figure 7-18 illustrates this asymmetric sandwich beam. The sandwich samples were cured in two steps in order to control the pressure in the honeycomb cells during the first cure. The first cure was made with the solar cell and adjacent prepreg layers and honeycomb on it. The upper side of honeycomb was open, so that the relative pressure in the honeycomb cell could be controlled, and this was fixed either at -0.9 bar for 18 samples, or -0.3 bar for 12 samples, in order to observe the effect of different processing pressures on the strength of the sample and on the adhesive menisci formation. The second skin was cured in a second step, on the vacuum bag side, so that the solar cell on the mould side was not damaged. The same pressure was used in both cures.

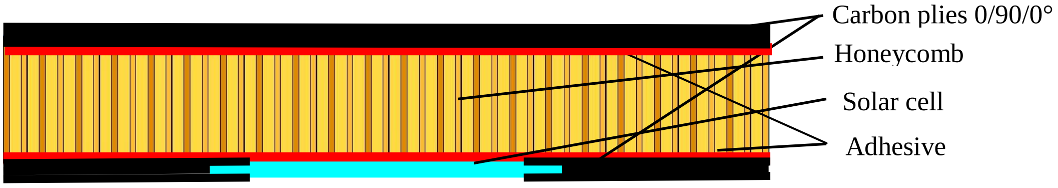

**Figure 7-18: Schematic lay-up of the sample with one solar cell as skin**

The beams were then tested in 4-point bending with a 400 mm span between the outer supports, and a 100 mm span between the loading points with the solar cells centered on the set-up. To calculate stresses in the cell at failure, equations for asymmetric sandwich structures as described in section 2.1.4, should be considered. The equivalent Young's modulus of the carbon skin under compression was calculated with CLT and is given in Table 7-4. The Young's modulus of the cell was the modulus of silicon in (100) direction. The thickness considered for the cell was the same as for the tensile test in section 7.1, i.e. the mean measured thickness minus the pyramid height. Considering that silicon was the skin number 2 and carbon the skin number 1 in Figure 2-3, and assuming a weak core and thin skins, the neutral axis position was

$$e = \frac{E_{f1} t_{f1} \left( \frac{t_{f1}}{2} + \frac{t_{f2}}{2} \right)}{E_{f1} t_{f1} + E_{f2} t_{f2}} = 4.24\ mm \tag{7.12}$$

which is nearly in the center of the sandwich beam, showing a well balanced structure in terms of stiffness. The bending stiffness was

$$D_B = B\left( E_{f1} t_{f1} (d - e)^2 + E_{f2} t_{f2} e^2 \right) = 15.07\ Nm^2 \tag{7.13}$$

and the stress and line load in the solar cell were then given by

$$\sigma_{f2} = \frac{M E_{f2} e}{D_B} = \frac{M}{d t_{f2} B} \qquad N_{f2} = \frac{M E_{f2} e t_{f2}}{D_B} = \frac{M}{dB} \tag{7.14}$$

where *M* was the applied moment on the beam.

**Table 7-4: mechanical properties considered for the calculation of the neutral axis position and bending stiffness of the asymmetric sandwich in order to calculate the stresses.**

| | Modulus in length direction | Thickness |
|---|---|---|
| **Carbon skin** | 70 GPa | 210 µm |
| **Silicon cell** | 130 GPa | 105 µm |

In bending, all the beams tested broke due to tensile failure of the cell. Mean stress calculated in the cell for the 18 samples cured with 0.9 bar pressure was 221 +/-59 MPa, which corresponded exactly to the strength measured during pure tensile tests (see section 7.1). The dispersion of the measurements was very similar to that observed during the tensile tests, and the Weibull probability curves for both loading cases shown in Figure 7-19 were almost identical. This demonstrated that the sandwich processing did not damage the cells. This was further confirmed by the strength of the 12 samples produced with reduced process pressure at 0.3 bar. The strength measured was 211 +/- 59 MPa, which can be considered to be very similar to the previous measurements due to a wide standard deviation and reduced number of samples. As the strength of the cells did not increase by reducing the process pressure, this confirms that when the cells are placed on mould side pressure on the cells does not cause any severe defects during processing. However, if the cells were placed on the vacuum bag side, then the risk of cells breaking during processing would be higher with high process pressure. However, this configuration was not studied in detail, as it presents significant disadvantages. Firstly, the risk of breaking a cell during processing is higher. Secondly, as the cells are air tight, air circulation in the core would be very poor and a good vacuum could not be achieved in the honeycomb cells. Finally, the processing of multi-cell modules is easier when the cells can be placed directly onto the mould and the reinforcing ribbons laid on top of it.

The mean load per unit width in the cell at failure for the samples cured with 0.9 bar pressure was $N_{cell}$ = 23.3 +/- 6 N/mm. In comparison, the line load was 28 N/mm in the case of the 0/90° carbon skin of the sandwich manufactured in one shot with -0.9 bar relative pressure, with 50 g/m$^2$ adhesive and tested with the smooth side under compression (section 5.4). This shows that the mean tensile strength of the cell was not far from the compressive strength of the 0/90° carbon skin. However, the 95% survival stress level, as calculated with the Weibull probability curve of the pure tensile test, was at 136 MPa, which corresponded to a line load of 14.3 N/mm. This load value can be considered for the pre-design of the final structure.

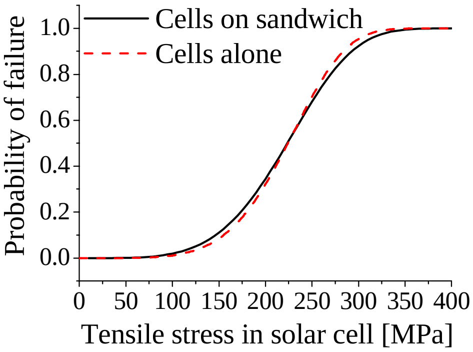

**Figure 7-19: Failure probability of solar cells under tensile loading, calculated using the Weibull parameters measured with 40 tensile tests on solar cells (Weibull modulus m = 5.11 and $\sigma_0$ = 240 MPa), and 18 bending tests on sandwiches comprising solar cells (m = 4.46 and $\sigma_0$ = 243 MPa)**

Micrographs of the cross-sections showed that the resin fillets formed properly on the silver face of the solar cells. Taking into account the size of the fillets measured, an equivalent adhesive weight of about 31 g/m$^2$ could be calculated with the model developed in section 4.1. It showed that nearly half of the adhesive film remained on the surface of the solar cell, as can be observed in Figure 7-20 between the two honeycomb cell walls. The size of the resin fillet was identical for curing at -0.3 or -0.9 bar relative pressure. This was expected as, contrary to the case where the carbon prepreg skin was cured directly under the honeycomb, the amount of adhesive available to form the menisci was not dependent on the pressure exerted by the honeycomb cell walls on the skin. Thus, as soon as the pressure was sufficient to ensure a good contact between core and skin, process pressure had no further influence on the bonding of the solar cells to the core.

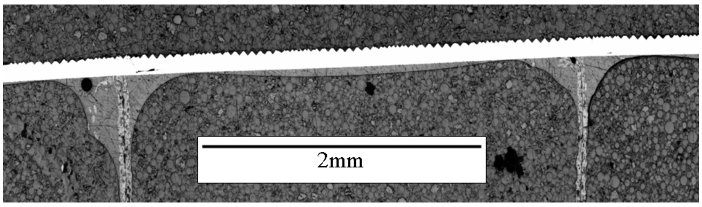

**Figure 7-20: Cross-section of the solar sandwich structure. The solar cell face and 2 honeycomb cell walls are shown. Curing was carried out with -0.9 bar relative pressure in the vacuum bag.**

## 7.5. Development of stress transfer ribbon

To maximize the solar cell surface area, the gap between the cells is smaller than 1 mm. To transfer the stresses from one cell to the next one, the basic idea was to glue a small ribbon made, for example, of glass fibers under the cells over the gap. Figure 7-21 shows a schematic representation of this reinforcing ribbon. It should be noted that in reality the ribbon was very thin and lay between the solar cell and the honeycomb core, and not in the core as represented in the figure. The thickness $t_R$, the overlap length $L_o$, and the material of the ribbon should be chosen to ensure stress transfer so that the reinforcement does not break at a lower line load than the cell. As the tensile strength of the cells is quite low, a very thin glass fiber ribbon, for example, is sufficient to transfer the tensile stresses. Also, under compression, and as the gap between the cells is very small, the risk of local instability of the reinforcing ribbon between the cells is reduced. Therefore, a thin ribbon may also be strong enough to ensure good stress transfer under compression. The first tests were carried out using a ribbon made of one layer of the 70 g/m$^2$ UD carbon prepreg used for the carbon skin. This choice allowed mechanical testing, but could not be used for electrical testing because of the risk of a short-circuit.

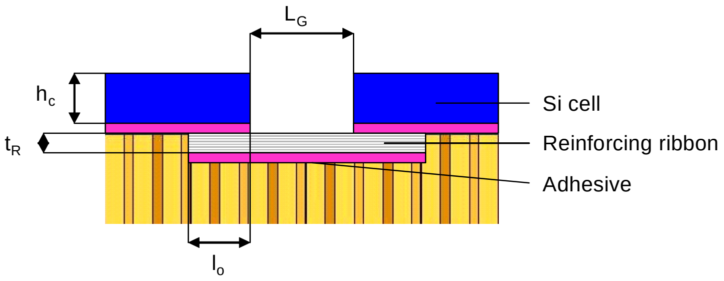

**Figure 7-21: Schematic detail of the local reinforcement between two solar cells**

As the tensile strength of this prepreg was 1700 MPa, the maximum line load with one layer was 119 N/mm, which was significantly higher than the maximum line load causing tensile failure of the cell. Under compression, the strength was 1500 MPa, so that the line load was 105 N/mm. If we consider a worst case in which the ribbon behaves as a slender cantilever beam of length $L_G$ =1 mm, then the Euler formula allows the line load for buckling to be calculated as

$$N_{Euler} = \frac{\pi^2 E\, t_R^3}{3L_G^2} = 113\ N/mm \tag{7.15}$$

with $E$ = 100 GPa and $t_R$ = 0.07 mm. This high line load is perhaps not sufficient to break the solar cell in compression, but as it is not usual to design a structure with high bending strength in one direction and low strength in the other, then the maximum tensile line load of the cells can be considered as the limit in both loading directions. The thin ribbon should therefore be sufficient to ensure a good stress transfer.

Sufficient overlap length should be used to avoid debonding of the ribbon from the cell due to shear. The lap shear strength of the VTA 260 adhesive on Al is given by the supplier at $\tau_{cr}$ = 33 MPa. The adhesion of VTA 260 onto Ag was shown in section 7.3 to be also very good, so that this lap shear value allowed a first pre-design to be made. Considering that the maximal line load supported by the cell $N_{cell}$ = 23 N/mm was transformed in shear at the interface, the overlap length required for the transfer was

$$L_o = \frac{N_{cell}}{\tau_{cr}} = 0.67\ mm \tag{7.16}$$

This calculation did not take into account the stress concentrations on the edge of the ribbon, and more accurate results could be obtained by using a shear lag analysis. But as, for manufacturing requirements and precision, the overlap should be at least 2-3 mm, a margin was present for the design.

Sandwich beams were produced as in section 7.4, but with two solar cells and a 10 mm long UD carbon prepreg ribbon in-between, with the fibers oriented in the length direction of the beam. The local supplementary thickness of the ribbon did not cause any deformation or failure of the cell during processing. The thickness of the ribbon was “absorbed” by the honeycomb.

The beams were tested in 4-point bending as in section 7.4, with the cell and the ribbon under compression. To calculate the stress in the ribbon, an asymmetric sandwich with one skin made of one layer at 0° under compression (E = 100 GPa), and a second skin made of a 0/90/0° layer in tension (E = 83 MPa) was considered for the gap. The neutral axis position was at 5.83 mm from the middle of the ribbon, and the bending stiffness was 10.6 $Nm^2$ over the ribbon. The curvature of the sandwich beam under bending would therefore not be constant, but would be more pronounced over the ribbon.

All the beams failed due to compressive failure of the ribbon at a mean stress of 396MPa corresponding to a line load of 27.7 N/mm. This was smaller than the theoretical strength, but still larger than the maximum line load supported in tension by the cell and therefore sufficient to build panels with symmetrical strength. The difference between the predicted and the experimental strength was due to bad compaction of the carbon ribbon over the gap as it was not pressed against the mould during processing. This could be improved by filling the gap between the solar cells with an encapsulant, so that the ribbon is on a completely flat surface.

Small size fiber ribbons thus showed sufficient strength to ensure a load transfer from cell to cell. The carbon ribbons actually used should be replaced by glass fiber ribbons of similar mechanical properties to avoid electrical short-circuits.

## 7.6. Encapsulation of solar cells

Solar cells have to be protected against environmental attacks. As the aim of this project is to produce the lightest possible solar sandwich structures, a light polymer encapsulation was used instead of the traditional, heavy glass encapsulation. The materials used have to satisfy following requirements:

- High light transmission (>95% ) in visible and UV range
- Operating temperature from -60 to 100°C (for a high-altitude solar plane)
- UV stability to avoid loss of properties during lifetime
- Good moisture barrier properties
- Light weight

Various materials can be used for this special application. Some examples are proposed in Table 9-2 and Table 9-3 in appendix 9.4. Every material has advantages and disadvantages, so the best compromises have to be found. The fluoropolymers delivered by Solvay-Solexis were especially studied, as their high light transmission is promising when targeting maximum solar module efficiency. The encapsulation process using these films was investigated, with special attention to adhesion problems.

As the encapsulated solar cell comprises layers with various thermal and mechanical properties, thermo-mechanical stresses may appear in the encapsulation due to the wide temperature variation. An FEM model was developed to assess the thermo-mechanical stresses in the encapsulation materials, in the cells, and the electrical connections between cells. Details of this model can be found in appendix 9.6.

### 7.6.1. Materials and methods

A 50 µm thick fluoropolymer film was used. Figure 7-22 shows that its light transmission, as a function of wavelength, is in the order of 96 % on the largest part of the solar spectrum (see appendix 9.5), which is better than glass. Its surface reflection is also low due to its low refractive index (~1.34). To compare the adhesion obtained, a 12 µm thick polyethylene terephthalate (PET) film coated with $SiO_2$ by plasma enhanced chemical vapor deposition (PECVD) (film used, for example, in the packaging industry [172]) was also used for encapsulation.

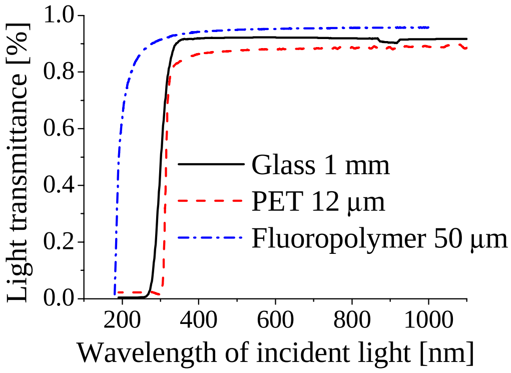

**Figure 7-22: light transmission of 50 µm thick fluoropolymer film, 12 µm thick PET film and 1 mm thick glass (microscope slides)**

Like most of the fluoropolymers, the selected film does not adhere with adhesives. Therefore to improve adhesion, a $SiO_2$ layer was sputtered onto the film under $O_2$ plasma with a Pfeiffer Vacuum Spider-600. The film was exposed to $O_2$ plasma during 30 sec at room temperature with 300W power and $SiO_2$ was then sputtered during 1 min at a deposition rate of 39.1 nm/min. The film and silicon solar cell of S32 type were then treated with a primer (DowCorning 1200) and glued with silicone. The two parts of the silicone were mixed and then left for 1 hour in the pot to allow removal of the air introduced during mixing of the silicone. A thin layer of silicone was spread on the active side of the solar cell, and this was put under vacuum for 2 min to remove all air bubbles. The film was carefully laid on top of the cell in order to avoid trapping air bubbles. A flat Al plate was laid on the assembly with a 1 kg weight on it (~5 kPa pressure on the cell) and the silicone was cured at 60°C.

Using a razor blade, bands of 10 mm width were cut in the encapsulation on the surface of the cell and peeled from the cell with 90° peel test at a speed of 10 mm/min to evaluate the adhesion. Figure 7-23 shows the encapsulation film peeled from the solar cell, which was fixed on a sliding carriage to ensure a constant 90° peel angle. An evaluation of the adhesive fracture toughness would have required knowing precisely the elasto-plastic behavior of the film in tension and in bending [161, 173-176] and was thus beyond the scope of this study. Instead, the peeling force per unit width was used in order to compare the different samples.

As moisture penetration in encapsulation has to be avoided mainly because of the freezing / unfreezing cycles during use, water vapor transmission rate (WVTR) was measured for the fluoropolymer and PET films at 27°C to evaluate their water barrier properties. A Systech permeation cell with accuracy equal to 2 $mg/m^2/day$ was used. The moisture permeability was obtained by multiplying the WVTR by the thickness of the film.

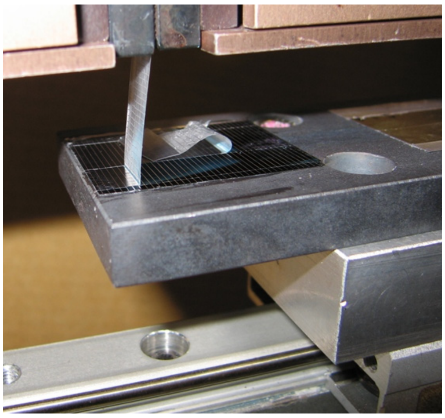

**Figure 7-23: peel test of the encapsulation on solar cell**

### 7.6.2. Results

The $SiO_2$ coated PET film had very good adhesion and a peel force of ~520 N/m, while the fluoropolymer film without surface treatment had no adhesion with the silicone glue. The peel force could not be measured, as the film was removed only by bending.

The $SiO_2$ plasma deposition completely changed the surface properties. The wettability of the surface was increased, as illustrated by the water droplets shown in Figure 7-24. This then allowed very good adhesion to be obtained with silicone adhesive. The mean peel force measured was 586 N/m. The peel arm deformed plastically, so the peeling energy could not be calculated easily. After peeling, some silicone was found on both the film and the cell, showing that the cohesive limit of silicone was reached.

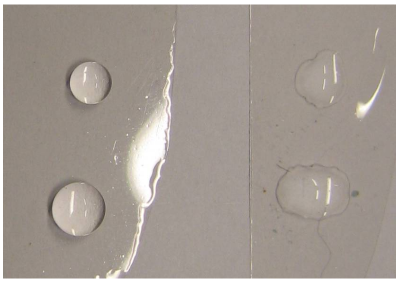

**Figure 7-24: water droplets on fluoropolymer film without surface treatment (left) and with $SiO_2$ plasma deposition (right). Wettability was increased and the droplets spread onto the film.**

The WVTR and light transmittance are summarized in Table 7-5. Contrarily to $SiO_2$ coated PET, the water vapor permeability of the fluoropolymer films was not significantly reduced by $SiO_2$ sputtering, probably due to the discontinuity of the coating layer.

**Table 7-5: WVTR at 27°C, moisture permeability, and light transmittance of PET and fluoropolymer films, with $SiO_2$ coating.**

| | **WVTR [g/m$^2$/day]** | **Permeability [g μm/m$^2$/day]** | **Transmittance at 700 nm** |
|---|---|---|---|
| **PET 12 μm** | 17 | 204 | 0.88 |
| **PET 12 μm + 10nm $SiO_2$** | 1 | 12 | 0.89 |
| **Fluoropolymer 50 μm** | 0.47 | 23.5 | 0.96 |
| **Fluoropolymer 50 μm + 20 nm $SiO_2$** | 0.36 | 18 | - |

## 7.7. Prototype 4 cells curved sandwich panel

In order to prove the manufacturability of curved asymmetric sandwiches with solar cells as a skin, a prototype module was produced. Four cells were fixed together with adhesive tape with a 1 mm gap in-between and placed in an Al mould with a simple curvature of 2 m$^{-1}$. Reinforcing ribbons of width equal to 10 mm were placed over the gaps around the cells. Adhesive film (50g/m$^2$) was laid over that, and the honeycomb core was then placed on top of it, and closed using the 0/90° prepreg skin with 50 g/m$^2$ adhesive. The assembly was cured under a vacuum bag with -0.7 bar relative pressure. The cells did not break during manufacturing due to the curvature, but broke locally where the adhesive tapes were placed. This underlined the need to have a very regular molding surface. In fact, as during the final process the cells would be held together by a continuous encapsulation, the surface in contact with the mould would be smooth.

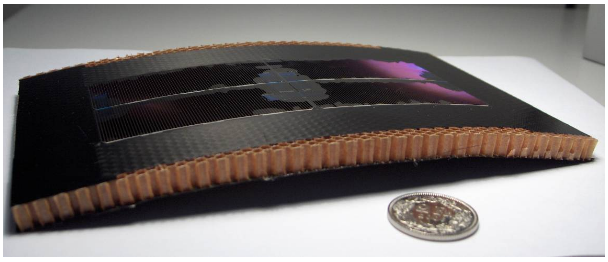

**Figure 7-25: curved prototype sandwich panel with 4 integrated solar cells as a skin**

## 7.8. Summary

- The strength of mono-crystalline Si solar cells in 3-point bending was found to be equal to 420 MPa, which is only 6% of Si intrinsic strength. The strength was similar when measured in bending with the textured side under tension or compression, as well as with the smooth cells without texturation. This showed that the texture is not responsible for the early failure of the solar cells. More severe defects cause the failure of the cell.

- The polymer encapsulation did not improve the load-carrying capacity of the cell, as confirmed by a numerical analysis. Only a hypothetical high modulus encapsulant (~10 GPa), sufficiently fluid to fill cracks completely, would increase efficiently the load-carrying capacity of the cell, so that the most effective approach to increase the strength is to suppress superficial defects on the cell.

- The calculated thermo-mechanical stresses in the texturation, caused by the CTE mismatch with a silicone encapsulant, were negligible and can thus be disregarded in the design of structures with integrated cells.

- The bonding of solar cells onto Nomex® honeycomb was shown to be very good with only 5 g/m$^2$ adhesive. This offers the possibility of further weight saving by using a small adhesive quantity.

- The mean strength of an asymmetric sandwich beam integrating solar cells was, in the worst loading case, 80 % of the strength of a symmetric sandwich beam with 0/90° skins of 0.14 mm thickness. The strength of the cells was not changed by sandwich processing.

- A potential encapsulation solution was developed using fluoropolymer films having high transmittance, together with Sylgard 184 silicone. The adhesion problem was solved by $SiO_2$ plasma sputtering onto the films.

- Thin glass-fiber ribbons were sufficient to ensure a good stress transfer between the cells, thus enabling the manufacture of large-size flat or curved panels of the desired geometry with balanced properties, i.e. similar failure loads of the different elements of the sandwich structure.

# CHAPTER 8. CONCLUSIONS AND PERSPECTIVES

## 8.1. General summary

The aim of this thesis was to investigate the detailed failure mechanisms and their relation to the strength of ultra-light composite sandwich structures integrating solar cells as a load-carrying element, in order to eventually achieve an optimized structural design. Such ultra-light solar panels can be used as structural elements, for example, on solar aircraft, solar cars, or satellites. This investigation presented two major challenges.

Firstly, optimal selection and dimensioning of the constituents of the structure had to be established, i.e. each component had to be selected so that it would fail at the same load level in the final composite structure. Therefore, an accurate knowledge of the mechanical properties of each component, as well as an understanding of the dominant failure mechanisms, required special attention. To this end, the unknown mechanical properties of the solar cells had to be identified. Similarly, an in-depth study of core / skin debonding mechanisms was carried out.

Secondly, a processing window had to be defined in order to achieve optimal processing parameters, which might not necessarily be the same for the individual components, so that the highest strength-to-weight ratio of the complete structure could be attained. It was anticipated that high levels of consolidation pressure, usually beneficial to limit skin porosity, would lead to a number of instability phenomena such as local buckling of the skin, or even failure of the brittle solar cells.

The materials selected were low density Nomex® honeycomb for the core, carbon fiber prepregs and mono-crystalline silicon solar cells for the skins, and epoxy adhesives for core-to-skin bonding. Both symmetric (CFRP / honeycomb / CFRP) and asymmetric (Si cell / honeycomb / CFRP) sandwich structures were studied.

The bonding of the honeycomb core to the skins was investigated by measuring the debonding energy in mode I as a function of adhesive weight. To this end, a method was developed to allow fine tailoring of the adhesive quantity between 5 and 100 g/m$^2$. In addition, a model was devised to predict the size and geometry of the menisci forming between the honeycomb cell walls and the skin, based on the contact angles. This was used to find a correlation between adhesive weight and debonding energy. A new video-based method was also developed to measure the tearing energy of the honeycomb core. Debonding of pre-cured carbon skin from the core revealed two different failure regimes, depending on adhesive weight. Below 40 g/m$^2$ adhesive, failure was mainly due to cohesive failure of the adhesive menisci and partly to adhesive failure between the honeycomb cell wall and menisci, in which case debonding energy increased quickly with adhesive weight. Above 40 g/m$^2$, the honeycomb tore and debonding energy increased slowly with adhesive weight. Debonding energy measured in this regime corresponded well to the tearing energy of honeycomb measured with the video-based method. The transition point between the two regimes offered the highest debonding energy-to-weight ratio, as represented in Figure 8-1a and the optimum adhesive weight for this failure mode was thus 35-40 g/m$^2$ adhesive in the resin menisci. Bonding of the Ag back contact of the solar cells onto the core was very good. The debonding energy could not be measured accurately due to the brittle behavior of the cells, but the honeycomb began to tear with only 5 g/m$^2$ adhesive, indicating that such a low adhesive weight was indeed sufficient to ensure good core-to-solar cell skin bonding.

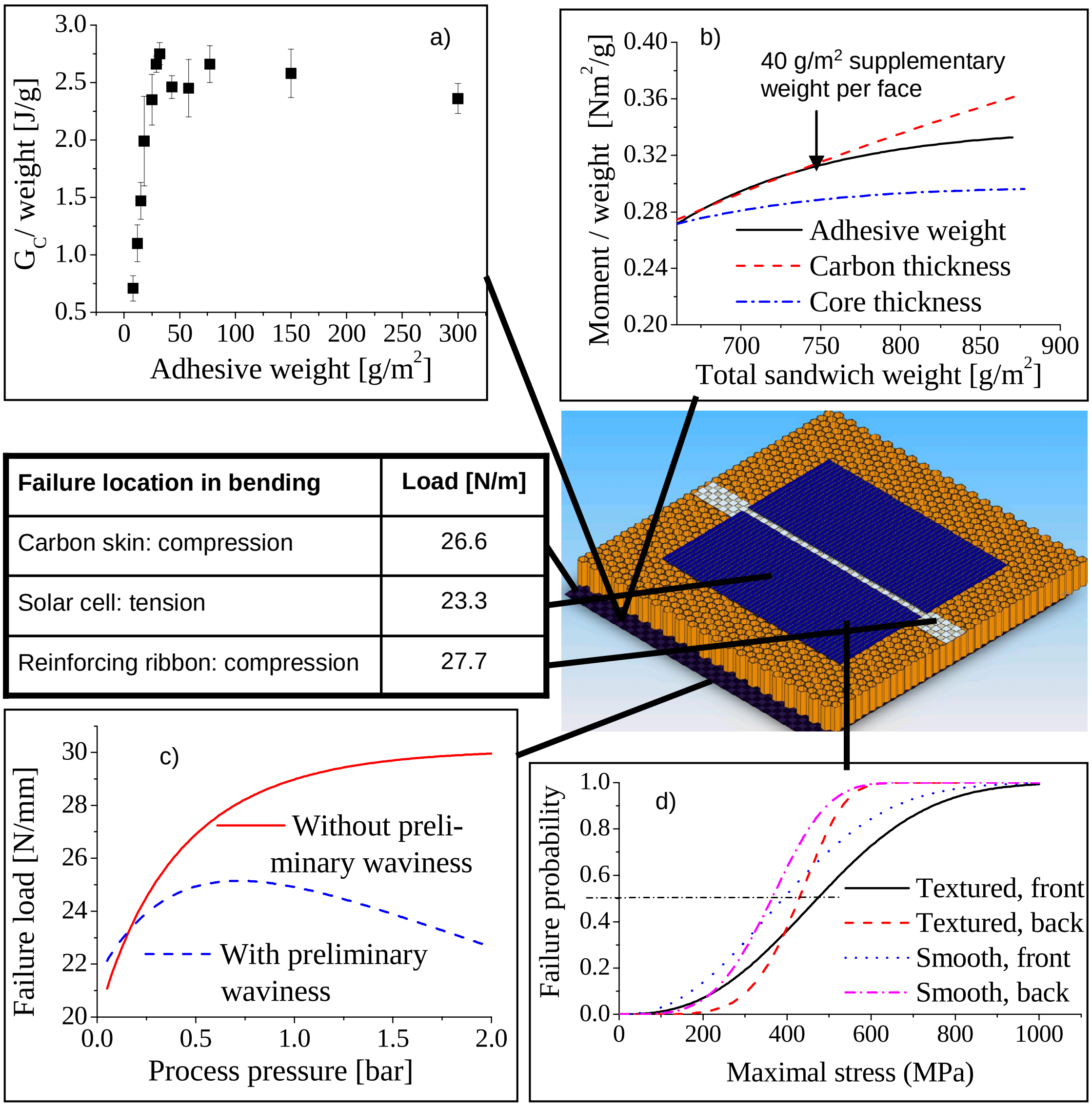

| Failure location in bending | Load [N/m] |
|---|---|
| Carbon skin: compression | 26.6 |
| Solar cell: tension | 23.3 |
| Reinforcing ribbon: compression | 27.7 |

**Figure 8-1: Successive steps for investigating ultra-light photovoltaic sandwich structures: a) measurements of core / skin debonding energy and correlation with the failure mechanisms, b) influence of adhesive weight on sandwich bending strength, c) investigation of the relation between processing pressure, micro-structure, and strength, d) mechanical analysis of solar cells in bending, with various surface preparations.**

The bending strength of symmetric sandwich beams as a function of adhesive weight was also analysed. It was highlighted that the adhesive had a stabilizing effect on the skin and increased the bending strength of the beam by increasing the dimpling and wrinkling loads of the skin. Classic models predicting dimpling and wrinkling loads of the skin were improved to take into account the stabilizing effect of the resin menisci, leading to a very good correlation with the experimental measurements. The models were used to calculate the strength-to-weight ratio by varying either adhesive quantity, carbon, or core thickness, as represented in Figure 8-1b. The results showed that the best adhesive quantity for the selected materials was ~40 g/m$^2$, less adhesive providing lower strength-to-weight ratio, more adhesive being less efficient than an increased carbon thickness.

Processing pressure was found to have a considerable influence on the strength of the sandwich elements. The size of adhesive menisci, and skin waviness, both increased with processing pressure. As these two effects had a conflicting influence on the strength of the sandwich beams, an optimum pressure providing the highest strength-to-weight ratio was determined and found to be equal to 0.7 bar, as shown in Figure 8-1c. To this end, a wrinkling model taking into account preliminary waviness of the skin and menisci size was developed, and this confirmed the observation of local compressive failure of the core.

The experiments also pinpointed the difficulty of controlling vacuum pressure inside the honeycomb cells closed on both sides by the skins during curing. Deficient vacuum in the cells could impede menisci formation and lead to poor bonding of the skin.

Mechanical analysis of solar cells confirmed their brittle behavior. The mean tensile strength was 221 MPa (only 3% of silicon intrinsic strength) and the 95 % survival level determined with a Weibull probability curve ($m = 5.11$, $\sigma_0 = 240$ MPa) was 136 MPa. Similar bending strength measured for textured and smooth cells (Figure 8-1 d) showed that the texturation of the cells was not responsible for the low strength, but that more severe defects were present either on the surface or on the edges of the cells. FE modeling of the textured surface confirmed this observation. FEM also revealed that no significant reinforcing effect can be obtained with polymer encapsulation, and that the thermo-mechanical stresses caused by the CTE mismatch with encapsulation can be disregarded. Furthermore, successful encapsulation of the solar cells with highly transparent fluoropolymer films was made possible by sputtering $SiO_2$ onto the films in order to enhance adhesion with silicone adhesive.

Finally asymmetric sandwich structures with integrated solar cells and local reinforcing ribbons showed balanced mechanical properties. These different elements did in fact have similar failure loads between 23.3 and 27.7 N/m as represented in the table in

Figure 8-1. This demonstrated the feasibility and the interest of such ultra-light photovoltaic structures with a total weight of ~ 800 g/m$^2$ and a specific power density of ~250W/kg, and with similar strength and stiffness as symmetric (CFRP / honeycomb / CFRP) sandwiches weighing ~750 g/m$^2$.

## 8.2. Concluding discussion

Material and process optimization in multi-material structures requires a knowledge of the interplay between material parameters (eg, mechanical and rheological properties), processing variables (eg, temperature, pressure and consumables), residual stress state (due to thermo-mechanical contrasts between constituents) and ultimate properties. In the case of ultra-light photovoltaic sandwich structures, and more generally to optimize functional integration, a further challenge is due to structural asymmetry (and corresponding complex failure modes) and processing asymmetry (and associated complex micro-structural asymmetry).

Step-by-step analysis of the manufacturing process enables the key phenomena to be highlighted which control the microstructure and mechanical properties of the sandwich structure. When vacuum pressure is applied during one-shot vacuum bag processing, air is evacuated from the honeycomb cell at a rate depending on skin, consumables or honeycomb permeability. This creates a differential pressure pressing the skins against the honeycomb, but with limited deformation due to high prepreg resin viscosity at room temperature.

The following temperature rise for curing initiates many phenomena. The pressure of the air not evacuated from the honeycomb cells increases proportionally to temperature and can cause air to flow through the skin out of the cell when pressure in the cell is higher than pressure out of the vacuum bag. At the same time, the viscosity of the adhesive and prepreg resin drops and enables the resin to flow. The driving forces for the resin to flow are capillarity phenomena (controlled by the surface tensions of the constituents), differential pressure (and associated air flowing out of the core) and gravity. These three competing forces determine the amount of adhesive participating in menisci formation, but also the quantity of “lost” resin flowing to the skin surface and thus the void content of the skins. Whereas gravity can be disregarded when menisci are small, and the capillarity phenomena can be predicted when contact angles are known, the flow phenomenon due to pressure rise in the cell is intricate, since the pressure is not well-controlled, unless perforated core or skin is used. Furthermore, as air circulation is different on the mould side and the vacuum bag side, flow phenomena, and thus microstructure, are asymmetric.

In addition, a drop in the viscosity of the adhesive and prepreg resin enables the fibers to slide on the core and to form waves over the honeycomb cells due to the differential pressure. The depth of the waves, which were shown to favor local instability in the skins, is thus closely related to adhesive and resin viscosities and quantities, to fiber type, to the orientation of plies, and, of course, to differential pressure. Also, pressure can even cause solar cell cracking, or crushing of the core if the strength at curing temperature is too low.

Furthermore, the processing temperature causes polymerization of the resin, which thus modifies the viscosity of the adhesive and prepreg resin. If this occurs during the flow of resin and adhesive, a time-dependency is added to the problem, which makes the prediction of microstructures, especially waves and menisci size, very complex.

Finally, cool-down after curing causes residual stresses to appear in the structure, especially at interfaces between high CTE (adhesive) and low CTE materials (Si, carbon). Despite the fact that no effects of these stresses were observed in the present case, they could nevertheless become more critical when higher curing temperatures or low application temperatures are used, and then cause deformation of the structure, additional micro-damages, and thus a decrease in the strength of the structure [11, 185-187].

All these intricate phenomena were not extensively studied in this work. Nevertheless, it was clearly established that maximum processing pressure was not necessarily the best choice for such ultra-light structures. This constitutes a very useful step towards the selection of optimal processing parameters, in particular the choice of pressure and temperature. A main conclusion is also that the control of pressure in the honeycomb cells is a key for the optimization of the microstructure.

Detailed modeling of the processing dynamics and micro-structural changes is, however, useless if the targeted optimal microstructure is unknown. In depth understanding of the microscopic failure mechanisms, and especially of the role of resin menisci, is thus required. The adhesive menisci were shown to have two major effects on the mechanical behavior of the sandwich. First of all, they ensured a very strong core-to-skin bonding, enabling the debonding energy to be higher than the cracking energy of bulk adhesive, as already stated by Okada and Kortschot [70] in the case of heavier honeycomb core. Secondly, in contrast to thicker skins [52], the menisci have a considerable effect on the thin sandwich skins, by enhancing the strength to local instability of a skin under compression, which was shown to be the dominant failure mode of the CFRP skins.

Due to the complex 3D geometries of honeycomb cells and adhesive menisci, the relation between meniscus size, geometry, and measured debonding energy is difficult to establish. It would require an accurate identification of the crack path and constitutive micro-damage models for each different zone on this path (crack initiation in the meniscus, crack propagation in the meniscus, crack propagation at meniscus / Nomex® interface, etc). Such modeling could lead to an understanding as to which meniscus geometry favors the maximization of debonding energy, and thus confirm whether high menisci are advantageous, as measured by Chanteranne [102], or if other shapes could further improve bonding. Similarly, the present investigation enabled a relation to be established between menisci size and reinforcement of the skin, but a 3D model of the skin with adhesive menisci on the surface would enable the shape of the menisci to be optimized in order to maximize the strength.

The positive effects of the resin menisci on the mechanical properties thus show that the processing parameters have to be carefully selected, in order to maximize menisci size. However, as observed in this work, the stiffening effect of the adhesive is comparable to that obtained by increasing skin thickness (with the same weight increase) with an adhesive weight smaller than 40 g/m$^2$, whereas the stiffening effect obtained with a thicker skin is then much more pronounced if more than 40 g/m$^2$ are added. This further demonstrates that the adhesive joint cannot be optimized in isolation, but that the structure has to be considered globally.

Another prerequisite for optimal design and processing is a detailed knowledge of material properties. Silicon solar cells are not usually used as structural elements and their strength therefore had to be determined. The highly brittle behavior of the silicon was highlighted, due to its low toughness (0.9 MPa m$^{1/2}$ [142], glass is 0.8 MPa m$^{1/2}$). In fact, a defect size in the order of 10 nm can already dramatically reduce the strength of the cells [137]. Thus, despite the very high intrinsic strength of silicon (6.9 GPa), its brittleness is clearly the limiting factor for the use of solar cells as load carrying elements. As it is very difficult to remove all the defects from the entire solar cell surface with chemical etching, and as defects are also created during solar cell processing after the etching of the wafer [149], the use of a defect healing technique would be necessary in order to increase the strength. Such techniques were, for example, used for defect healing of $SiO_2$–coated PET films with aminosilane solutions [172], or silane sizing of glass fibers [188], and similar treatment could be imagined for solar cells, providing, however, that a healing agent can be found that is able to penetrate the defects and to react chemically with silicon. A surface treatment such as thermal oxidation [137] in order to incorporate defects into the oxide layer could also be used. However, a major challenge of these treatments with solar cells is that they must not alter the optical and electrical properties of the cells, a constraint which further complicates defect healing. Finally, due to the brittleness of the silicon, a classic strength criterion is not sufficient to design a reliable structure. In fact, with such constituents, probabilistic failure analysis has to be used to allow for the possible very low strength of a few cells in a sandwich panel. This has thus to be taken into account when dimensioning a large photovoltaic sandwich structure in order to ensure global reliability.

Finally, despite limited insight into complex chemo-rheological phenomena and 3D failure micro-mechanisms, the methodology and models developed in this work for the optimization of bonding joints and processing pressure are highly useful tools when selecting core, CFRP skin, adhesive, and processing pressure as functions of the type and strength of solar cells used. The following guidelines are suggested for the selection of optimal constituents and processing parameters for such lightweight sandwich structures:

- Select an adhesive with good wetting of core, carbon, and PV skin, and limited viscosity to allow good menisci formation.
- Deposit adhesive on the top of the honeycomb cell walls so as to favor menisci formation
- Select an adhesive quantity such that debonding occurs with a mixity of core tearing and menisci failure
- Ensure good air circulation in the core to avoid resin flowing out of the skin with air, and avoid consumables that absorb resin in order to maximize menisci size and skin quality

- Select a limited curing pressure to avoid skin instability, core crushing, and solar cell failure
- Select a curing temperature that is sufficient to obtain low adhesive viscosity and to ensure good menisci formation, but not too high to avoid too rapid polymerization, to limit residual stresses, and to ensure dimensional stability

## *8.3. Future developments*

Modeling of the processing influences on microstructure, and of the microscopic failure mechanisms can be further improved so as to predict debonding energy and bending strength with other materials. Particular attention should be paid to changing pressure in the honeycomb cells during curing since this determines meniscus formation and skin quality. An interesting complement to the present work could thus be to study the use of perforated consumables, the goal being to find a suitable perforation that allows good air circulation without sucking too much resin out of the prepreg. The use of perforated or notched honeycomb would also enable the so-called caul plates to be used, i.e. rigid plates having the shape of the sandwich structure and placed on the skin under the vacuum bag to ensure flat skins. Thus, many different solutions can still be explored in order to improve the quality.

Future research should also validate a number of new ideas, which emerged during the present investigation of failure mechanisms. Any increase in the strength of the structure closely depends on the strength increase of the silicon cells, which was shown to be difficult. However, as the symmetric (CFRP / honeycomb / CFRP) sandwich always broke due to local instability of the skin, either a stiffer and stronger core, or more stable skins could be used. To this end, stiffer core material such as carbon honeycomb [189, 190] is a potential solution, which could bring enhanced mechanical properties, however at a significantly higher price. The low buckling strength of the skin was due to its low thickness. Therefore, a solution to increase the thickness with constant weight would be to use discrete fiber tows instead of continuous plies. However, if a cross-ply skin is used, waviness of the crossing tows will be induced, which would thus favor instability, as in the case of fiber cloth [191-194]. An interesting solution could thus be the combination of UD plies and fiber tows, for example with a thin UD ply on the core at 90° to the main loaded direction, and discrete fiber tows on it aligned with the loading direction. Detailed investigation of the mechanical properties, and also of the possible manufacturing solutions, of such a lay-up is thus an interesting further development of this work.

Another solution to increase the bending stiffness of the skin without adding weight is to voluntarily introduce voids in it. This will decrease the compressive strength of the skin [195, 196] and is thus the contrary of usual composite processing which aims at removing all voids; however, it might increase the buckling strength of the skin by increasing the moment of inertia [197]. A processing technique allowing a controlled increase in the void content of the skin, by ensuring good skin bonding needs to be developed, for example, by introducing air or solvent in the prepreg resin.

Finally, several challenges still need to be considered in order to implement the present ultra-light photovoltaic sandwich structure in real applications. The size of the samples produced during this work was small compared to the size of the various potential applications previously listed, and a study of methods by which the process could be scaled-up without decreasing quality is necessary. Control of the pressure in honeycomb cores of large-sized panels represents an interesting technical challenge. Similarly, the adhesive deposition method also needs to be adapted to larger sized panels, for example by using heated rollers which press the adhesive onto the core and then peel it.

Moreover, the ultra-light photovoltaic sandwich structure was designed only for static loadings. However, in real applications, it would undergo cyclic loading, cyclic thermal loading, moisture exposure, UV exposure etc. Therefore, complete endurance testing of the structure is necessary to identify the weak points and fatigue resistance of the structure under real conditions. To this end, a test matrix should be designed to take into account the various parameters, and the potential damage to the cells needs to be monitored by electrical measurements in order to ensure maximal photovoltaic efficiency during the lifetime of the sandwich panel. These tests would thus completely validate the structure and open doors for real applications.

# CHAPTER 9. APPENDIX

## 9.1. *Woven carbon fiber skins*

For applications requiring lighter skins than the two plies of UD prepregs at 0/90°, the use of woven carbon can be considered. This solution was briefly studied by producing sandwich panels with 80 g/m$^2$ of plain woven carbon fabric skins, with 20mm wide warp and weft tapes of the type Oxeon-Textrem$^{TM}$. The skins were impregnated by a wet lay-up with R&G Epoxy-L Resin, so that the matrix-weight ratio was about 50% plus 40g/m$^2$ for core-to-skin bonding. The panels were fabricated in two steps. The first skin was laminated onto an Al mould, as presented in Figure 9-1, then a 29 kg/m$^3$ 8 mm thick Nomex® honeycomb core was laid onto the skin, and pressure was applied by a vacuum bag during polymerization at room temperature. The second skin was then produced identically. Panels were made with one and two layers of carbon fabric. The panels were then cut into 460x30 mm beams and tested in 4-point bending with 400 mm between the outer supports, and 100 mm between the loading points.

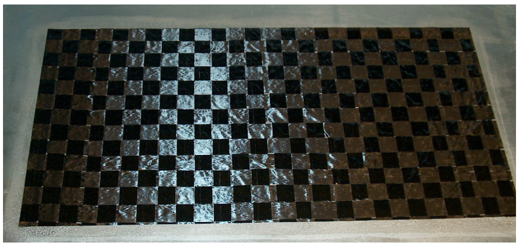

**Figure 9-1: Plain woven Oxeon-Textrem$^{TM}$ fabric skin laminated onto the Al mould**

All the samples broke in the skin under compression between the loading points in 4-point bending at the intersection between warp and weft tapes, due to the step effect. For panels with skins composed of one single layer of fabric, the mean line load measured was 6.8 +/- 0.6 N/mm, corresponding to a mean stress in the skin of 84 +/- 8 MPa. This low strength was due to the very small thickness of the skin, making it highly sensitive to local instabilities on the honeycomb core, which were also favored by the weave of the fabric.

The panels with two layers broke with a mean line load in the skin of 21.6 +/- 2 N/mm, corresponding to a mean stress of 135 +/- 13 MPa in the skin. Greater thickness ensured higher stability and, consequently, significantly increased the strength of the skin under compression. However, the line load at failure was still 23 % lower than for the skins with two 0.07mm thick UD layers at 0/90°. This was partly due to the steps at the intersections between warp and weft, but also to the better quality obtained by using UD prepregs instead of a wet lay-up.

## 9.2. *Effect of the silver layer in bending of solar cells*

Stress reduction in the silicon on the back side of the solar cell is described when considering the silver layer. First, the position of the neutral axis represented in the schematic cross-section of the cell in Figure 9-2 has to be calculated from

$$\int_0^{t_{Ag}+t_{Si}} E\left(z-e\right)dz = E_{Ag}\int_0^{t_{Ag}}\left(z-e\right)dz + E_{Si}\int_{t_{Ag}}^{t_{Si}+t_{Ag}}\left(z-e\right)dz = 0 \tag{9.1}$$

giving

$$e = \frac{\dfrac{t_{Ag}^2 E_{Ag}}{2} + \left(t_{Si}t_{Ag} + \dfrac{t_{Si}^2}{2}\right)E_{Si}}{t_{Ag}E_{Ag} + t_{Si}E_{Si}} \tag{9.2}$$

The bending stiffness can then be calculated as

$$D_{cell} = B\left(\frac{t_{Ag}^3 E_{Ag}}{12} + \frac{t_{Si}^3 E_{Si}}{12} + t_{Ag}E_{Ag}\left(e - \frac{t_{Ag}}{2}\right)^2 + t_{Si}E_{Si}\left(e - t_{Ag} - \frac{t_{Si}}{2}\right)^2\right) \tag{9.3}$$

And finally the maximum stresses at the surface of the silver layer, at the Si surface against the Ag layer, and on the opposite Si face are given by

$$\begin{aligned} \sigma_{\max Ag} &= \frac{MeE_{Ag}}{D_{cell}} \\ \sigma_{\max Si1} &= \frac{M\left(e-t_{Ag}\right)E_{Si}}{D_{cell}} \\ \sigma_{\max Si2} &= \frac{M\left(e-t_{Ag}-t_{Si}\right)E_{Si}}{D_{cell}} \end{aligned} \tag{9.4}$$

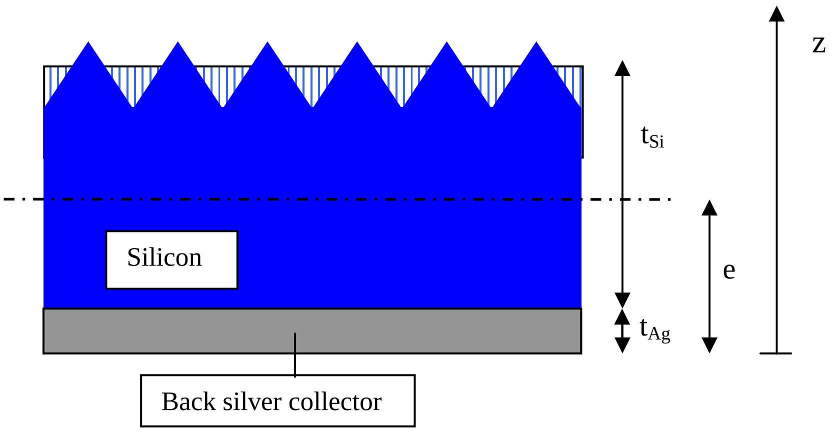

**Figure 9-2: Schematic cross-section of the solar cell with the thickness of silver layer $t_{Ag}$, the equivalent thickness of silicon without texture $t_{Si}$ (calculated to match measured bending stiffness), and the position of the neutral axis.**

To calculate the influence of the silver layer, the thickness of the silver layer was fixed between 3 and 11 µm and the equivalent thickness of the silicon was calculated, so that the bending stiffness measured during a 3-point bending test was equal to that calculated with equation (9.3). Considering $E_{\mathrm{Ag}}$ = 78 GPa, and $E_{\mathrm{Si}}$ = 130 GPa, the stress reduction in the silicon on the silver side was 3% with 3µm silver, and 12% with 11µm silver. Stress in the silicon was almost unchanged on the textured side. The stresses calculated are reported in Table 9-1. This calculation assumed that the silver layer had an elastic behavior, but the yield strength may be exceeded depending on the quality of silver layer (the yield strength varies from 7 MPa for bulk fully annealed silver to more than 400 MPa for cold-worked sheets). If the silver layer deformed plastically, then stress reduction in silicon would be less pronounced.

**Table 9-1: Stresses in the silicon on both surfaces and in the silver calculated for different silver thicknesses. The stresses are mean values calculated according to the results of a 3-point bending test with the textured side under compression.**

| | **No silver** | **3 µm silver** | **11 µm silver** |
|---|---|---|---|
| **$\sigma_{\mathrm{maxAg}}$ [MPa]** | - | 296 | 310 |
| **$\sigma_{\mathrm{maxSi1}}$ [MPa]** | 483 | 468 | 425 |
| **$\sigma_{\mathrm{maxSi2}}$ [MPa]** | - 483 | -483 | -482 |

## *9.3. Thermo-mechanical properties of encapsulation polymers*

Changes in the mechanical properties of the polymers used for encapsulation were measured between -60 and 100°C in order to obtain the appropriate data for simulation.

### 9.3.1. Fluoropolymer film

The fluoropolymer used had very high light transmission in the complete visible range, and also partly in UV, making it very suitable for solar applications. The Young's modulus of the film changed noticeably between -100 and 100°C, i.e. for example, within the temperature range required for high altitude solar plane applications.

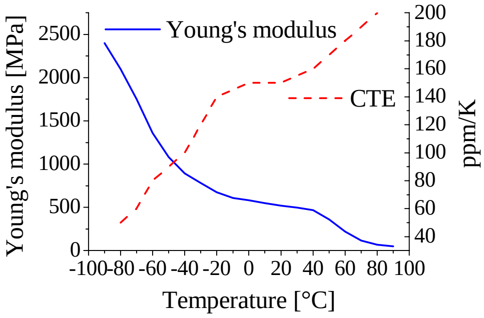

**Figure 9-3: measurements of the Young's modulus and the coefficient of thermal expansion of fluoropolymers films as a function of temperature (measured by supplier)**

For FEM, the properties were approximated by linear segments and were:

- $E_{fluo}$ = 1360 MPa at -60°C, $E_{fluo}$ = 48 MPa at 90°C
- CTE : 80 ppm/K at -60°C, 200 ppm/K at 80°C
- Poisson's coefficient (datasheet): 0.35

### 9.3.2. Silicone

In order to measure changes in the mechanical properties of silicone as a function of the temperature, a 70 µm thick film of silicone DC Sylgard 184 was manufactured in the press and cured at 100°C. It was then cut into 9x50mm samples and measured with a Dynamic Mechanical Analyzer Q800 from the company TA. A mean strain of 3% was used to determine the Young's modulus. Changes in the Young's modulus as a function of temperature are shown in Figure 9-4. The modulus was low and stayed in the same order of magnitude when temperature rose from -65°C to 150°C. This is an advantage as it limits the thermal stresses due to the CTE mismatch between the Si cell and the silicone.

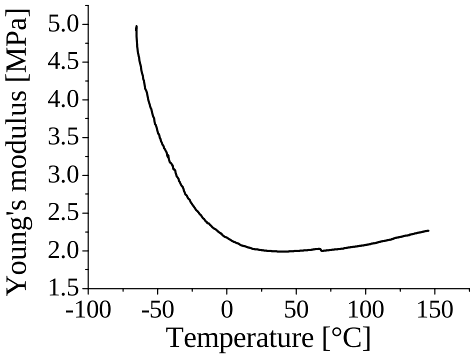

**Figure 9-4: measurement of the Young's modulus of silicone as a function of temperature**

For FEM, the properties were approximated by linear segments and were:

- $E_{sylgard}$ = 4.3MPa at -60°C, $E_{sylgard}$ = 2MPa at 20°C, $E_{sylgard}$ = 2.1MPa at 100°C
- CTE (datasheet): 310 ppm/K
- Poisson's coefficient: 0.49 (almost incompressible elastomer)

## 9.4. Polymer encapsulation materials

**Table 9-2: examples of different possible encapsulation films**

| Material | Advantages | Disadvantages |
|---|---|---|
| Fluoropolymer film by Solexis | T and UV stable<br>High light transmission | Bad adhesion properties |
| Tefzel by DuPont | T and UV stable<br>High light transmission | Limited adhesion properties |
| PET (Mylar type D by DuPont, Terphane10/21) | Easily available and well-known material | Tg at ~80°C |
| PVDC (Ixan PV 910) | Very good moisture barrier properties | Poor UV stability<br>Tg at 7°C |
| Tedlar/PET/Tedlar by Krempel | T and UV stable<br>Good moisture barrier properties | Only 88% light transmission<br>At least 140 mm thick |
| Etimex Vitasolar fiberglass/EVA films | Good mechanical properties<br>Low CTE | At least 500 mm thick |

**Table 9-3: examples of possible encapsulation adhesives**

| Material | Advantages | Disadvantages |
|---|---|---|
| EVA (Elvax 150W by DuPont, Escorene 309 by EXXON) | Often used for encapsulation | Processing at 120°C<br>Yellowing with UV<br>Unknown at low T |
| Silicone DC93 500 or Sylgard 184 | Very good T and UV stability (space use) | Low adhesion without surface treatment<br>Very expensive for DC 93500 |
| TPU (thermoplastic polyurethane) by Etimex | Excellent UV and moisture stability | Available with at least 600 µm thickness<br>Unknown at low T |

## 9.5. Terrestrial solar spectrum

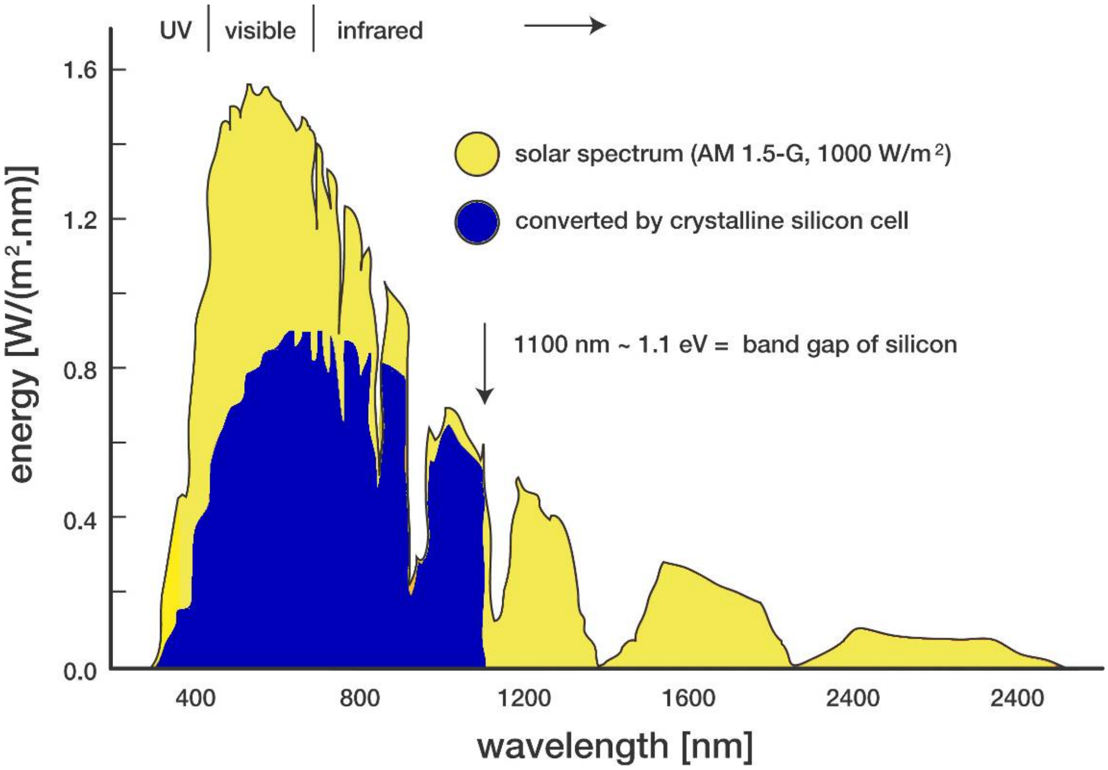

**Figure 9-5: incident solar energy on the earth as a function of wavelength. The complete spectrum has a power of 1000 W/m$^2$ (under standardized conditions AM 1.5 [198]), but only the dark part can be theoretically converted into electricity by silicon solar cells.**

## 9.6. *FEM simulation of stresses in multilayer solar skin*

The solar cell and its encapsulation is a multilayer structure. As the materials in this multilayer structure have different mechanical and thermal properties, the stress and deformation level is different in every layer. This causes interlaminar stresses which can lead to delamination or failure of one layer. To predict the stresses in the different layers, an FEM model was developed. This model consisted of two solar cells connected with a silver contact, and encapsulated on both sides with polymer films. This model enabled the stress level due to CTE mismatch to be evaluated and also predicted the critical points for failure.

### Material and methods

To be able to identify any critical point the simulation consisted of two solar cells connected with one silver contact. Figure 9-6 illustrates the geometry studied. The exact geometry of the solar cells was reproduced, but without surface texturation. Special attention was devoted to the gap between solar cells, as this may be a stress concentration point due to discontinuities.

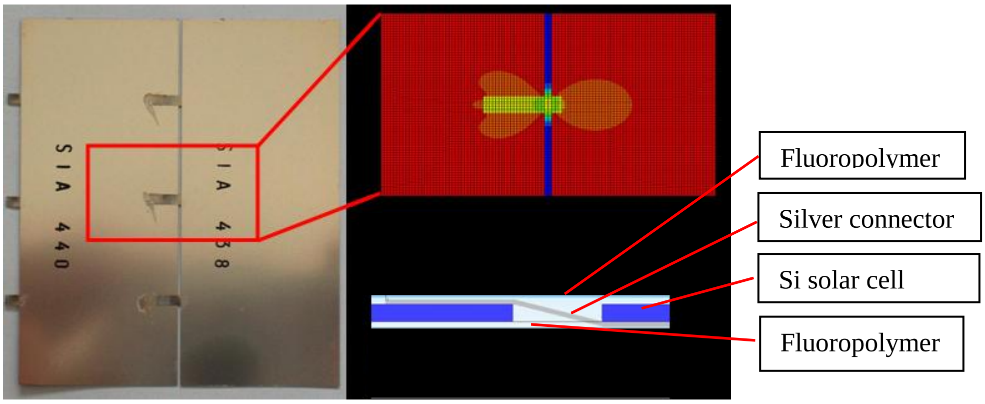

**Figure 9-6: geometry used for thermo-mechanical simulation. Back view of two connected solar cells (left) and schematic cross-section of the cells with silver connector (right)**

For this simulation, the properties of fluoropolymer film were considered for encapsulation film as well as for the encapsulant between the cells. The silver back side of the cells was not taken into account. The material parameters used were the following:

- Si, CTE = 1.4 ppm at -70°C, 2.28 ppm at107°C (linear variation), E = 160 GPa isotropic

- Silver, CTE= 19ppm, E = 78 Gpa
- Fluoropolymer film, CTE = 50ppm at -80°C, 135 ppm at 100°C (linear variation)

  E = 2100Mpa at -80°C, 60 Mpa at 80°C

The material properties were all assumed to be linear elastic. This was only an approximation for small deformations. Depending on the stress level reached in the encapsulation, this hypothesis was no longer true.

The stress-free state was considered to be at 20 °C, and simulations were made at -60°C and 80°C. No external loads were applied.

### Results

Using the simulation model, important stresses were found at the bonding point between Ag electrical connectors and the silicon at low temperature. However, as this technology is used in space conditions, i.e. with greater temperature variations, this point should not be critical.

At a high temperature (80°C) stresses in the electrical connectors due to dilatation of the encapsulant were significant. A maximum tensile stress of 35 MPa was reached. It was still less than the measured tensile strength of the connectors (178 MPa measured in appendix 9.7), but this stress level has to be taken into account for thermal fatigue investigations. However, stresses in connectors could be easily avoided by making a slight “zigzag” shape of the connector between the cells. In the encapsulation, the stress level was under the elastic limit of the material.

So in the conditions used in this simulation, thermal stresses did not cause any failure or permanent deformation. However, the stress level in electrical connectors was not negligible and should be considered when external loads are applied.

## 9.7. *Mechanical strength of Ag electrical connectors*

The voltage of the solar cells is low (~0.6 V/cell). They have to be connected electrically in series in order to reach sufficient voltage. Fine silver connectors are therefore used. If stresses (due to thermal or mechanical loads) are present in the cells, and as the cells have a finite size, there should be a stress transfer from cell to cell. Therefore, the electrical connection would probably undergo stresses too.

To predict the acceptable load on the connector, tensile tests were conducted on the connector of the cells. The same supports were used to glue the cell as those used for tensile test on cells (section 7.1), and the electrical connector was pulled with a grip. Figure 9-7 shows such a connector pulled from part of a broken cell. The connectors broke every time at the cell edge, probably because of stress concentrations due to discontinuities. The mean failure load was 15 N, which represents a mean tensile stress of 178 MPa.

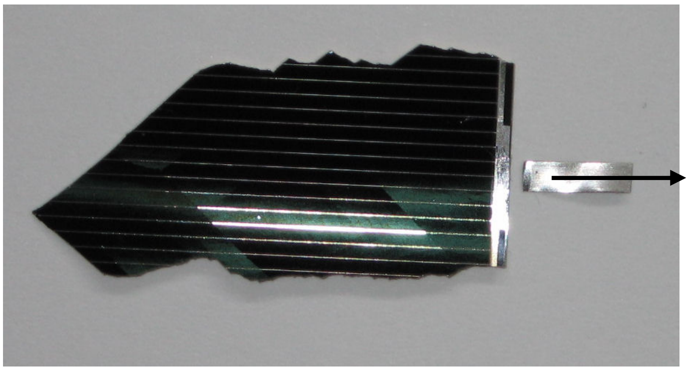

Figure 9-7: Broken connector after pull test on a broken solar cell part

# CHAPTER 10. REFERENCES

1. **B. Beral. *Airbus structure and technology - next steps and vision*. in *16th International Conference on Composite Materials*. 2007. Kyoto.**
2. **W.G. Roesler, B. Sarh, and M.U. Kismarton. *Composite structures: The first 100 years*. in *16th International Conference on Composite Materials*. 2007. Kyoto.**
3. **H. Funke, *Systematische Entwicklung von Ultra-leichtbaukonstruktionen in Faserverbund-wabensandwichbauweise am Beispiel eines Kleinflugzeuges*. 2001: Doctoral Thesis, Universität-GH Paderborn.**
4. **H. Funke, *Development of the ultralight aircraft silence.* JEC - Composites, 2004. 10: p. 52-54.**
5. **A.A. Baker, S. Dutton, and D. Kelly, *Composite materials for aircraft structures*. 2004, Reston, Virginia: American Institute of Aeronautics and Astronautics.**
6. **D.H. Middleton, *Composite materials in aircraft structures,* Longman Group UK Limited. 1990, Harlow: Longman.**
7. **O. Rozant, P.E. Bourban, and J.A.E. Månson, *Manufacturing of three dimensional sandwich parts by direct thermoforming.* Composites Part A: Applied Science and Manufacturing, 2001. 32 (11): p. 1593-1601.**
8. **N. Baldock and M.R. Mokhtarzadeh-Dehghan, *A study of solar-powered, high-altitude unmanned aerial vehicles.* Aircraft Engineering and Aerospace Technology, 2006. 78 (3): p. 187-193.**
9. **E. Cestino, *Design of solar high altitude long endurance aircraft for multi payload & operations.* Aerospace Science and Technology, 2006. 10 (6): p. 541-550.**

10. **G. Romeo, G. Frulla, E. Cestino, and G. Corsino, *Heliplat: Design, aerodynamic, structural analysis of long-endurance solar-powered stratospheric platform.* Journal of Aircraft, 2004. 41 (6): p. 1505-1520.**

11. **E.H. Glaessgen, J.R. Reeder, D.W. Sleight, J.T. Wang, I.S. Raju, and C.E. Harris, *Debonding failure of sandwich-composite cryogenic fuel tank with internal core pressure.* Journal of Spacecraft and Rockets, 2005. 42 (4): p. 613-627.**

12. **D.R. Polland, S.R. Finn, K.H. Griess, J.L. Hafenrichter, and C.T. Hanson, *Global cost and weight evaluation of fuselage side panel design concept.* NASA CR 4730, 1997.**

13. **H.M. Hsiao, S.M. Lee, and R.A. Buyny, *Core crush problem in manufacturing of composite sandwich structures: Mechanisms and solutions.* AIAA Journal, 2006. 44 (4): p. 901-907.**

14. **C.J. Martin, J.W. Putnam, B.S. Hayes, J.C. Seferis, M.J. Turner, and G.E. Green, *Effect of impregnation conditions on prepreg properties and honeycomb core crush.* Polymer Composites, 1997. 18 (1): p. 90-99.**

15. **D.J. Renn, T. Tulleau, J.C. Seferis, R.N. Curran, and K.J. Ahn, *Composite honeycomb core crush in relation to internal-pressure measurement.* Journal of Advanced Materials, 1995. 27 (1): p. 31-40.**

16. **V. Altstadt, F. Diedrichs, T. Lenz, H. Bardenhagen, and D. Jarnot, *Polymer foams as core materials in sandwich laminates (comparison with honeycomb).* Polymers & Polymer Composites, 1998. 6 (5): p. 295-304.**

17. **C. Kassapoglou, S.C. Fantle, and J.C. Chou, *Wrinkling of composite sandwich structures under compression.* Journal of Composites Technology & Research, 1995. 17 (4): p. 308-316.**

18. **F.J. Plantema, *Sandwich construction*. 1966, New York: John Wiley & Sons.**

19. **H.G. Allen, *Analysis and design of structural sandwich panel*. 1969, Oxford: Pergamon Press.**

20. **D. Zenkert, *An introduction to sandwich construction*. 1995, London: Engineering Materials Advisory Services Ltd.**

21. **D. Zenkert, *The handbook of sandwich construction*, EMAS. 1997, Cradley Heath: EMAS.**

22. **T. Bitzer, *Honeycomb technology*. 1997, London: Chapman & Hall.**

23. **J.R. Vinson, *The behavior of sandwich structures of isotropic and composite materials*. 1999, Lancaster: Technomic.**

24. **J.M. Davies, *Lightweight sandwich construction*. 2001, Oxford: Blackwell Science Ltd.**

25. **Hexcel Composites, *Hexweb$^{tm}$ honeycomb sandwich design technology.***

26. **M.F. Ashby and Y.J.M. Brechet, *Designing hybrid materials.* Acta Materialia, 2003. 51 (19): p. 5801-5821.**

27. **J. Verrey, Y. Winkler, V. Michaud, and J.A.E. Månson, *Interlaminar fracture toughness improvement in composites with hyperbranched polymer modified resin.* Composites Science and Technology, 2005. 65 (10): p. 1527-1536.**

28. **A.C. Meeks, *Fracture and mechanical properties of epoxy resins and rubber-modified epoxy resins.* Polymer, 1974. 15 (10): p. 675.**

29. **K.F. Karlsson and B.T. Astrom, *Manufacturing and applications of structural sandwich components.* Composites Part A-Applied Science and Manufacturing, 1997. 28 (2): p. 97-111.**

30. **H. Mahfuz, S. Islam, M. Saha, L. Carlsson, and S. Jeelani, *Buckling of sandwich composites; effects of core-skin debonding and core density.* Applied Composite Materials, 2005. 12 (2): p. 73-91.**

31. **P.A. Lagace and L. Mamorini, *Factors in the compressive strength of composite sandwich panels with thin facesheets.* Journal of Sandwich Structures and Materials, 2000. 2 (4): p. 315-330.**

32. **D. Gay, *Matériaux composites*. 2005, Paris: Lavoisier.**

33. **I.M. Daniel, E.E. Gdoutos, K.A. Wang, and J.L. Abot, *Failure modes of composite sandwich beams.* International Journal of Damage Mechanics, 2002. 11 (4): p. 309-334.**

34. **A. Petras and M.P.F. Sutcliffe, *Failure mode maps for honeycomb sandwich panels.* Composite Structures, 1999. 44 (4): p. 237-252.**

35. **E.E. Gdoutos, I.M. Daniel, and K.A. Wang, *Compression facing wrinkling of composite sandwich structures.* Mechanics of Materials, 2003. 35 (3): p. 511-522.**

36. **A.S. Benson and J. Mayers, *General instability and face wrinkling of sandwich plates - unified theory and applications.* AIAA Journal, 1967. 5 (4): p. 729-740.**

37. **S. Yusuff, *Theory of wrinkling in sandwich construction.* Journal of the Royal Aeronautical Society, 1955. 59 (529): p. 30-36.**

38. **R.S. Chen, *Effect of curing process on mechanical-properties of honeycomb-core sandwich plates.* Composites Engineering, 1994. 4 (4): p. 445-458.**

39. **A.J. Gutierrez and J.P.H. Webber, *Flexural wrinkling of honeycomb sandwich beams with laminated faces.* International Journal of Solids and Structures, 1980. 16 (7): p. 645-651.**

40. **B.J. Harris and W.C. Crisman, *Face wrinkling mode of buckling of sandwich panels.* ASCE Journal of the Engineering Mechanics Division, 1965. 91: p. 93-111.**

41. **W.S. Hemp, *On a theory of sandwich construction*. 1948, Aeronautical Research Council Reports and Memoranda.**

42. **H.R. Meyer-Piening, *Sandwich plates: Stresses, deflection, buckling and wrinkling loads - a case study.* Journal of Sandwich Structures & Materials, 2006. 8 (5): p. 381-394.**

43. **C.B. Norris, *Short column strength of sandwich construction as affected by the size of cells of honeycomb core materials*. U.S. Forest service research note FPL-026. 1964, Wisconsin: Forest Product Laboratory.**

44. **C.B. Norris, K.H. Boller, and A.W. Voss, *Wrinkling of the facings of sandwich construction subjected to edgewise compression. Sandwich construction having honeycomb cores*. 1953, Forest products laboratory: Wisconsin.**

45. **C.B. Norris, W.S. Ericksen, H.W. March, C.B. Smith, and K.H. Boller, *Wrinkling of the facings of sandwich construction subjected to edgewise compression*. 1961, Forest products Laboratory: Wisconsin.**

46. **T.R.A. Pearce, *Buckling of sandwich panels with laminated face plates.* Aeronautical Quarterly, 1972. 23 (May): p. 148.**

47. **T.R.A. Pearce and J.P.H. Webber, *Experimental buckling loads of sandwich panels with carbon-fiber faceplates.* Aeronautical Quarterly, 1973. 24 (Nov): p. 295-312.**

48. **J.P.H. Webber, S. Kyriakides, and C.T. Lee, *Wrinkling of honeycomb sandwich columns with laminated cross-ply faces.* Aeronautical Journal, 1976. 80 (786): p. 264-272.**

49. **R.C. Weikel and A.S. Kobayashi, *On the local elastic stability of honeycomb face plate subjected to uniaxial compression.* Journal of the Aerospace Sciences, 1959. 26 (10): p. 672-674.**

50. **S. Yusuff, *Face wrinkling and core strength in sandwich construction.* Journal of the Royal Aeronautical Society, 1960. 64: p. 164-167.**

51. **N.J. Hoff and S.E. Mautner, *The buckling of sandwich-type panels.* Journal of the Aeronautical Sciences, 1945. 12 (3): p. 285-297.**

52. **R.P. Ley, W. Lin, and U. Mbanefo, *Facesheet wrinkling in sandwich construction*. 1999, NASA: Langley Research Center.**

53. **L. Fagerberg and D. Zenkert, *Imperfection-induced wrinkling material failure in sandwich panels.* Journal of Sandwich Structures & Materials, 2005. 7 (3): p. 195-219.**

54. **S. Yussuf, *Face wrinkling and core strength in sandwich construction.* Journal of the royal aeronautical society, 1960. 64: p. 164-167.**

**55. O.T. Thomsen and W.M. Banks, *An improved model for the prediction of intra-cell buckling in CFRP sandwich panels under in-plane compressive loading.* Composite Structures, 2004. 65 (3-4): p. 259-268.**

**56. P. Minguet, J. Dugundji, and P.A. Lagace, *Buckling and failure of sandwich plates with graphite-epoxy faces and various cores.* Journal of Aircraft, 1988. 25 (4): p. 372-379.**

**57. M. del Pedro, T. Gmür, and J. Botsis, *Introduction à la mécanique des solides et des structures*. 2004: Presses Polytechniques et Universitaires Romandes.**

**58. *ASTM C 393-94, standard test method for flexural properties of sandwich constructions.* Annual Book of ASTM Standards, 1994. 15.03.**

**59. *ASTM C 297-94, standard test method for flatwise tensile strength of sandwich constructions.* Annual Book of ASTM Standards, 1994. 15.03.**

**60. *ASTM D 5528-94a, standard test method for mode 1 interlaminar fracture toughness of unidirectionnal fiber-reinforced polymer matrix composites.* Annual Book of ASTM Standards, 1994. 15.03.**

**61. J.D. Gunderson, J.F. Brueck, and A.J. Paris, *Alternative test method for interlaminar fracture toughness of composites.* International Journal of Fracture, 2007. 143 (3): p. 273-276.**

**62. J.R. Rice, *A path independent integral and approximate analysis of strain concentration by notches and cracks.* Journal of Applied Mechanics, 1968. 35 (2): p. 379.**

**63. J.G. Williams, *Large displacement and end block effects in the DCB interlaminar test in mode-I and mode-II.* Journal of Composite Materials, 1987. 21 (4): p. 330-347.**

**64. J.G. Williams, *End corrections for orthotropic DCB specimens.* Composites Science and Technology, 1989. 35 (4): p. 367-376.**

**65. W.J. Cantwell and P. Davies, *A test technique for assessing core skin adhesion in composite sandwich structures.* Journal of Materials Science Letters, 1994. 13 (3): p. 203-205.**

**66. W.J. Cantwell and P. Davies, *A study of skin-core adhesion in glass fibre reinforced sandwich materials.* Applied Composite Materials, 1996. 3 (6): p. 407-420.**

**67. W.J. Cantwell, R. Scudamore, J. Ratcliffe, and P. Davies, *Interfacial fracture in sandwich laminates.* Composites Science and Technology, 1999. 59 (14): p. 2079-2085.**

**68. J. Ratcliffe and W.J. Cantwell, *A new test geometry for characterizing skin-core adhesion in thin-skinned sandwich structures.* Journal of Materials Science Letters, 2000. 19 (15): p. 1365-1367.**

**69. J. Ratcliffe and W.J. Cantwell, *Center notch flexure sandwich geometry for characterizing skin-core adhesion in thin-skinned sandwich structures.* Journal of Reinforced Plastics and Composites, 2001. 20 (11): p. 945-970.**

**70. R. Okada and M.T. Kortschot, *The role of the resin fillet in the delamination of honeycomb sandwich structures.* Composites Science and Technology, 2002. 62 (14): p. 1811-1819.**

**71. L.A. Carlsson, *On the design of the cracked sandwich beam (CSB) specimen.* Journal of Reinforced Plastics and Composites, 1991. 10 (4): p. 434-444.**

**72. L.A. Carlsson, L.S. Sendlein, and S.L. Merry, *Characterization of face sheet core shear fracture of composite sandwich beams.* Journal of Composite Materials, 1991. 25 (1): p. 101-116.**

**73. S. Prasad and L.A. Carlsson, *Debonding and crack kinking in foam core sandwich beams .1. Analysis of fracture specimens.* Engineering Fracture Mechanics, 1994. 47 (6): p. 813-824.**

**74. S. Prasad and L.A. Carlsson, *Debonding and crack kinking in foam core sandwich beams .2. Experimental investigation.* Engineering Fracture Mechanics, 1994. 47 (6): p. 825.**

**75. A. Shipsha, M. Burman, and D. Zenkert, *Interfacial fatigue crack growth in foam core sandwich structures.* Fatigue & Fracture of Engineering Materials & Structures, 1999. 22 (2): p. 123-131.**

76. **K.N. Shivakumar and S.A. Smith, *In situ fracture toughness testing of core materials in sandwich panels.* Journal of Composite Materials, 2004. 38 (8): p. 655-668.**

77. **D. Vionnet, *Caractérisation des interfaces peau-coeur en nid d'abeille de structures sandwich*. Master thesis, 2006: EPFL.**

78. **M. Charalambides, A.J. Kinloch, Y. Wang, and J.G. Williams, *On the analysis of mixed-mode failure.* International Journal of Fracture, 1992. 54 (3): p. 269-291.**

79. **J.G. Williams, *On the calculation of energy-release rates for cracked laminates.* International Journal of Fracture, 1988. 36 (2): p. 101-119.**

80. **W.S. Burton and A.K. Noor, *Structural analysis of the adhesive bond in a honeycomb core sandwich panel.* Finite Elements in Analysis and Design, 1997. 26 (3): p. 213-227.**

81. **S. Goswami and W. Becker, *Analysis of debonding fracture in a sandwich plate with hexagonal core.* Composite Structures, 2000. 49 ( 4): p. 392.**

82. **T.S. Han, A. Ural, C.S. Chen, A.T. Zehnder, A.R. Ingraffea, and S.L. Billington, *Delamination buckling and propagation analysis of honeycomb panels using a cohesive element approach.* International Journal of Fracture, 2002. 115 (2): p. 101-123.**

83. **D.L. Grau, X.S. Qiu, and B.V. Sankar, *Relation between interfacial fracture toughness and mode-mixity in honeycomb core sandwich composites.* Journal of Sandwich Structures & Materials, 2006. 8 (3): p. 187-203.**

84. **J.D. Whitcomb and K.N. Shivakumar, *Strain-energy release rate analysis of plates with postbuckled delaminations.* Journal of Composite Materials, 1989. 23 (7): p. 714-734.**

85. **D. Guedra-Degeorges, *Recent advances to assess mono- and multi-delaminations behaviour of aerospace composites.* Composites Science and Technology, 2006. 66 (6): p. 796-806.**

86. ***ASTM D 1781-98, standard test method for climbing drum peel for adhesives.* Annual Book of ASTM Standards, 1998. 15.06.**

87. **L.J. Gibson and M.F. Ashby, *Cellular solids, structure and properties*, Pergamon Press. 1988, Cambridge: Cambridge University press.**

88. **G.R. Froud, *Your sandwich order, sir?* Composites, 1980. 11 (3): p. 133.**

89. **J.C.M. Theulen and A.A.J.M. Peijs, *Optimization of the bending stiffness and strength of composite sandwich panels.* Composite Structures, 1991. 17 (1): p. 87.**

90. **O. Murthy, N. Munirudrappa, L. Srikanth, and R. Rao, *Strength and stiffness optimization studies on honeycomb core sandwich panels.* Journal of Reinforced Plastics and Composites, 2006. 25 (6): p. 663-671.**

91. **L.J. Gibson, *Optimization of stiffness in sandwich beams with rigid foam cores.* Materials Science and Engineering, 1984. 67 (2): p. 125.**

92. **T.C. Triantafillou and L.J. Gibson, *Failure mode maps for foam core sandwich beams.* Materials Science and Engineering, 1987. 95: p. 37-53.**

93. **T.C. Triantafillou and L.J. Gibson, *Minimum weight design of foam core sandwich panels for a given strength.* Materials Science and Engineering, 1987. 95: p. 55-62.**

94. **Y. Ding, *Optimum design of honeycomb sandwich constructions with buckling constraints.* Computers & Structures, 1989. 33 (6): p. 1364.**

95. **J. Kim and S.R. Swanson, *Effect of unequal face thickness on load resistance of sandwich beams.* Journal of Sandwich Structures & Materials, 2004. 6 (2): p. 145-166.**

96. **J. Pflug and I. Verpoest, *Sandwich materials selection charts.* Journal of Sandwich Structures & Materials, 2006. 8 (5): p. 407-421.**

97. **A. Ural, A.T. Zehnder, and A.R. Ingraffea, *Fracture mechanics approach to facesheet delamination in honeycomb: Measurement of energy release rate of the adhesive bond.* Engineering Fracture Mechanics, 2003. 70 (1): p. 93-103.**

98. **J.L. Avery and B.V. Sankar, *Compressive failure of sandwich beams with debonded face-sheets.* Journal of Composite Materials, 2000. 34 (14): p. 1176-1199.**

99. **C.K. Berkowitz and W.S. Johnson, *Fracture and fatigue tests and analysis of composite sandwich structure.* Journal of Composite Materials, 2005. 39 (16): p. 1417-1431.**

100. **S.M. Grove, E. Popham, and M.E. Miles, *An investigation of the skin/core bond in honeycomb sandwich structures using statistical experimentation techniques.* Composites Part A-Applied Science and Manufacturing, 2006. 37 (5): p. 804-812.**

101. **G. Allegri, U. Lecci, M. Marchetti, and F. Poscente, *FEM simulation of the mechanical behaviour of sandwich materials for aerospace structures,* in *Experimental techniques and design in composite materials 5*. 2002. p. 209-220.**

102. **J. Chanteranne, *Use of ultra-light adhesive for the metal-honeycomb bonding.* Annales de Chimie-Science des Matériaux, 1987. 12 (2): p. 199-204.**

103. **B.S. Hayes, J.C. Seferis, and R.R. Edwards, *Self-adhesive honeycomb prepreg systems for secondary structural applications.* Polymer Composites, 1998. 19 (1): p. 54-64.**

104. **S. El-Sayed and S. Sridharan, *Imperfection-sensitivity of integral and debonded sandwich beams under compression.* Journal of Sandwich Structures & Materials, 2002. 4 (1): p. 49-69.**

105. **F. Aviles and L.A. Carlsson, *Three-dimensional finite element buckling analysis of debonded sandwich panels.* Journal of Composite Materials, 2006. 40 (11): p. 993-1008.**

106. **F. Aviles and L.A. Carlsson, *Post-buckling and debond propagation in sandwich panels subject to in-plane compression.* Engineering Fracture Mechanics, 2007. 74 (5): p. 794-806.**

107. **U. Hansen, *Compression behavior of FRP sandwich specimens with interface debonds.* Journal of Composite Materials, 1998. 32 (4): p. 335-360.**

108. **A.J. Vizzini and P.A. Lagace, *The buckling of a delaminated sublaminate on an elastic-foundation.* Journal of Composite Materials, 1987. 21 (12): p. 1106-1117.**

109. **A.J. Vizzini and P.A. Lagace, *An elastic-foundation model to predict the growth of delaminations.* Journal of Composites Technology & Research, 1989. 11 (3): p. 81-86.**

110. **C.B. Hwu and J.S. Hu, *Buckling and postbuckling of delaminated composite sandwich beams.* Aiaa Journal, 1992. 30 (7): p. 1901-1909.**

111. **Y. Frostig and O.T. Thomsen, *Non-linear behavior of delaminated unidirectional sandwich panels with partial contact and a transversely flexible core.* International Journal of Non-Linear Mechanics, 2005. 40 (5): p. 633-651.**

112. **W.C. Kim and C.K.H. Dharan, *Facesheet debonding criteria for composite sandwich panels under inplane compression.* Engineering Fracture Mechanics, 1992. 42 (4): p. 643-652.**

113. **W.C. Kim, T.C. Miller, and C.K.H. Dharan, *Strength of composite sandwich panels containing debonds.* International Journal of Solids and Structures, 1993. 30 (2): p. 211-223.**

114. **D. Zenkert, *Strength of sandwich beams with interface debondings.* Composite Structures, 1991. 17 (4): p. 331-350.**

115. **S. Sequeira Tavares, N. Caillet-Bois, V. Michaud, and J.-A.E. Månson. *Non-autoclave processing of sandwich structures: The role of prepreg through thickness air permeability*. in *International Conference on Composite Materials, ICCM 16*. 2007. Kyoto.**

116. **S.K. Deb, *Recent developments in high efficiency photovoltaic cells.* Renewable Energy, 1998. 15 (1-4): p. 467-472.**

117. **A. Goetzberger, C. Hebling, and H.W. Schock, *Photovoltaic materials, history, status and outlook.* Materials Science & Engineering R-Reports, 2003. 40 (1): p. 1-46.**

118. **J.H. Zhao, A.H. Wang, P.P. Altermatt, S.R. Wenham, and M.A. Green, *24% efficient perl silicon solar cell: Recent improvements in high efficiency silicon cell research.* Solar Energy Materials and Solar Cells, 1996. 41 (2): p. 87-99.**

119. **R.C. Neville, *Solar energy conversion, the solar cell.* Second edition ed. 1995: Elsevier.**

120. **H. Matsubara, T. Tanabe, A. Moto, Y. Mine, and S. Takagishi, *Over 27% efficiency GaAs/InGaAs mechanically stacked solar cell.* Solar Energy Materials and Solar Cells, 1998. 50 (3): p. 177-184.**

121. **E. Cestino, *Design of solar high altitude long endurance aircraft for multi payload & operations.* Aerospace Science and Technology. In Press, Uncorrected Proof.**

122. **T. Lamp, K. Reinhardt, and A. Colozza, *Photovoltaic power for long endurance unmanned aerial vehicles.* GRC Technical reports, 1999.**

123. **M.J. Nowlan, J.C. Maglitta, G. Darkazalli, and T. Lamp. *Ultralight photovoltaic modules for unmanned aerial vehicles*. in *26th PVSC*. 1997. Anaheim: IEEE.**

124. **M. Tomas, *Solar electricity, second edition*. Wiley ed. 2000, Southampton.**

125. **A.V. Shah, H. Schade, M. Vanecek, J. Meier, E. Vallat-Sauvain, N. Wyrsch, U. Kroll, C. Droz, and J. Bailat, *Thin-film silicon solar cell technology.* Progress in Photovoltaics, 2004. 12 (2): p. 113-142.**

126. **M. Cid, N. Stem, C. Brunetti, A.F. Beloto, and C.A.S. Ramos, *Improvements in anti-reflection coatings for high-efficiency silicon solar cells.* Surface & Coatings Technology, 1998. 106 (2): p. 117-120.**

127. **J. Zhao and M.A. Green, *Optimized antireflection coatings for high-efficiency silicon solar-cells.* IEEE Transactions on Electron Devices, 1991. 38 (8): p. 1925-1934.**

128. **A.W. Smith and A. Rohatgi, *A new texturing geometry for producing high-efficiency solar-cells with no antireflection coatings.* Solar Energy Materials and Solar Cells, 1993. 29 (1): p. 51-65.**

129. **J.H. Zhao, A.H. Wang, M.A. Green, and F. Ferrazza, *19.8% efficient "Honeycomb" textured multicrystalline and 24.4% monocrystalline silicon solar cells.* Applied Physics Letters, 1998. 73 (14): p. 1991-1993.**

130. **J.M. Gee, W.K. Schubert, H.L. Tardy, T.D. Hund, and G. Robison, *The effect of encapsulation on the reflectance of photovoltaic.* 1994. 2 (-): p. 1558.**

131. **P. Fath, C. Borst, C. Zechner, E. Bucher, G. Willeke, and S. Narayanan, *Progress in a novel high-throughput mechanical texturization technology for highly efficient multicrystalline silicon solar cells.* Solar Energy Materials and Solar Cells, 1997. 48 (1-4): p. 229-236.**

132. **H. Nussbaumer, G. Willeke, and E. Bucher, *Optical behavior of textured silicon.* Journal of Applied Physics, 1994. 75 (4): p. 2202-2209.**

133. **W.A. Brantley, *Calculated elastic constants for stress problems associated with semiconductor devices.* Journal of Applied Physics, 1973. 44 (1): p. 534-535.**

134. **K.E. Petersen. *Silicon as a mechanical material*. 1982: Proceedings of the IEEE.**

135. **T.C. Yi, L. Li, and C.J. Kim, *Microscale material testing of single crystalline silicon: Process effects on surface morphology and tensile strength.* Sensors and Actuators, 2000. 83: p. 172-178.**

136. **L.D. Chen, M.J. Zhang, and S. Zhang, *Determination of bending stress of Si wafer using concentrated load.* Journal of Applied Physics, 1994. 76 (3): p. 1547-1551.**

137. **F. Ericson and J.-A. Schweitz, *Micromechanical fracture strength of silicon.* Journal of applied physics, 1990. 68 (11): p. 5840-5844.**

138. **M. Stefancich, M. Butturi, D. Vincenzi, and G. Martinelli, *Mechanical effects of chemical etchings on monocrystalline silicon for photovoltaic use.* Solar Energy Materials and Solar Cells, 2001. 69 (4): p. 371-377.**

139. **G. Wang, D. Yang, D. Li, Q. Shui, J. Yang, and D. Que, *Mechanical strength of nitrogen-doped silicon single crystal investigated by three-point bending method.* Physica B-Condensed Matter, 2001. 308: p. 450-453.**

140. **C.J. Wilson and P.A. Beck, *Fracture testing of bulk silicon microcantilever beams subjected to a side load.* Journal of microelectromechanical Sysrems, 1996. 5 (3): p. 142-150.**

141. **R. Labbens, *Introduction à la mécanique de la rupture*. 1980: Editions Pluralis.**

142. **Behnken H., Apel M., and Franke D. *Simulation of mechanical stress during bending tests for crystalline wafers*. in *3rd World Conference on Photovoltaic Energy Conversion*. 2003. Osaka, Japan.**

143. **F.I. Baratta, *Requirements for flexure testing of brittle materials*, in *Methods for assessing the structural reliability of brittle materials*, Freiman and Hudson, Editors. 1984, ASTM STP 844: Philadelphia. p. 194-222.**

144. **S. Schoenfelder, M. Ebert, C. Landesberger, K. Bock, and J. Bagdahn, *Investigations of the influence of dicing techniques on the strength properties of thin silicon.* Microelectronics Reliability, 2007. 47 (2-3): p. 168-178.**

145. **D. Kray, H Kampwerth, E. Schneiderlöchner, A. Grohe, and S. W. Glunz. *Comprehensive experimental study on the performance of very thin laser-fired high-efficiency solar cells*. in *19th European Photovoltaic Solar energy Conference*. 2004. Paris.**

146. **W.J. Kröninger. *Flexibility and strength of back-side treated silicon chips*. in *APIA-Seminar*. 2002.**

147. **Schneider A, Rueland E, Kraenzl A, and F. P. *Mechanical and electrical characterisation of thin multi-crystalline silicon solar cells*. in *19thEuropean Solar Energy Conference and Exhibition*. 2004. Paris.**

148. **K.A. Munzer, K.T. Holdermann, R.E. Schlosser, and S. Sterk, *Thin monocrystalline silicon solar cells.* IEEE Transactions electron devices, 1999. 46 (10): p. 2055-2061.**

149. **Schneider A, Bühler G, Huster F, Peter K, and Fath P. *Impact of individual process steps on the stability of silicon solar cells studied with a simple mechanical stability tester*. in *Conference on PV in Europe from PV Technology to Energy Solutions*. 2002. Rome.**

150. **Schneider A, Pernau T, Peter K, and Fath P. *Mechanical wafer stability enhancements and texturing effects of remote downstream plasma etching*. in *3rdWorld Conference on Photovoltaic Energy Conversion*. 2003. Osaka.**

151. **S.C. Agro and R.T. Tucker, *Development of new low-cost. High-performance, PV module encapsulant/packaging materials*, Phase 1 22 October 2002 - 30 September 2003 Annual Technical Report, Editor. 2004, National Renewable Energy Laboratory: Golden, Colorado.**

152. **D. Snowdon, J. Green, P. Cousins, and S. Stone. *Composite curved laminates for the UNSW sunswift II solar array*. in *Solar World Congress*. 2001: ISES.**

153. **F.J. Pern and S.H. Glick, *Photothermal stability of encapsulated Si solar cells and encapsulation materials upon accelerated exposures.* Solar Energy Materials and Solar Cells, 2000. 61 (2): p. 153-188.**

154. **P. Klemchuk, M. Ezrin, G. Lavigne, W. Holley, J. Galica, and S. Agro, *Investigation of the degradation and stabilization of EVA-based encapsulant in field-aged solar energy modules.* Polymer Degradation and Stability, 1997. 55 (3): p. 347-365.**

155. **F. Bonjour, R. Amacher, V. Michaud, B. Cardis, and J.-A.E. Månson. *Vacuum bag processing of large composite structures for America's cup class boats*. in *24th International Conference and Forum - SAMPE Europe Conference*. 2003. Paris.**

156. **R. Olsson, *A simplified improved beam analysis of the DCB specimen.* Composites Science and Technology, 1992. 43 (4): p. 329-338.**

157. ***ASTM D5045 - 91a: Plane-strain fracture toughness and strain energy release rate of plastic materials.* Annual Book of ASTM Standards, 1991. 08.02.**

158. **Q. Benard, M. Fois, and M. Grisel, *Peel ply surface treatment for composite assemblies: Chemistry and morphology effects.* Composites Part A-Applied Science and Manufacturing, 2005. 36 (11): p. 1562-1568.**

159. **L.J. Hart-Smith, *Adhesive bonding of composite structures - progress to date and some remaining challenges.* Journal of Composites Technology & Research, 2002. 24 (3): p. 133-151.**

**160. A.W. Adamson and A.P. Gast, *Physical chemistry of surfaces*. 6th ed. 1997, New-York: John Wiley & Sons.**

**161. A.J. Kinloch, *Adhesion and adhesives: Science and technology*. Reprinted 1990 ed. 1987, London: Chapman and Hall.**

**162. D.E. Packham, *Handbook of adhesion*. 2nd ed. 2005, Chichester: John Wiley & Sons**

**163. R.N. Wenzel, *Resistance of solid surfaces to wetting by water.* Industrial and Engineering Chemistry, 1936. 28: p. 988-994.**

**164. R.N. Wenzel, *Surface roughness and contact angle.* Journal of Physical and Colloid Chemistry, 1949. 53 (9): p. 1466-1467.**

**165. G. Wolansky and A. Marmur, *Apparent contact angles on rough surfaces: The Wenzel equation revisited.* Colloids and Surfaces a-Physicochemical and Engineering Aspects, 1999. 156 (1-3): p. 381-388.**

**166. Q. Benard, M. Fois, and M. Grisel, *Roughness and fibre reinforcement effect onto wettability of composite surfaces.* Applied Surface Science, 2007. 253 (10): p. 4753-4758.**

**167. S.A. Page, R. Mezzenga, L. Boogh, J.C. Berg, and J.-A.E. Manson, *Surface energetics evolution during processing of epoxy resins.* Journal of Colloid and Interface Science, 2000. 222 (1): p. 55-62.**

**168. P.G. Smith and T.G.M. Van De Ven, *Profiles of slightly deformed axisymmetric drops.* Journal of Colloid and Interface Science, 1984. 97 (1): p. 1-8.**

**169. F.M. Orr, L.E. Scriven, and A.P. Rivas, *Pendular rings between solids - meniscus properties and capillary force.* Journal of Fluid Mechanics, 1975. 67 (FEB25): p. 723-742.**

**170. T. Juvonen, J. Harkonen, and R. Kuivalainen, *High efficiency single crystalline silicon solar cells.* Physica Scripta, 2002. T101: p. 96-98.**

**171. Y. Okada and Y. Tokumaru, *Precise determination of lattice-parameter and thermal-expansion coefficient of silicon between 300-K and 1500-K.* Journal of Applied Physics, 1984. 56 (2): p. 314-320.**

**172. B. Singh, J. Bouchet, Y. Leterrier, J.A.E. Månson, G. Rochat, and P. Fayet, *Durability of aminosilane-silica hybrid gas-barrier coatings on polymers.* Surface & Coatings Technology, 2007. 202: p. 208-216.**

**173. A.N. Gent and S.Y. Kaang, *Effect of peel angle upon peel force.* Journal of Adhesion, 1987. 24 (2-4): p. 173-181.**

**174. A.J. Kinloch, C.C. Lau, and J.G. Williams, *The peeling of flexible laminates.* International Journal of Fracture, 1994 (66): p. 45-70.**

**175. L.F. Kawashita, D.R. Moore, and J.G. Williams, *Protocols for the measurement of adhesive fracture toughness by peel tests.* Journal of Adhesion, 2006. 82 (10): p. 973-995.**

**176. D.R. Moore and J.G. Williams, *The determination of adhesive fracture toughness for laminates by the use of different test geometry and consideration of plastic energy correction factors,* in *Fracture of polymers, composites and adhesives ii,* B. R. K. Blackman, A. Pavan, and J. G. Williams, Editors. 2003. p. 341-353.**

**177. *Japanese patent 2003161013 a: Solar cell panel and its mounting method*. 06.06.2003.**

**178. *Japanese patent 2002353489 a: Sandwich panel for mounting solar cell.* 06.12.2002.**

**179. *German patent 197 15 788 c1: Solargenerator für Satelliten*. 08.10.1998.**

**180. *United states patent 4.394.529: Solar cell array with lightweight support structure*. 19.07.1983.**

**181. *United states patent 6.005.184: Solar panels having improved heat dissipation properties.* 21.12.1999.**

**182. *United states patent 4.833.029: Honeycomb facesheet material and honeycomb made therewith*. 23.05.1989.**

**183. *German patent 198 48 747 c1: Solargenerator für Satelliten.* 28.10.1999.**

184. **L. Vitos, A.V. Ruban, H.L. Skriver, and J. Kollar, *The surface energy of metals.* Surface Science, 1998. 411 (1-2): p. 186-202.**

185. **P. Casari and L. Gornet, *Characterization of residual stresses in a composite curved sandwich beam.* Composites Part A-Applied Science and Manufacturing, 2006. 37 (4): p. 672-678.**

186. **Y.N. Cheng and S.Y. Lee, *Reduction of the concentrated residual stress on the edges of a sandwich plate.* Journal of Materials Processing Technology, 2002. 123 (3): p. 371-376.**

187. **J. Ju, B.D. Pickle, R.J. Morgan, and J.N. Reddy, *An initial and progressive failure analysis for cryogenic composite fuel tank design.* Journal of Composite Materials, 2008. 42 (6): p. 569-592.**

188. **E.K. Drown, H. Almoussawi, and L.T. Drzal, *Glass-fiber sizings and their role in fiber matrix adhesion.* Journal of Adhesion Science and Technology, 1991. 5 (10): p. 865-881.**

189. **T. Komine, K. Katoh, and K. Atoh, *Lightweight honeycomb structure|on corrugated and flat carbon fibre bases is useful in MFR. Of sandwich panels for aircraft and machinery*. 1996, Showa Aircraft Ind Co Ltd; Showa Hikouki Kogyo Kk.**

190. **C. Le. *New developments in honeycomb core materials*. in *AF/NASA Sandwich Structures for Space Systems, Ultracor Inc.***

191. **N.K. Naik and P.S. Shembekar, *Elastic behavior of woven fabric composites .1. Lamina analysis.* Journal of Composite Materials, 1992. 26 (15): p. 2196-2225.**

192. **P.S. Shembekar and N.K. Naik, *Elastic behavior of woven fabric composites .2. Laminate analysis.* Journal of Composite Materials, 1992. 26 (15): p. 2226-2246.**

193. **N.K. Naik, P.S. Shembekar, and M.V. Hosur, *Failure behavior of woven fabric composites.* Journal of Composites Technology & Research, 1991. 13 (2): p. 107-116.**

194. **J. Carey, M. Munro, and A. Fahim, *Longitudinal elastic modulus prediction of a 2-d braided fiber composite.* Journal of Reinforced Plastics and Composites, 2003. 22 (9): p. 813-831.**

195. **P. Olivier, J.P. Cottu, and B. Ferret, *Effects of cure cycle pressure and voids on some mechanical-properties of carbon-epoxy laminates.* Composites, 1995. 26 (7): p. 509-515.**

196. **J.M. Tang, W.I. Lee, and G.S. Springer, *Effects of cure pressure on resin flow, voids, and mechanical-properties.* Journal of Composite Materials, 1987. 21 (5): p. 421-440.**

197. **P.O. Hagstrand, F. Bonjour, and J.A.E. Månson, *The influence of void content on the structural flexural performance of unidirectional glass fibre reinforced polypropylene composites.* Composites Part A-Applied Science and Manufacturing, 2005. 36 (5): p. 705-714.**

198. ***ASTM G173-03e1: Standard tables for reference solar spectral irradiances: Direct normal and hemispherical on 37° tilted surface.* Annual Book of ASTM Standards, 2003. 14.04.**

# PUBLICATIONS RELATED TO THIS THESIS

## *Journal papers*

1. J. Rion, Y. Leterrier, J.-A. E. Månson, “Prediction of the adhesive fillet size for skin to honeycomb core bonding in ultra-light sandwich structures”, Accepted in Composite Part A
2. J. Rion, F Demarco, Y. Leterrier, J.-A. E. Månson, “A new video based method for crack propagation and energy release analysis in cantilever beam testing”, Submitted to Composite Science and Technology.
3. J. Rion, S. Stutz, Y. Leterrier, J.-A. E. Månson, “Influence of process pressure on local facesheet instability for ultralight sandwich structures”, Submitted to Journal of Sandwich Structures and Materials
4. J. Rion, Y. Leterrier, J.-A. E. Månson, “Ultra-light asymmetric photovoltaic sandwich structures”, Submitted to Composite Part A

## *Conferences*

- J. Rion, Y. Leterrier, J.-A. E. Månson, “Influence of the adhesive layer on the mechanical properties of ultralight composite sandwich materials”, Solvay Science and Innovation Days, Brussels, September 2005
- J. Rion, A. Geiser, Y. Leterrier, J.-A. E. Månson, “Ultralight composite sandwich structure: optimization of skin to honeycomb core bonding”, 27th International Conference Sampe Europe, Paris, March 2006
- J. Rion, F. Demarco, Y. Leterrier, J.-A. E. Månson, “Damage analysis of ultralight sandwich structures”, ICCM-16 Sixteenth International Conference on Composite Materials, 8 - 13 July 2007, Kyoto, Japan
- J. Rion, S. Stutz, Y. Leterrier, J.-A. E. Månson, “Influence of process pressure on local facesheet instability for ultralight sandwich structures”, ICSS-8 International Conference on Sandwich Structures, 6-8 May 2008, Porto

# CURRICULUM VITAE

Julien Rion
2855 Glovelier, Switzerland
Born on April 10th, 1981

## Education

---

| | |
|---|---|
| 2004-2008 | Ecole Polytechnique Fédérale de Lausanne (EPFL), Laboratoire de Technologie des Composites et Polymères (LTC), Lausanne<br>PhD Thesis : “Optimization of ultralight photovoltaic sandwich structures” |
| 1999-2004 | Ecole Polytechnique Fédérale de Lausanne (EPFL), Lausanne<br>Diploma in Mechanical Engineering : “Finite element analysis of low-cost foot prosthesis”<br>Awards: “prix Cousin” (best results in 1st and 2nd year exams at EPFL), “Prix Bombardier Transport – Vevey Technologies” (best result in mechanical engineering on complete studies duration), “Prix A3-EPFL” (2nd best result in engineering cycle on complete studies duration at EPFL) |
| 2002-2003 | Eidgenössische Technische Hochschule Zürich (ETHZ)<br>Exchange student |
| 1996-1999 | Lycée cantonal de Porrentruy, Jura<br>Baccalaureate type C (scientific), best result with 89/90 pts |

## Professional experience

---

| | |
|---|---|
| 2004-2008 | Ecole Polytechnique Fédérale de Lausanne (EPFL), Laboratoire de Technologie des Composites et Polymères (LTC), Lausanne<br>Research and teaching assistant |